ABSTRACT

Parity Nonconservation in ^{106}Pd, ^{108}Pd and ^{238}U Using Neutron-Transmission and Neutron-Capture Techniques

by

Bret Edward Crawford

Measurements were made of the parity-nonconserving (PNC), helicity-dependent neutron resonance cross sections for epithermal neutrons incident on ^{106}Pd, ^{108}Pd and ^{238}U. By reversing the spin direction of longitudinally polarized, epithermal neutrons produced at the Manuel Lujan Neutron Scattering Center in Los Alamos, the longitudinal cross section asymmetry was measured using neutron-transmission (^{238}U) and neutron-capture (^{106}Pd and ^{108}Pd) techniques. The experiments employed a dynamically polarized proton target to polarize the neutrons and a magnetic neutron-spin flipper. In transmission the neutrons were detected by a 55-element ^{10}B-loaded liquid scintillator. The capture experiment used 24 CsI crystals to detect the neutron-capture γ-rays, a spin-transport system and a neutron polarimeter. In addition to extracting cross section asymmetries, neutron resonance parameters were determined for 12 s-waves and 16 p-waves in ^{106}Pd (60–1900 eV); 9 s-waves and 21 p-waves in ^{108}Pd (100–2300 eV); and 13 s-waves and 24 p-waves in ^{238}U (6–300 eV).

In the analysis of experiments of this type, the compound nucleus is treated statistically and the PNC asymmetries are expected to be randomly distributed about zero. The width of the distribution of asymmetries in a given nucleus is related to the root-mean-squared PNC matrix element, $\mathcal{M}$. In order to compare the strength of the weak interaction in different nuclei, a spreading width, Γ_{W}, can be calculated from $\mathcal{M}$ for each nucleus.

Six resonances in ^{238}U showed effects, three positive and three negative, giving $\mathcal{M} = 0.67^{+0.24}_{-0.16}$ meV and $\Gamma_{\mathrm{W}} = \left(1.35^{+0.97}_{-0.64}\right) \times 10^{-7}$ eV. One negative PNC effect was seen in ^{106}Pd at 593.4 eV. However, the effect is most likely due to a p-wave that is unresolved

from the s-wave at 593.4 eV. If this is true, the lack of p-wave resonance information prohibits further analysis. If the 593.4 eV resonance is in fact a p-wave, then the analysis gives $\mathcal{M} = 11.0^{+7.7}_{-4.5}$ meV and $\Gamma_{\mathrm{w}} = \left(48^{+67}_{-39}\right) \times 10^{-7}$ eV. Further experimentation is required to resolve this issue. No effects were seen in ^{108}Pd which leads to $\mathcal{M} < 4.2$ meV and $\Gamma_{\mathrm{w}} < 7.0 \times 10^{-7}$ eV.

Acknowledgements

I am indebted to many people who have helped me in completing this dissertation. I would first like to thank Dr. Russell Roberson for his guidance as my advisor. His experience and insight have continuously clarified my understanding and pushed me forward. I am continually impressed by his enthusiasm and dedication to physics. I would also like to thank Dr. Gary Mitchell for numerous interesting discussions and his contributions to our understanding of these experiments. I extend thanks also to Dr. Eduard Sharapov for his wealth of knowledge of the physics of neutrons and his spirited interest in things simple and complex.

The experiments described in this dissertation required the efforts of many people, and I am thankful for the opportunity to have worked with the members of the TRIPLE collaboration, which includes scientists from the Los Alamos National Laboratory, the Triangle Universities Nuclear Laboratory, Kyoto University, KEK, the Joint Institute for Nuclear Research, TRIUMF, and Delft University. I would like to thank Dr. David Bowman, whose ingenuity and insistence on excellence pervade these experiments. I am grateful to Dr. Sue Seestrom and Dr. Chris Frankle for the design and construction of a superb capture detector and for their introduction to Los Alamos and work on the mesa. I thank Dr. Yi-Fen Yen for her work on the transmission detector and the initial modeling of the neutron beam and detector response functions. Special thanks goes to Dr. Seppo Penttilä whose expertise and dedication insured the success of these experiments.

I would like to thank Tom Langston for his excellence in electronics and Russ

Mortensen for his tireless work on every part of the beam line. Thanks also to the Duke University Instrument Shop for the construction of the capture target holders. To the fellow graduate students, former or otherwise, Tomohito Haseyama, Dr. Lisa Lowie, Yasuyuki Matsuda, and Dr. Sharon Stephenson, I extend many thanks for all the help getting the experiment up and running, taking shift, discussing the physics, working on the analysis, etc. Also, thanks go to Yasu for his work on the fitting code, FITXS, and to Lisa and Yi-Fen for the dead time and background corrections.

I would like to thank my family and friends for their support. I also appreciate all of the people at TUNL who have created an enjoyable and productive work environment. I thank Dr. Charlie Bowman for his encouragement to pursue a doctorate, in particular at Duke. I would like to thank my parents for giving me the confidence in myself and others that allows endeavors such as these. Finally, I would like to thank Sharon for her presence during this project and the ones to come.

This work was supported by the United States Department of Energy.

To my folks, Bea and Todd Crawford

Contents

List of Figures

List of Tables

Chapter 1

Introduction

1.1 Parity Nonconservation

The connection between the symmetry of a system and conserved quantities has long been understood and is fundamental to physics. Examples of such relationships are time-translation symmetry and the conservation of energy; spatial-translation symmetry and the conservation of linear momentum; and rotational symmetry and the conservation of angular momentum. The above three situations are examples of continuous symmetries, but there are also discrete symmetries such as time reversal, charge conjugation and spatial inversion. The last of these is equivalent to a reflection along one axis coupled with a 180° rotation about that axis and is also called a parity transformation. Since rotational symmetry is believed to hold for all of the four known forces, symmetry under a parity transformation is often referred to as a reflection symmetry. Therefore, the parity transformed system is equivalent to a mirror image of the system. A system has even parity if its wave function does not change sign under a parity transformation. Conversely, if the wave function changes sign, the system is said to have odd parity. Viewed in a mirror, a left-handed coordinate system appears as a right-handed coordinate system, and this corresponds to a parity transformation of the coordinate axes. When the reflection symmetry is broken, the parity of the system is not conserved; that is, the character of the system is changed from being even (odd) under a parity transformation to being odd (even) under a parity transformation.

Until 1956 all of the symmetries listed above were believed to be good symmetries for all of the four known forces. In 1956 Lee and Yang reviewed the status of experiments relevant to parity conservation and concluded that although parity was shown to be conserved by the electromagnetic and strong forces, no experiment had shown one way or the other whether this was true for the weak interaction [Lee56]. Following a proposal for an experiment to test this question by Lee and Yang, Wu and collaborators showed in 1957 that parity was not conserved by the weak interaction [Wu57]. The Wu experiment measured the fore-aft asymmetry of electrons emitted from the β-decay of polarized ^{60}Co nuclei.

Since that time much progress has been made in understanding the weak interaction, in particular the leptonic and semi-leptonic processes, examples of which are $\mu^+ \to e^+ + \nu_e + \bar{\nu}_\mu$ and $n \to p + e^- + \bar{\nu}_e$, respectively [Per87]. However, understanding the non-leptonic or hadronic component has proven more difficult. The hadronic processes can either conserve strangeness ($\Delta S = 0$) or not ($\Delta S = \pm 1$). Since the strangeness conserving hadronic decays are so dominated by the strong interaction, detecting weak decays in the presence of such a large background is very difficult. Therefore, measurements of parity-nonconserving (PNC) interactions between nucleons and nuclei provides the most promising technique for studying the $\Delta S = 0$ hadronic component of the weak interaction.

Nonetheless, these are challenging experiments as the weak component is a very small fraction of the nucleon-nucleon (NN) interaction. The process is usually imagined to proceed by the emission of a meson (π, ρ, ω) from one nucleon through a weak coupling and the absorption of the same meson by the other nucleon through a strong coupling, or vice-versa [Bow93]. Therefore, the relative strength of the weak part to the strong part of the NN interaction can be estimated as the ratio between the strength of the weak coupling and the strength of the strong coupling, $G_{\mathrm{F}} m_\pi^2 / 4\pi \sim 10^{-7}$.

In 1980 Desplanques, Donoghue and Holstein (DDH) [Des80] parameterized the weak NN potential and gave "reasonable ranges" and estimates of "best values" for seven meson coupling constants. The NN experiments below mass 20 that are discussed below can be viewed as attempts to measure these coupling constants.

The most direct method of measuring the DDH parameters is through single NN interactions. Several experiments have been done with p-p and n-p scattering. The proton experiments measured the asymmetry of longitudinally polarized protons incident on unpolarized protons. In the n-p experiments two techniques have been used: measurement of the circular polarization of γ-rays emitted from unpolarized neutrons captured by protons and measurement of the asymmetry in the γ-rays emitted when longitudinally polarized neutrons are captured on protons. Despite the success of these measurements in seeing very small PNC effects (at the 10^{-7} level), the experiments were not able to place very stringent limits on the DDH parameters [Ade85].

Another system in which to look for parity nonconservation is light nuclei. In most cases this system poses problems in analyzing the effect, since a detailed knowledge of all of the relevant nuclear wave functions is required. However, in special cases close lying states of opposite parity, called parity doublets, can be exploited. Not only does the close proximity of the states enhance the size of the measured effect, but it also simplifies the analysis, since to good approximation only a few states are involved in producing the PNC effect. Several successful experiments have been made in three nuclei: the circular polarization of the γ-rays emitted from the decay of the 1081 keV 0^- state in ^{18}F, the circular polarization of the γ-rays emitted from the decay of the 2789 keV $\frac{1}{2}^-$ state in ^{21}Ne and the asymmetry of the γ-rays emitted from the 110 keV $\frac{1}{2}^-$ decay of polarized ^{19}F nuclei. Adelberger and Haxton reviewed the single NN and light nuclei experiments and summarized the limits they place on the meson coupling constants [Ade85].

The last nuclear regime to be discussed and the first to produce PNC effects is that of heavy nuclei. In 1964 Abov measured a non-zero effect in the γ-ray asymmetry from the capture of polarized thermal neutrons on ^{113}Cd [Abo64, Abo74]. This effect and others with thermal neutrons were seen in ^{113}Cd and ^{117}Sn in the 1970s [Kru87]. With sizes of a few times 10^{-4}, the effects in heavy nuclei using thermal neutrons are on average an order of magnitude larger than those seen in light nuclei.

In 1980 Sushkov and Flambaum explained that large PNC effects could be seen in the neutron resonance region due to the mixing of s-wave and p-wave resonances [Sus80, Sus82]. They examined three types of experiments with neutrons and heavy targets: the spin rotation of transversely polarized neutrons, the polarization of an unpolarized neutron beam and the longitudinal asymmetry in a polarized neutron beam. In 1982 Alfimenkov, et al. in Dubna, Russia, measured PNC longitudinal asymmetries in ^{81}Br, ^{111}Cd, ^{117}Sn and ^{139}La [Alf83]. The most surprising effect was at the 0.75 eV p-wave resonance in ^{139}La which showed a PNC effect of nearly 10%, two orders of magnitude larger than anything previously seen. The papers of Sushkov and Flambaum showed that the large effects were due to two types of compound nuclear enhancements (see Section 2.2.2), which implied that these effects were ubiquitous in the dense resonance region of compound nuclei. These experiments and their explanation generated a great deal of excitement and led to the formation of the TRIPLE (Time Reversal and Parity at Low Energies) collaboration[1].

1.2 The TRIPLE Collaboration

Experimentally, the high neutron flux at the Manuel Lujan Neutron Scattering Center (MLNSC) has allowed TRIPLE to extend these experiments to an energy range (~0.5–2000 eV) not available to the Dubna group. With the wider energy range, TRIPLE is able to measure many PNC effects per nucleus; the need for this will become clear later. Theoretically, TRIPLE has developed analysis techniques that allow the extraction of meaningful quantities from the experimental data. If viewed as a continuation of the parity-nonconservation measurements in the $A < 20$ region discussed above, where the primary focus was on measuring the meson coupling constants, the TRIPLE program appears very

[1] See [Bow93] and [Fra93b] for reviews of the TRIPLE experiments.

difficult if not impossible because of the inability to calculate the wave functions of the very complex compound nucleus. A different approach was needed.

In the 1980s great advances were being made in understanding the statistical nature of the compound nucleus. Researchers found that fluctuation properties of compound nuclear resonance data followed the principles of Random Matrix Theory [Boh88]. In addition, the role of symmetries and symmetry breaking was found to be very important. Studies of isospin breaking showed that even a small amount of mixing led to large effects in the fluctuation properties of the resonance level spacing [Mit88, Guh90]. A useful measure of the variation of the strength of the symmetry breaking was found to be the spreading width [Har86],

$$\Gamma_{\mathrm{T}} = 2\pi M_{\mathrm{T}}^2/D, \tag{1.1}$$

where M_T is the isospin nonconserving (Coulomb) matrix element and D is the level spacing. Defined in this way, the spreading width was found to be essentially constant over the entire range in which it was studied ($A = 23$–209).

The nature of symmetry breaking in the compound nucleus illustrated by the isospin studies is believed to also hold for parity, and thus the parity nonconservation experiments can be viewed in this light. The PNC effects are assumed to be random variables from a Gaussian distribution centered at zero, so that by measuring several PNC effects in a single nucleus, the width of the distribution can be extracted. The width of the distribution can be related to the root-mean-squared PNC matrix element and thus a weak spreading width. One of the goals of the TRIPLE collaboration, then, is to measure the weak spreading width as a function of nuclear mass.

It should be mentioned that there remains the possibility of relating the average PNC matrix elements measured by TRIPLE to the meson coupling constants discussed earlier. Although some work has been done in this area [Joh91], it remains a theoretical challenge.

1.3 Experimental Overview

The TRIPLE collaboration measures the total p-wave cross section asymmetry for longitudinally polarized neutrons incident on unpolarized targets. The idea is to make two mirror image measurements of the neutron cross section such as is shown in the cartoon of the TRIPLE experiment in Figure 1.1. Referring to Figure 1.1, the spin, $\vec{s}$, does not reverse sign under a parity transformation (in the mirror reflection), whereas the momentum, $\vec{k}$, does. Therefore, the helicity, defined as $\hat{s} \cdot \hat{k}$, changes sign under a parity transformation, so that a measurement of the cross section for both positive and negative helicities is sensitive to whether parity is conserved in the interaction. The asymmetry between the two cross section measurements, $\mathcal{P}$, is called the parity nonconservation asymmetry and is defined by

$$\mathcal{P} = \frac{\sigma_p^+ - \sigma_p^-}{\sigma_p^+ + \sigma_p^-}, \tag{1.2}$$

where the superscripts refer to the positive and negative helicity neutrons and σ_p indicates the p-wave cross section. The helicity can be changed by either reversing the direction of the neutron momentum or the neutron spin. In the TRIPLE experiments the spin is continuously reversed while measuring the neutron cross sections so that both helicities are measured simultaneously.

The spallation source at the Manuel Lujan Neutron Scattering Center produces a large flux of neutrons in the epithermal range (~0.5–2000 eV). Neutron time of flight (*ToF*) is then used to separate the energies of the neutrons that reach the detector at the end of the beam line. This produces energy spectra such as the ^{238}U transmission spectrum shown in Figure 1.2. The dips in the number of neutron counts versus neutron energy correspond to peaks in the neutron cross section at the energies of resonances. The very large dips (for example near 103 eV and 190 eV) are due to s-wave resonances ($\ell = 0$), whereas the small dips (for example near 63 eV and 153 eV) are due to p-wave resonances ($\ell = 1$). The parity of the neutron resonance is given by $(-1)^\ell$, where ℓ is the orbital angular momentum. Therefore, s-waves have even parity while p-waves have odd parity.

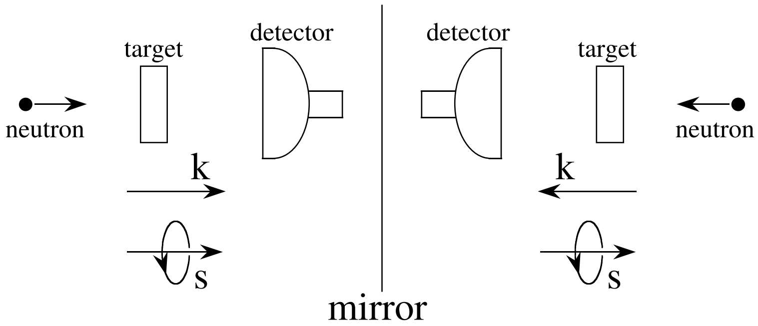

Figure 1.1: Cartoon of parity nonconservation experiment. The neutron helicity is given by $\hat{s} \cdot \hat{k}$ and changes sign under a parity transformation. The parity transformation, which is equivalent to a mirror-image reflection, is accomplished by reversing the momentum direction, $\hat{k}$, as is shown in the figure or by reversing the spin direction, $\hat{s}$.

Helicity-dependent changes in the size of the p-wave cross sections are due to the mixing of s-waves and p-waves and indicate the nonconservation of parity.

The usual experiments have measured the transmission of the neutrons through large samples of target material (the ^{238}U target weighs 9 kg). Typically, PNC measurements can be made in about a week. Such large samples are often not available for isotopically pure targets, however, and this necessitates another measurement method.

Neutron capture has been shown to be a viable method for measuring parity nonconservation [Mas89, Sha91, Shi93]. Neutron time of flight is still used to determine the neutron energy, but rather than detecting the neutrons that are transmitted through the target, the γ-rays emitted when a neutron is captured in the target are detected. Since the transmission detector counts all neutrons that are transmitted, the small change in that number due to a p-wave resonance is swamped by the high count rate unless a very large target is used. The capture measurements are only sensitive to the capture of resonant neutrons and thus are much more sensitive to the small p-waves which are of interest in these measurements. In addition, since the error in the measured asymmetry is proportional to $1/\sqrt{n\sigma_p}$ for capture and $1/n\sigma_p$ for transmission, where $n\sigma_p$ is the number of mean

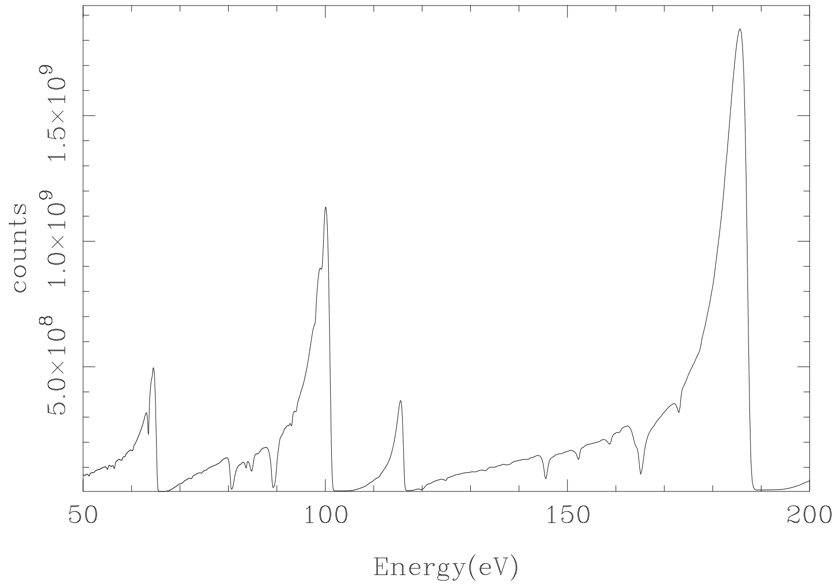

Figure 1.2: Partial energy spectrum for ^{238}U. The large, broad dips in the spectrum correspond to s-wave resonances ($\ell = 0$). The small dips on the sides of the s-waves correspond to p-wave resonances ($\ell = 1$).

free paths in the target for the given p-wave, capture is more sensitive to asymmetries for small targets. Capture is not a useful technique for large targets, however, since multiple scattering of the neutrons becomes a problem once the number of mean free paths is close to or larger than one. In 1995 TRIPLE commissioned a capture detector and other equipment discussed in Chapter 3 to allow measurements with small amounts of material ($\sim$ 100 g). Figure 1.3 shows an energy spectrum for ^{106}Pd taken with the capture detector.

1.4 Current Motivation

The TRIPLE experiments gained greater interest when in 1990 measurements in ^{232}Th revealed a discrepancy with the assumption that the PNC effects were randomly distributed about zero; of the seven non-zero effects, all seven were positive [Fra92]. In addition, these effects happened to have the same sign as the large effect in ^{139}La and

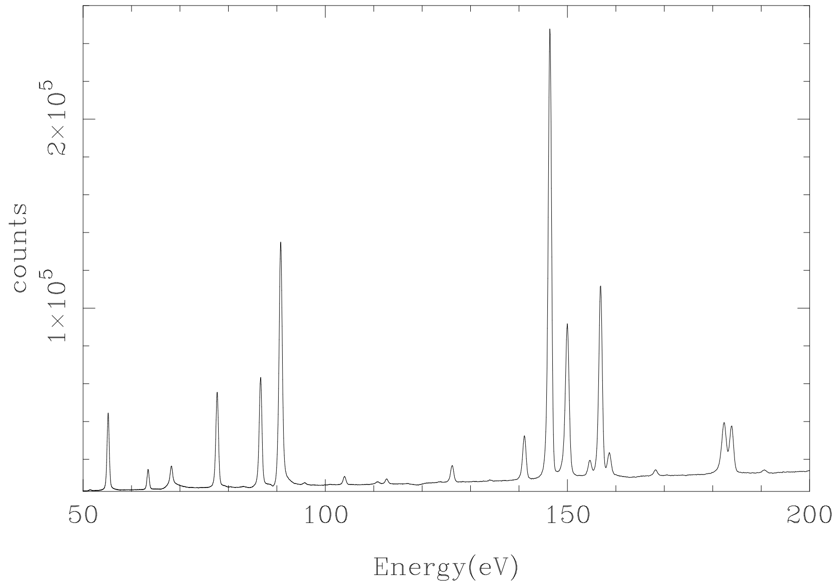

Figure 1.3: Partial energy spectrum for ^{106}Pd. The large peaks in the spectrum correspond to s-wave resonances ($\ell = 0$). The small peaks are due to p-wave resonances ($\ell = 1$) and contaminant resonances.

the one strong effect seen in ^{238}U [Zhu92]. This prompted a great deal of theoretical and experimental interest in what came to be called the "sign effect". Several questions were immediately raised: could the experiment in ^{232}Th be a mistake? Could the weak interaction be so modified in the nucleus that all PNC effects have the same sign or is there something unique about ^{232}Th? To answer these questions, TRIPLE made several improvements to the experimental apparatus with the hope of performing more accurate measurements in ^{232}Th and in ^{238}U. The new ^{232}Th measurement confirmed the sign effect in the ^{232}Th nucleus [Ste96], and the ^{238}U measurement comprises part of this dissertation. Since ^{238}U is so near ^{232}Th on the periodic chart, the ^{238}U measurement provides an especially good test of the universality of the sign effect. In the meantime, work was begun on the theoretical side, primarily trying to understand how nuclear structure could be responsible for the sign effect in ^{232}Th[2]. In an effort to measure the mass dependence of the weak

[2]See [Bow93, Ste96] for reviews of these theories.

spreading width TRIPLE has to date measured PNC effects in eleven different elements in the mass 100 [Low96, See97, Smi97b, Mat97] and mass 230 [Zhu92, Fra92, Ste96] regions. TRIPLE has focused on these two regions because this is where the p-wave strength function peaks [Mug88a], thereby increasing the likelihood of seeing PNC effects.

Other than the mass region to which they belong, the targets divide into two groups, even and odd, that is, targets with zero spin and targets with non-zero spin, and this affects the analysis. With a spin-zero target, an incident neutron can form angular momentum states with $J = \frac{1}{2}$ for s-waves and $J = \frac{1}{2}$ or $\frac{3}{2}$ for p-waves. From angular momentum conservation, only the p-waves with $J = \frac{1}{2}$ can mix with the s-waves. For non-zero targets, the situation is more complicated as there are two types of s-wave states and three types of p-wave states. This complicates the analysis since it is less certain which states are mixing [Bow96a]. In addition, when the spins of the resonances are not known, the uncertainty in the resulting average matrix element can be quite large. Therefore, when possible, it is desirable to use spin-zero targets. Since ^{106}Pd and ^{108}Pd have spins equal to zero and were available in isotopically pure form, they were chosen for these experiments. Only about 20 g each were available, however, and thus these targets were studied in capture.

The ^{238}U transmission measurements made in 1993 and the ^{106}Pd and ^{108}Pd capture measurements made in 1995 are the subject of this dissertation. In addition to extracting PNC effects and root-mean-squared PNC matrix elements, the resonance parameters for all of the measured neutron resonances were extracted. This was made possible by the development of a multilevel fitting code, FITXS. Chapter 2 discusses the calculation of the resonant cross sections and the procedure for extracting of the root-mean-squared PNC matrix element from the data. Chapter 3 describes the experimental apparatus. The analysis procedures are detailed in Chapter 4, and a summary is given in Chapter 5. The fitting code, FITXS, and the measurement of the beam response parameters are discussed in Appendix A. The neutron spin-depolarization calculations are given in Appendix B, and sample fits of all of the resonances studied as well as histograms of the PNC effects are given in Appendix C.

Chapter 2

Theory

This chapter describes the neutron resonance cross section formulae, the manifestation of parity nonconservation in these resonances and the use of a statistical analysis to extract the root-mean-squared PNC matrix element. Because the angular momentum barrier excludes the measurement of $\ell > 1$ resonances for the neutron beam energies used in this work, only s-waves ($\ell = 0$) and p-waves ($\ell = 1$) are discussed. For neutrons incident on ^{106}Pd, ^{108}Pd, and ^{238}U targets the fission channels are very small or nonexistent, and therefore, only neutron and gamma channels are considered.

2.1 Multichannel, Multilevel Neutron Cross Sections

One of the standard cross section approximations used to extract resonance parameters in the compound nuclear resonance region is that of Reich and Moore [Rei58]. The authors derive neutron cross sections that include neutron, fission and gamma channels using a multichannel-multilevel R-Matrix formalism [Wig47, Lan58]. This approach includes interference between all levels and is thus more complete than other formalisms such as that of Feshbach [Fes54], which include interference between only two levels. Since for the present experiments the ratio of the total resonance width, Γ, to the level spacing, D, is small ($\Gamma/D \sim 0.005$), the Feshbach approach is sufficient. However, since the Reich-

Moore formalism is standard and is widely used in the ENDF/B-VI evaluations [Gro97], it is adopted here for the s-waves. For the p-waves, the Reich-Moore approximation reduces to a sum of single-level Breit-Wigner cross sections.

Following Reich-Moore for the case of no fission, the s-wave elastic cross section for a given total angular momentum, J, is given by

$$\sigma^{el}_{s:\mathrm{J}} = \pi \lambda\!\!\!^{-2} g_{\mathrm{J}} \left| 1 - e^{-2ikR} \left[1 + \frac{2if_{\mathrm{J}}}{1 - if_{\mathrm{J}}} \right] \right|^2 , \tag{2.1}$$

where

$$f_{\mathrm{J}} = \sum_{s:\mathrm{J}} \frac{\Gamma^s_n/2}{E_s - E - i\Gamma^s_\gamma/2}, \tag{2.2}$$

$g_{\mathrm{J}} = \frac{2J+1}{2(2I+1)}$, I is the target spin, J is the total resonance angular momentum, k is the neutron wave number, R is the neutron channel radius and the sum is over all s-waves with the same total angular momentum. The experimentally determined potential scattering radius [Mug88b] is used for R. The resonant energy is given by $E_{s,p}$, the neutron width by $\Gamma^{s,p}_n$, the gamma width by $\Gamma^{s,p}_\gamma$ and the total width by $\Gamma^{s,p}$ for the s- and p-waves, respectively. The s-wave capture cross section for a given value of J is given by

$$\sigma^{\gamma}_{s:\mathrm{J}} = 4\pi \lambda\!\!\!^{-2} g_{\mathrm{J}} \frac{\mathrm{Im}\{f_{\mathrm{J}}\}}{\left[1 + \mathrm{Im}\{f_{\mathrm{J}}\}\right]^2 + \mathrm{Re}\{f_{\mathrm{J}}\}^2}. \tag{2.3}$$

Since for p-waves $\Gamma_n \ll \Gamma_\gamma$, the cross sections can be simplified. With the p-wave hard-sphere phase shift [Lyn68] set equal to zero, the elastic cross section for a given value of J with $\Gamma_n \ll \Gamma_\gamma$ is

$$\sigma^{el}_{p:\mathrm{J}} = 4\pi \lambda\!\!\!^{-2} g_{\mathrm{J}} \left| \sum_{p:\mathrm{J}} \frac{i\Gamma^p_n/2}{E_p - E - i\Gamma^p_\gamma/2} \right|^2 , \tag{2.4}$$

where the sum is over all p-waves with the same total angular momentum. This can be further simplified since $\Gamma_\gamma \ll D$, so that

$$\sigma^{el}_{p:\mathrm{J}} = \pi \lambda\!\!\!^{-2} g_{\mathrm{J}} \sum_{p:\mathrm{J}} \frac{\Gamma^p_n \Gamma^p_n}{(E_p - E)^2 + (\Gamma^p)^2/4}, \tag{2.5}$$

where the fact that $\Gamma = \Gamma_n + \Gamma_\gamma \simeq \Gamma_\gamma$ has been used. Similar simplifications can be used for the capture cross section [Rei58] so that

$$\sigma^{\gamma}_{p:\mathrm{J}} = \pi \lambda\!\!\!^{-2} g_{\mathrm{J}} \sum_{p:\mathrm{J}} \frac{\Gamma^p_n \Gamma^p_\gamma}{\left(E_p - E\right)^2 + \left(\Gamma^p\right)^2/4}. \tag{2.6}$$

The neutron widths are calculated at the energy of interest, E, such that

$$\Gamma^{s,p}_n(E) = \Gamma^{s,p}_n(E_{s,p}) \left[E/E_{s,p}\right]^{\ell+1/2}. \tag{2.7}$$

The total cross sections are formed by summing the elastic and capture γ-ray cross sections for all allowed values of J. Resonances with $\ell = 0$, s-waves, can form $J = I \pm \frac{1}{2}$ whereas resonances with $\ell = 1$, p-waves, can form states with $J = I \pm \frac{1}{2}$ or $J = I \pm \frac{3}{2}$. The cross sections are given by

$$\sigma_s = \sum_{J=I-\frac{1}{2}}^{I+\frac{1}{2}} \left(\sigma^{el}_{s:\mathrm{J}} + \sigma^{\gamma}_{s:\mathrm{J}}\right) \tag{2.8}$$

and

$$\sigma_p = \sum_{J=I-\frac{3}{2}}^{I+\frac{3}{2}} \left(\sigma^{el}_{p:\mathrm{J}} + \sigma^{\gamma}_{p:\mathrm{J}}\right). \tag{2.9}$$

As discussed in Appendix A, the above Reich-Moore cross sections are used in the fitting code, FITXS, to calculate the total cross section due to s- and p-waves of all allowed total angular momentum values for all isotopes in the beam.

2.2 Parity Nonconservation in the Compound Nucleus

2.2.1 PNC Cross Section

The effect of parity nonconservation in neutron resonance cross sections can be calculated by assuming that the parity nonconservation arises due to the mixing of two levels of opposite parity, an s-wave and a p-wave for example, with the same total angular momentum [Sus82]. The derivation of the PNC cross section will start with the expression derived by Frankle [Fra91] for the total cross section for two levels, $\ell = 0$ and $\ell = 1$, for the case of longitudinally polarized neutrons incident on a spin-zero target ($I = 0$),

$$\sigma = \pi \lambda\!\!\!^{-2} \sum_{c'} \left(|T_{0c'}|^2 + |T_{1c'}|^2 + 2 f_n \mathrm{Re} \left[T_{0c'} T_{1c'}^* \right] \right), \tag{2.10}$$

where f_n is the neutron polarization, and the sum is over all outgoing channels, c'. The above cross section has the same form for (n, n) and (n, γ) [Van88], and thus the sum over final states includes outgoing neutron and gamma channels. The $T_{cc'}$ matrix elements are calculated using the R-Matrix formalism. The matrix elements can be written as

$$T_{cc'} = \delta_{cc'} - e^{i(\phi_c + \phi_{c'})} W_{cc'}, \tag{2.11}$$

where the subscripts refer to incoming and outgoing channels (primed) and ϕ_c and $\phi_{c'}$ are the hard-sphere phase shifts for the incoming and outgoing channels, respectively. The $\mathbf{W}$ matrix can be written in terms of a level matrix, $\mathbf{A}$, such that

$$W_{cc'} = \delta_{cc'} + P_c^{1/2} \sum_{\lambda\mu} \left(\gamma_{\lambda c} \gamma_{\mu c'} \right) A_{\lambda\mu} P_{c'}^{1/2}, \tag{2.12}$$

where the sum is over all levels, λ and μ; $\gamma_{\lambda c}$ is the reduced width amplitude for level λ and channel c; and P_c and $P_{c'}$ are the penetrability matrices. The penetrability matrices are defined such that the channel width for a given level is given by $\Gamma_{\lambda c} = 2 P_c \gamma_{\lambda c}^2$.

The level matrix is constrained by the equation

$$A_{\lambda\mu} \left(E_\lambda - E \right) - i \sum_{\nu} \sum_{c} P_c \left(\gamma_{\lambda c} \gamma_{\nu c} \right) A_{\nu\mu} = \delta_{\lambda\mu}, \tag{2.13}$$

where the energy shift has been ignored [Lyn68]. From the formulation of the problem as a two level problem, the level matrix has dimension two. Furthermore, since the reduced width amplitudes connect a particular channel to a given level, there are four reduced width amplitudes for each of the neutron and gamma channels corresponding to the four combinations of $\ell = 0$ and $\ell = 1$.

The reduced width amplitudes are directly proportional to the wave functions which are obtained in the following way. Treating the mixing of the s-wave and p-wave as a perturbation of the nuclear Hamiltonian, H, the perturbed Hamiltonian can be written $H' = H + H_{\mathrm{W}}$, where H_{W} is the weak perturbation. First order perturbation theory is then used to express the perturbed wave functions (denoted by primes) in terms of the unperturbed wave functions,

$$\begin{aligned} \psi'_s &= \psi_s + \frac{\langle \psi_s \left| H_w \right| \psi_p \rangle}{E_s - E_p} \psi_p \\ \psi'_p &= \psi_p - \frac{\langle \psi_s \left| H_w \right| \psi_p \rangle}{E_s - E_p} \psi_s . \end{aligned} \tag{2.14}$$

Since the reduced width amplitudes are directly proportional to the wave functions [Lyn68], the perturbed reduced width amplitudes can be written in terms of the unperturbed amplitudes

$$\begin{aligned} \gamma_{00} &= \gamma_s & \gamma_{01} &= \frac{V_{sp}}{E_s - E_p} \gamma_p \\ \gamma_{10} &= -\frac{V_{sp}}{E_s - E_p} \gamma_s & \gamma_{11} &= \gamma_p \end{aligned} \tag{2.15}$$

where $\langle \psi_s \left| H_w \right| \psi_p \rangle$ has been replaced by V_{sp}. The resulting level matrix is

$$\mathbf{A} = \begin{pmatrix} \frac{1}{[S]} & \frac{i}{2} \left(\frac{V_{sp}}{E_s - E_p} \right) \frac{[\Gamma^p - \Gamma^s]}{[S][P]} \\ \frac{i}{2} \left(\frac{V_{sp}}{E_s - E_p} \right) \frac{[\Gamma^p - \Gamma^s]}{[S][P]} & \frac{1}{[P]} \end{pmatrix} , \tag{2.16}$$

where $[S, P] = E_{s,p} - E - \frac{i}{2} \Gamma^{s,p}$ and the total level widths are given by $\Gamma^{s,p} = 2 \sum_c P_c \gamma^2_{(s,p)c}$.

In calculating the $W_{cc'}$ terms it is necessary only to calculate the four angular momentum combinations, recognizing that the prime indicates that the neutron and gamma channels for each of the angular momentum combinations are summed in the sum over outgoing channels in Equation 2.10. Excluding terms with V_{sp}^2 and using the definitions $g_{s,p} = \sqrt{\Gamma_n^{s,p}}$ for the incoming neutron and $g'_{s,p} = \sqrt{\Gamma_{c'}^{s,p}}$ for the outgoing particle, the four $W_{cc'}$ terms can be written

$$\begin{aligned} W_{00} &= 1 + \frac{i g_s g'_p}{[S]} & W_{01} &= \frac{-i V_{sp} g_p g'_s}{[S][P]} \\ W_{10} &= \frac{-i V_{sp} g_s g'_p}{[S][P]} & W_{11} &= 1 + \frac{i g_p g'_p}{[P]} . \end{aligned} \tag{2.17}$$

Substituting these expressions into the $T_{cc'}$ terms in Equation 2.10, excluding all V_{sp}^2 terms, summing over the two angular momentum states and neglecting the hard-sphere phase shifts which are small at epithermal energies, the total cross section is

$$\sigma = \pi \lambda\!\!\!^{-2} \sum_{n',\gamma'} \left(|T_{00}|^2 + |T_{11}|^2 + 2 f_n Re\left[T_{00} T_{10}^* + T_{01} T_{11}^*\right] \right)$$

$$= \pi \lambda\!\!\!^{-2} \sum_{n',\gamma'} \left(\begin{array}{c} \left| \frac{-i g_s g_s'}{[S]} \right|^2 + \left| \frac{-i g_p g_p'}{[P]} \right|^2 \\ \\ -\, 2 f_n \mathrm{Re}\left[\frac{g_s g_s' V_{sp} g_s' g_p}{[S][S]^*[P]^*} + \frac{g_s g_p' V_{sp} g_p' g_p}{[S][P][P]^*} \right] \end{array} \right) \tag{2.18}$$

$$= \pi \lambda\!\!\!^{-2} \left(\begin{array}{c} \frac{\Gamma_n^s \Gamma^s}{(E_s - E)^2 + (\Gamma^s)^2/4} + \frac{\Gamma_n^p \Gamma^p}{(E_p - E)^2 + (\Gamma^p)^2/4} \\ \\ -\, \frac{2 f_n V_{sp} \sqrt{\Gamma_n^s \Gamma_n^p}\left[\Gamma^s (E_p - E) + \Gamma^p (E_s - E)\right]}{\left[(E_s - E)^2 + (\Gamma^s)^2/4\right]\left[(E_p - E)^2 + (\Gamma^p)^2/4\right]} \end{array} \right)$$

where in the first two expressions the sum is over the outgoing particles for the primed quantities. The difference between the cross sections for the two helicity states is given by

$$\Delta\sigma = -4\pi \lambda\!\!\!^{-2} f_n \frac{V_{sp} \sqrt{\Gamma_n^s \Gamma_n^p}\left[\Gamma^p (E_s - E) + \Gamma^s (E_p - E)\right]}{\left[(E_s - E)^2 + (\Gamma^s)^2/4\right] + \left[(E_p - E)^2 + (\Gamma^p)^2/4\right]}, \tag{2.19}$$

which agrees with previous derivations [Bun83, Van88]. Traditionally the PNC asymmetry, $\mathcal{P}$, used in the analysis of experimental data is defined to be the difference over the sum of the p-wave resonance cross section. Evaluating the above expression at the p-wave energy and using the fact that $|E_s - E_p| \gg \Gamma_p$, the PNC asymmetry can be found,

$$\mathcal{P} \equiv \frac{\sigma_p^+ - \sigma_p^-}{\sigma_p^+ + \sigma_p^-} \simeq -2 f_n \frac{V_{sp}}{(E_s - E_p)} \sqrt{\frac{\Gamma_n^s}{\Gamma_n^p}}, \tag{2.20}$$

where

$$\sigma_p^+ + \sigma_p^- = 2\pi \lambda\!\!\!^{-2} \frac{\Gamma_n^p \Gamma^p}{(E_p - E)^2 + (\Gamma^p)^2/4} \tag{2.21}$$

has been used.

2.2.2 Enhancements in the Compound Nucleus

Inspection of equation 2.20 reveals two forms of enhancement of the PNC effect in the compound nucleus relative to the same effect in the single particle regime. The first to be discussed is often called dynamic enhancement and refers to the $\frac{V_{sp}}{(E_s - E_p)}$ part of Equation 2.20. Following Sushkov [Sus82], the compound nuclear states can be formed from a sum of single particle states such that the matrix element can be written as

$$V_{sp} = \sum_{i,j}^{N} a_i b_j^* \langle i \,| H_w |\, j \rangle. \tag{2.22}$$

By taking the ratio of the range of the strong interaction inside the nucleus ($\Delta E \sim 1$ MeV) to the compound nuclear level spacing of heavy nuclei ($D \sim 10$ eV), the number of single particle states, N, is estimated to be $\sim 10^5$. The matrix element between single particle states can be estimated in the following way. The single particle matrix element, $\langle i \,| H_w |\, j \rangle$, is expected to be nonzero only when the two wave functions differ by a single particle and thus for only a few values of j for a given i. Furthermore, the nonzero elements are expected to have random sign, making the sum in Equation 2.22 incoherent. From the normalization of the wave functions, the coefficients, a_i and b_j, have magnitudes of order $1/\sqrt{N}$. Therefore, one can write

$$\langle V_{sp}^2 \rangle \simeq \sum_{i=1}^{N} \left(\frac{\langle H_{\mathrm{W}} \rangle}{N} \right)^2 = \frac{\langle H_{\mathrm{W}} \rangle^2}{N}. \tag{2.23}$$

Since

$$\frac{\Delta E}{D} \sim N, \tag{2.24}$$

one can write

$$\frac{V_{sp}}{D} \sim \sqrt{N} \frac{\langle H_{\mathrm{W}} \rangle}{\Delta E}, \tag{2.25}$$

leading to a dynamic enhancement of $\sqrt{N}$. For $N = 10^5$ the dynamic enhancement is roughly 300.

The other type of enhancement is usually called kinematic enhancement and results from the ratio of the neutron widths in Equation 2.20. The neutron widths can be expressed in terms of the penetrabilities of the preceding section, where the penetrabilities are given by [Lyn68]

$$P_0 = kR, \quad P_1 = \frac{(kR)^3}{1 + (kR)^2} \sim (kR)^3 . \tag{2.26}$$

For these experiments $R \sim 10$ fm, and for a 1 eV neutron $k \sim 2 \times 10^{-4}$ fm^{-1}. In such a case the kinematic enhancement is quite large,

$$\sqrt{\frac{\Gamma_n^s}{\Gamma_n^p}} = \frac{1}{kR} \sim 500. \tag{2.27}$$

Combining the dynamic and kinematic enhancements leads to an overall enhancement of $\sim 10^5$.

Although these calculations are only estimates, it is interesting to compare the average level of enhancement for the ^{238}U and ^{106,108}Pd experiments. Table 2.1 shows that

Table 2.1: Comparison of ^{238}U and ^{106}Pd PNC enhancements. The column labeled "Average E" lists the average energy of the p-waves analyzed. The dynamic enhancement is given by $\sqrt{\frac{1\text{ MeV}}{D}}$, and the kinematic enhancement is given by $\frac{1}{kR} = \frac{4552}{R\sqrt{E}}$.

				Enhancements		
Isotope	D (eV)	R (fm)	Average E (eV)	Dynamic	Kinematic	Total
^{238}U	21	10	150	220	40	8800
^{108}Pd	159	7	1000	80	20	1600

for the same statistical precision the ^{238}U experiment is ~ 6 times more sensitive to parity nonconservation than the ^{106}Pd and ^{108}Pd experiments. The difference is due primarily to the large level spacing in the even mass 100 targets. The dynamic enhancement goes as the inverse of the square root of the level spacing. The kinematic enhancement is affected in a more indirect way. Since the level spacing is much larger in the even mass 100 targets, there are fewer p-waves in a given energy range. Thus, to include about the same number of p-waves in the Pd measurement as in the ^{238}U measurement, it is necessary to include higher energy resonances. Hence, on average the kinematic enhancement is less.

2.3 Statistical Distribution of PNC Effects

The expression for the PNC asymmetry in Equation 2.20 was derived considering the mixing between only two levels. However, in general a given p-wave can mix with all s-waves. The asymmetry due to all s-waves can be written

$$\mathcal{P}_p = \sum_s \frac{-2V_{sp}}{(E_s - E_p)} \sqrt{\frac{\Gamma_n^s}{\Gamma_n^p}}\,, \tag{2.28}$$

where it is assumed that the $\mathcal{P}_p$ values have been corrected for neutron polarization (see Equation 2.20). The sum of two level mixing is a reasonable approximation given the large spacing between levels ($\Gamma/D \ll 1$) for these nuclei.

From studies of compound nuclear energy spacing [Haq82] and reduced width amplitudes [Mit85], it has been found that the compound nucleus can be treated statistically. Thus, it is assumed that the matrix elements in Equation 2.28 are random variables from a Gaussian distribution with a mean of zero. Since the $\mathcal{P}_p$ values are sums of Gaussian random variables, they are also random variables from a Gaussian distribution with a mean of zero. If the variance of the matrix elements is defined to be $\mathcal{M}^2$, then the probability density function for the $\mathcal{P}_p$ values with errors $\delta\mathcal{P}_p$ is

$$\mathrm{PDF}(\mathcal{P}_p) = \frac{1}{\sqrt{2\pi\left(A_p^2 M^2 + \delta\mathcal{P}_p^2\right)}} e^{-\frac{\mathcal{P}_p^2}{2(A_p^2 M^2 + \delta\mathcal{P}_p^2)}}\,, \tag{2.29}$$

where

$$A_p^2 = \sum_s \left[\frac{2}{(E_s - E_p)} \sqrt{\frac{\Gamma_n^s}{\Gamma_n^p}}\right]^2. \tag{2.30}$$

Since the $\mathcal{P}_p$ values are random variables, a measurement of a single PNC effect says little about the nature of the weak component of the nuclear interaction. However, by measuring several effects in a given nucleus the root-mean-squared matrix element, $\mathcal{M}$, can be found. A likelihood analysis is used to extract $\mathcal{M}$ from a group of $\mathcal{P}_p$ values.

2.4 Root-Mean-Squared PNC Matrix Element, $\mathcal{M}$

2.4.1 Extraction of $\mathcal{M}$ from Likelihood Analysis

The likelihood function is formed by taking the product of the probability density functions for each $\mathcal{P}_p$ value. Equation 2.29 is the probability density function if the p-wave has $J = \frac{1}{2}$. If the resonance has $J = \frac{3}{2}$ then from angular momentum conservation there can be no mixing. Thus, the $\mathcal{P}_p$ distribution is due only to the measurement uncertainty,

$$\mathrm{PDF}(\mathcal{P}_p) = \frac{1}{\sqrt{2\pi\delta\mathcal{P}_p^2}} e^{-\frac{\mathcal{P}_p^2}{2\delta\mathcal{P}_p^2}}. \tag{2.31}$$

If the resonance spin is unknown the probability density function is given by

$$\mathrm{PDF}(\mathcal{P}_p) = \frac{p}{\sqrt{2\pi\left(A_p^2 M^2 + \delta\mathcal{P}_p^2\right)}} e^{-\frac{\mathcal{P}_p^2}{2\left(A_p^2 M^2 + \delta\mathcal{P}_p^2\right)}} + \frac{q}{\sqrt{2\pi\delta\mathcal{P}_p^2}} e^{-\frac{\mathcal{P}_p^2}{2\delta\mathcal{P}_p^2}}, \tag{2.32}$$

where p and q are the respective probabilities for a given resonance to have $J = \frac{1}{2}$ or $J = \frac{3}{2}$.

Neglecting experimental limitations, p and q can be found from a calculation of the spin distribution, $F(J)$ [Gil65],

$$F(J) \simeq \frac{2J+1}{2\sigma_c^2} \exp - \frac{(J+1/2)^2}{2\sigma_c^2}, \tag{2.33}$$

where the spin cutoff parameter, σ_c, [vE88] is given by

$$\sigma_c = 0.98 A^{0.29}, \tag{2.34}$$

and A is the target mass number. The probabilities p and q can be written

$$p = \frac{F\left(\frac{1}{2}\right)}{F\left(\frac{1}{2}\right) + F\left(\frac{3}{2}\right)} \qquad \text{and} \qquad q = \frac{F\left(\frac{3}{2}\right)}{F\left(\frac{1}{2}\right) + F\left(\frac{3}{2}\right)}. \tag{2.35}$$

In an experimental measurement only resonances above a certain size will be measured. The fraction of the total number of p-waves that are measured, f, can be estimated as the ratio of the number of p-waves analyzed to the total number expected. For a spin-zero target the total number of p-waves is expected to be $\sim 3\Delta E/D$, where ΔE is the range of energies analyzed and D the s-wave level spacing. The fraction f can also be related to a minimum width parameter, $u = \frac{\gamma_{1/2}^{min}}{\langle\gamma_{1/2}\rangle}$, by integrating Porter-Thomas distributions in the width parameter, $y = \frac{\gamma^2}{\langle\gamma^2\rangle}$, for the $p\frac{1}{2}$ and $p\frac{3}{2}$ resonances,

$$\begin{aligned} f &= p\int_{u^2}^{\infty} \frac{1}{\sqrt{2\pi y}} e^{-y/2}\, dy + q\int_{\frac{q}{p}u^2}^{\infty} \frac{1}{\sqrt{2\pi y}} e^{-y/2}\, dy \\ &= p\,\mathrm{erfc}\left(u/\sqrt{2}\right) + q\,\mathrm{erfc}\left(\sqrt{\frac{q}{2p}}u\right). \end{aligned} \tag{2.36}$$

Given the experimental value for f, the above equation can be solved for u. Finally, a new p' and a new $q' = 1 - p'$ are found from the u and f values using,

$$p' = p\,\mathrm{erfc}\left(\sqrt{\frac{q}{2p}}u\right)/f. \tag{2.37}$$

In general the likelihood function can contain a mixture of probability distribution functions, for the case that the spins are known (L_k) and for the case that they are not known (L_{unk}),

$$L_k(m) = N_\circ \prod_{p\frac{1}{2}} \frac{1}{\sqrt{2\pi\left(A_p^2 m^2 + \delta\mathcal{P}_p^2\right)}} e^{-\frac{\mathcal{P}_p^2}{2\left(A_p^2 m^2 + \delta\mathcal{P}_p^2\right)}} \tag{2.38}$$

$$L_{unk}(m) = N_\circ \prod_{p} \left[\frac{p'}{\sqrt{2\pi\left(A_p^2 m^2 + \delta\mathcal{P}_p^2\right)}} e^{-\frac{\mathcal{P}_p^2}{2\left(A_p^2 m^2 + \delta\mathcal{P}_p^2\right)}} + \frac{q'}{\sqrt{2\pi\delta\mathcal{P}_p^2}} e^{-\frac{\mathcal{P}_p^2}{2\delta\mathcal{P}_p^2}}\right], \tag{2.39}$$

where $\mathcal{M}$ has been changed to m to indicate that it is now the variable of the likelihood function. If there is mixed knowledge about resonance spins, then the likelihood function is a product of Equation 2.38 for the resonances whose spins are known and Equation 2.39 for the resonances whose spins are not known. $N_\circ$ is the normalization constant and is found by normalizing the likelihood function to the peak.

A plot of $L(m)$ versus m gives the likelihood for the distribution of matrix elements to have a variance of m. The peak of the likelihood function gives the most likely value of m, $\mathcal{M}$, and the width is an indication of the uncertainty in this determination.

2.4.2 Assigning Errors in $\mathcal{M}$

When the likelihood function has a well defined peak away from $m = 0$, the uncertainty in $\mathcal{M}$ can be found by assuming that since the likelihood function is a product of Gaussians, the error, $\Delta\mathcal{M}$, corresponds to where $L(m) = e^{-1/2}L(\mathcal{M})$ [Ead71].

When a measurement fails to produce statistically significant values of $\mathcal{P}$, then the likelihood function peaks at $m = 0$. It is then desirable to place an upper limit on expected values of $\mathcal{M}$. The upper limit is given by the value of m below which falls 68% of the area under the likelihood curve. The calculation of areas requires integrating the likelihood function. However, in most cases this integral divergences. The terms for unknown spins in Equation 2.39, can be rewritten for large m,

$$\lim_{m\to\infty} L(m) = N_\circ \prod_{p=1}^{n} \left[\frac{p'}{\sqrt{2\pi A_p m}} + \frac{q'}{\sqrt{2\pi\delta\mathcal{P}_p^2}} e^{-\frac{\mathcal{P}_p^2}{2\delta\mathcal{P}_p^2}} \right]. \tag{2.40}$$

The integral of this expression diverges at large large m due to the constant term for the $p\frac{3}{2}$ resonances and the terms that contain $1/m$ from the $p\frac{1}{2}$ resonances. In order to estimate the errors in $\mathcal{M}$, the likelihood function needs to be made integrable[1].

Consider the case that all p-waves have spin 1/2. For this case, $\lim_{m\to\infty} L(m) \propto 1/M^n$ for n resonances, and thus the integral of the likelihood function converges as long as $n > 1$. In other words, what causes the likelihood function to diverge is the possibility of having less than two $p\frac{1}{2}$ resonances. The likelihood function for the case of 0 $p\frac{1}{2}$ resonances and n $p\frac{3}{2}$ resonances is

$$L(m) = N_\circ \prod_{p=1}^{n} \left[\frac{q'}{\sqrt{2\pi\delta\mathcal{P}_p^2}} e^{-\frac{\mathcal{P}_p^2}{2\delta\mathcal{P}_p^2}} \right], \tag{2.41}$$

[1]The analysis technique used here was suggested by J. D. Bowman.

and the probability for this being the case for n resonances is

$$\begin{pmatrix} n \\ 0 \end{pmatrix} q'^{n}. \tag{2.42}$$

For the case of 1 $p\frac{1}{2}$ resonance and $(n-1)$ $p\frac{3}{2}$ resonances, the likelihood function can be written

$$L(m) = N_\circ \frac{p'}{\sqrt{2\pi\left(A_p^2 m^2 + \delta\mathcal{P}_p^2\right)}} e^{-\frac{\mathcal{P}_p^2}{2\left(A_p^2 m^2 + \delta\mathcal{P}_p^2\right)}} \prod_{p=2}^{n} \frac{q'}{\sqrt{2\pi\delta\mathcal{P}_p^2}} e^{-\frac{\mathcal{P}_p^2}{2\delta\mathcal{P}_p^2}} \tag{2.43}$$

with the probability for occurrence

$$\begin{pmatrix} n \\ 1 \end{pmatrix} p'^{1} q'^{n-1}. \tag{2.44}$$

Since these expressions are what cause the integral of the likelihood function to diverge, a non-divergent likelihood function can be formed by subtracting from the usual likelihood function, the likelihood functions for the case of zero $p\frac{1}{2}$ resonances and the case of one $p\frac{1}{2}$ resonance. It should be noted that there is one term such as Equation 2.41 and n terms such as Equation 2.43 contained in the likelihood function of Equation 2.39. For the case of $\mathcal{M} = 0$ and unknown spins the integrable likelihood function is

$$L(m) = N_\circ \left(\begin{array}{l} \displaystyle\prod_{p=1}^{n} \left[\frac{p'}{\sqrt{2\pi\left(A_p^2 m^2 + \delta\mathcal{P}_p^2\right)}} e^{-\frac{\mathcal{P}_p^2}{2\left(A_p^2 m^2 + \delta\mathcal{P}_p^2\right)}} + \frac{q'}{\sqrt{2\pi\delta\mathcal{P}_p^2}} e^{-\frac{\mathcal{P}_p^2}{2\delta\mathcal{P}_p^2}} \right] \\ \displaystyle - \sum_{i=1}^{n} \left[\frac{p'}{\sqrt{2\pi\left(A_i^2 m^2 + \delta\mathcal{P}_i^2\right)}} e^{-\frac{\mathcal{P}_i^2}{2\left(A_i^2 m^2 + \delta\mathcal{P}_i^2\right)}} \prod_{p\neq i}^{n} \frac{q'}{\sqrt{2\pi\delta\mathcal{P}_p^2}} e^{-\frac{\mathcal{P}_p^2}{2\delta\mathcal{P}_p^2}} \right] \\ \displaystyle - \prod_{p=1}^{n} \frac{q'}{\sqrt{2\pi\delta\mathcal{P}_p^2}} e^{-\frac{\mathcal{P}_p^2}{2\delta\mathcal{P}_p^2}} \end{array} \right). \tag{2.45}$$

This procedure increases the uncertainty of the resulting analysis by the amount given by the probability of having less than 2 $p\frac{1}{2}$ resonances, which is typically small. If 20 resonances are analyzed with $p' = 1/3$ and $q' = 2/3$, the probability for having 0 or 1 $p\frac{1}{2}$ resonances is 0.3%.

2.5 Weak Spreading Width

In order to compare the strength of the weak interaction in nuclei of different mass, $\mathcal{M}$ is converted to a weak spreading with, Γ_{W} [Wei89]. The weak spreading with is defined by

$$\Gamma_{\mathrm{W}} \equiv 2\pi \frac{\mathcal{M}^2}{D}. \tag{2.46}$$

In this equation D is the level spacing for the p-waves of the same total angular momentum as the resonances analyzed to determine $\mathcal{M}$. For spin-zero targets, D is for the $p\frac{1}{2}$ resonances. Since the $s\frac{1}{2}$ and $p\frac{1}{2}$ resonances should have the same level density and since the s-wave level spacing is more accurately known, the s-wave level spacing is used for D.

Chapter 3

Experimental Apparatus

In order to measure the longitudinal asymmetry in the total neutron cross section for longitudinally polarized neutrons incident on heavy targets, an apparatus was developed to take advantage of the high flux, epithermal neutron beams at the Manuel Lujan Neutron Scattering Center (MLNSC) in Los Alamos. In addition to the neutron beam, the experimental apparatus consists of a neutron flux monitor, a neutron polarizer, a spin flipper which has the ability to rotate the neutron spins 180°, transmission and capture detectors, and a data acquisition system. For the transmission experiments there is also a target chiller that cools the transmission target to liquid nitrogen temperature. For the capture experiments, there is a spin transport system which preserves the neutron spin direction as the neutrons travel the length of the beam line and a neutron polarimeter which monitors the neutron polarization at the end of the beam line.

Schematics of the beam line setup for transmission and capture experiments are shown in Figures 3.1 and 3.2. In the transmission experiment the target is placed at the end of the spin flipper so that there is no depolarization of the neutrons before they interact with the target. The 60 m flight path is needed to separated the different energy neutrons in time, thereby yielding a neutron time-of-flight spectrum which can be converted to a neutron energy spectrum (See Section 4.1.3). Since in capture the neutron time of flight is determined through the detection of capture γ-rays, the target and the capture detector are placed at the end of the 60 m flight path. This necessitates a spin-transport system to preserve the spins of the neutrons as the travel from the end of the spin flipper to the target. By flipping the spin of the neutrons, two neutron time-of-flight spectra are taken, one for each helicity state. By comparing the p-wave cross sections of the two spectra, neutron resonance asymmetries are measured.

Each of the pieces of equipment are discussed in the following sections. The equipment for the transmission experiments have been discussed previously [Rob93, Zhu91, Fra91, Ste96, Low96].

3.1 Neutron Beam

The MLNSC epithermal neutron beam is produced by the spallation process when 800 MeV protons from the Los Alamos Neutron Science Center (LANSCE) linear accelerator strike a tungsten target. The spallation process proceeds in two steps. In the first step, the highly energetic incident particles (protons in this case) interact directly with the nucleons of the target producing an intranuclear cascade of energetic nucleons and pions. Many of these hadrons collide with nearby nuclei leaving them in highly excited states. During second step of the spallation process, called the evaporation phase, these excited nuclei de-excite emitting primarily neutrons [Rus91].

The LANSCE facility produces H^+ and H^- ions that are initially accelerated to 750 keV, at which time they are chopped and bunched to create $\sim 800\ \mu$s macro-pulses at a rate of 120 Hz (see Figure 3.3). The beams (H^+, H^-) are then accelerated to 100 MeV in a 62 m long 201.25 MHz drift tube, and finally to 800 MeV in the 48-sector coupled-cavity accelerator operating at 805 MHz. The macro pulses contain micro-pulses ~ 60 ps wide separated by ~ 5 ns.

Twenty of the 120 macro-pulses per second are H^- ions which are deflected to the Proton Storage Ring (PSR). Before injection into the LANSCE linac, the H^- macro-pulses

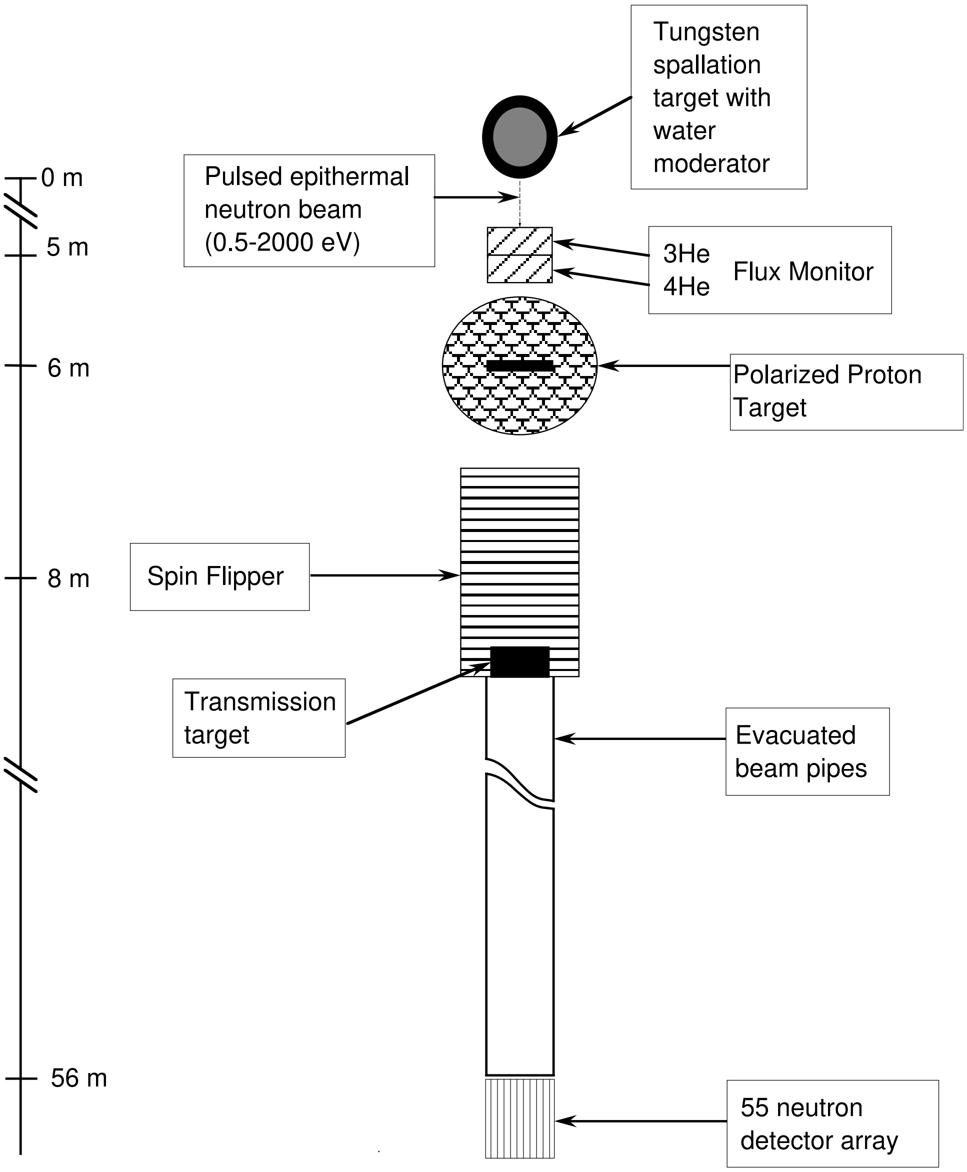

Figure 3.1: Beamline schematic for transmission.

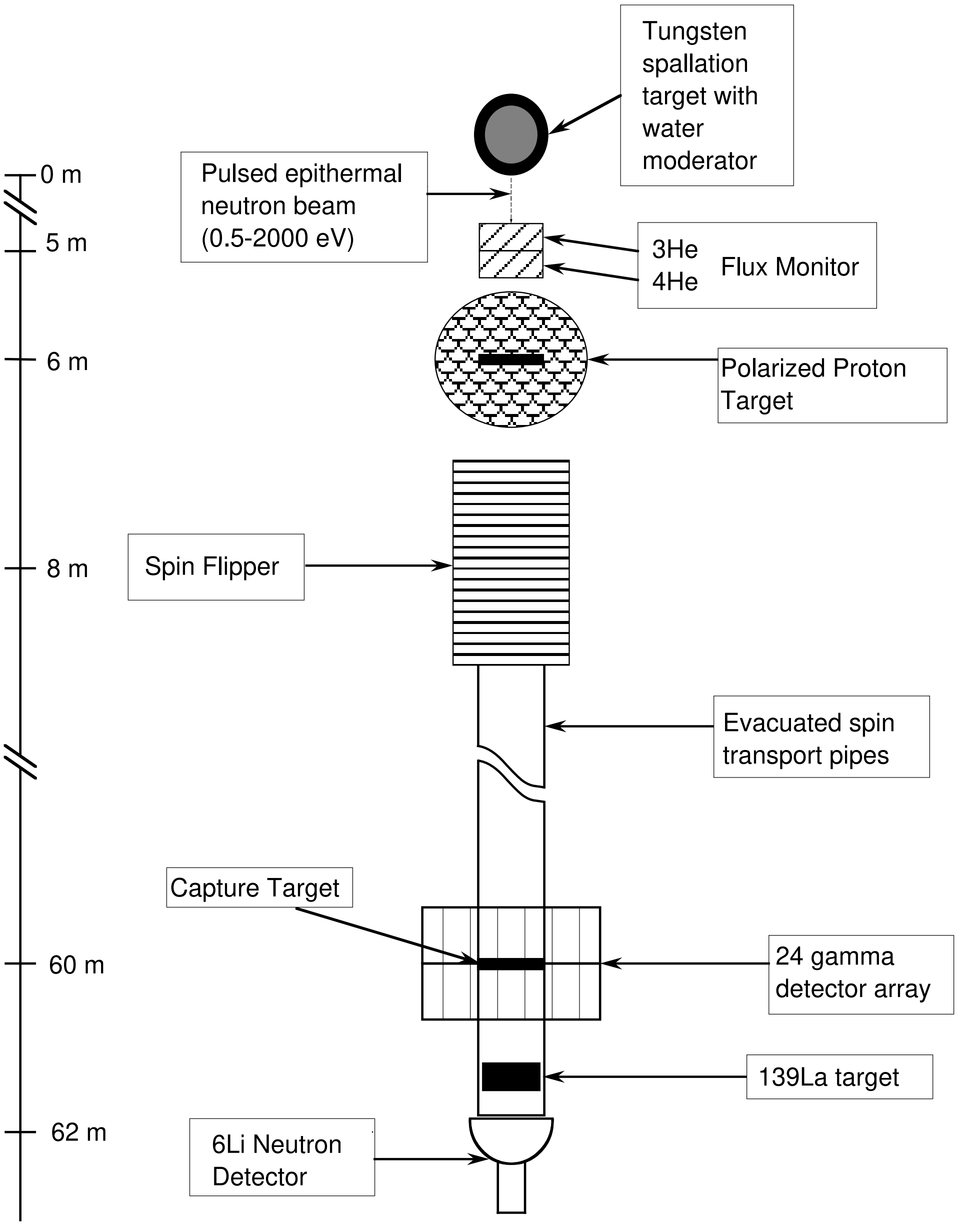

Figure 3.2: Beamline schematic for capture.

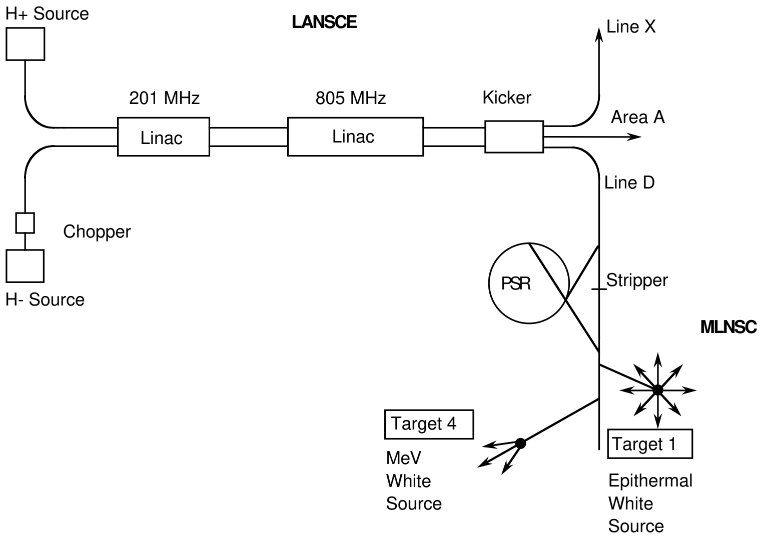

Figure 3.3: LANSCE and MLNSC beam schematic.

are chopped to produce 250 ns-wide pulses separated by 110 ns. Just before being injected into the PSR, the H^- beam is stripped of one electron by a strong transverse field. The second electron is removed by a 200 μg/cm^2 Carbon foil located in the PSR. Since the transit time around the PSR is 360 ns, the 250 ns proton bunches are stacked one bunch on top of another with a 110 ns gap and accumulated in the PSR. The resulting proton pulse has the shape of an isosceles triangle, where the base of the pulse is 250 ns long. The accumulated 20 Hz, 70 μA proton beam is then ejected from the PSR and directed vertically downward onto the tungsten spallation target.

The spallation target consists of two 10 cm diameter pieces of tungsten oriented vertically. The upper (7.25 cm long) and lower (27 cm long) pieces are separated by a 14 cm gap. Around the gap are four moderators which are viewed by 12 beam-lines. The moderator for flight-path 2 (the beam line used by the TRIPLE collaboration) is a high-resolution water moderator with gadolinium poison and a cadmium decoupler/liner. All of the moderators are surrounded by a beryllium reflector.

For each incident proton the spallation process produces approximately 17 neutrons with energies up to 800 MeV with the distribution peaking at about 2 MeV [Rus91]. The moderator serves to reduce the neutron energies to the epithermal range such that the energy distribution peaks at about 40 meV [Lis90].

In addition to the width of 250 ns the neutrons acquire from the proton beam, further time broadening is introduced by the neutron moderation process. As discussed in Appendix A, the neutron beam timing resolution can be described by the sum of two convolutions between a Gaussian (G) and an exponential (E),

$$G(t, t_0, \eta) \otimes E(t, t_0, \tau_1) + \epsilon\, G(t, t_0, \eta) \otimes E(t, t_0, \tau_2), \tag{3.1}$$

where

$$G(t, t_0, \eta) = \frac{1}{\sqrt{2\pi\eta^2}} e^{\frac{-(t-t_0)^2}{2\eta^2}} \tag{3.2}$$

and

$$E(t, t_0, \tau) = \frac{1}{\tau} e^{-\frac{t-t_0}{\tau}} u(t - t_0). \tag{3.3}$$

The function $u(t-t_0)$ is the unit step function. From Monte-Carlo studies and experimental measurements discussed in Appendix A, the resolution parameters are given by

$$\begin{aligned} \epsilon &= 0.20 \\ t_0 &= 2.79 \times E^{-0.48} \quad \mu\text{s} \\ \eta &= 0.65 \times E^{-0.51} \quad \mu\text{s} \\ \tau_1 &= 0.99 \times E^{-0.37} \quad \mu\text{s} \\ \tau_2 &= 3.90 \times E^{-0.38} \quad \mu\text{s} \end{aligned} \tag{3.4}$$

where E is in units of eV.

Measurements of the flux [Rob93] give the number of neutrons, ΔN, between the energy interval E and $E + \Delta E$ to be

$$\Delta N = 5.8 \times 10^{-3} \frac{\Delta E}{E^{0.9}} \frac{i}{\nu e} f\Omega, \tag{3.5}$$

where i is the proton beam current, ν is the proton pulse rate, e is the proton charge in Coulomb, f is the fraction of the moderator viewed by the detector and Ω is the detector solid angle. Integrating from 1 to 1000 eV and using the values from the transmission experiment of $f = 0.54$ and $\Omega = 4.0 \times 10^{-5}$ sr, leads to an integrated flux of $\sim 2 \times 10^7$ neutrons per beam burst.

3.2 Beam Monitor

As the neutron beam enters the TRIPLE beam line, the flux is monitored by a pair of ionization chambers [Szy94]. The first chamber is filled with ^{3}He gas and the second with ^{4}He gas, both 2 cm thick and filled to 1 atm. In the center of each chamber is a collection plate with high voltage plates (+600 V) on either side. At 1 eV about 10% of the neutrons that pass through the ^{3}He chamber interact with the ^{3}He following an ionization reaction,

$$\mathrm{n} + {}^3\mathrm{He} \rightarrow \mathrm{p} + {}^3\mathrm{H} + 0.764 \text{ MeV}. \tag{3.6}$$

The ionized charge (about 5000 electrons per neutron) produces about 0.6 μA of current at the collection plate per beam burst. Both the ^{3}He and ^{4}He chambers are sensitive to γ-rays through the photoelectric effect and pair production. The current from each chamber is fed to a voltage-to-frequency converter, and the resulting pulses are gated by a 3 ms gate and sent to scalers in the data acquisition system. Since both chambers are sensitive to γ-rays but only the ^{3}He chamber responds to neutrons, the scaler counts from the two chambers are subtracted to yield the number of neutrons entering the beam line. In addition, since the neutron pulses come every 50 ms, there is time between pulses to measure the background and any zero offset for the two chambers 1/60th of a second after each pulse. This greatly reduces the effects of 60 Hz noise.

This system has been shown to have a statistical precision of 0.1% per beam pulse for typical beam currents and a temperature sensitivity of less than 0.3% over the temperature range 29°C–50°C [Szy94, Rob93]. The monitors are not used for an absolute measure of the neutron flux but rather as a monitor of the stability of the beam. This is discussed in more detail in Section 3.11.

3.3 Polarizer

The neutron beam is polarized by transmitting only neutrons with the desired spin direction through a polarized proton target. Since the n-p cross section has a large spin dependence that is essentially constant from 0.1 eV to 50 keV, a polarized proton target filters out neutrons with opposite spins in an energy independent way with high efficiency. The n-p cross section for the case that the neutron and proton spins are aligned (not aligned) is equal to 3.7 b (37.2 b). For a given proton polarization, f_p, the neutron polarization is given by

$$f_n = \tanh\left(n\sigma_{\mathrm{P}} f_p\right), \tag{3.7}$$

where n is the areal density of the proton target and σ_{P} is the polarization cross section, defined to be the difference between the anti-aligned and aligned cross sections divided by two, $\sigma_{\mathrm{P}} \equiv \left(\sigma_{\rightleftarrows} - \sigma_{\rightrightarrows}\right)/2 = 16.7$ b.

The protons are polarized through the dynamic polarization of a cryogenically cooled 8 cm in diameter, 1.3 cm thick ammonia target [Pen94]. The target is cooled in liquid ^{4}He to 1 K and is located at the center of a 5 T split-coil superconducing magnet that has a homogeneity of 10^{-4} over the target volume. A cooling power of 2 W at 1.1 K is achieved by pumping on the ^{4}He bath with a speed of 8000 m^3/hr.

Dynamic polarization takes advantage of the interaction between "free" electrons and nuclear protons in the presence of a high magnetic field. The "free" electrons are also called polarization centers and refer to unpaired electrons. They are produced by irradiating the ammonia with $\sim 3 \times 10^{16}$ electrons/cm^2. Figure 3.4 shows the energy configuration for the electron-proton pairs in the presence of a large magnetic field. Several transitions can take place: the spin of the electrons can flip via transitions between states 1 and 3 or

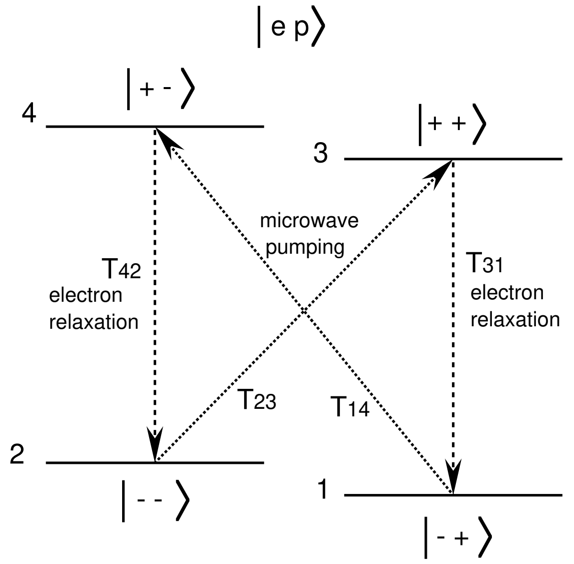

Figure 3.4: Electron-proton pair energy diagram. The + (−) refers to whether the electron and the proton are aligned (anti-aligned) with the field. In the ket for each electron-proton state the electron is labeled on the left and the proton on the right.

between states 2 and 4, the spin of the protons can flip via transitions between states 1 and 2 or between states 3 and 4, and both the electron and proton spins can flip via transitions between states 1 and 4 or between states 2 and 3. The first two situations can happen due to the influence of the lattice, where at 1 K the lattice relaxation times for the electrons and protons are about 10 ms and 300 minutes, respectively. Therefore, the low temperature assures that most electron-proton pairs will occupy states 1 and 2. The simultaneous electron and proton spin flip can only happen with the influence of a sufficiently intense magnetic field from an outside source [Sli90]. For instance, if microwave power with a frequency corresponding to transition T_{23} is applied, the sample will populate state 3. State 3 will then quickly relax to state 1 leaving the proton aligned with the magnetic field. Because of the large difference in electron and proton relaxation times, the process of pumping to state 3 (state 4) can produce nearly 100% aligned (anti-aligned) protons.

Using Equation 3.7, a relative measure of the neutron polarization is obtained from an NMR (Nuclear Magnetic Resonance) measurement of the proton polarization. A Q-meter circuit is used which consists of an RLC circuit, where the inductor is a single turn around the ammonia target. The area of the resonance peak in the voltage versus frequency curve of the Q-meter circuit is proportional to the ammonia magnetic susceptibility and thus the proton polarization. The NMR area can be calibrated to the thermal polarization (no microwave power) to provide an absolute measure of the proton polarization. Since the NMR measurement is not sensitive to inhomogeneities of the target, however, it may not give an accurate measure of the true proton polarization. However, since the measurement can be done with a precision of 3–4% in about 30 s, it provides a reliable relative measure of the proton polarization.

The NMR measurement can be calibrated by measuring the neutron polarization directly in two ways. The first involves measuring the neutron transmission through the target which is given by

$$T = T_0 \cosh\left(n\sigma_{\mathrm{P}} f_p\right), \tag{3.8}$$

where T_0 is the transmission when the target is unpolarized. Combining Equations 3.7 and 3.8 leads to an expression for f_n,

$$f_n = \sqrt{1 - \frac{T_0^2}{T^2}}, \tag{3.9}$$

so that by comparing the transmission when the target is polarized and unpolarized, the neutron polarization can be measured.

The second way of measuring the neutron polarization directly involves measuring the known PNC effect at the 0.75 eV p-wave in ^{139}La. The well known value of $\mathcal{P} = (9.57 \pm 0.19)\%$ (weighted average of the LANSCE and KEK measurements [Yua91]) can be used to extract the neutron polarization from the measured asymmetry. During the ^{106}Pd and ^{108}Pd measurements both methods were used and agreed within error.

By comparing the NMR measurement of f_p with the direct measurement of the neutron polarization, the NMR signal can be calibrated. The calibrated NMR measurements provide a continuous, absolute measurement of the neutron polarization during the parity nonconservation measurements.

3.4 Spin Flipper

The TRIPLE parity nonconservation measurements with longitudinally polarized neutrons require a method of quickly reversing the spin of the neutrons over a wide range of energies (∼1–1000 eV) and over the entire diameter of the beam (∼9 cm). The spin flipper, developed to satisfy these requirements [Bow96b], consists of a series of longitudinal and transverse coils. The 21 cm diameter longitudinal coils form a solenoidal field that points along the beam direction for half the length of the spin flipper and opposite the beam direction for the last half of the spin flipper. The magnitude of the solenoidal field is given by a sine function,

$$B_z(z) = -B_0 \sin\left(\frac{\pi z}{L}\right), \tag{3.10}$$

where L is the length of the spin flipper, z is distance in the direction of the beam, where $z = 0$ at the midpoint of the spin flipper, and B_0 is the magnitude of the field. The transverse field is produced by Helmholtz coils on either side of the spin flipper. It points in the x-direction and has a magnitude given by a cosine function,

$$B_x(z) = B_0 \cos\left(\frac{\pi z}{L}\right). \tag{3.11}$$

Adding the two components, yields a field with constant magnitude that rotates 180° over the distance of the spin flipper. Figure 3.5 shows the longitudinal and transverse field components.

The spin flipper operates in two ways. In the first situation, called the NOFLIP state, the transverse coils are turned off. The neutrons pass through a field that reverses

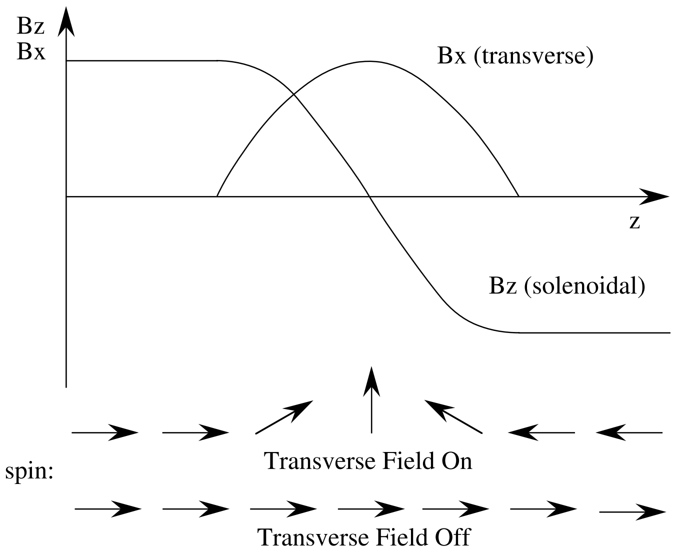

Figure 3.5: Magnetic fields of the spin flipper. The bottom of the figure shows the direction of the neutron spin for the case of the transverse field on and off.

direction at the center of the spin flipper but which contains very small transverse components. For most energies used in these experiments, the neutrons are traveling too fast through the region of changing field to be flipped. Bowman et al. [Bow96b] have analytically calculated the average polarization (averaging over distances off axis from zero to the beam radius) for the NOFLIP state provided the depolarization is small ($\lesssim 2\%$),

$$\langle \sigma_z \rangle_{\text{NOFLIP}} \simeq 1 - \frac{\pi^3 R^2}{8\gamma L^2}, \tag{3.12}$$

where R is the beam radius and γ is the adiabaticity parameter. Parameter γ is given by the ratio of the angular rotation of the magnetic field, $\omega_{\text{B}} = \pi v/L$, to the Larmor precession frequency, $\omega_{\text{L}} = 2\mu B_0/\hbar$, where v is the neutron velocity and μ the magnetic moment of the neutron. Inserting the known values for the above parameters and expressing the velocity in terms of energy, one can write

$$\gamma = 2.37 \times 10^{-4} \frac{\sqrt{E}}{LB_0}, \tag{3.13}$$

where the energy is in eV, L is in meters, and B_0 is in Tesla.

When the transverse coils are turned on, the constant magnitude spin flipper field rotates 180° over the length of the spin flipper. For the energies of interest here, the neutron spins adiabatically follow the rotating field and emerge from the spin flipper with their spins reversed. The average polarization of the beam in the FLIP state is

$$-\langle\sigma_z\rangle_{\mathrm{FLIP}} = 1 - \left(1+\gamma^{-2}\right)^{-1}\left[1-\cos\left(\pi\sqrt{1+\gamma^{-2}}\right)\right]. \tag{3.14}$$

The efficiency of the spin flipper can be calculated as the average polarization of the two states of the spin flipper, $\epsilon = \left(\langle\sigma_z\rangle_{\mathrm{NOFLIP}} - \langle\sigma_z\rangle_{\mathrm{FLIP}}\right)/2$. Figure 3.6 shows the efficiency calculation for two field strengths, $B_0 = 100$ G and $B_0 = 130$ G with $L = 2$ m and $R = 4$ cm.

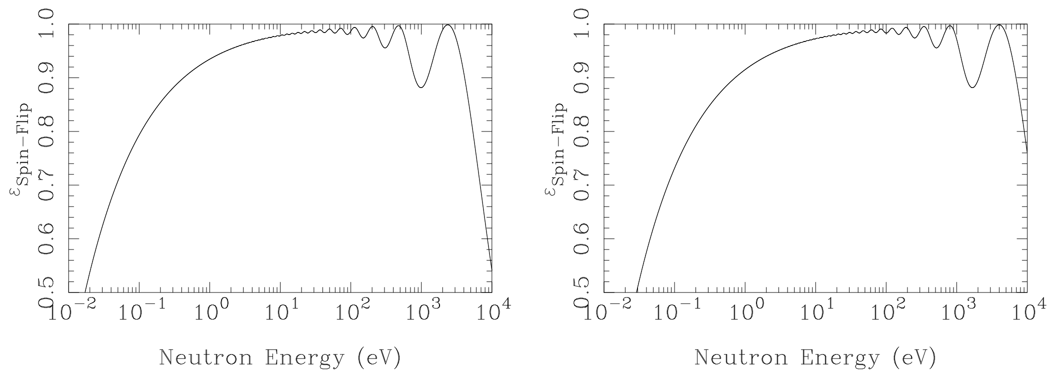

Figure 3.6: Spin-flipper efficiency with $L = 2$ m, $R = 4$ cm and two field strengths, 100 G (left) and 130 G (right).

3.5 Target Chiller

To reduce the effects of Doppler broadening on the resonance line shape, the ^{238}U target was cooled to 77 K by a target chiller. Figure 3.7 shows a schematic of the chiller. The target sits inside the inner vessel that contains liquid nitrogen. Surrounding the inner vessel is the chiller body which is evacuated to provide insulation. The entire chiller slides into the end of the spin flipper such that the solenoidal magnetic field serves as a guide field for the neutron spins as they interact with the target.

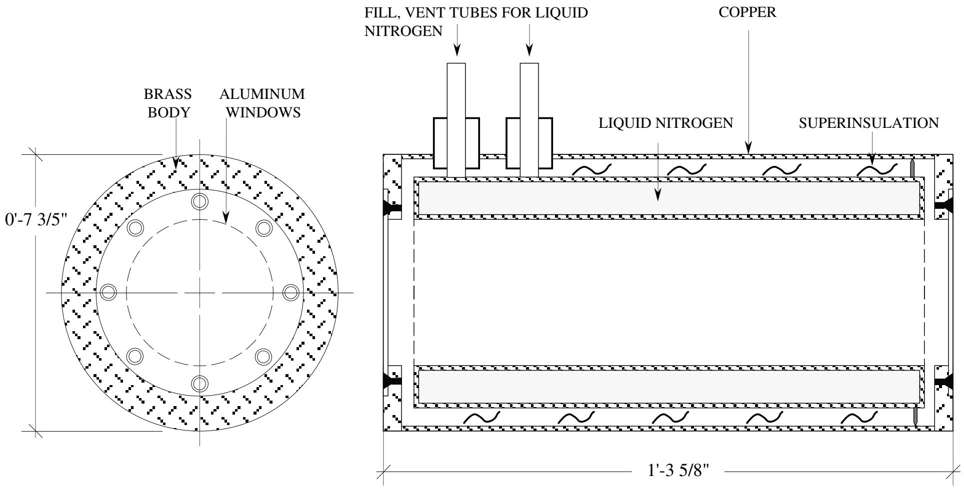

Figure 3.7: Target chiller schematic.

The Doppler width is given by $\Gamma_D = \sqrt{4k_B T_{\text{eff}} E/A}$, where k_B is the Boltzmann constant, E is the neutron energy and A is the mass number. The effective temperature can be expressed [Fod71] as

$$T_{\text{eff}} = \frac{3}{2}\theta_D \int_0^1 z^3 \coth\left(z\frac{\theta_D}{2T}\right) dz, \tag{3.15}$$

where θ_D is the Debye temperature, T is the target temperature and z is the frequency of the lattice vibration. If $T \sim 300$ K then the above expression can be simplified [Sha95],

$$T_{\text{eff}} \simeq T\left(1 + \frac{\theta_D^2}{20T^2}\right). \tag{3.16}$$

Using a Debye temperature for uranium of 210 K [Ash76], a room temperature target (293 K) has an effective temperature of 301 K. A 77 K target, however, has an effective temperature of 103 K leading to a Doppler width that is 1.7 times smaller.

The palladium targets were not chilled and have a Debye temperature of 275 K, leading to an effective temperature of 306 K.

3.6 Spin Transport System

Since the neutrons travel 50 m to the capture target after being polarized, there exists the possibility that they will be depolarized by the Earth's magnetic field as well as by stray magnetic fields along the flight path[1]. To reduce depolarization, the beam pipes have been wire wrapped to form a 50 m, 10 Gauss solenoidal field. The stray fields add small components to the solenoidal field and therefore have a small effect in depolarizing the neutron beam. A small depolarization still occurs, however, due to stray fields and the presence of transverse field components both at gaps in the solenoid coil and at places where the coil diameter changes. To minimize the latter effects, the pipes are double wound before and after large gaps. At two places, there are pipe bellows ($\sim$ 25 cm long) which can not be wound. To reduce the effect of these large gaps, "healing" coils, wrapped PVC pipe, were placed around the bellows. Table 3.1 lists information about the coils of the spin transport system. The smallest gap is 1.5 cm and the largest gap is 10 cm with typical gaps about 5 cm.

As is discussed in detail in Appendix B, a Monte Carlo code has been developed to calculate the average depolarization of 100 neutrons with random trajectories through the spin transport system. The cumulative effects of multiple gaps in the spin transport system coupled with the Earth's field produce a dependence of the depolarization on neutron energy. Figure 3.8 shows the results of the Monte-Carlo calculation for the TRIPLE spin transport system (see Table 3.1), including a 0.3 Gauss field directed 90° to the beam direction to simulate the Earth's field. The highly erratic dependence of the depolarization on neutron energy is caused by the combination of the Earth's field and the combination of 25 coils, each with its own energy dependence (see Appendix B). These calculations were done for a final neutron position at the capture target ($z = 5918.2$ cm).

The depolarization calculations have also been done for the position of the ^{139}La

[1]A 1 eV neutron traveling 50 m in a 0.3 Gauss magnetic field perpendicular to the neutron direction will rotate through 360° about 3 times. This rate scales as $1/\sqrt{E}$.

Table 3.1: Spin-transport coils. Listed are the starting position of the coil relative to the MLNSC water moderator surface, z; the length of the coil, L; the radius of the coil, R; and the amp-turns/cm of the coil, NI. A coil constitutes any continuous length of winding around a particular pipe. The second layer of the overlap coils are treated as separate coils and are indicated by o superscripts. The "healing" coils are indicated by h superscripts. In order to match the downstream end of the spin flipper field, the current loops are such to produce a field that points opposite to the beam direction.

z (cm)	L (cm)	R (cm)	NI (A-turn/cm)
970.8	33.7	11.6	11.80
1008.6	204.5	10.9	5.86
1216.3	455.9	8.9	6.90
1674.7	455.9	8.9	5.68
2125.7	4.6	9.2	5.68^o
2137.7	104.1	14.5	6.44
2245.6	14.0	14.5	6.44
2258.2	30.2	23.2	7.33^h
2285.9	362.0	14.5	7.84
2285.9	75.9	14.8	7.84^o
2651.7	362.0	14.5	9.61
3017.5	362.0	14.5	7.02
3302.9	76.5	14.8	7.02^o
3376.9	30.2	23.2	5.98^h
3404.5	72.1	14.5	7.10
3404.5	70.8	14.8	7.10^o
3480.7	291.2	14.5	7.10
3781.7	598.2	21.9	6.91
4387.8	598.2	21.9	6.67
4993.9	598.2	21.9	6.05
4993.9	76.2	22.2	6.05^o
5597.2	217.8	16.4	7.31
5809.9	107.6	5.1	7.36
5919.0	123.8	5.1	6.55
6042.8	105.4	10.2	7.35

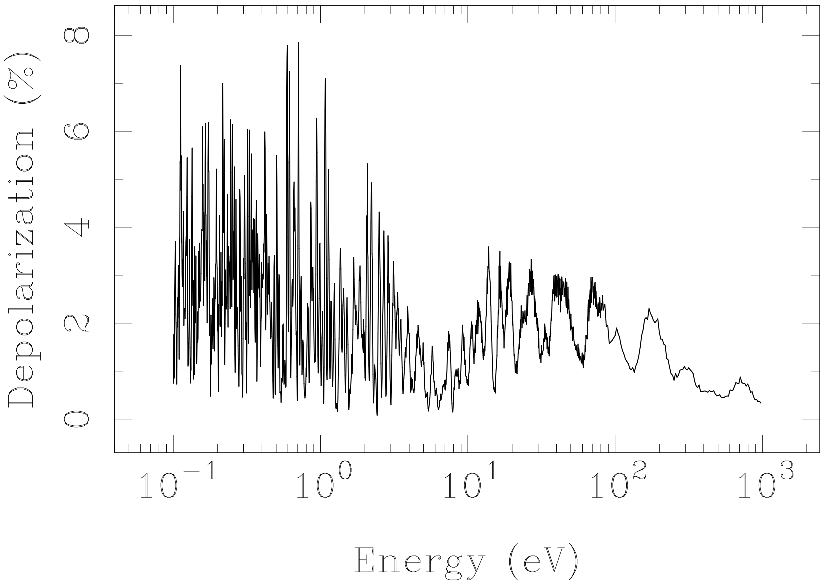

Figure 3.8: Depolarization calculation for the TRIPLE spin transport system. In addition to the fields from the solenoid winding (see Table 3.1), a 0.3 G field directed 90° to the beam direction was introduced to mimic the Earth's field.

target in the neutron polarimeter ($z = 6095.5$ cm) and can be compared with the measured depolarization at 0.75 eV. The measurement involved making parity nonconservation measurements of the 0.75 eV p-wave in ^{139}La with the target placed at the end of the spin flipper ($z = 10$ m) and at neutron polarimeter position ($z = 61$ m). Given the known value of the PNC effect for this resonance, the neutron polarization can be extracted from each measurement, leading to the measured depolarization, $\mathcal{D}$, given by

$$\mathcal{D} = 1 - \frac{f_n^{10\mathrm{m}}}{f_n^{61\mathrm{m}}}. \tag{3.17}$$

The measured depolarization of $(2 \pm 4)\%$ agrees with the calculated value of 2.5%.

3.7 Neutron-Transmission Detector

The neutron transmission detector consists of 55 photomultiplier tubes (PMTs) optically coupled with Dow Corning Sylgard "cookies" to a ^{10}B-loaded liquid scintillator [Yen94]. The liquid scintillator has a diameter of 43 cm and is 4 cm thick. The PMTs are 2 inches in diameter and are arranged in a honeycomb pattern at the downstream side of the scintillator. An incident neutron is moderated in the liquid scintillator to thermal energies, where it is captured by ^{10}B. The energetic ^{7}Li nuclei, alpha particles and γ-rays released from the ^{10}B capture reaction,

$$\begin{aligned} \mathrm{n} + {}^{10}\mathrm{B} \;\; \rightarrow \;\; & {}^{7}\mathrm{Li}^{*} + {}^{4}\mathrm{He} + 2.31 \text{ MeV} \\ & \quad \downarrow \\ & {}^{7}\mathrm{Li} + \gamma \, (0.48 \text{ MeV}), \end{aligned} \tag{3.18}$$

induce scintillation light which is detected by the PMTs. Each of the 55 PMTs views an individual section of the scintillator. The segmented nature of the detector allows very high instantaneous count rates (as high as 500 MHz). The thickness of the scintillator is such that most of the neutrons are thermalized and captured, giving the detector a high efficiency. As discussed in Appendix A, for the energies of these experiments the neutron detector has an energy independent moderation time of 416 ns.

The PMT dark current pulse rise time is $\sim$ 2 ns, with a full-width-half-maximum of $\sim$ 2.7 ns. To aid in pulse discrimination, the PMT anode output is filtered with a 5 ns filter to smooth the single photoelectron pulses. Each of the 55 PMT outputs is filtered and discriminated to a produce 5 ns wide NIM (Nuclear Instrument Module) logic pulse before being sent through $\sim$ 500 ft of low-loss cable to the data room. There, the signals are re-discriminated, filtered to the data-sampling period (usually 100, 200 or 1000 ns), and linearly combined. The resulting voltage waveform represents the count rate as a function of time and is digitally sampled by a transient recorder. The remainder of the data acquisition is described in Section 3.11.

The dead time for the detector is modeled by

$$Y = S(t) M e^{-S(t) M \tau}, \tag{3.19}$$

where Y is the measured neutron yield per second, $S(t)$ is some function of time that describes the true rate that neutrons strike the detector per monitor count, M is the monitor count and τ is the deadtime. Measurements are made of the neutron yield and monitor signal for the case of different beam intensities (full, half, quarter and eighth beam). By comparing two of these runs (Y_1, M_1 and Y_2, M_2), one can obtain an expression for the dead time,

$$\tau = \frac{1}{Y_1} \frac{M_1}{M_2 - M_1} \ln\left(\frac{Y_1 M_2}{Y_2 M_1}\right) \exp\left[\frac{M_1}{M_2 - M_1} \ln\left(\frac{Y_1 M_2}{Y_2 M_1}\right)\right]. \tag{3.20}$$

Dead time values are extracted for all *ToF* channels, and an average is taken [Yen96a]. In 1993 at some *ToF* channels the detector signal saturated the transient recorder (see Section 3.11), and thus the extracted dead time of 23 ns should be considered an effective dead time. The experiments in 1995 did not have this problem, and the extracted deadtime was 13 ns. With the measured value of τ the time-of-flight spectra are corrected for the effect of dead time by numerically solving Equation 3.19 for $S(t)M$ given Y for each *ToF* channel.

3.8 Neutron Absorbers

Two types of neutron absorbers are used in these experiments and both are located at the upstream end of the spin flipper. The purpose of the first type of absorber is to remove low energy (slow) neutrons from the beam to prevent them from reaching the detector after the next neutron pulse has occurred. The usual material is a 1/32 inch thick piece of natural Cd. In addition to having a large thermal cross section, Cd also has a very large resonance at 0.178 eV ($\sim$ 7000 b) due to ^{113}Cd. Because of a resonance at 89.5 eV in ^{110}Cd, the 89.216 eV resonance in ^{238}U was obscured. For this reason, a $\sim$ 1/100 inch thick piece of ^{10}B, which also has a large thermal cross section, was used for about half of the ^{238}U measurements.

The other type of absorber is used in experiments to measure the amount of γ-ray background being detected with the neutrons [Yen97]. Several materials (In, Ta, Co, Mn) are placed in the beam first with one thickness and then with twice that thickness. What all of these materials have in common is the presence of very large resonances at various energies of interest in these experiments. The resonances are so large that they absorb all of the neutrons in the beam at the resonant energy. By measuring the counts under these so called black resonances, the amount of γ-ray background can be measured. In addition, by measuring the background for the two thicknesses, the level of background for the case of zero thickness (no absorber in the beam) can be found by extrapolation. From the measurements of resonances in several energy regions, the energy dependent γ-ray background is determined for each PNC target and is used to correct the *ToF* spectra.

3.9 Capture γ-ray Detector

The initial design of the capture γ-ray detector was discussed by Frankle [Fra93a]. The primary design considerations were fast timing characteristics, high efficiency and reasonable cost. The material chosen to optimize these three considerations was pure CsI which provides good efficiency with fast light components of 6 and 23 ns at a wavelength of 310 nm. There is in fact a slow light component of 3300 ns with a wavelength of $\geq$ 480 nm as well. However, the slow light component is initially less than 30% of the total light output and is further reduced by a factor of five by an optical filter.

The detector consists of two annular rings of CsI, as shown in Figure 3.9, that cover a 3.3π solid angle. During the experiment, the detector and shielding are placed on a movable table. The target sits in the middle of the two detector rings and can be accessed by sliding the two detector halves apart. The photomultiplier tubes are attached to the front and rear faces of the two rings and lie parallel to the beam direction. The signals from the 24 detector elements are linearly summed in pairs such that the two annular rings are equivalent to one ring of 12 elements. These signals are shaped by 30 ns passive filters, which by smoothing the single-electron pulses improve pulse height discrimination. To minimize possible time jitter in the discrimination process, the photomultiplier tube pulses

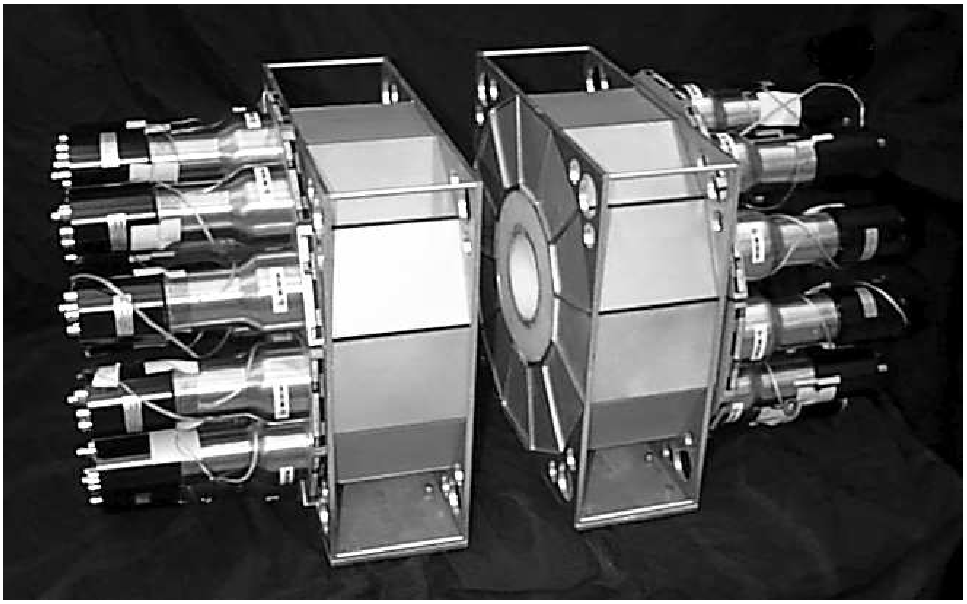

Figure 3.9: Photograph of the CsI capture γ-ray detector with ^{6}Li-loaded polyethylene shielding. The CsI crystals are 15 cm long wedges that form two annular rings with inner diameters equal to 20 cm and outer diameters equal to 40 cm. Photomultiplier tubes extend parallel to the beam direction from the front and rear faces of the two annular rings. The ^{6}Li-loaded polyethylene has an inner diameter of 10 cm and an outer diameter of 20 cm. At the position of the target, inside the ^{6}Li-loaded polyethylene cylinder, the beam profile has a 9 cm diameter.

are discriminated by constant fraction discriminator modules. The 12 pulse trains from the discriminator modules are transmitted to the data room, where they are re-discriminated and linearly summed. The output of the linear summer is discriminated at such a level as to trigger only on pulses with heights corresponding to at least two γ-rays in coincidence. The output pulses from the discriminator are then shaped by 100, 200 or 1000 ns filters before being input to the transient recorder.

In commissioning the detector, studies were done to determine the running conditions that optimized the ability to measure PNC effects. The three primary adjustments were: the photomultiplier tube pulse discriminator level which set the γ-ray energy threshold, the γ-ray coincidence level and the minimization of background. Figure 3.10 shows a neutron energy spectrum for the capture γ-ray detector for a ^{108}Pd target. It compares data taken with the requirement of two γ-rays in coincidence and with no such requirement. It also shows the effect of lowering the γ-ray detection threshold from 0.6 MeV to 0.3 MeV. Although it is important to maximize the peak-to-background ratio, high count rate is of primary importance in these experiments and thus the final running conditions reflect the need to maximize count rate while retaining acceptable peak-to-background ratios. The final running configuration was to discriminate above 0.3 MeV γ-rays and to require two-fold γ-ray coincidence.

The overall capture efficiency for these running conditions was measured for the 15.5 eV resonance in ^{121}Sb to be 51%. The 15.5 eV resonance is saturated in the capture spectrum; that is, all of the neutrons are absorbed at the resonance energy. In this situation, the capture yield depends only on the neutron flux, the detector efficiency, the target area and the resonance parameters. All of these parameters are known except the neutron flux and detector efficiency. The flux was found at this energy in a separate measurement using a 1 cm diameter neutron detector that uses a ^{6}Li-loaded glass scintillator. From the above information, the capture detector efficiency was calculated.

The primary method for eliminating background was the use of shielding. Since the

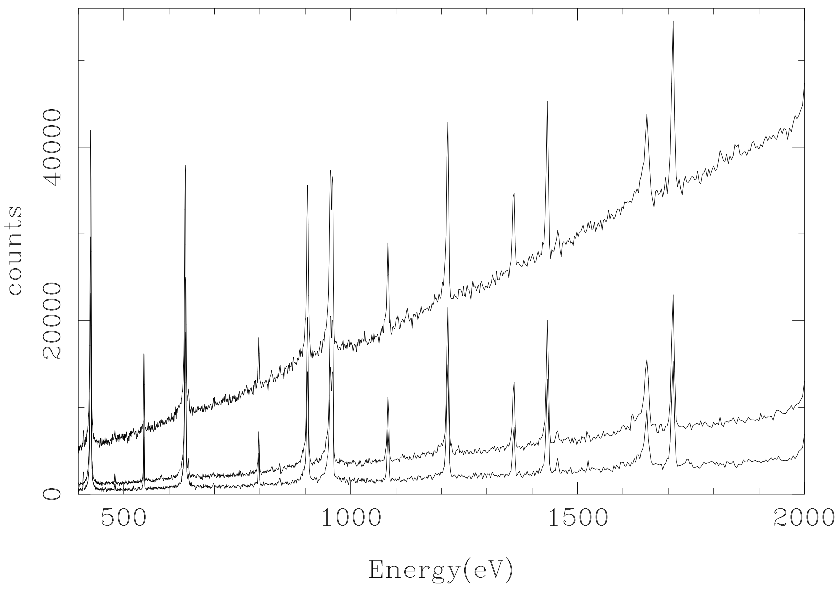

Figure 3.10: Capture γ-ray detected neutron energy spectrum for ^{108}Pd. The data in the three curves were obtained with the complete shielding configuration and the following conditions: 0.3 MeV γ-ray detection threshold with no coincidence requirement (top), 0.6 MeV γ-ray threshold with no coincidence requirement (middle), and 0.3 MeV γ-ray threshold with two-fold coincidence requirement (bottom).

CsI crystals are sensitive to neutrons, the detector was designed with a 5 cm thick, 10% by weight ^{6}Li-loaded polyethylene cylinder between the target and detector (see Figure 3.9). To shield from external γ-rays and neutrons, the detector was surrounded by 10 cm of lead and 15 cm of B-loaded polyethylene. Although the lead walls surrounding the detector are needed to reduce time independent background, they create background as well. They form a reflective cavity in which fast neutrons scattered out of the beam can be scattered into the detector after some thermalization in the lead walls. To reduce this source of background, the open cavity between the detector and the lead shielding was filled with B-loaded polyethylene. Figure 3.11 shows the effect of this final shielding.

The use of a γ-ray detection system poses two potential problems. First, the efficiency can change from resonance to resonance due to differing decay schemes. A sensitive test of the dependence of the efficiency on resonance energy is the constancy of the ratio

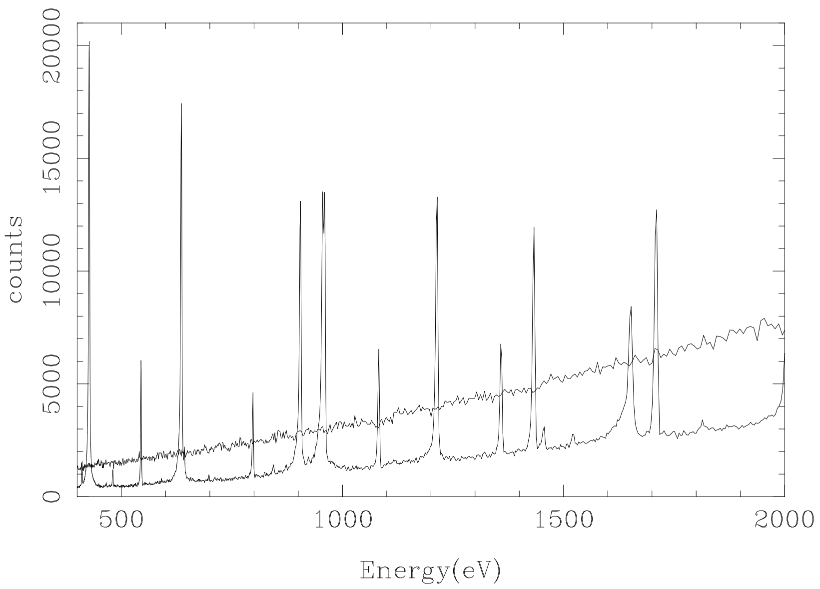

Figure 3.11: Capture γ-ray detected neutron energy spectrum taken with 0.3 MeV γ-ray threshold and two-fold γ-ray coincidence. The data in the two curves were taken with: (top) an Al target holder and no internal B-loaded polyethylene shielding and (bottom) a 22 g ^{108}Pd target in an Al target holder with internal B-loaded polyethylene shielding.

of the count rate for no γ-ray coincidence to the count rate for two-fold γ-ray coincidence over many resonances. A study of data taken with ^{121}Sb, ^{123}Sb and ^{108}Pd targets and the above detector shows that this ratio is reasonably constant for both s-waves and p-waves. Figure 3.12 shows a plot of the ratio of resonance areas of data taken with the no γ-ray coincidence requirement to that of two-fold γ-ray coincidence plotted as a function of resonance energy. Another potential problem is the influence of angular distributions of specific γ-ray transitions on the PNC effect. Experiments at KEK with a La target [Mas89, Shi93] demonstrated that even with smaller detectors than those used here, the angular distributions were effectively averaged and did not influence the extracted PNC effect.

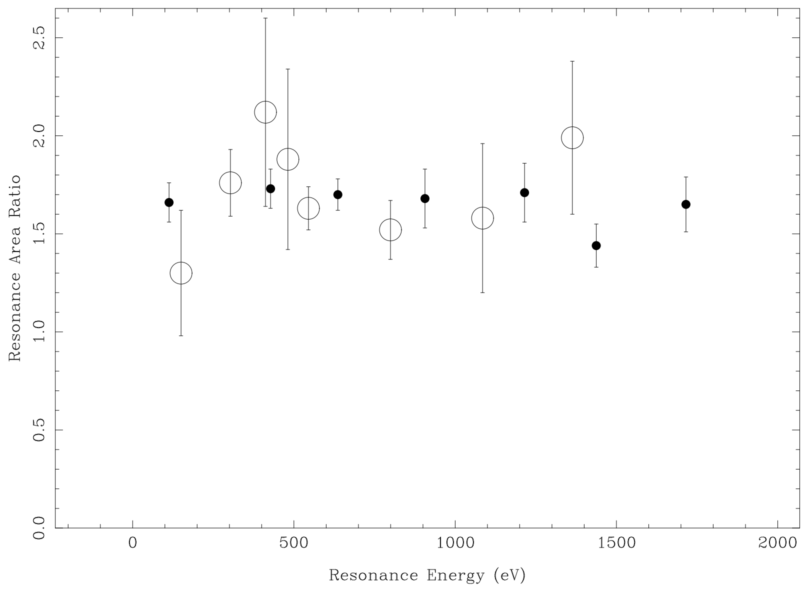

Figure 3.12: Ratio of resonance areas in ^{108}Pd for no γ-ray coincidence to two-fold γ-ray coincidence for s-waves (dots) and p-waves (circles).

3.10 Neutron Polarimeter

The neutron polarimeter consists of two parts, a 0.06534 atoms/b ^{139}La target located downstream from the capture target and a 1 cm thick, 13 cm diameter, 6% by weight ^{6}Li-glass neutron detector downstream from the ^{139}La target. Since the capture targets used for these experiments are thin (0.001-0.004 atoms/b), most of the neutron flux is transmitted through the targets and available for the transmission measurement of parity nonconservation in ^{139}La.

The data acquisition system is designed such that while the data are being collected from the capture detector into a time-of-flight spectrum, the signals from the ^{6}Li-glass detector are counted by three scalers. Each scaler counts neutrons arriving at predetermined times corresponding to an energy region on either side of the 0.75 eV resonance (region A and C) and one region at the resonance (region B) (see Figure 3.13). By comparing the number of counts in these three regions for the different helicity neutrons, the PNC effect

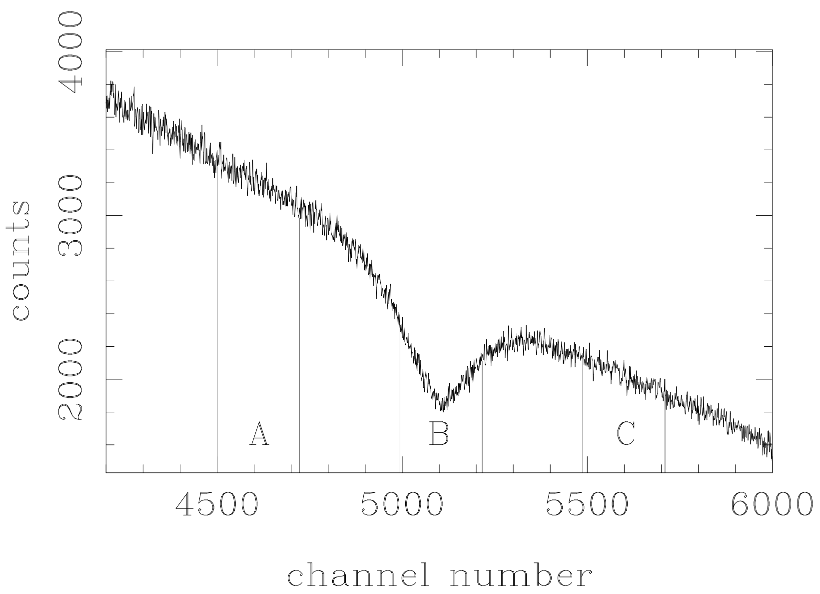

Figure 3.13: ^{139}La time-of-flight spectrum. The counts in the three timing windows, A,B, and C, are counted by scalers for both helicity states in order to determine the yield asymmetry.

in ^{139}La can be calculated. The yield in the resonance region is given by

$$Y_{\mathrm{B}}^{\pm} = \frac{\left(Y_{\mathrm{A}}^{\pm} + Y_{\mathrm{C}}^{\pm}\right)}{2} e^{-[n_0\sigma_0 + n\sigma_p(1 \pm f_n \mathcal{P})]}, \tag{3.21}$$

where $\pm$ refers to the positive and negative helicity states, f_n is the neutron polarization, $\mathcal{P}$ is the PNC asymmetry and $n_0\sigma_0$ is the areal density times cross section for everything except the 0.75 eV p-wave cross section in ^{139}La which is given by $n\sigma_p$. By taking the ratio of the yields for the positive and negative helicity states, one finds

$$\begin{aligned} f_n &\simeq \frac{1}{n\sigma_p\mathcal{P}} \left[\frac{Y_{\mathrm{B}}^{-}\left(Y_{\mathrm{A}}^{+} + Y_{\mathrm{C}}^{+}\right)}{Y_{\mathrm{B}}^{+}\left(Y_{\mathrm{A}}^{-} + Y_{\mathrm{C}}^{-}\right)} - 1 \right] \\ &= \frac{1}{\kappa} \left[\frac{Y_{\mathrm{B}}^{-}\left(Y_{\mathrm{A}}^{+} + Y_{\mathrm{C}}^{+}\right)}{Y_{\mathrm{B}}^{+}\left(Y_{\mathrm{A}}^{-} + Y_{\mathrm{C}^{-}}\right)} - 1 \right]. \end{aligned} \tag{3.22}$$

Since σ_p in the above equation includes all of the experimental broadenings, a calibration coefficient κ is introduced. It is found by comparing the neutron polarization value found from the above method with that found from fitting a ^{139}La *ToF* spectrum.

Figure 3.14 shows the neutron polarization calculated by the above method as a function of run number for the ^{106}Pd and ^{108}Pd runs. The count rates were sufficient to produce a 10% measurement of the neutron polarization for every thirty minute run. This method provided a run-by-run monitor of the neutron polarization in the vicinity of the target.

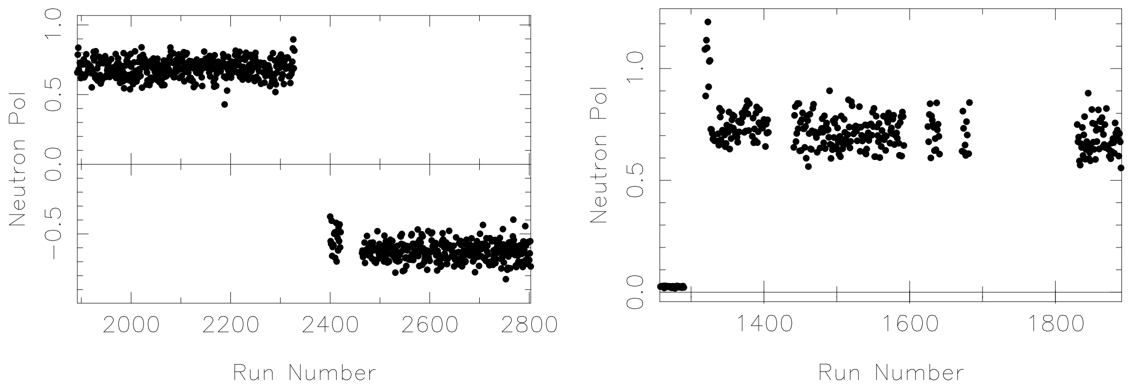

Figure 3.14: Neutron polarization from the neutron polarimeter for ^{106}Pd (left) and ^{108}Pd (right). The first several runs of ^{108}Pd data did not have the timing gates set and were not properly calibrated.

3.11 Data Acquisition

The data acquisition system consists of a Digital MicroVax II running the IUCF XSYS data acquisition code coupled to the electronics modules through two CAMAC (Computer Automated Measurement and Control) crates interfaced with the computer via an MBD (Multi-Branch Driver). The data acquisition process is initiated with each proton burst. An inductive coil on the proton beam leg before the spallation target provides an electronic pulse called $t_\circ$. The $t_\circ$ pulse triggers the formation of a second pulse, $t'_\circ$, 1/60th of a second later.

As discussed in the detector sections (Section 3.7 and 3.9), the detector signals are linearly summed and filtered to 100, 200 or 1000 ns, the time depending on the digital sampling interval (dwell time). A 12-bit ADC (Analog to Digital Converter) transient recorder digitally samples the summed detector signal 8192 times in intervals determined by the dwell time. The 8192 words from the transient recorder are added to a summation memory for 200 beam bursts before being stored in the computer. Since the neutron pulse rate is 20 Hz, there is time between pulses to sample the detector signal after all the neutrons from the previous burst have left. The $t'_\circ$ pulse initiates this sweep 1/60th of a second after each neutron pulse and triggers a subtract pulse that causes the summation memory to subtract the next 8192-word sweep from the stored data. In this way, each sweep is corrected for background and electronic noise.

This technique is also used with the beam monitor signal. Four scalers are used to scale the gated monitor signals from the ^{3}He and ^{4}He ionization chambers, two for the $t_\circ$ pulse and two for the $t'_\circ$ pulse. In the data acquisition software, the counts from the $t'_\circ$ trigger are subtracted from those from the $t_\circ$ trigger for each chamber to form corrected ^{3}He and ^{4}He counts. The ^{4}He counts are then subtracted from the ^{3}He counts and stored in a spectrum of neutrons per beam burst.

This process is done for 200 beam bursts ($t_\circ$ pulses). At this time the 8192-channel detector spectrum and all scaler data are transfered to computer memory, and the spin flipper state is changed according to an 8-step sequence. In order to reduce the effects of detector gain drifts and the effects of the spin flipper magnetic field on the detectors, the transverse coil of the spin flipper is turned on and off according to the following sequence, $0++0-00-$, where 0 indicates that the transverse field is off, $+$ that it is on in the positive x-direction and $-$ that it is on in the negative x-direction. Each spin flipper state lasts 10 s (200 $t_\circ$ pulses divided by 20 Hz). The 8-step sequence cancels gain drifts to second order and magnetic effects from the spin flipper to first order. False asymmetries from the effect of the spin flipper on the detectors, which are 50 m away, is estimated to be less than 2×10^{-10} [Rob93]. The data acquisition software stores all data in separate spectra, one for the NOFLIP state (0) and one for the FLIP state (+ or −).

At the end of each 8-step sequence the beam-monitor data are averaged, and if during the last 8-step sequence the flux from any beam burst deviated from the mean by more than 8%, the entire 8-step sequence is considered bad. The data are stored in computer memory but in "bad" spectra. If the flux is stable, the data are stored in "good" spectra[2]. Once 20 8-step sequences have been taken, the run is stopped and a new run is started. A run lasts about 30 min.

In addition to storing the detector and monitor signals, for each 8-step sequence the NMR proton polarization measurements are stored; the scaler counts of each individual detectors are stored to monitor the detectors; and in capture the neutron polarimeter counts are stored.

[2] An easy first cut of the data is to throw out runs with more than 50% bad data.

Chapter 4

Analysis

The analysis divides primarily into two sections: analysis of the mass 100 targets, ^{106}Pd and ^{108}Pd, and analysis of the mass 230 target, ^{238}U. Within these two sections, the analysis divides again into the determination of resonance parameters, the extraction of PNC effects, and the determination of the root-mean-squared PNC matrix element.

The resonance parameters and PNC effects were extracted using the fitting code FITXS which is described in Appendix A. Figures of the sample fits and PNC-asymmetry histograms can be found in Appendix C.

4.1 Mass 100 Region, ^{106}Pd and ^{108}Pd

The analysis procedures for ^{106}Pd and ^{108}Pd are essentially the same and thus will be discussed together.

4.1.1 Data

The parity nonconservation measurements for the ^{106}Pd and ^{108}Pd targets were taken with the capture experimental setup. A first cut of the data consisted of removing those runs for which there were 1) abnormalities logged in the log book, 2) fluctuations in peak height of selected resonances throughout the spectrum which would indicate unstable timing, and 3) less than 50% "good" $t_\circ$ timing pulses as described in Section 3.11. All of the runs were also checked for asymmetric flux that could cause the extraction of false asymmetries. This was done by calculating the ratio of the counts in the NOFLIP to the FLIP spectra for selected regions throughout the *ToF* spectra. No asymmetries were seen in this analysis.

In order to determine neutron resonance parameters for the large s-waves, which were distorted in capture, transmission measurements were also performed. The targets were placed at 0° and 60° with respect to the beam line. Since many resonances were not seen in the 0° data due to the thinness of the target, only the 60° data are discussed.

Table 4.1 provides an overview of the runs taken with the ^{106}Pd and ^{108}Pd targets.

^{106}Pd

A total of 798 half-hour capture runs were taken, 437 with positive neutron polarization and 361 with negative neutron polarization. In each of these two sets 7 runs were discarded due to intermittent beam during the run, less than 50% "good" data, and invalid number of beam pulses recorded in the data acquisition. That leaves 430 good capture runs for positive polarization and 354 good capture runs for negative polarization.

In transmission, 10 half-hour runs were taken with the target placed at 0° with respect to the beam line and 11 runs with the target at 60°.

^{108}Pd

During the ^{108}Pd experiments, the spin flipper field was increased to shift the efficient range of the spin flipper to higher energies. Thus, the ^{108}Pd data were analyzed in two groups: Group A consisting of 116 runs of which 115 were analyzed and Group B with 246 runs of which 235 were considered good runs. The analysis of the different spin flipper settings for these two groups is discussed in Section 3.4.

In transmission, 5 runs were taken with the target placed at 0° and 12 runs with the target at 60°. In addition, for each of the transmission targets 6 runs with different absorbers were taken to determine the background correction which is discussed in Section 3.8.

Table 4.1: Good runs for the ^{106}Pd and ^{108}Pd targets. Unless labeled otherwise, the length of each run was 30 minutes.

No. good runs	Proton Pol.	Spin Flipper Field	Measurement
115	+	100 G	^{108}Pd parity
235	+	130 G	^{108}Pd parity
10	+	100 G	^{139}La parity at 10 m
6	+	100 G	^{139}La parity at 60 m
21	+	130 G	^{139}La parity at 10 m
24	+	130 G	^{139}La parity at 60 m
115 (3 min)	+	130 G	NMR calibration
430	+	130 G	^{106}Pd parity
354	−	130 G	^{106}Pd parity
27 (3 min)	−	130 G	NMR calibration
5	+	130 G	^{108}Pd trans. 0°
12	0	130 G	^{108}Pd trans. 60°
10	+	130 G	^{106}Pd trans. 0°
11	0	130 G	^{106}Pd trans. 60°
1	+	130 G	Al can 0°
3	0	130 G	Al can 60°
12 (5 min)	0	130 G	dead time

4.1.2 Targets

The ^{106}Pd and ^{108}Pd targets consisted of metal powder pressed into the shape of a 3.5 inch diameter disk and sealed in Al cans. The Al cans were made of Al 1100 and had a 3.5 inch inner-diameter with 20 mil thick front and back faces. Al 1100 is the purest Al alloy that is still reasonably machinable. The purity is needed to reduce the presence of contaminant peaks in the capture spectrum (Al has a flat cross section in the energy range of interest, whereas typical alloy constituents such as Cu and Mn do not.). The machinability was required to produce thin wall thicknesses (20 mil) which limit neutron scattering ($\sim 1\%$ of the beam). Both targets were at room temperature, and an effective temperature of 300 K was used in the fitting code, FITXS.

^{106}Pd

The 98.51% pure ^{106}Pd target weighed 23.3279 g, which gives an areal density of $n = 2.11 \times 10^{21}$ atoms/cm^2 assuming uniformly distributed metal powder. The ^{106}Pd powder, however, was not of even grain size, but rather had many large "chunks" that made for a non-uniform target. X-ray films of this target showed an uneven powder density as seen in Figure 4.1. These figures are the result of laser scanning the x-ray film. The laser intensity is converted to units of gray scale (1–256) which corresponds the amount of transmission of the x-rays through the material being x-rayed. For the descriptive purposes here, the gray scale has been inverted and should be interpreted as a relative measure of target thickness – the darker the plot, the higher the gray scale and the thicker the target. Figure 4.1 shows a three dimensional surface plot and a cross sectional graph of laser intensity measured in gray scale versus distance across the diameter of the target in units of pixels. The light gray circle around the edge of the left plot of Figure 4.1 is from the Al can, which although is physically thicker than the ^{106}Pd, attenuated the x-rays less.

Since in capture the entire target was illuminated by the beam, target non-uniformity was not an issue, as the experiment was only sensitive to the average thickness. In transmission, however, the diameter of the collimation was much smaller near the target, and thus only a fraction of the target was illuminated. The thickness for the illuminated section, therefore, was required.

This was best done by fitting a known resonance in the data, allowing the target thickness parameter to vary.[1] The 281.1 eV peak seen in the 60° transmis-

[1] The target thickness was also estimated with the use of the x-ray laser scans. Several Cu wires of known thickness were placed on the x-ray film with the targets. From calculations of x-ray transmission through

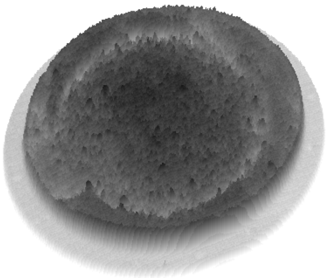
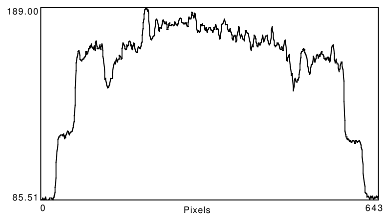

Figure 4.1: Surface plot (left) and cross sectional slice (right) of the laser scanned x-ray film of the ^{106}Pd target. In the left plot the darker the image the thicker the material. The vertical scale of the left graph corresponds to thickness given in gray scale (1–256).

sion data was due to an isolated, large resonance with a known neutron width of $g\Gamma_n = (529 \pm 25)$ meV [Mug88b]. A value of $\Gamma_\gamma = 91$ meV was assumed and was found by averaging the ^{108}Pd Γ_γ values listed by Mughabghab [Mug88b]. The statistics of these data were such that the fit was sensitive to both the size and shape of the peak. Therefore, both the target thickness and neutron width were varied to minimize χ^2. The best-fit value for the target thickness was found to be $(5.5 \pm 0.4) \times 10^{21}$ atoms/cm^2 with $g\Gamma_n = 519$ meV. The error in the target thickness is an estimate based on the sensitivity of χ^2 to the target thickness parameter.

^{108}Pd

The 21.6691 g, ^{106}Pd target was 98.59% pure and had an areal density of $n = 1.92 \times 10^{21}$ atoms/cm^2. The ^{108}Pd powder did not have the large, uneven grain sizes that the ^{106}Pd target did, and the x-ray film of this target showed uniformly distributed target material.

For the transmission data that were taken with the target at 60° to the beam

Pd and Cu and using the known thickness of the copper wires, the x-ray scan gray scale was calibrated to target thickness. This allowed a measure of the thickness of the illuminated portion of the target (by the neutron beam) relative to the whole target. This calculation of the thickness was in rough agreement with that of the method described in the text.

direction, the target thickness was roughly twice that listed above. A more exact ratio was obtained by looking at the ratio of resonance areas for the 0° data and the 60° data. For a thin target where $n\sigma \ll 1$, the area depends linearly on the target thickness [Mel53],

$$A = \frac{\pi}{2} n\sigma\Gamma. \tag{4.1}$$

From looking at seven resonances over the energy range of interest, the ratio between the target thickness for the 0° and 60° data was found to be 2.1 ± 0.1. Therefore, the areal density for the 60° data is given by $n = (4.09 \pm 0.19) \times 10^{21}$ atoms/cm^2.

4.1.3 Energy to Time-of-Flight Calibration

The time-of-flight channels were converted to neutron energy by identifying known resonances in the spectrum and then plotting *ToF* channel $\times \sqrt{E}$ versus $\sqrt{E}$ as shown in Figure 4.2. A fit of this plot yields the calibration using the relation

$$E = 5.23 \times 10^9 \frac{L^2}{\Delta^2 (C + C_\circ)^2} \quad \text{(eV)} \tag{4.2}$$

or rearranging and taking the square root of the equation,

$$C\sqrt{E} = -C_\circ \sqrt{E} + \frac{7.23 \times 10^4}{\Delta} L, \tag{4.3}$$

where L is the length of the beam line in m, Δ the dwell time of each *ToF* channel in ns, C the *ToF* channel and $C_\circ$ the *ToF*-channel offset. The Pd transmission data were calibrated by identifying 39 Cd resonances due to the Cd absorber. Figure 4.2 shows a linear fit of the Pd-transmission *ToF*-to-energy calibration.[2]

[2] For a straight line fit where $y = ax + b$, one can extract the parameters a, b and an estimated σ_y following [Gro84]. The variance in y is given by

$$\sigma_y^2 \mid_{est} \equiv (y - \bar{y})^2 \mid_{est} = \frac{1}{S_1} + \frac{S_1}{D}\left(x - \frac{S_x}{S_1}\right)^2, \tag{4.4}$$

where

$$D = S_1 S_{xx} - S_x^2 \tag{4.5}$$

and

$$S_1, S_x, S_{xx} = \sum_n \left(\frac{1, x_n, x_n^2}{\sigma_n^2}\right). \tag{4.6}$$

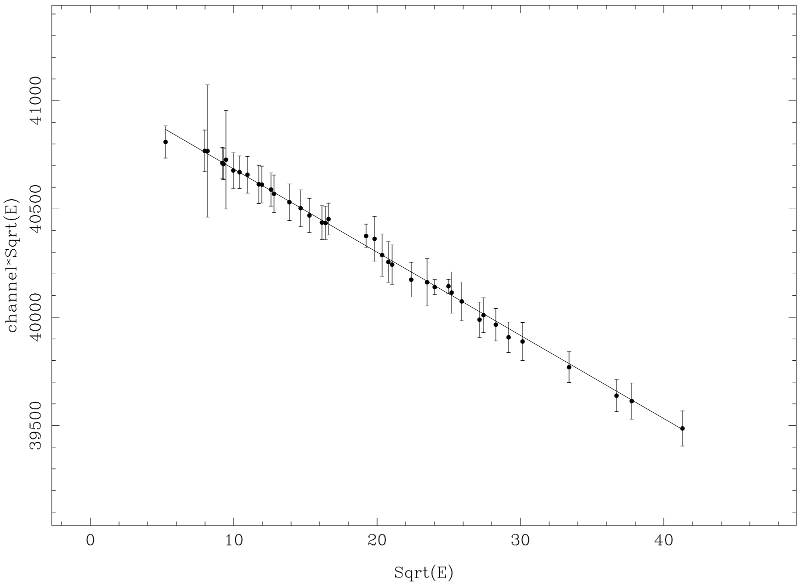

Figure 4.2: Energy to *ToF* calibration for ^{106}Pd and ^{108}Pd in transmission. Uncertainties in the ordinate include estimated *ToF* channel uncertainties (~ 1 channel) and energy uncertainties from Mughabghab.

For the energy calibration of the Pd-transmission data $L = (56.802 \pm 0.044)$ m, $C_\circ = 38.4 \pm 1.4$ and the neutron energy is given by

$$E = \left(\frac{41069}{C + 38.4}\right)^2 \quad \text{(eV)} \tag{4.8}$$

For Equation 4.3:

$$\begin{aligned} x &= \sqrt{E} \\ y &= C\sqrt{E} \\ a &= -C_\circ \\ b &= \frac{7.23 \times 10^4}{\Delta} L \\ E &= \left[\frac{b}{(C-a)}\right]^2 \\ \sigma_E &= 2E\sqrt{\left(\frac{\sigma_y}{y}\right)^2 + \left(\frac{\sigma_C}{C}\right)^2}. \end{aligned} \tag{4.7}$$

with

$$\sigma_E = 2E\sqrt{\frac{137.7 + 1.99\left(\sqrt{E} - 20.9\right)^2}{\left(41069 - 38.4\sqrt{E}\right)^2} + \left(\frac{\sigma_C}{C}\right)^2} \quad \text{(eV)}. \tag{4.9}$$

The energy calibration for the capture setup was found by identifying 49 ^{105}Pd resonances in the capture spectrum. The fit for this calibration is shown in Figure 4.3. For the energy calibration of the Pd-capture data $L = (59.340 \pm 0.014)$ m, $C_\circ = 508.31 \pm 0.37$ and the neutron energy is given by

$$E = \left(\frac{42903}{C + 508.3}\right)^2 \quad \text{(eV)} \tag{4.10}$$

with

$$\sigma_E = 2E\sqrt{\frac{9.46 + 0.140\left(\sqrt{E} - 25.7\right)^2}{\left(42903 - 508.3\sqrt{E}\right)^2} + \left(\frac{\sigma_C}{C}\right)^2} \quad \text{(eV)}. \tag{4.11}$$

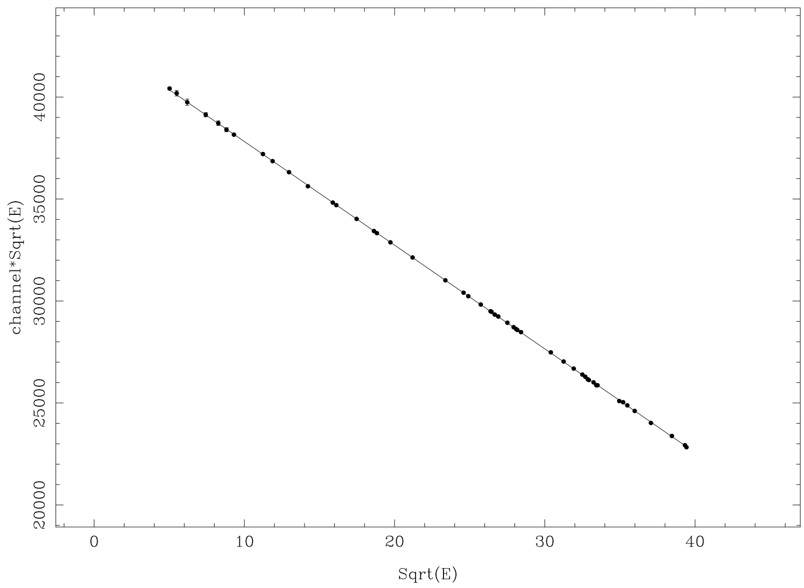

Figure 4.3: Energy to *ToF* calibration for ^{106}Pd and ^{108}Pd in capture.

4.1.4 Extraction of $g\Gamma_n$ from Transmission

In order to extract resonance parameters, the 60° ^{106}Pd and ^{108}Pd runs listed in Table 4.1 were each summed. The summed spectra were corrected for dead time and background as discussed in Sections 3.7 and 3.8. Since the level density of Cd is much higher than ^{106}Pd and ^{108}Pd and since the 1/32 inch Cd absorber was about the same thickness as the Pd isotopes, there were many Cd peaks visible throughout the Pd spectra. The problem of having to fit the Cd as well as the Pd peaks was eliminated by dividing the monitor-normalized target-in spectrum by the monitor-normalized target-out spectrum. Figure 4.4 illustrates the utility of this procedure.

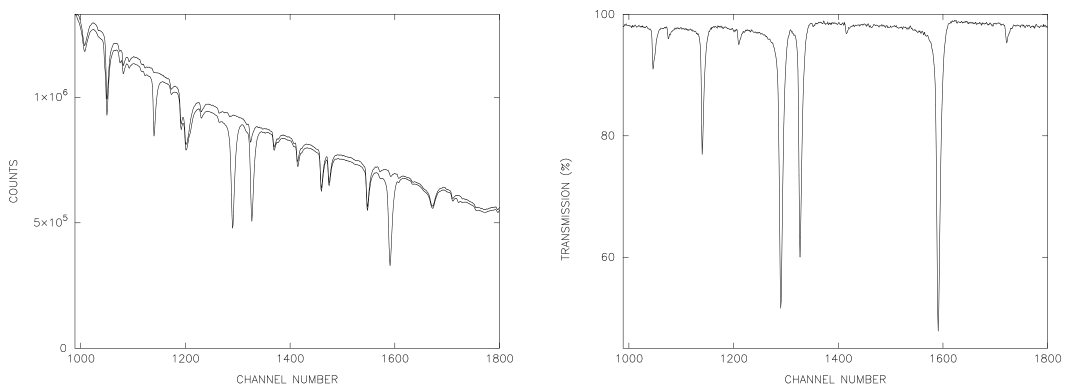

Figure 4.4: Spectra from ^{108}Pd with the target in and target out data (left) and with the target-in spectra divided by the target-out spectra (right).

The target-in over target-out spectra were fit using FITXS to extract neutron resonance widths. Since none of the resonances were sensitive to Γ_γ, the value of 91 meV was used. Although the amount of ^{105}Pd contamination was small in both the ^{106}Pd and ^{108}Pd targets, there were many peaks in the spectrum due to ^{105}Pd. The amount of contamination was found by fitting isolated, known ^{105}Pd resonances and letting the amount of contamination vary. The results from many resonances were then averaged. For ^{106}Pd the amount of ^{105}Pd contamination was found to be $(0.93 \pm 0.09)\%$. For ^{108}Pd the value found in capture was used, $(0.29 \pm 0.02)\%$. Table 4.2 lists the extracted $g\Gamma_n$ values for ^{106}Pd and ^{108}Pd. The errors include statistical errors and the uncertainties in the target

Table 4.2: $g\Gamma_n$ values from transmission data.

^{106}Pd		^{108}Pd	
E (eV)	$g\Gamma_n$ (meV)	E (eV)	$g\Gamma_n$ (meV)
63.41±0.07	0.012±0.001	112.7±0.1	1.02±0.08
146.4±0.2	0.54±0.04	149.7±0.2	0.036±0.009
156.7±0.2	0.26±0.02	302.9±0.2	3.57±0.18
281.1±0.3	519±38	411.6±0.5	0.55±0.06
406.7±0.3	0.78±0.07	426.9±0.3	390±19
462.3±0.4	1.20±0.10	480.1±0.4	0.66±0.09
522.1±0.4	6.65±0.49	544.3±0.5	4.72±0.26
563.3±0.5	5.39±0.40	635.3±0.6	433±22
593.4±0.5	12.2±0.9	797.4±0.8	6.09±0.38
871±1	925±67	905±1	594±30
922±1	745±54	956±1	888±44
967±1	15.0±1.1	1082±1	21.3±1.2
1005±1	38.4±2.8	1215±2	418±21
1207±2	7.61±0.68	1358±2	27.4±1.5
1398±2	231±17	1433±2	147.6±7.5
1513±3	17.7±1.5	1652±3	1269±64
1586±3	158±12	1710±3	76.9±4.0
1840±4	914±67	2008±4	696±35

thicknesses. The ^{108}Pd 149.7 eV resonance is partially obscured by a ^{105}Pd resonance at approximately the same energy. The uncertainty in the contamination (7%) times the size of the ^{105}Pd peak relative to the ^{108}Pd peak (60%) leads to an additional 4% error that has been included in the error listed in Table 4.2. According to Mughabghab [Mug88b] there is a resonance at 962.4 eV, but this resonance is not resolved from the 956 eV resonance in the spectrum. The 962.4 eV neutron width was held constant to 47.1 meV when the 956 eV resonance was fit.

4.1.5 Capture Normalization

In order to determine the resonance parameters from the capture measurements, the data needed to be normalized. That is, the energy dependent flux times the efficiency for the capture detector needed to be found. This was done by comparing the area in a capture peak to the area in a transmission peak of the same resonance. The area in a capture peak in the *ToF* spectrum is given by

$$A_\gamma = \Phi(E)\epsilon\frac{\Gamma_\gamma}{\Gamma}A_T, \tag{4.12}$$

where A_T is the resonance area from the transmission spectrum in units of energy which is normalized to 100% transmission off resonance. The energy dependence of the neutron flux times capture-detector efficiency, $\Phi(E)\epsilon$, is modeled by:

$$\begin{aligned}\Phi(E)\epsilon &= \frac{\alpha}{E^\beta}\\ &= \frac{A_\gamma}{\frac{\Gamma_\gamma}{\Gamma}A_T}.\end{aligned} \tag{4.13}$$

Using Equation 4.13, the extracted values of α and β were found by determining the area in both the capture and the 60° transmission peaks for several resonances, where $g\Gamma_n < \Gamma_\gamma$. The fit of $A_\gamma/\frac{\Gamma_\gamma}{\Gamma}A_T$ versus E is shown in Figure 4.5. The resulting expression for the capture normalization is given by

$$\Phi(E)\epsilon = \frac{6.20\times10^8}{E^{1.00}} \quad \text{(neutrons)} \tag{4.14}$$

with error given by

$$\frac{\Delta\Phi(E)\epsilon}{\Phi(E)\epsilon} = \sqrt{0.00221 + 0.00243[\ln(E) - 6.12]^2}. \tag{4.15}$$

The error includes the uncertainty in the 60° target thickness and is about 9% at 100 eV and about 6% at 1000 eV.

4.1.6 Extraction of $g\Gamma_n$ from Capture

For both the ^{106}Pd and ^{108}Pd data, 70 capture runs were summed and fit with FITXS to determine neutron-resonance widths. Since in general only low energy resonance shapes

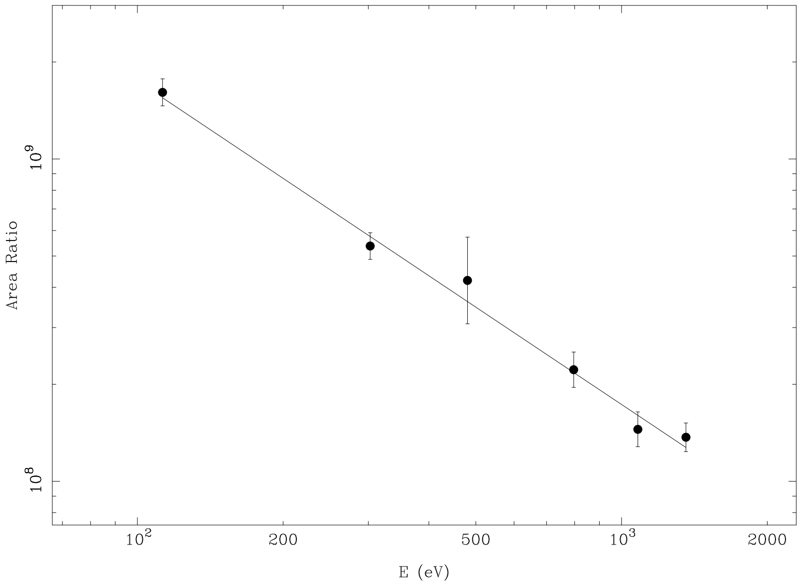

Figure 4.5: Capture normalization using ^{108}Pd capture and transmission data. Plotted is $A_\gamma/\frac{\Gamma_\gamma}{\Gamma}A_T$ versus neutron energy.

are sensitive to Γ_γ (see Figure A.1 of Appendix A), in all cases except five $\Gamma_\gamma = 91$ meV was used. The errors in $g\Gamma_n$ and Γ_γ include the uncertainty in the capture normalization. The energies listed in Tables 4.3 and 4.4 were found by identifying the resonance peak channel and using Equation 4.10.

^{106}Pd

From the fits of 13 ^{105}Pd resonances, the amount of ^{105}Pd contamination in ^{106}Pd was found to be $(1.01 \pm 0.02)\%$, which agrees with the value found from the transmission data. The contamination level was held constant, and known values of ^{105}Pd resonance parameters were used in subsequent fits. Only the 63.43 eV, 146.36 eV and 156.88 eV resonances showed appreciable sensitivity to Γ_γ. The weighted average of the three extracted Γ_γ values gives $\Gamma_\gamma = (106 \pm 2)$ meV.

The energies found from transmission and capture agree very well. There are dis-

Table 4.3: ^{106}Pd $g\Gamma_n$ values from capture data.

E (eV)	$g\Gamma_n$ (meV)	Γ_γ (meV)
63.43±0.04	0.0099±0.0011	107±4
146.36±0.07	0.534±0.039	91.0
156.88±0.07	0.244±0.017	107±8
300.0±0.2	0.179±0.010	91.0
406.7±0.3	0.862±0.044	91.0
462.3±0.3	1.14±0.05	91.0
521.9±0.4	6.02±0.28	91.0
563.4±0.5	5.29±0.25	91.0
593.4±.5	12.5±0.6	91.0
644.9±0.6	0.516±0.026	91.0
967.5±0.6	16.2±1.0	91.0
1005.3±0.7	57.9±3.5	91.0
1147.9±0.9	4.00±0.26	91.0
1206.2±0.9	10.0±0.7	91.0
1306±1	3.42±0.24	91.0
1323±1	7.78±0.55	91.0
1377±1	2.15±0.16	91.0
1511±1	28.0±2.1	91.0
1557±2	1.66±0.13	91.0
1585±2	153±12	91.0
1597±2	11.8±0.9	91.0
1624±2	10.2±0.8	91.0
1764±2	17.9±1.5	91.0

Table 4.4: ^{108}Pd $g\Gamma_n$ values from capture data.

E (eV)	$g\Gamma_n$ (meV)	Γ_γ (meV)
112.70±0.07	0.94±0.08	114±10
149.76±0.07	0.060±0.006	91.0
302.88±0.17	3.20±0.16	102±5
411.0±0.3	0.65±0.03	91.0
480.5±0.4	0.57±0.03	91.0
544.4±0.4	5.63±0.27	91.0
642.2±0.6	1.30±0.07	91.0
797.4±0.8	6.33±0.35	91.0
843.4±0.9	0.83±0.05	91.0
1082.3±0.8	17.2±1.0	91.0
1121±2	0.51±0.05	91.0
1140±2	0.083±0.018	91.0
1359±1	28.3±2.0	91.0
1456±1	4.49±0.34	91.0
1505±2	0.33±0.05	91.0
1523±2	2.79±0.22	91.0
1743±2	0.47±0.07	91.0
1815±2	2.35±0.20	91.0
2118±3	7.50±0.68	91.0
2165±3	2.59±0.26	91.0
2287±4	36.8±3.4	91.0

crepancies between the transmission and capture analyses of the neutron widths for the 1005.3 eV, 1206.2 eV and 1511 eV resonances. The values from capture will be used in future analyses.

^{108}Pd

From the fits of 9 ^{105}Pd resonances, the amount of ^{105}Pd contamination in ^{108}Pd was found to be $(0.29 \pm 0.02)\%$. Only the 112.70 eV and 302.88 eV resonances show significant sensitivity to Γ_γ. The weighted average of these Γ_γ values gives $\Gamma_\gamma = (104 \pm 4)$ meV. The 149.76 eV resonance listing includes additional uncertainty from the ^{105}Pd contaminant peak. Multiplying the 7% uncertainty in the amount of ^{105}Pd contamination by the percentage of the total area (45%) that the ^{105}Pd resonance comprises, adds 3% error to the other fitting errors for this resonance.

The energies found from transmission and capture agree very well. There are discrepancies between the transmission and capture analyses of the neutron widths for the 149.76 eV, 544.4 eV and 1082.3 eV resonances. The values from capture will be used in future analyses.

4.1.7 Orbital Angular Momentum

Following the Bayesian technique of Bollinger and Thomas [Bol68] and using the notation of Frankle [Fra94], the probability of a resonance being a p-wave can be expressed in the following way:

$$P\left(p, g\Gamma_n\right) = \left(1 + \frac{\pi_s}{\pi_p}\sqrt{3\frac{\pi_s}{\pi_p}\frac{S_1 C_0\left(E\right)}{S_0 C_1\left(E\right)}}\exp\left[\frac{-g\Gamma_n}{2}\frac{C_0\left(E\right)}{D_0}\left(\frac{1}{S_0} - \frac{\pi_p}{3\pi_s}\frac{C_1\left(E\right)}{C_0\left(E\right) S_1}\right)\right]\right)^{-1}, \quad (4.16)$$

where $\frac{\pi_s}{\pi_p}$ is the ratio of the *a priori* probability of forming an s-wave to that of forming a p-wave, D_0 is the s-wave level spacing, $S_{0,1}$ are the s- and p-wave strength functions and

$$C_\ell\left(E\right) = \frac{1 + \left(kR\right)^\ell}{\left(kR\right)^{2\ell}\sqrt{E(eV)}}. \quad (4.17)$$

The strength functions are given by

$$S_\ell = \frac{1}{2\ell+1}\frac{\langle g\Gamma_n^\ell\rangle}{D_\ell}, \tag{4.18}$$

where $g\Gamma_n^\ell$ is the reduced neutron width given by

$$g\Gamma_n^\ell = C_\ell\,(E)\,g\Gamma_n. \tag{4.19}$$

In deriving Equation 4.16 it was assumed that $D_1 = \frac{\pi_s}{\pi_p} D_0$. Resonances with probabilities greater than the *a priori* p-wave probability (0.75 for target spin zero), were assigned $l = 1$. The neutron widths used in calculating the p-wave probabilities were taken from the capture analysis, Tables 4.3 and 4.4, for all the resonances that were analyzed using the capture data. The rest were taken from the transmission analysis as given in Table 4.2, unless marked with an asterisk indicating values taken from Mughabghab. Initially the level spacing and strength functions listed in Mughabghab were used to determine p-wave probabilities. From the probabilities, s- and p-wave assignments were made, and a new level density and new strength functions were calculated. The process was then repeated until the assignments were stable.

^{106}Pd

The initial parameters taken from Mughabghab were the following: $D_0 = 67$ eV, $S_0 = 0.34 \times 10^{-4}$, $S_1 = 5.2 \times 10^{-4}$ and $R = 6.6$ fm. Figures 4.6 and 4.7 show the cumulative number of levels and cumulative reduced width for s-waves and p-waves versus neutron energy. The s-wave level spacing was determined from the slope of the fit of the cumulative number of levels to be $D_0 = (159 \pm 18)$ eV. From the slopes of the fits of the cumulative reduced width data, the strength functions were found to be $S_0 = (0.69 \pm 0.27) \times 10^{-4}$ for the s-waves and $S_1 = (2.0 \pm 0.7) \times 10^{-4}$ for the p-waves. For the p-waves, only resonances below 750 eV were included in the fit. The fractional error in the strength function is given by $\sqrt{2/N}$, where N is the number of levels analyzed [Mal70]. Table 4.5 lists the s-wave and p-wave assignments for ^{106}Pd.

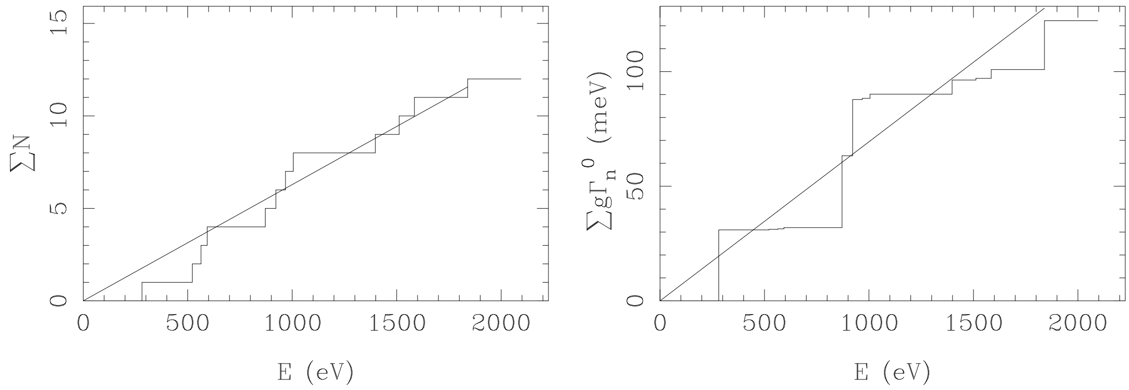

Figure 4.6: Cumulative number of levels (left) and cumulative reduced neutron width (right) for ^{106}Pd s-waves.

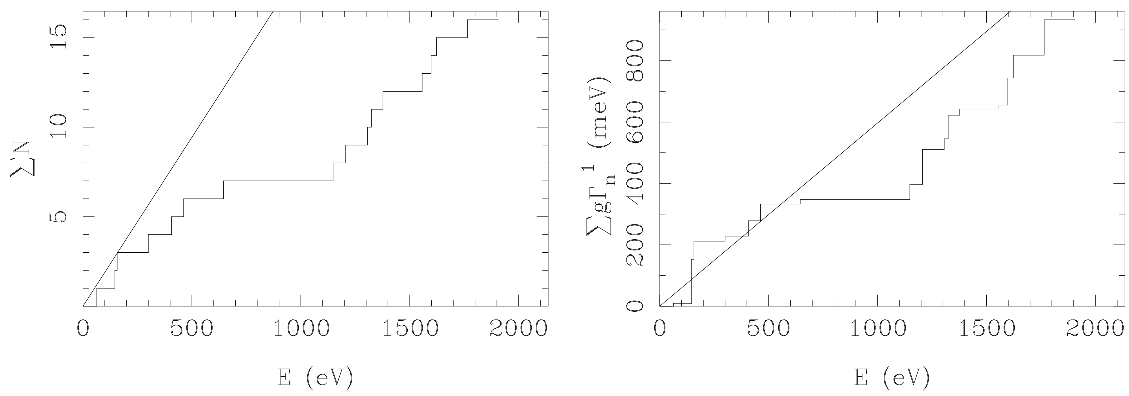

Figure 4.7: Cumulative number of levels (left) and cumulative reduced neutron width (right) for ^{106}Pd p-waves. The solid line in the left hand plot corresponds to a p-wave level spacing equal to $D_0/3$.

Table 4.5: ^{106}Pd angular momentum assignments, where the probability is the Bayesian p-wave probability.

E (eV)	$g\Gamma_n$ (meV)	Probability	l
63.43±0.04	0.0099±0.0011	0.99	1
146.36±0.07	0.534±0.039	0.91	1
156.88±0.07	0.244±0.017	0.98	1
281.1±0.3	519±38	0.00	0
300.0±0.2	0.179±0.010	0.98	1
406.7±0.3	0.862±0.044	0.97	1
462.3±0.3	1.14±0.05	0.96	1
521.9±0.4	6.02±0.28	0.55	0
563.4±0.5	5.29±0.25	0.73	0
593.4±0.5	12.5±0.6	0.07	0
644.9±0.6	0.516±0.026	0.97	1
871±1	925±67	0.00	0
922±1	745±54	0.00	0
967.5±0.6	16.2±1.0	0.42	0
1005.3±0.7	57.9±3.5	0.00	0
1147.9±0.9	4.00±0.26	0.94	1
1206.2±0.9	10.0±0.7	0.86	1
1306±1	3.42±0.24	0.95	1
1323±1	7.78±0.55	0.91	1
1377±1	2.15±0.16	0.96	1
1398±2	231±17	0.00	0
1511±2	28.0±2.1	0.48	0
1557±2	1.66±0.13	0.96	1
1585±2	153±12	0.00	0
1597±2	11.8±0.9	0.89	1
1624±2	10.2±0.8	0.91	1
1764±2	17.9±1.5	0.83	1
1839±4	914±67	0.00	0

^{108}Pd

In calculating the p-wave probabilities for ^{108}Pd, the following parameters were used initially: $D_0 = 45$ eV, $S_0 = 0.78 \times 10^{-4}$, $S_1 = 4.4 \times 10^{-4}$ and $R = 6.5$ fm. The level spacing and strength functions were found from the graphs in Figure 4.8 and 4.9 as discussed for ^{106}Pd. The final values were found to be $D_0 = (159 \pm 18)$ eV, $S_0 = (1.1 \pm 0.4) \times 10^{-4}$ and $S_1 = (5.5 \pm 1.7) \times 10^{-4}$. Table 4.6 lists the s-wave and p-wave assignments for ^{108}Pd.

Table 4.6: ^{108}Pd angular momentum sssignments, where the probability is the Bayesian p-wave probability. An asterisk indicates parameters taken from Mughabghab.

E (eV)	$g\Gamma_n$ (meV)	Probability	l
33.10±0.17*	117±8*	0.00	0
90.8±0.2*	199±8*	0.00	0
112.70±0.07	0.94±0.08	0.91	1
149.76±0.07	0.060±0.006	0.99	1
302.9±0.2	3.20±0.16	0.91	1
411.0±0.3	0.65±0.03	0.97	1
426.9±0.3	390±19	0.00	0
480.5±0.4	0.57±0.03	0.97	1
544.4±0.4	5.63±0.27	0.92	1
635.3±0.6	433±22	0.00	0
642.2±0.6	1.30±0.07	0.97	1
797.4±0.8	6.33±0.35	0.94	1
843.4±0.9	0.83±0.05	0.97	1
905±1	594±30	0.00	0
956±1	888±44	0.00	0
962.4±0.96*	47.1±0.4*	0.27	0
1082.3±0.8	17.2±1.0	0.88	1
1121±2	0.51±0.05	0.96	1
1140±2	0.083±0.018	0.97	1
1215±2	418±21	0.00	0
1359±1	28.3±2.0	0.84	1
1433±2	147.6±7.5	0.01	0

continued on the next page

continued from the previous page

E (eV)	$g\Gamma_n$ (meV)	Probability	l
1456±1	4.49±0.34	0.95	1
1505±2	0.33±0.05	0.96	1
1523±2	2.79±0.22	0.96	1
1652±3	1269±64	0.00	0
1710±3	76.9±4.0	0.53	0
1743±2	0.47±0.07	0.96	1
1815±2	2.35±0.20	0.95	1
2008±2*	10±3*	0.94	1
2008±4	696±35	0.00	0
2118±3	7.50±0.68	0.94	1
2165±3	2.59±0.26	0.95	1
2287±4	36.8±3.4	0.89	1

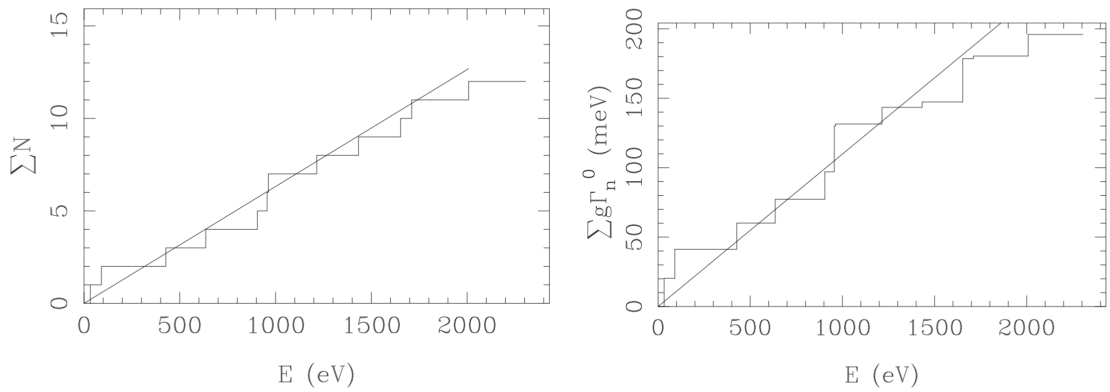

Figure 4.8: Cumulative level spacing (left) and cumulative reduced neutron width (right) for ^{108}Pd s-waves.

4.1.8 Neutron Polarization

During each parity nonconservation run, the proton polarization was monitored by taking NMR scans of the proton target as discussed in Section 3.3. The resulting NMR measurements of the proton polarization were stored along with the other run information.

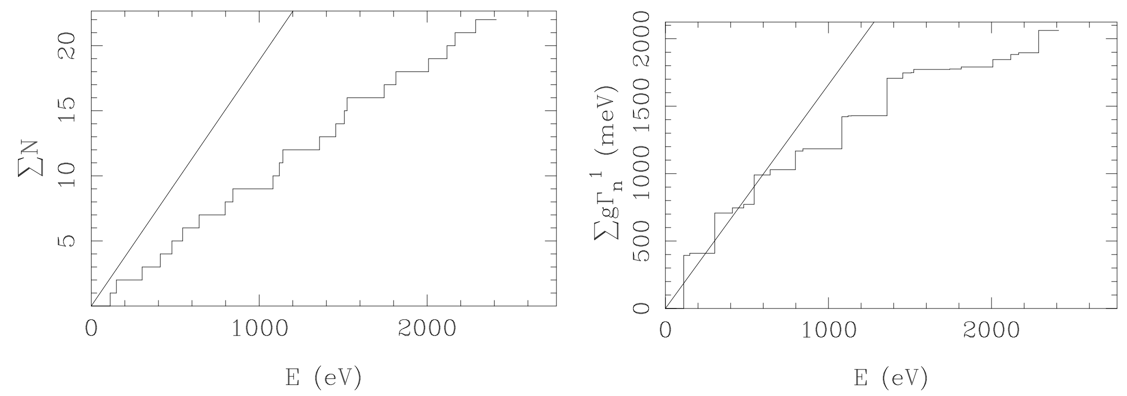

Figure 4.9: Cumulative level spacing (left) and cumulative reduced neutron width (right) for ^{108}Pd p-waves. The solid line in the left hand plot corresponds to a p-wave level spacing equal to $D_0/3$.

To calibrate the NMR measurements, f_{NMR}, to the neutron polarization, f_n, a series of short runs for various proton polarizations were taken. For this study the microwave power to the proton target was turned on and then off causing the proton polarization to grow to a normal operating value and then decay to zero. Since this process took a few hours, many three minute runs were taken, allowing the measurement of the neutron transmission through the proton target as a function of proton polarization. The neutron transmission depends on the proton polarization, and thus the NMR measurement, in the following way:

$$\begin{aligned} T &= T_\circ \cosh\left(n\sigma_{pol} f_p\right) \\ &= T_\circ \cosh\left[\mathcal{F}\left(f_{\mathrm{NMR}}\right)\right], \end{aligned} \tag{4.20}$$

where T and $T_\circ$ are the polarized and unpolarized transmissions, respectively; n is the proton target areal density; $\sigma_{pol} = \left(\sigma_{\rightleftarrows} - \sigma_{\rightrightarrows}\right)/2$; f_p is the proton polarization; and $\mathcal{F}$ is some function of the NMR measurement, f_{NMR}. The neutron polarization can be expressed in terms of the proton polarization and thus the NMR measurement,

$$\begin{aligned} f_n &= \tanh\left(n\sigma_{pol}f_p\right) \\ &= \tanh\left[\cosh^{-1}\left(\frac{T}{T_\circ}\right)\right] \\ &= \tanh\left[\mathcal{F}\left(f_{\text{NMR}}\right)\right], \end{aligned} \tag{4.21}$$

where $\mathcal{F}\left(f_{\text{NMR}}\right) = \cosh^{-1}\left(T/T_\circ\right)$. Figure 4.10 shows how the proton polarization changed as the polarization grew and decayed for several energies. The data points were calculated by determining the counts in a particular region of the *ToF* spectrum, and then calculating $\cosh^{-1}$ of the ratio of the counts in a given run to the counts in the same region for a run with zero polarization. The data taken for the negative polarization showed detector instability in the energy region above about 3–4 eV, so only energies below this are shown in the bottom figure of Figure 4.10.

The NMR calibration, $\mathcal{F}\left(f_{\text{NMR}}\right)$, was found by fitting a plot of $\cosh^{-1}$ of the transmission ratio versus the NMR measurement, f_{NMR}. The fits for the two polarization states are shown in Figure 4.11 and yield the following expressions for the NMR calibration. For positive proton polarization,

$$\mathcal{F}_+\left(f_{\text{NMR}}\right) = 1.50 f_{\text{NMR}} - 0.026, \tag{4.22}$$

and for negative proton polarization

$$\mathcal{F}_-\left(f_{\text{NMR}}\right) = -1.33 f_{\text{NMR}} + 0.032. \tag{4.23}$$

The values plotted in Figure 4.11 were found by averaging the calculations from 1, 3, 10 and 100 eV for the positive polarization and 1 and 3 eV for the negative polarization. Using Equations 4.22 and 4.23 with 4.21, the neutron polarizations for each parity nonconservation run were determined. Typical values of the neutron polarization were 85% for positive proton polarization and 82% for negative proton polarization. The primary source of error is from the energy dependence of the NMR measurement, seen in

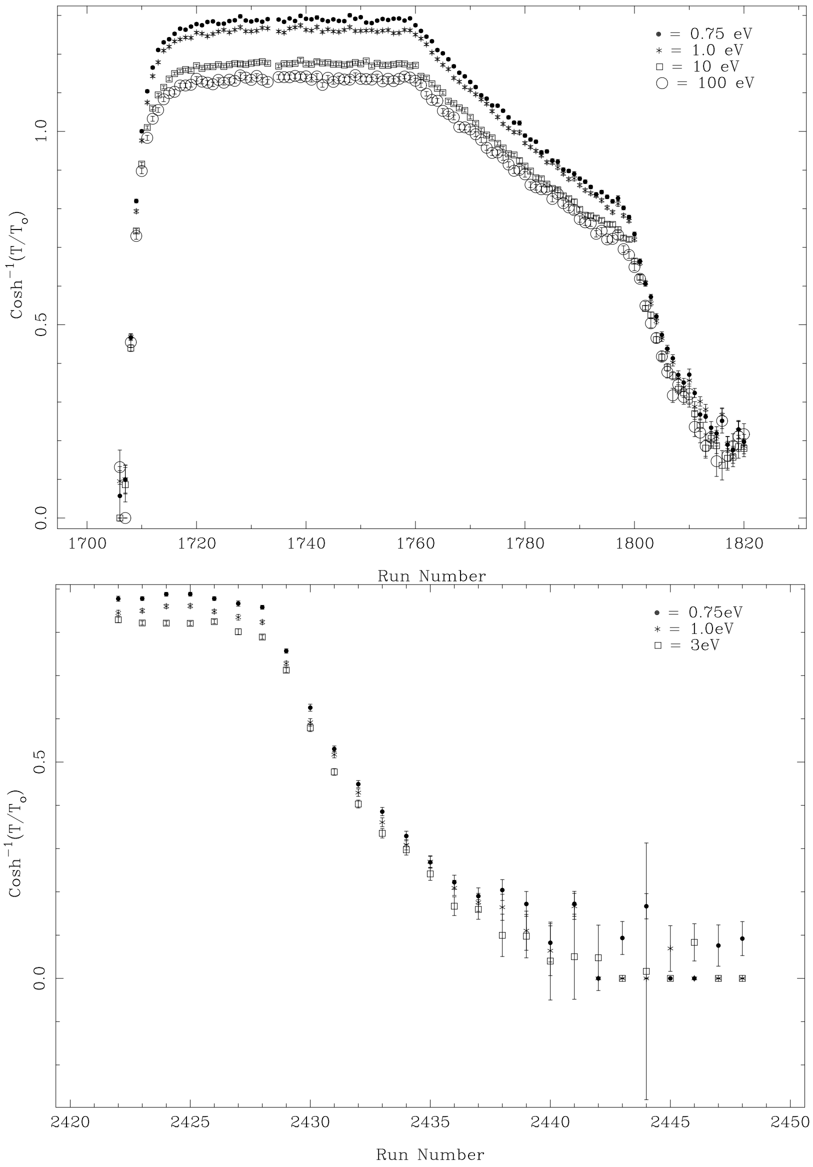

Figure 4.10: Proton polarization times target thickness, $n\sigma_{pol}f_p$, as a function of run number for the positive (top) and negative (bottom) polarization states. Plotted are calculations for several energies.

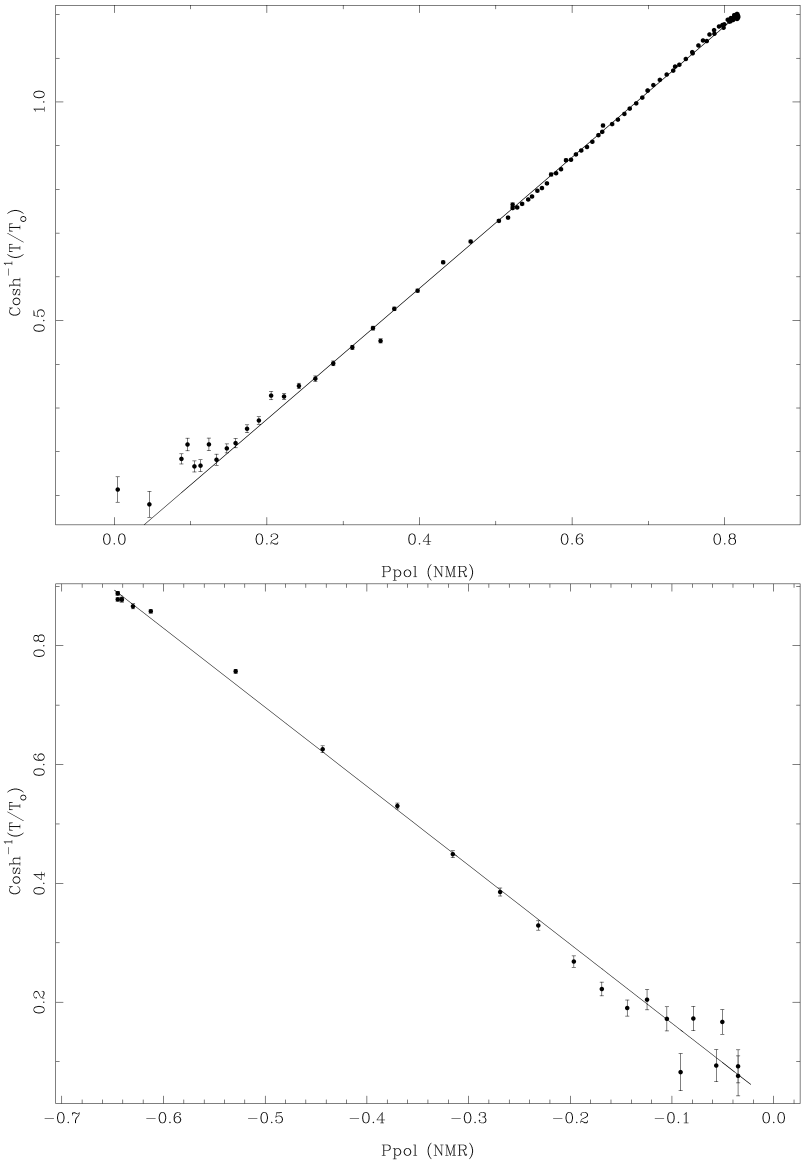

Figure 4.11: Proton polarization times target thickness, $n\sigma_{pol}f_p$, as a function of $f_{\rm NMR}$ for the positive (top) and negative (bottom) polarization states.

Figure 4.10. From averaging calculations for the four energies (1, 3, 10, 100 eV) for the positive polarization, the relative error in the neutron polarization is estimated to be $\sim 3\%$ (Averaging the neutron polarization from the peak of the four energy calculations for the top figure of Figure 4.10 gives $f_n = (84 \pm 2)\%$).

4.1.9 PNC Asymmetries

The PNC asymmetries were obtained by using FITXS to fit each run varying the asymmetry parameter while holding all other parameters constant. First FITXS fit the sum of the two helicity states (NOFLIP+FLIP) to determine the flux and background parameters for a single run. Then holding all parameters fixed except the asymmetry parameter, the code fit each helicity state (NOFLIP, FLIP) separately to extract asymmetries, $\mathcal{P}^+$ and $\mathcal{P}^-$, for each run. Since the PNC asymmetry, $\mathcal{P}$, is given by

$$\mathcal{P} = \frac{\sigma_p^+ - \sigma_p^-}{\sigma_p^+ + \sigma_p^-} \tag{4.24}$$

and

$$\sigma_p^\pm = \sigma_p \left(1 + \mathcal{P}^\pm\right), \tag{4.25}$$

one can solve for $\mathcal{P}$ to obtain

$$\mathcal{P} = \frac{\mathcal{P}^+ - \mathcal{P}^-}{2 + \mathcal{P}^+ + \mathcal{P}^-}. \tag{4.26}$$

The asymmetries were averaged over all runs, each run weighted with the monitor counts for that run. Table 4.7 lists the PNC asymmetries for ^{106}Pd. The only statistically significant effect is for the 593.4 eV resonance which is listed in Table 4.5 as an s-wave. This anomalous effect is discussed further in Section 4.1.10. The asymmetries for ^{108}Pd are listed in Table 4.8. There are no statistically significant effects for ^{108}Pd. The spin flipper efficiency calculations are discussed in Section 3.4.

Table 4.7: ^{106}Pd PNC asymmetries. The letter "s" indicates an s-wave. The "pos" and "neg" subscripts refer to the polarity of the proton filter. The primes indicate values not corrected for the spin flipper efficiency, $\epsilon_{\rm sf}$. An asterisk indicates an effect with a statistical significance greater than 2.5 σ.

E (eV)	$\mathcal{P}'_{\rm pos}(\%)$	$\mathcal{P}'_{\rm neg}(\%)$	$\epsilon_{\rm sf}$	$\bar{\mathcal{P}}(\%)$	$\bar{\mathcal{P}}/\Delta\bar{\mathcal{P}}$
63.43±0.04	0.25±0.25	−0.37±0.34	0.99	0.03±0.20	0.1
146.36±0.07	−0.017±0.055	0.129±0.074	0.98	0.035±0.045	0.8
156.88±0.07	0.071±0.090	−0.01±0.13	0.98	0.047±0.075	0.6
300.0±0.2	0.14±0.30	0.27±0.38	0.99	0.19±0.24	0.8
406.7±0.3	−0.09±0.15	−0.02±0.19	0.98	−0.07±0.12	−0.6
462.3±0.3	−0.025±0.15	−0.06±0.21	0.96	−0.04±0.13	−0.3
^{s}521.9±0.4	−0.054±0.068	−0.054±0.093	0.96	−0.057±0.058	−1.0
^{s}563.4±0.5	0.036±0.078	−0.19±0.11	0.96	−0.044±0.066	−0.7
^{s}593.4±0.5	−0.173±0.051	−0.156±0.078	0.97	−0.174±0.044	−4.0*
644.9±0.6	0.28±0.45	1.27±0.67	0.98	0.60±0.38	1.6
1147.9±0.9	0.72±0.29	0.25±0.37	0.94	0.58±0.24	2.4
1206.2±0.9	−0.11±0.17	−0.07±0.22	0.93	−0.11±0.15	−0.7
1306±1	0.32±0.43	0.34±0.68	0.91	0.36±0.40	0.9
1323±1	−0.15±0.23	−0.15±0.34	0.91	−0.17±0.21	−0.8
1377±1	−0.90±0.74	0.27±98	0.90	−0.53±0.66	−0.8
^{s}1511±2	0.01±0.13	0.20±0.17	0.89	0.09±0.12	0.8
1557±2	−1.1±1.3	−1.1±2.2	0.88	−1.2±1.2	−1.0
1597±2	−0.20±0.24	−0.05±0.33	0.88	−0.17±0.22	−0.8
1624±2	−0.14±0.28	0.02±0.53	0.88	−0.12±0.28	−0.4
1764±2	0.32±0.22	−0.34±0.34	0.88	0.15±0.21	0.7

Table 4.8: ^{108}Pd PNC asymmetries. For Group A the spin flipper field was 100 G. For Group B the spin flipper field was 130 G. The primes indicate values not corrected for the spin flipper efficiency, $\epsilon_{\rm sf}$.

E (eV)	$\mathcal{P}'_{\rm A}(\%)$	$\epsilon^{\rm A}_{\rm sf}$	$\mathcal{P}'_{\rm B}(\%)$	$\epsilon^{\rm B}_{\rm sf}$	$\bar{\mathcal{P}}(\%)$	$\bar{\mathcal{P}}/\Delta\bar{\mathcal{P}}$
112.70±0.07	0.084±0.066	0.99	0.009±0.050	0.99	0.037±0.040	0.9
149.76±0.07	0.11±0.49	0.97	0.03±0.37	0.98	0.06±0.30	0.2
302.9±0.2	0.13±0.10	0.96	−0.026±0.069	0.99	0.026±0.057	0.5
411.0±0.3	−0.06±0.43	0.99	−0.30±0.30	0.98	−0.22±0.25	−0.9
480.5±0.4	−0.41±0.49	1.00	0.31±0.39	0.96	0.03±0.31	0.1
544.4±0.4	−0.22±0.15	0.99	0.07±0.11	0.96	−0.036±0.090	−0.4
642.2±0.6	0.02±0.57	0.95	0.52±0.40	0.98	0.37±0.34	1.1
797.4±0.8	−0.06±0.25	0.90	0.19±0.17	1.00	0.12±0.14	0.8
843.4±0.9	−0.26±0.97	0.89	−0.53±0.81	1.00	−0.45±0.65	−0.7
1082.3±0.8	−0.02±0.19	0.89	0.12±0.13	0.95	0.09±0.12	0.7
1121±2	−0.2±3.2	0.89	1.3±2.7	0.94	0.7±2.3	0.3
1140±2	4.2±9.7	0.89	−8.1±6.3	0.94	−5.0±5.7	−0.9
1359±1	0.08±0.22	0.92	0.00±0.16	0.90	0.03±0.14	0.2
1456±1	−0.02±0.85	0.93	0.63±0.59	0.89	0.45±0.54	0.8
1505±2	1.5±8.6	0.94	−2.3±5.5	0.89	−1.2±5.2	−0.2
1523±2	−2.2±1.5	0.94	1.0±1.0	0.89	−0.11±0.93	−0.1
1743±2	3.4±7.8	0.97	−14.0±5.5	0.88	−8.7±4.9	−1.8
1815±2	−0.1±2.7	0.98	1.9±2.1	0.88	1.2±1.8	0.7
2118±3	0.0±1.3	0.99	0.34±0.94	0.90	0.23±0.81	0.3
2165±3	−3.4±3.7	1.00	3.2±3.0	0.91	0.4±2.5	0.2
2287±4	−0.83±0.43	1.00	0.13±0.36	0.92	−0.31±0.29	−1.1

4.1.10 Root-Mean-Squared PNC Matrix Element

The root-mean-squared PNC matrix element, $\mathcal{M}$, is determined by finding the peak of the likelihood function which corresponds to the most likely value of $\mathcal{M}$. For the cases where the likelihood function peaked at $\mathcal{M} = 0$, Equation 2.45 was integrated to 1000 meV to determine the upper limits on $\mathcal{M}$. Following the discussion in Section 2.4.1, the $p\frac{1}{2}$ and $p\frac{3}{2}$ probabilities were found to be $p' = 0.42$ and $q' = 0.58$ for ^{106}Pd and $p' = 0.41$ and $q' = 0.59$ for ^{108}Pd.

Table 4.9: A_i values for ^{106}Pd and ^{108}Pd.

^{106}Pd	
E (eV)	A_i (1/meV)
63.43	$1.56E-03$
146.36	$4.07E-04$
156.9	$6.62E-04$
300.0	$5.80E-03$
406.7	$4.61E-04$
462.3	$3.25E-04$
644.9	$5.36E-04$
1147.9	$2.02E-04$
1206.2	$1.14E-04$
1306	$2.31E-04$
1323	$1.74E-04$
1377	$1.00E-03$
1557	$7.50E-04$
1597	$6.10E-04$
1624	$2.28E-04$
1764	$1.95E-04$
questionable p-wave	
593.4	$1.00E-04$

^{108}Pd	
E (eV)	A_i (1/meV)
112.70	$1.46E-03$
149.76	$2.54E-03$
302.9	$2.21E-04$
411.0	$3.07E-03$
480.5	$1.09E-03$
544.4	$2.54E-04$
642.2	$5.31E-03$
797.4	$2.06E-04$
843.4	$7.12E-04$
1082	$1.51E-04$
1121	$8.64E-04$
1140	$2.35E-03$
1359	$1.02E-04$
1456	$5.43E-04$
1505	$1.11E-03$
1523	$3.93E-04$
1743	$1.45E-03$
1815	$3.71E-04$
2118	$1.93E-04$
2165	$2.43E-04$
2287	$4.18E-05$

^{106}Pd

Using the resonance parameters from Table 4.5, a list of A_i values was created and is shown in Table 4.9. This list combined with the PNC asymmetries were used to calculate a likelihood function for ^{106}Pd. However, the resonance at 593.4 eV complicates the likelihood analysis.

Although orbital angular momentum analysis gives strong evidence that the resonance at 593.4 eV is an s-wave, the fact that a PNC effect is seen at this energy seems to imply the resonance is a p-wave. There seem to be five ways to interpret the situation:

1. The 593.4 eV resonance is a p-wave and shows a PNC effect.
2. The 593.4 eV resonance is an s-wave and shows a PNC effect.
3. The 593.4 eV resonance is an s-wave, and a problem with the experiment or analysis caused the observance of the effect.
4. The 593.4 eV resonance is an s-wave and the observance of the effect is due only to statistical fluctuations of the measurement and thus is not a "real" effect.
5. The 593.4 eV resonance is an s-wave. In addition, there is an as yet unknown p-wave unresolved in the *ToF* spectrum from the 593.4 eV s-wave, and it is this second resonance that exhibits the parity nonconservation.

These five arguments are discussed below in order.

1. Since the orbital angular momentum study gave the 593.4 eV resonance a p-wave probability of 7%, it seems unlikely that the resonance is a p-wave. In addition, if the resonance is in fact treated as a p-wave, the resulting $\mathcal{M}$ is quite large. Figure 4.12 shows the likelihood function for this situation. The resulting $\mathcal{M}$ value is

$$\mathcal{M} = 11.0^{+7.7}_{-4.5} \quad (\text{meV}). \tag{4.27}$$

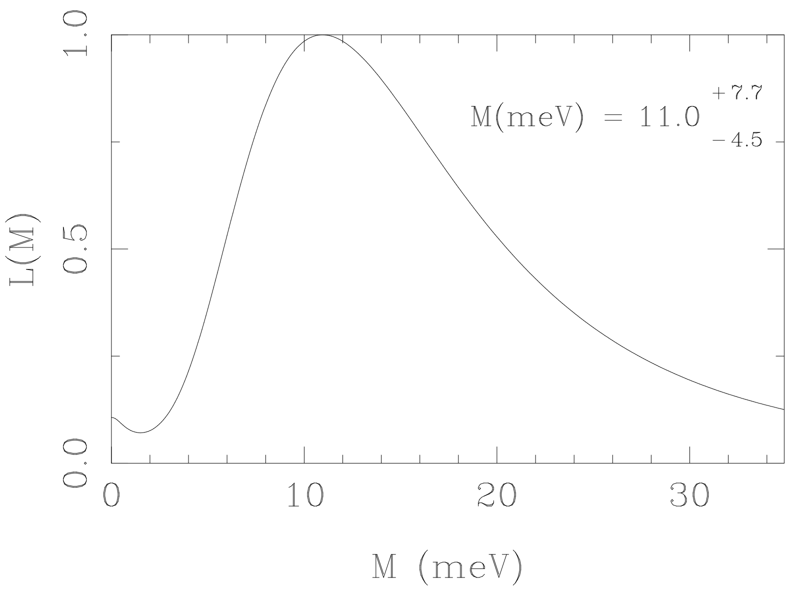

Figure 4.12: Likelihood function for ^{106}Pd assuming the 593.4 eV resonance is a p-wave with a PNC effect.

Using the equation for the weak spreading width given in Section 2.5 with the level spacing given by $D_0 = 159$ eV, the weak spreading width is given by

$$\Gamma_{\mathrm{W}} = \left(4.8^{+6.7}_{-3.9}\right) \times 10^{-6} \quad (\mathrm{eV}) \tag{4.28}$$

which is much larger than what has been observed in previous measurements in both the mass 100 and mass 230 regions [Ste96, Low96, See97, Smi97b].

2. Following the discussion of the PNC cross section asymmetry in Section 2.2.1, one can show that the magnitude of the ratio of the measured PNC asymmetry in an s-wave cross section to that in a p-wave cross section is equal to Γ_n^p/Γ_n^s. Comparing the 593.4 eV neutron width to the nearest p-wave neutron width shows that the size of the PNC asymmetry at the p-wave should be about 25 times larger than at the s-wave. Therefore, if the 593.4 eV resonance is an s-wave, then it is very unlikely that there would be an effect here without there also being effects at nearby p-waves.

3. Given that the nearby s-waves at 521.9 eV and 563.4 eV are of about the same strength and do not show effects, it would be surprising if the effect at 593.4 eV were due to an experimental or analysis problem. Nonetheless, a possible experimental problem could be some sort of electronic noise in the vicinity of 593.4 eV. However, fits of contaminant resonances in the same region of the ^{108}Pd spectrum show no asymmetry. Since only the targets changed when changing between the ^{106}Pd and ^{108}Pd experiments, it is reasonable that there is no false asymmetry coming from the data acquisition system or the analysis. In addition, Table 4.7 shows that the asymmetry was of approximately the same value for the positive- and negative-polarization data sets. That is, the observed asymmetry changed sign when the neutron polarization was reversed giving further confidence in the validity of the effect.

4. The chance of a four standard deviation effect being false is 0.0063%. Here again, the fact that the observed effect changed sign when the neutron polarization was reversed suggests that the effect is real.

5. The presence of a p-wave at very close proximity to the 593.4 eV resonance seems the most likely possibility. In an attempt to determine if this is plausible, a new resonance was added to the input file for FITXS with $E = 592.4$ eV and $g\Gamma_n = 0.30$ meV. This gave a good fit as seen in Figure 4.1.10. Next, a likelihood function was calculated with the new parameters and $\mathcal{P} = (-7.3 \pm 1.8)\%$. The $\mathcal{P}$ value was calculated by multiplying the 593.4 eV value by the ratio of $g\Gamma_n$ for the 593.4 eV resonance to $g\Gamma_n$ for the new resonance. Figure 4.1.10 shows the resulting likelihood function, where $\mathcal{M}$ is found to be

$$\mathcal{M} = 4.1^{+3.9}_{-1.7} \quad (\text{meV}), \tag{4.29}$$

leading to a spreading width of

$$\Gamma_{\text{w}} = \left(6.6^{+12.6}_{-5.5}\right) \times 10^{-7} \quad (\text{eV}). \tag{4.30}$$

This value is in general agreement with previous measurements [Ste96, Low96, See97, Smi97b].

The final option seems the most probable. However, since it is not possible with the present data to fix the location and the strength of a possible overlapping p-wave, the final matrix element and spreading width for ^{106}Pd are not given. It is interesting, however, to calculate the matrix element without the effect. The resulting $\mathcal{M}$ value is

$$\mathcal{M} = 0.00^{+8.4}_{-0.0} \quad \text{(meV)}, \tag{4.31}$$

where the upper limit is determined from the 68% confidence interval as discussed in Section 2.4.2. The upper limit on the weak spreading width from the ^{106}Pd analysis is

$$\Gamma_{\rm w} < 2.8 \times 10^{-6} \quad \text{(eV)}, \tag{4.32}$$

which is consistent with other measurements. The likelihood function for this situation is shown in Figure 4.14.

^{108}Pd

Using the resonance parameters from Table 4.6, a list of A_i values was created and is shown in Table 4.9. Together with the PNC effects in Table 4.8 for the p-waves, these A_i values were used to produce the likelihood function of Figure 4.15. This leads to an $\mathcal{M}$ value of

$$\mathcal{M} = 0.00^{+4.2}_{-0.0} \quad \text{(meV)} \tag{4.33}$$

and an upper limit on the weak spreading width of

$$\Gamma_{\rm w} < 7.0 \times 10^{-7} \quad \text{(eV)}, \tag{4.34}$$

which is in general agreement with previous measurements.

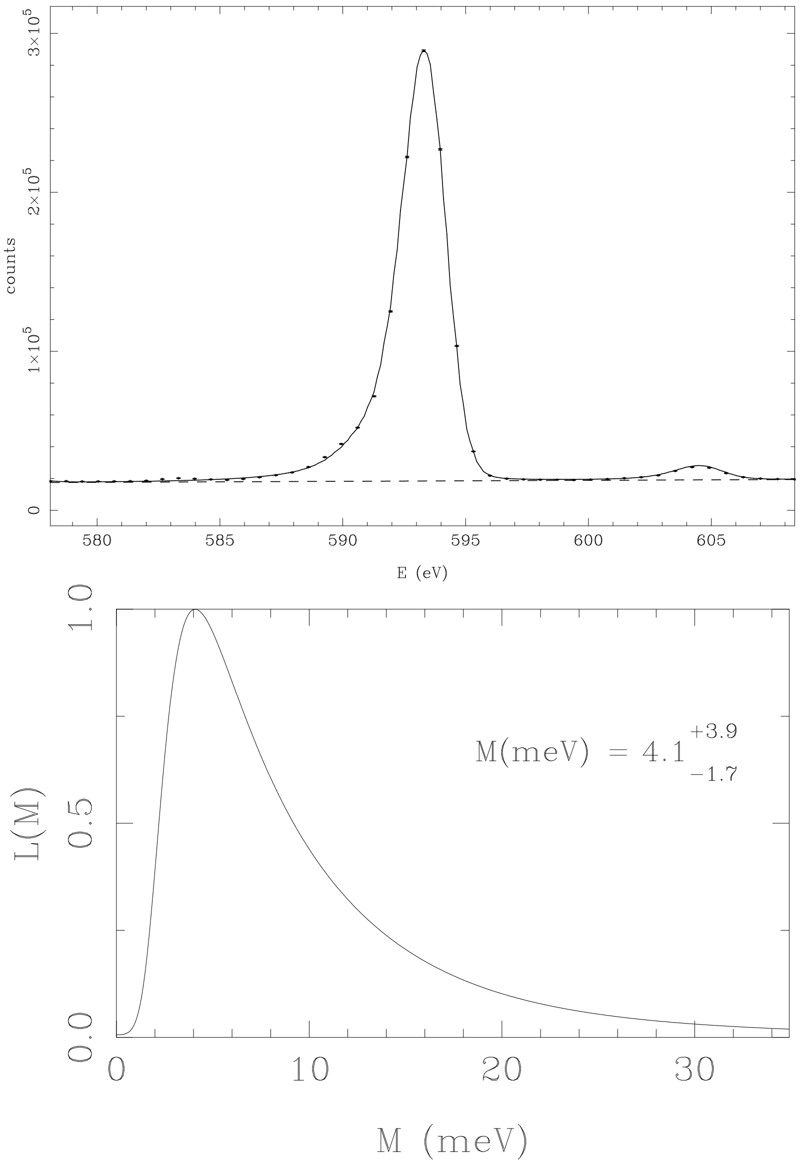

Figure 4.13: Study of a hypothetical p-wave in ^{106}Pd. The top figure is a fit of the ^{106}Pd spectrum, where a hypothetical resonance at 592.4 eV with $g\Gamma_n = 0.3$ meV has been included. The bottom figure shows the ^{106}Pd likelihood function, where the hypothetical resonance has been included. The 593.4 eV resonance was assumed to be an s-wave, and the 592.4 eV resonance was assumed to be a p-wave with $\mathcal{P} = (-7.3 \pm 1.8)\%$.

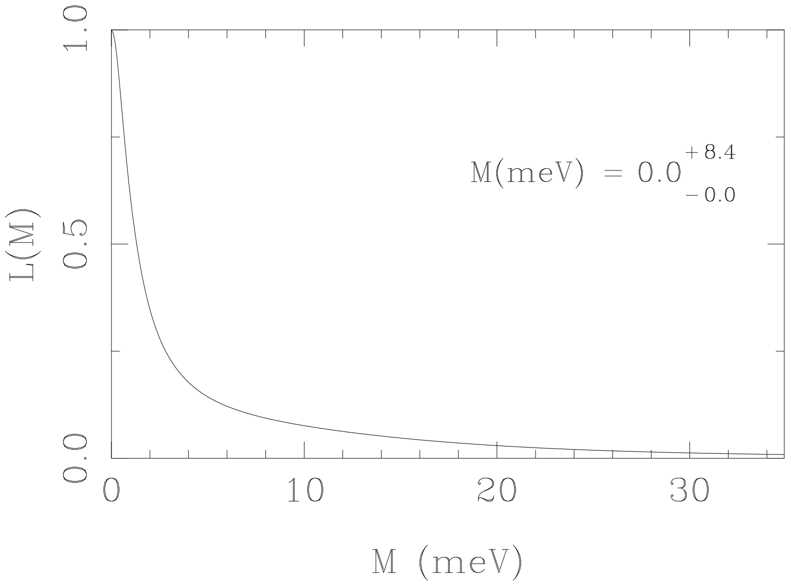

Figure 4.14: Likelihood function treating the 593.4 eV resonance as an s-wave and ignoring the PNC effect.

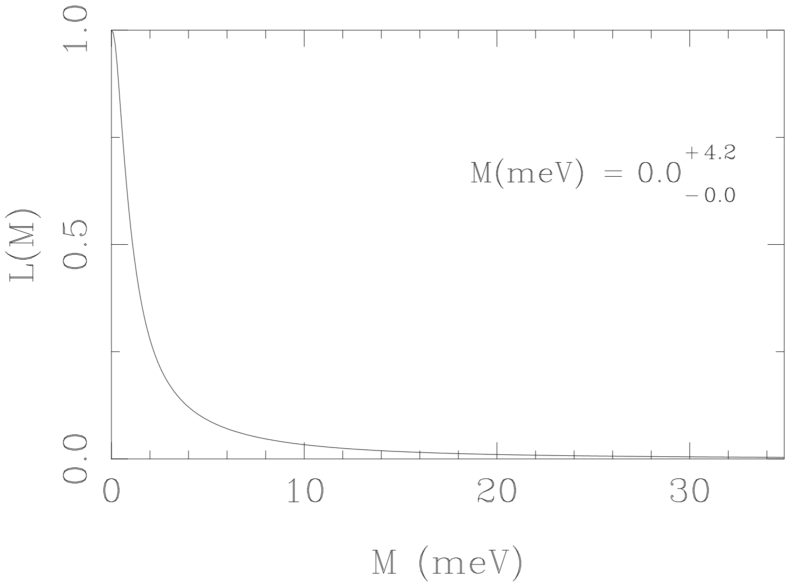

Figure 4.15: Likelihood function for ^{108}Pd.

4.2 Mass 230 region, ^{238}U

4.2.1 Data

The ^{238}U experiment was run during the 1993 run cycle and lasted approximately one week. After making a first cut of the data as discussed in Section 4.1.1, there were 157 good runs which are listed in Table 4.10. In addition, Table 4.10 lists the runs that were taken to determine the dead time of the system (see Section 3.8) and the NMR calibration runs which used a ^{139}La target (see Section 4.2.6).

Before being analyzed, all of the data were corrected for dead time effects and background as described in Sections 3.7 and 3.8.

Table 4.10: Run listing for ^{238}U.

Number of Good Runs	Absorber	Proton Polarization	Measurement
59	Cd	+	^{238}U parity
31	B	+	^{238}U parity
24	Cd	+	^{238}U parity
43	B	−	^{238}U parity
9	Cd	+	dead time
20	Cd	+	^{139}La parity
23	Cd	−	^{139}La parity

4.2.2 Target

The ^{238}U target was a 6.32 cm long, 9.79 cm in diameter depleted ^{238}U target. For a density of 18.9 g/cm^3, this leads to an areal density of 3.025×10^{23} atoms/cm^2. From fitting known ^{235}U resonances the amount of ^{235}U contamination was found to be $(0.21 \pm 0.01)\%$.

The target was chilled to liquid nitrogen temperature, which leads to an effective temperature of 103 K.

4.2.3 Energy to Time-of-Flight Calibration

The initial energy calibration for ^{238}U was found following the same procedure as described in Section 4.1.3 for the Pd data, using known resonances from ^{235}U and ^{238}U. This calibration was then used with the fitting code, FITXS, and known resonances to fit the spectrum varying the beam line length and the *ToF* offset. The resulting values were found to be $L = 56.736$ m and $C_\circ = 2.712$ channels, where the statistical errors returned by the fitting code were 2×10^{-5} m and 4×10^{-4} channels, respectively.

The total error on the above parameters is unknown because the errors on the ENDF/B-VI energies [Mox88] that were used in the input to FITXS are also unknown. Therefore, the errors on the resulting resonance energies are also uncertain. The statistical fitting errors for the smallest resonances were less than 0.006 eV. Tables 4.11 (s-waves) and 4.12 (p-waves) list the energies found from fitting the data with the above energy calibration, the energies from a study of ^{238}U at ORELA in 1978 on a 200 m flight path [Ols79] and the ENDF/B-VI evaluated energy values. It is clear from the tables that the energies extracted from FITXS agree very well with the ORELA values but not as well with the ENDF/B-VI values. It appears that although the ORELA experiment had a much longer flight path than the TRIPLE flight path (200 m versus 60 m), the error on the FITXS energy values is comparable to the ORELA data. In the case of the p-waves, the FITXS values may even have smaller error, due largely to the much higher statistics on the small p-waves in the TRIPLE experiments. There is uncertainty in the 6.683 eV s-wave because the *ToF* spectra only include the high energy half of the resonance. The value of 6.672 eV will be used in the following analyses.

The energy calibration from the above beam line length and channel offset is

$$E = \left(\frac{20510}{C + 2.71} \right)^2 \quad (\text{eV}). \tag{4.35}$$

Table 4.11: Comparison of the ^{238}U s-wave resonance energies from ENDF/B-VI, from ORELA and from fitting the data with FITXS. The parentheses indicate that only the high energy half of the 6.672 eV resonance was visible in the spectrum, so the energy obtained with FITXS is questionable.

E (eV) for s-waves		
ENDF/B-VI	ORELA	FITXS
6.674	6.6720±0.00002	(6.683)
20.871	20.864±0.001	20.855
36.682	36.671±0.001	36.670
66.032	66.015±0.001	65.992
80.749	80.729±0.002	80.732
102.66	102.54±0.01	102.53
116.902	116.87±0.01	116.85
145.66	145.63±0.01	145.64
165.29	165.26±0.01	165.29
189.67	189.64±0.01	189.73
208.51	208.47±0.01	208.46
237.38	237.34±0.01	237.31
273.66	273.62±0.01	273.63
291.00	290.96±0.01	290.97

Table 4.12: Comparison of the ^{238}U p-wave resonance energies from ENDF/B-VI, from ORELA and from fitting the data with FITXS. The s-superscript indicates that the ENDF/B-VI evaluation assigned the 257.22 eV resonance as an s-wave.

E (eV) for p-waves		
ENDF/B-VI	ORELA	FITXS
10.228	10.236±0.003	10.234
11.347	11.309±0.002	11.308
19.6279	19.523±0.004	19.520
45.21	45.166±0.037	45.157
49.641	49.626±0.072	49.611
63.5	63.505±0.012	63.494
72.367	–	72.372
83.695	83.684±0.027	83.677
89.221	–	89.216
93.075	93.097±0.050	93.081
98.00	–	97.978
111.151	111.21±0.12	111.18
124.994	124.98±0.07	124.94
133.236	133.29±0.15	133.18
152.419	152.42±0.03	152.40
158.936	158.95±0.09	158.94
173.15	173.19±0.04	173.19
214.814	214.85±0.12	214.85
218.28	218.32±0.19	218.33
242.702	242.71±0.04	242.71
253.88	253.89±0.06	253.87
^{s}257.216	257.24±0.27	257.22
263.906	263.93±0.03	263.92
282.4	282.43±0.07	282.44

4.2.4 Extraction of $g\Gamma_n$

To determine resonance parameters, ten runs were summed for the case of the Cd-absorber and likewise for the B-absorber. Since the absorbers effected the shape of the flux, especially in the low energy region, the two data sets were analyzed separately. In addition, Cd has several resonances that were seen in the spectrum and in some cases obscured ^{238}U resonances. Although this problem could be avoided by dividing the target-in data by the target-out data, as was done for the ^{106}Pd and ^{108}Pd isotopes, this was found to be unnecessary. In addition, since these data needed to be fit for the purposes of extracting parity nonconservation, unlike the ^{106}Pd and ^{108}Pd transmission data, the contaminants needed to be fit.

Because the ^{238}U target was very thick, many of the s-waves absorbed all neutrons at the resonance energy. The counts under these black resonances were due to background. Although these data were background corrected [Yen97], there was a certain amount of background unaccounted for. Therefore, it was necessary to determine a set of background parameters to be used in FITXS. This was done by simply fitting the counts under the black resonances to a polynomial function of $1/ToF$. The coefficients of this polynomial were used by FITXS to determine a background curve and were held constant for the rest of the fitting process.

Because there were so many large s-waves, the shape of the entire spectrum was dominated by these resonances. Figure 4.16 shows an example of this. The fitting procedure is given below:

1. Fit a large energy region with known parameters and allow the flux and energy dependence of the flux to vary. The energy dependence was found to be $E^{-0.948}$ and was then held constant.

2. Fit small energy regions containing only two to three s-waves. Start at the low energy end of the spectrum and allow E, $g\Gamma_n$ and Γ_γ of the s-waves to vary along with the

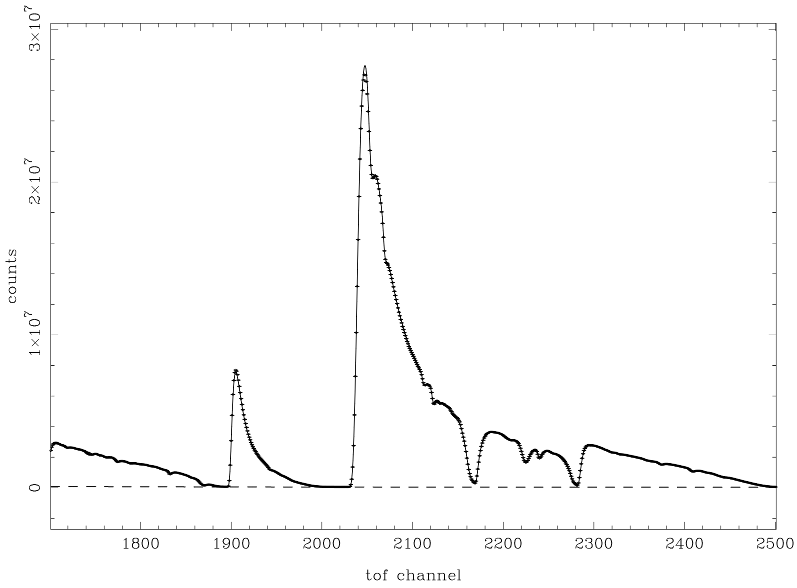

Figure 4.16: Sample fit of the Cd-absorber ^{238}U spectrum. The dashed line is the background curve.

flux.

3. Continue Item 2 at higher energies holding previously fit s-wave parameters constant and varying the parameters of new s-waves. Repeat this process until the parameters are stable.

4. Fit p-waves in isolated regions allowing the flux and p-wave $g\Gamma_n$ values to vary.

Table 4.13 contains a list of the s-wave resonance parameters along with those from the ENDF/B-VI evaluation. Since the count rate was quite high in these experiments, the statistical errors were very small for all cases but the smallest resonances. Thus, the overall fitting error was estimated by averaging the values found from the Cd-absorber and B-absorber data.

The neutron and γ-ray widths agree well except for the 6.672 eV resonance, which as discussed above is only partially seen in the data.

Table 4.13: ^{238}U s-wave $g\Gamma_n$ and Γ_γ values.

	Cd-absorber		B-absorber		Cd-B average		ENDF/B-VI	
E (eV)	$g\Gamma_n$ (meV)	Γ_γ (meV)	$g\Gamma_n$ (meV)	Γ_γ (meV)	$g\Gamma_n$ (meV)	Γ_γ (meV)	$g\Gamma_n$ (meV)	Γ_γ (meV)
6.672	(1.706)	(20.75)	(1.607)	(18.89)	(1.657±0.077)	(19.8±1.2)	1.493	23
20.855	10.67	21.08	10.56	21.03	10.62±0.23	21.06±0.84	10.26	22.9
36.670	34.65	19.96	34.92	20.59	34.79±0.72	20.28±0.87	34.13	22.9
65.992	25.06	21.82	24.41	21.92	24.74±0.68	21.87±0.88	24.6	23.4
80.732	1.67	28.55	1.71	25.06	1.69±0.17	26.8±3.7	1.865	23
102.53	71.8	24.02	71.7	23.63	71.7±1.4	23.83±0.97	71.7	23.4
116.85	25.72	24.24	24.86	22.29	25.29±0.79	23.3±1.3	25.49	23
145.64	0.740	27.05	0.748	26.77	0.744±0.016	26.91±0.57	0.847	23
165.29	3.26	20.91	3.07	24.85	3.17±0.15	22.9±2.2	3.367	23
189.73	173.7	31.26	174.7	28.02	174.2±3.6	29.6±2.0	173.2	22.4
208.46	51.8	25.18	50.5	22.39	51.0±1.2	23.8±1.7	51.11	23.9
237.31	25.45	24.02	26.18	22.05	25.82±0.73	23.4±1.3	27.16	24.5
273.63	24.30	24.94	24.23	24.24	24.27±0.49	24.6±1.0	25.78	22.1
290.97	16.07	23.49	16.02	23.18	16.05±0.32	23.34±0.95	16.87	22.1

Table 4.14 lists the p-wave neutron widths found from the above procedure. In the last step of the fitting procedure, the flux was allowed to vary because of imperfect fitting of the s-waves. When fitting a small energy region with a small p-wave, the off resonance region of the spectrum was very sensitive to the s-wave parameters. Rather than adjusting the s-wave parameters, the flux for that local energy region was varied. Figures 4.17 and 4.18 are plots of the flux parameter in units of neutrons per monitor sum as a function of energy. There is a noticeable energy dependence to the flux that is apparently due to an incorrect energy dependence of the flux found in the first step of the the fitting procedure. However, since a similar trend was seen while fitting the s-waves and since the s-waves agree with the known values, there does not appear to be a systematic error in the extracted widths. That is, it was necessary to vary the flux when fitting isolated regions in order to adjust the incorrect energy dependence determined in the first step of the fitting procedure. The fluctuation about the linear trend is $\sim 2\%$. The fluctuation in the variation of the flux directly affected the extraction of the $g\Gamma_n$ values. The additional 2% error is included in the $g\Gamma_n$ errors quoted in Table 4.14.

4.2.5 Orbital Angular Momentum

Following the same procedure as described in Section 4.1.7, the probability for a resonance being a p-wave was determined for the average $g\Gamma_n$ values listed in Table 4.13 and Table 4.14. The following values from Mughabghab were used: $D_0 = (20.9 \pm 1.1)$ eV, $S_0 = (1.2 \pm 0.1) \times 10^{-4}$, $S_1 = (1.7 \pm 0.3) \times 10^{-4}$ and $R = 6.6$ fm. Figures 4.19 and 4.20 show the cumulative number of levels and cumulative reduced width for s-waves and p-waves versus neutron energy. The s-wave level spacing was determined from the slope of the fit of the cumulative number of levels to be $D_0 = (18.8 \pm 1.8)$ eV which agrees with the value from Mughabghab. From the slopes of the fits of the cumulative reduced width data, the strength functions were found to be $S_0 = (1.4 \pm 0.5) \times 10^{-4}$ for the s-waves and $S_1 = (1.4 \pm 0.4) \times 10^{-4}$ for the p-waves which both agree with Mughabghab.

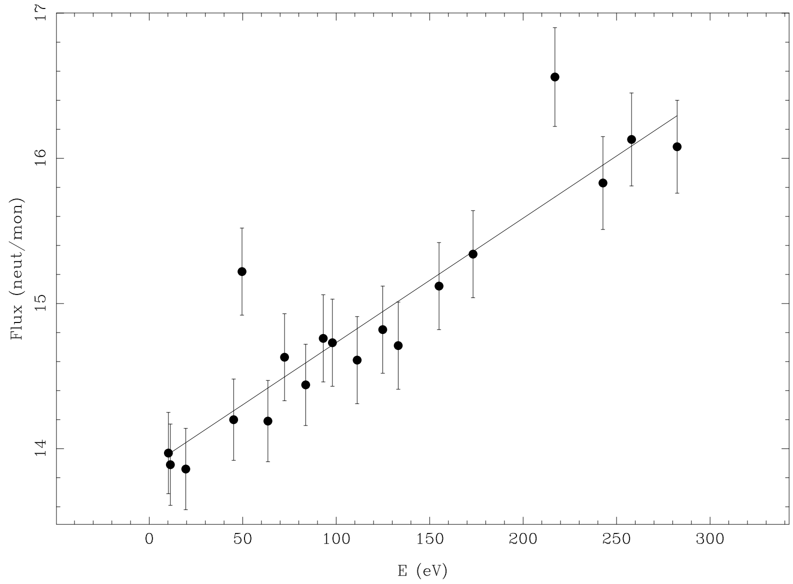

Figure 4.17: Flux from p-wave fits in units of neutrons per monitor sum versus energy for the Cd-absorber data. Each error bar represents a 2% standard deviation.

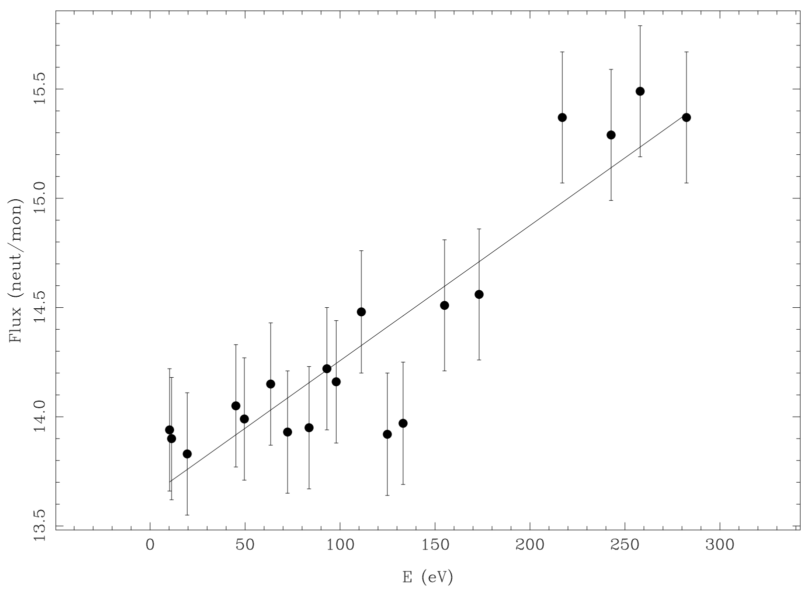

Figure 4.18: Flux from p-wave fits in units of neutrons per monitor sum versus energy for the B-absorber data. Each error bar represents a 2% standard deviation.

Table 4.14: ^{238}U p-wave $g\Gamma_n$ values.

	$g\Gamma_n$ (meV)			
E (eV)	Cd-absorber	B-absorber	Cd-B average	ENDF/B-VI
10.234	0.00168	0.00168	0.00168±0.00003	0.00168
11.308	0.000410	0.000411	0.000411±0.000008	0.0004
19.520	0.00150	0.00150	0.00150±0.00003	0.00232
45.157	0.00207	0.00203	0.00205±0.00005	0.002
49.611	0.00108	0.00107	0.00108±0.00002	0.0012
63.494	–	0.00944	0.00944±0.00019	0.0132
72.372	0.00171	0.00187	0.00179±0.00022	0.003
83.676	0.00902	0.00904	0.00903±0.00018	0.0123
89.216	–	0.0853	0.0853±0.0017	0.098
93.081	0.00617	0.00617	0.00617±0.00012	0.006
97.978	0.00443	0.00433	0.00438±0.00011	0.0048
111.18	0.00651	0.00681	0.00666±0.00044	0.0088
124.94	0.0194	0.0198	0.0196±0.0005	0.023
133.18	0.00793	0.00771	0.0078±0.0003	0.008
152.40	0.0519	0.0525	0.0522±0.0012	0.053
158.94	–	0.0164	0.0164±0.0004	0.019
173.19	0.0479	0.0478	0.0479±0.0010	0.050
214.85	–	0.055	0.055±0.002	0.072
218.33	0.0389	0.0332	0.0360±0.0042	0.031
242.71	0.199	0.207	0.203±0.008	0.194
253.87	0.117	0.115	0.116±0.003	0.109
257.22	0.026	0.025	0.025±0.002	0.034
263.92	0.257	0.260	0.256±0.006	0.276
282.44	0.113	0.111	0.112±0.003	0.107

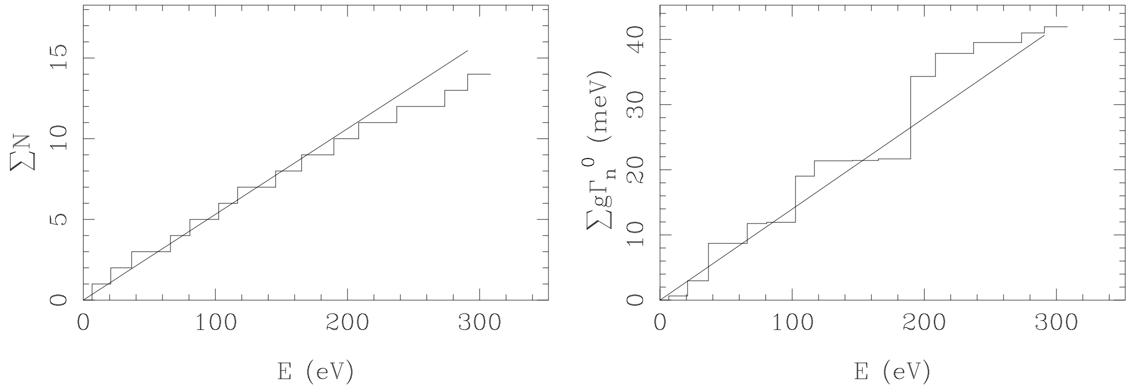

Figure 4.19: Cumulative number of levels (left) and cumulative reduced neutron width (right) for ^{238}U s-waves.

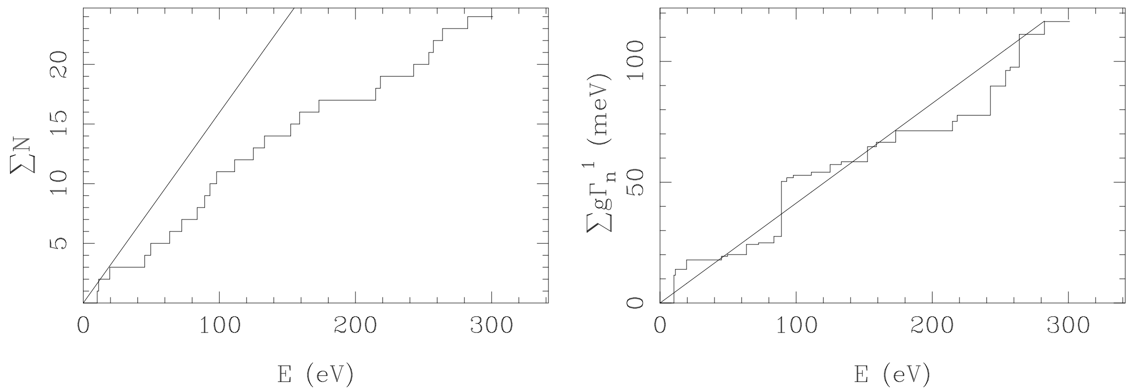

Figure 4.20: Cumulative number of levels (left) and cumulative reduced neutron width (right) for ^{238}U p-waves. The solid line in the left hand plot corresponds to a p-wave level spacing equal to $D_0/3$.

Table 4.15 lists the momentum assignments, where the Mughabghab values of D_0, S_0 and S_1 were used. This analysis agrees with the ENDF/B-VI assignments except for the 257.22 eV resonance which is determined in this analysis to be a p-wave.

Table 4.15: ^{238}U angular momentum assignments, where the probability is the Bayesian p-wave probability.

E (eV)	$g\Gamma_n$ (meV)	Probability	ℓ
6.672	(1.657±0.077)	0.00	0
10.234	0.00168±0.00034	0.99	1
11.308	0.000411±0.000008	1.00	1
19.520	0.00150±0.00003	0.99	1
20.855	10.62±0.23	0.00	0
36.670	34.79±0.72	0.00	0
45.157	0.00205±0.00005	0.99	1
49.611	0.00108±0.00002	0.99	1
63.494	0.00944±0.00019	0.99	1
65.992	24.74±0.68	0.00	0
72.372	0.00179±0.0022	0.99	1
83.676	0.00903±0.0018	0.99	1
89.216	0.0853±0.0017	0.84	1
93.081	0.00617±0.00012	0.99	1
97.978	0.00438±0.00011	0.99	1
102.53	71.7±1.4	0.00	0
111.18	0.00666±0.00044	0.99	1
116.85	25.29±0.79	0.00	0
124.94	0.0196±0.0005	0.99	1
133.18	0.0078±0.0003	0.99	1
145.64	0.744±0.016	0.00	0
152.40	0.0522±0.0012	0.98	1
158.94	0.0164±0.0004	0.99	1
165.29	3.17±0.15	0.00	0
173.19	0.0479±0.0010	0.98	1
189.73	174.2±3.6	0.00	0
208.46	51.0±1.2	0.00	0
214.85	0.055±0.002	0.98	1

continued on next page

continued from previous page

E (eV)	$g\Gamma_n$ (meV)	Probability	ℓ
218.33	0.0360±0.0042	0.98	1
237.31	25.82±0.73	0.00	0
242.71	0.203±0.008	0.93	1
253.87	0.116±0.003	0.97	1
257.22	0.025±0.002	0.98	1
263.92	0.256±0.006	0.92	1
273.63	24.27±0.49	0.00	0
282.44	0.112±0.003	0.97	1
290.97	16.05±0.32	0.00	0

4.2.6 Neutron Polarization

During the 1993 run, NMR calibration runs of the sort described in Section 4.1.8 were not taken. Instead parity nonconservation runs with a ^{139}La target were performed. Using the known PNC asymmetry value for the 0.75 eV p-wave in ^{139}La, the neutron polarization was extracted from the measured longitudinal asymmetry. Taking a weighted average of the two measurements at KEK and the three measurements at LANSCE, the effect for the ^{139}La resonance is $\mathcal{P} = (9.57 \pm 0.19)\%$ [Yua91]. The NMR calibration measurements were done throughout the 1993 run cycle. The NMR measurement of the proton target polarization, f_{NMR}, was calibrated to neutron polarization by comparing the neutron polarization measured by a ^{139}La parity nonconservation run with the f_{NMR} value for that run. From the expression

$$\begin{aligned} f_n &= \tanh\left(n\sigma_{pol}f_p\right) \\ &= \tanh\left(\alpha_{\mathrm{NMR}}f_{\mathrm{NMR}}\right) \end{aligned} \tag{4.36}$$

it is seen that for a given NMR calibration, $\tanh^{-1}(f_n)/f_{\mathrm{NMR}}$ is a constant, α_{NMR}, assuming that the NMR measurement is stable. Figure 4.21 shows plots of $\tanh^{-1}(f_n)/f_{\mathrm{NMR}}$ versus run number for three different NMR calibrations, where f_n was found from fitting ^{139}La runs. The measurements show that the NMR measurements were indeed stable during the run cycle. Averaging the values of $\alpha_{\rm NMR}$ gives the NMR calibration for each of the three data sets. The results are listed in Table 4.16.

Table 4.16: NMR calibrations for the 1993 run cycle.

Run Number	f_p sign	$\alpha_{\rm NMR}$
< 32385	$-$	0.789±0.047
≥ 32385	$+$	1.025±0.023
≥ 32385	$-$	0.860±0.018

4.2.7 PNC Asymmetries

The PNC asymmetries were extracted using FITXS and the method described in Section 4.1.9 with one difference. In the initial fitting of the NOFLIP+FLIP spectrum, only the flux was varied. Table 4.17 lists the effects for the four data sets. Table 4.18 lists the final, spin flipper corrected PNC asymmetries. There are six effects with a statistical significance greater than 2.5 σ, three with a positive sign and three with a negative sign.

4.2.8 Root-Mean-Squared PNC Matrix Element

Using the values from Tables 4.14 and 4.13, A_i values were found for ^{238}U and are listed in Table 4.19. Using the A_i values listed in Table 4.19 and the $\mathcal{P}$ values listed in Table 4.18, a likelihood analysis was performed following the procedures outlined in Section 2.4.1. Figure 4.22 shows plots of the likelihood function for ^{238}U for: (a) the case of including only the 7 known $p\frac{1}{2}$ resonances [Cor94] and 7 resonances with unknown spins and (b) the case of including all the resonances in Table 4.19 assuming all have unknown spins. For the case of unknown spins the $p\frac{1}{2}$ and $p\frac{3}{2}$ probabilities were found following the

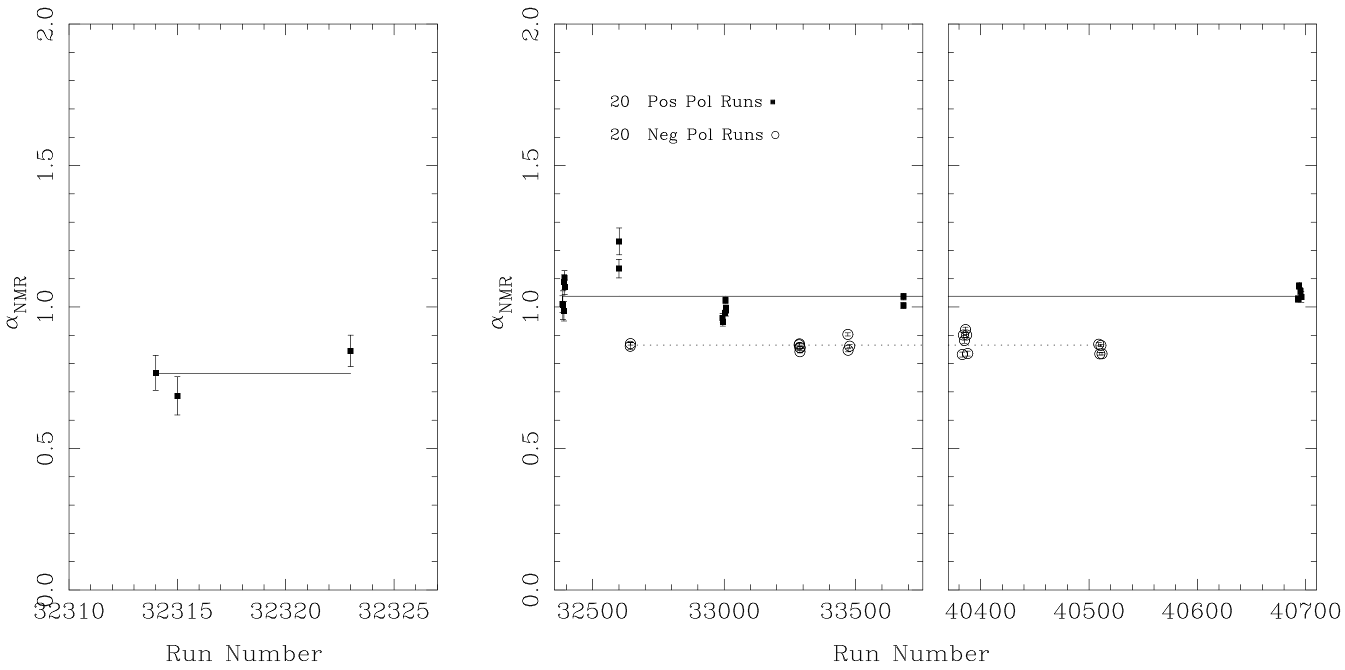

Figure 4.21: NMR calibrations for the 1993 run cycle.

Table 4.17: ^{238}U PNC asymmetries. The averages include the error in the neutron polarization, 6% for negative polarization and 2% for positive polarization. The primes indicate values not corrected for the spin flipper efficiency.

	$\mathcal{P}'_{\mathrm{neg}}$			$\mathcal{P}'_{\mathrm{pos}}$		
E (eV)	Cd	B	Cd-B avg.	Cd	B	Cd-B avg.
10.234	0.096±0.032	0.038±0.033	0.067±0.023	−0.021±0.033	0.031±0.037	0.002±0.025
11.308	0.727±0.095	0.762±0.076	0.748±0.074	0.819±0.055	0.713±0.075	0.782±0.048
19.520	0.015±0.039	0.055±0.038	0.035±0.027	−0.056±0.028	−0.092±0.061	−0.062±0.026
45.157	−2.73±0.41	−3.67±0.27	−3.37±0.30	−3.39±0.30	−3.27±0.44	−3.36±0.27
49.745	−0.669±0.642	0.644±0.487	0.164±0.388	−0.705±0.462	0.754±0.765	−0.315±0.396
63.494	4.52±0.07	4.46±0.05	4.48±0.277	4.80±0.06	4.66±0.07	4.74±0.11
72.372	−0.15±1.22	0.242±0.575	0.171±0.520	−0.150±0.765	0.34±1.26	−0.017±0.653
83.677	−0.177±0.277	0.041±0.165	−0.016±0.142	−0.091±0.125	−0.245±0.189	−0.138±0.105
89.216	–	−0.355±0.104	−0.355±0.106	–	−0.398±0.131	−0.398±0.131
93.081	0.227±0.264	0.154±0.149	0.171±0.130	0.157±0.141	−0.082±0.189	0.073±0.113
97.978	0.002±0.171	0.004±0.194	0.003±0.128	0.055±0.149	−0.224±0.193	−0.049±0.118
111.18	1.27±0.91	0.060±0.527	0.364±0.457	0.321±0.440	−0.270±0.708	0.156±0.374
124.94	0.672±0.420	0.231±0.321	0.394±0.256	0.222±0.341	0.033±0.543	0.169±0.289
133.18	0.15±1.12	0.333±0.553	0.298±0.496	0.049±0.535	−0.249±0.765	−0.049±0.438
152.40	−0.206±0.172	−0.161±0.160	−0.182±0.118	0.004±0.144	0.016±0.221	0.008±0.121
158.94	–	0.240±0.319	0.240±0.319	–	−0.394±0.354	−0.394±0.354
173.19	0.472±0.157	0.266±0.100	0.325±0.086	0.554±0.132	0.632±0.187	0.580±0.109
214.85	–	−1.41±0.86	−1.41±0.86	–	0.18±1.28	0.18±1.28
218.33	−0.314±0.863	−0.833±0.899	−0.563±0.623	0.202±0.900	0.34±1.09	0.256±0.694
242.71	−0.127±0.876	0.009±0.389	−0.014±0.356	0.786±0.559	−0.489±0.767	0.344±0.452
253.87	−0.362±0.362	−0.392±0.434	−0.374±0.279	0.452±0.319	−0.308±0.417	0.172±0.253
257.22	−2.32±0.79	−1.03±0.95	−1.79±0.61	−0.05±1.04	−1.10±0.82	−0.694±0.648
263.92	0.156±0.428	−0.060±0.295	0.010±0.243	−0.194±0.339	0.876±0.399	0.257±0.259
282.44	−1.19±0.61	0.115±0.303	−0.144±0.272	0.410±0.376	0.488±0.506	0.438±0.302

Table 4.18: ^{238}U PNC asymmetries averaging the Cd-absorber and B-absorber data sets and including the correction due to the spin flipper efficiency relative to the ^{139}La measurement. The prime indicates values not corrected for the spin flipper efficiency. The asterisk indicates effects with a statistical significance of greater than 2.5 σ.

E (eV)	$\bar{\mathcal{P}}'$ (%)	$\epsilon_{\rm sf}$	$\bar{\mathcal{P}}$ (%)	$\bar{\mathcal{P}}/\Delta\bar{\mathcal{P}}$
10.234	0.036±0.017	1.06	0.034±0.016	2.1
11.308	0.772±0.040	1.06	0.73±0.038	19.3*
19.520	−0.017±0.017	1.06	−0.016±0.018	−0.9
45.157	−3.37±0.20	1.07	−3.15±0.18	−17.1*
49.611	−0.071±0.277	1.07	−0.066±0.26	−0.3
63.494	4.70±0.10	1.07	4.41±0.10	44.9*
72.372	0.098±0.407	1.07	0.091±0.38	0.2
83.677	−0.095±0.084	1.06	−0.090±0.079	−1.1
89.216	−0.372±0.083	1.06	−0.351±0.078	−4.5*
93.081	0.115±0.085	1.06	0.108±0.080	1.4
97.978	−0.025±0.087	1.07	−0.024±0.081	−0.3
111.18	0.240±0.289	1.07	0.22±0.27	0.8
124.94	0.295±0.192	1.07	0.28±0.18	1.5
133.18	0.103±0.328	1.06	0.10±0.31	0.3
152.40	−0.089±0.084	1.05	−0.085±0.080	−1.1
158.94	−0.044±0.237	1.06	−0.04±0.22	−0.2
173.19	0.424±0.068	1.06	0.398±0.064	6.3*
214.85	−0.915±0.715	1.07	−0.85±0.67	−1.3
218.33	−0.197±0.464	1.07	−0.18±0.43	−0.4
242.71	0.123±0.280	1.06	0.12±0.26	0.4
253.87	−0.075±0.188	1.05	−0.07±0.18	−0.4
257.22	−1.28±0.44	1.05	−1.22±0.42	−2.9*
263.92	0.125±0.177	1.05	0.12±0.17	0.7
282.44	0.116±0.202	1.04	0.11±0.19	0.6

Table 4.19: A_i values for ^{238}U p-waves. The J values are from Corvi et al. [Cor94].

E (eV)	A_i 1/(meV)	J
10.234	$2.47E-02$	1.5
11.308	$4.69E-02$	0.5
19.520	$1.25E-01$	1.5
45.157	$3.57E-02$	0.5
49.611	$3.77E-02$	?
63.494	$4.11E-02$	0.5
72.372	$4.23E-02$	?
83.677	$1.56E-02$	0.5
89.216	$5.03E-03$	0.5
93.082	$2.43E-02$	1.5
97.978	$5.68E-02$	1.5
111.18	$3.31E-02$	?
124.94	$1.14E-02$	1.5
133.18	$1.20E-02$	?
152.40	$4.37E-03$	1.5
158.94	$9.12E-03$	1.5
173.19	$7.96E-03$	0.5
214.85	$1.09E-02$	?
218.33	$9.85E-03$	?
242.71	$4.63E-03$	0.5
253.88	$3.10E-03$	1.5
257.92	$6.58E-03$	?
263.92	$2.51E-03$	1.5
282.44	$4.74E-03$	1.5

description in Section 2.4.1 to be $p' = 0.39$ and $q' = 0.61$. The resulting root-mean-squared matrix element is

$$\mathcal{M} = 0.67^{+0.24}_{-0.16} \quad \text{(meV)} \tag{4.37}$$

for case (a) and

$$\mathcal{M} = 0.67^{+0.25}_{-0.16} \quad \text{(meV)} \tag{4.38}$$

for case (b). The above values for the RMS matrix element are somewhat higher than previous analyses of the earlier measurement, $\mathcal{M} = 0.56^{+0.41}_{-0.20}$ meV [Zhu92] and $\mathcal{M} = 0.58^{+0.33}_{-0.20}$ meV [Pos96]. Both analyses used the data from [Zhu92], where there was only one strong effect at the 63.494 eV resonance. In the former case the spins were not known, whereas in the latter case they were. By including an estimate of the bias in the analysis due to the small sample size, Postma et al. found a value of $\mathcal{M} = 0.62^{+0.33}_{-0.20}$ meV [Pos96].

The case where seven of the resonances have known spins and seven have unknown spins, leads to a weak spreading width of

$$\Gamma_{\mathrm{w}} = \left(1.35^{+0.97}_{-0.64}\right) \times 10^{-7} \quad \text{(eV)}. \tag{4.39}$$

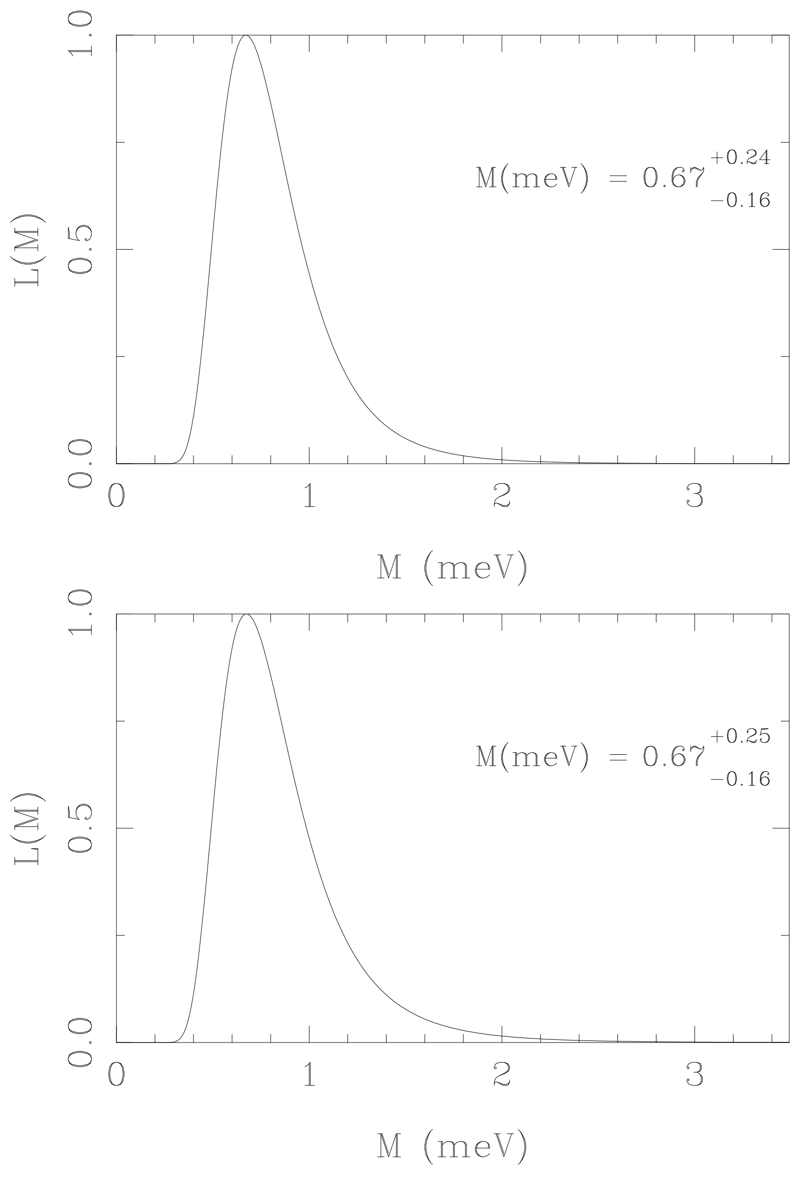

Figure 4.22: Likelihood function for ^{238}U for 7 $p\frac{1}{2}$ resonances and 7 resonances with unknown spin (top) and where all 24 p-waves are considered to have unknown spin (bottom).

Chapter 5

Summary

This dissertation has described the use of enhancements of parity nonconserving effects found in the neutron resonance region of heavy nuclei as a technique for measuring the strength of the weak interaction in the nuclear medium. The $\sim 10\%$ PNC effect seen in ^{139}La by the Dubna group in 1982 increased interest in this field and prompted the creation of the TRIPLE collaboration. By studying targets in two mass regions ($A \sim 100$ and $A \sim 230$) the TRIPLE collaboration has begun to map the strength of the weak component of the nucleon-nucleus interaction, quantified by the weak spreading width, Γ_{W}, as a function of nuclear mass. Three isotopes using two experimental techniques were studied for this dissertation, ^{106}Pd and ^{108}Pd using neutron capture and ^{238}U using neutron transmission.

Because of the small amount of material available for the ^{106}Pd and ^{108}Pd targets, long run times were required to achieve enough statistics to see parity-nonconserving effects. For the ^{106}Pd measurement 392 hours of data were analyzed, and one effect with a negative sign was seen. The effect was seen at the 593.4 eV resonance which was shown by a Bayesian analysis to be an s-wave. The various possibilities for how there could be an effect at this energy were discussed in Section 4.1.10. The most likely possibility is that there is an unresolved p-wave that shows the effect. If this is the case, then since the resonance parameters of the p-wave are unknown, a root-mean-squared matrix element can not be found. If the

593.4 eV resonance is actually a p-wave, the analysis shows that $\mathcal{M} = 11.0^{+7.7}_{-4.5}$ meV and $\Gamma_{\mathrm{W}} = (48^{+67}_{-39}) \times 10^{-7}$ eV. This situation suggests two experiments to resolve the issue: a neutron time-of-flight measurement at a facility with better energy resolution (ORELA or GELINA) and a direct measurement of the orbital angular momentum of the resonance. Experimenters at GELINA have developed methods for determining the spin and parity of neutron resonances [Cor94, Zan97].

For the ^{108}Pd measurement 175 hours of data were analyzed, and no effects were seen. The likelihood analysis of the ^{108}Pd data led to $\mathcal{M} < 4.2$ meV and an upper limit on the spreading width given by $\Gamma_{\mathrm{W}} < 7.0 \times 10^{-7}$ eV. This upper limit is in good agreement with other measurements in odd mass targets in this region. Preliminary measurements in natural palladium show at least one effect in ^{108}Pd [Smi97a]. These measurements will likely lead to a non-zero matrix element which when coupled with the limits placed by the current measurement will place tighter constraints on the weak spreading width in the mass-100 region.

The large ^{238}U target produced six effects with a statistical significance greater than 2.5σ in the analysis of 79 hours of data. The likelihood analysis led to $\mathcal{M} = 0.67^{+0.24}_{-0.16}$ meV and $\Gamma_{\mathrm{W}} = \left(1.35^{+0.97}_{-0.64}\right) \times 10^{-7}$ eV.

Figure 5.1 shows the measurements of the weak spreading width in both the mass-100 and mass-230 regions [Low96, See97, Ste96, Smi97b]. The darkened points indicate the measurements contributed by this dissertation. The open point is from the assumption that the 593.4 eV resonance in ^{106}Pd is a p-wave.

Finally, the fact the ^{238}U data produced three positive and three negative effects and the ^{106}Pd data produced one negative effect, demonstrates that the sign effect seen in ^{232}Th, where all of the effects were positive, is not universal.

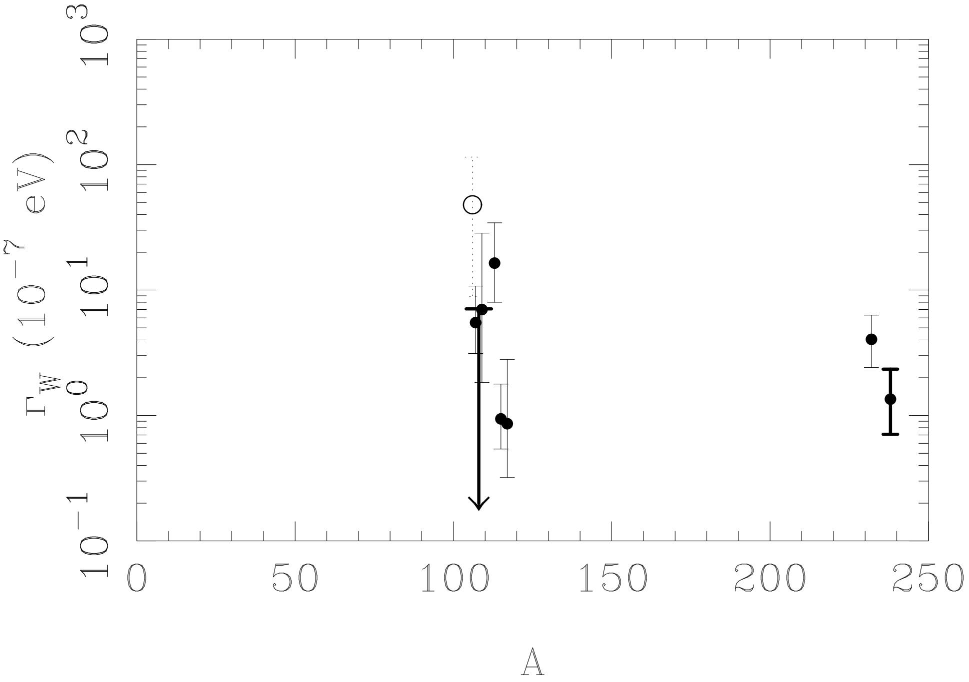

Figure 5.1: Weak spreading width versus mass number including the current work (darkened). The open point corresponds to the assumption that the 593.4 eV ^{106}Pd resonance is a p-wave.

Appendix A

FITXS

A.1 Introduction

The FITXS code was developed to fit the XSYS time-of-flight spectra measured by the TRIPLE collaboration [Mat97]. Many of the fitting parameters are specific to the Manuel Lujan Neutron Scattering Center (MLNSC) facility and the TRIPLE detection system and are discussed below. The FITXS code allows the user to choose a particular *ToF* region and a set of fitting parameters. It then uses a modified Marquardt χ^2 minimization routine to obtain the best values of the fitting parameters [Pre92]. The fitting function depends on the target areal density, n; the multilevel neutron cross sections, σ and σ_γ, discussed in Chapter 2; and broadening from three sources: the time structure of the neutron beam; the Doppler broadening due to the relative motion between the neutrons and the target nuclei; and the time response of the detection system. The broadening due to the beam and detection system can be combined analytically, as is discussed in Sections A.2 and A.3, to form response functions, $B_c(t)$ for capture and $B_t(t)$ for transmission. The latter includes the effect of the ^{10}B-neutron detector. For capture the fitting function, $\mathcal{F}$, can be written as

$$\mathcal{F}_c(t) = B_c(t) \otimes \left[N_\circ(t) \frac{\sigma_{\gamma\mathrm{D}}(t)}{\sigma_\mathrm{D}(t)} \left(1 - e^{-n\sigma_\mathrm{D}(t)}\right)\right] + \mathcal{B} \tag{A.1}$$

and for transmission

$$\mathcal{F}_t(t) = B_t(t) \otimes \left[N_\circ(t)e^{-n\sigma_{\rm D}(t)}\right] + \mathcal{B}, \tag{A.2}$$

where

$$\sigma_{\gamma{\rm D}}(t) = \left[D(v) \otimes \sigma_\gamma(v)\right]_{v\to t} \quad \text{and} \quad \sigma_{\rm D}(t) = \left[D(v) \otimes \sigma(v)\right]_{v\to t}. \tag{A.3}$$

$N_\circ$ is the neutron flux, $D(v)$ is the Doppler response function, $\mathcal{B}$ is the background function and the $v \to t$ symbol indicates that after the convolution in velocity space, the function is converted to a function of time.

It is important to note that the convolutions in Equations A.1 and A.2 do not commute. Therefore, to extract correct resonance parameters and PNC asymmetries, it is necessary to perform both convolutions separately and in the proper order. That is, the use of a generic fitting function that does not properly separate the effects of Doppler broadening from those of the beam and detection responses, has the possibility of extracting incorrect asymmetries for the case of strong resonances (large $n\sigma$) or resonances, where the intrinsic resonance width is small compared to the response width.

Since it is not possible to analytically perform these convolutions, FITXS determines $\mathcal{F}$ by calculating the two convolutions numerically. For a given *ToF* region FITXS first converts to velocity space and calculates the neutron cross sections on a velocity grid with a grid spacing less than $\frac{1}{10}$ the smallest of the following three widths: resonance, Doppler, and beam/detection response. FITXS uses a Fast Fourier Transform (FFT) to convolute the cross sections with the Doppler response function,

$$D(v) = \frac{M}{2\pi k_{\rm B} T_{\rm eff}} e^{\frac{-Mv^2}{2k_B T_{\rm eff}}}, \tag{A.4}$$

where M is the target mass, $k_{\rm B}$ is the Boltzmann constant and $T_{\rm eff}$ is the effective temperature [Fod71]. Inserting the result of these convolutions into the appropriate expression from equations A.1 and A.2, FITXS then converts back to *ToF* using a grid spacing less than $\frac{1}{10}$ the smaller between the Doppler width and the beam/detection response width.

Finally, the code performs the beam/detection response convolution to determine $\mathcal{F}$. At this point FITXS compares the $\mathcal{F}$ array with the data spectrum in the given channel region in order to determine χ^2. FITXS then chooses a new set of parameters and recalculates $\mathcal{F}$, repeating this process until χ^2 is minimized.

As part of the development of FITXS it was necessary to determine the characteristic response functions so that their parameters could be held constant when extracting neutron resonance parameters. The high statistical precision of these experiments combined with the use of FITXS allowed for the precise determination of the time dependence of the MLNSC beam for flight-path 2 and the ^{10}B-neutron detector moderation time.

A.2 MLNSC Neutron Beam Resolution Function

The initial investigations into the various resolution functions were done by Yi-Fen Yen et al. [Yen96b]. In this paper the authors describe Monte-Carlo calculations that were used to model the MLNSC beam time response for flight-path 2. They were able to fit the Monte-Carlo generated data with the following response function

$$\begin{aligned} M(t) &= \frac{1}{\sqrt{2\pi}} \exp\left[-\frac{(t-t_\circ)^2}{2\eta^2}\right] \otimes \frac{1}{\tau} \exp\left[\frac{-(t-t_\circ)}{\tau}\right] u(t-t_\circ) \\ &= \frac{1}{2\tau} \exp\left[\frac{-(t-t_\circ)}{\tau} + \frac{\eta^2}{2\tau^2}\right] (1 - \mathrm{erf}(Z)), \end{aligned} \tag{A.5}$$

where $u(t)$ is a unit step function and $Z = [\eta/\tau - (t-t_\circ)/\eta]/\sqrt{2}$. These calculations were performed at several energies in the range 1–1000 eV, and the energy dependence of the three parameters were found to be

$$\begin{aligned} t_\circ &= 2.79 \times E^{-0.48}\ \mu\mathrm{s} \\ \eta &= 0.65 \times E^{-0.51}\ \mu\mathrm{s} \\ \tau &= 0.99 \times E^{-0.37}\ \mu\mathrm{s} \end{aligned} \tag{A.6}$$

where the neutron energy is in units of eV.

There are two more sources of broadening that are common to both the capture and transmission systems, the proton beam shape from the proton storage ring and the electronic shaping before the transient digitizer. Both of these functions are approximated as Gaussians, and thus their widths can be added in quadrature with η in equation A.5, such that the response function for the capture system is given by

$$B_c(t) = \frac{1}{2\tau} \exp\left[\frac{-(t-t_\circ)}{\tau} + \frac{\kappa^2}{2\tau^2}\right](1 - erf(Z)), \tag{A.7}$$

where

$$\kappa = \sqrt{\eta^2 + \sigma_{\mathrm{PSR}}^2 + \sigma_{elec}^2}$$

and

$$\begin{aligned} \sigma_{\mathrm{PSR}} &= 51.0 \text{ ns} \\ \sigma_{elec} &= 42.5 \text{ ns.} \end{aligned}$$

The above electronic width is true when the sampling bin width of the transient recorder is 100 ns.

By fitting neutron capture resonances at energies above ~ 400 eV, it was possible to measure the beam resolution function, since for these resonances a large fraction of the total width is from the beam response (See Figure A.1.). The fits at these energies were not especially sensitive to the Gaussian width, η, but were quite sensitive to the exponential tail. When equation A.7 was used in FITXS to fit the ^{106}Pd and ^{108}Pd capture data it was found to be inadequate due to the presence of a long low energy (high *ToF*) tail. Several attempts were made to obtain better fits by:

- Altering the parameters in Equation A.7.
- Using the function:

$$B_c(t) = \frac{(t-t_\circ)^2}{\tau} e^{-\frac{t}{\tau}}. \tag{A.8}$$

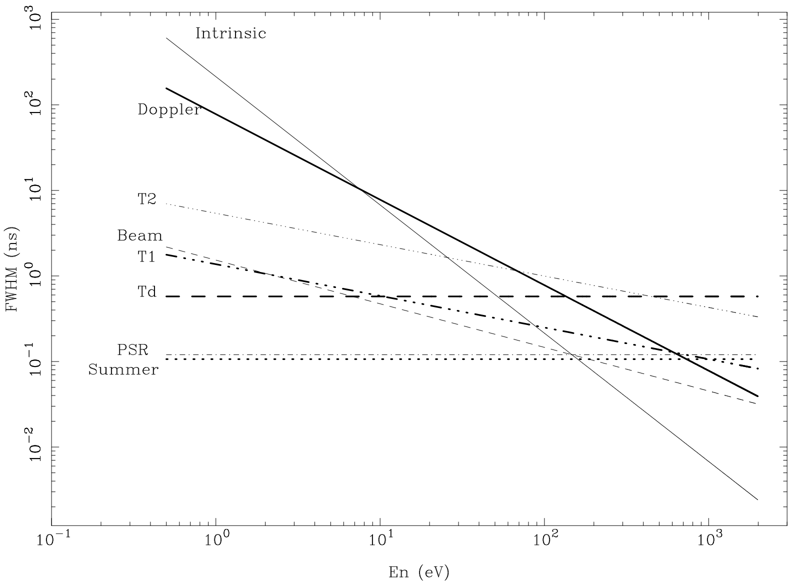

Figure A.1: Comparison of instrumental response and resonance widths plotted as full widths at half maximum converted to time for Γ (Intrinsic), Doppler broadening (Doppler), η (Beam), σ_{PSR} (PSR), σ_{elec} (Summer), τ (T1), τ_2 (T2) and τ_d (Td). These calculations were done for ^{108}Pd at an effective temperature of 300 K with $\Gamma = 100$ meV.

- Using the function:

$$B_c(t) = \begin{cases} \frac{1}{\sqrt{2\pi\sigma_G^2}} e^{-\frac{(t-t_\circ)^2}{2\sigma_G^2}} & t < t_\circ \\ \\ \frac{\sigma_G^2}{\sigma_G^2+(t-t_\circ)^2} & t \geq t_\circ . \end{cases} \quad \text{(A.9)}$$

- Using the function:

$$\begin{aligned} B_c(t) &= \frac{1}{2\tau} \exp\left[\frac{-(t-t_\circ)}{\tau} + \frac{\kappa^2}{2\tau^2}\right](1-\mathrm{erf}(Z)) \\ &+ \frac{\epsilon}{2\tau_2} \exp\left[\frac{-(t-t_\circ)}{\tau_2} + \frac{\kappa^2}{2\tau_2^2}\right](1-\mathrm{erf}(Z_2)), \end{aligned} \quad \text{(A.10)}$$

  where $Z_2 = [\kappa/\tau_2 - (t-t_\circ)/\kappa]/\sqrt{2}$.

The first two did a rather poor job of fitting the data. Although the latter two fit the data well, since the last was a straight forward extension of the work of Yen et al., it was adopted as the response function.

To determine the best values for ϵ and τ_2 in Equation A.10, thirteen resonances from ^{106}Pd and ^{108}Pd in the energy region 400–1780 eV were fit. First these resonances were fit letting both ϵ and τ_2 vary. Since there was greater error in τ_2 than in ϵ, these fits were used to determine ϵ which varied little from fit to fit from the average value of $(20.0 \pm 0.7)\%$. This value of ϵ was then held constant, and τ_2 was determined from the same resonances. The top plot in Figure A.2 shows a linear fit of the natural log of τ_2 versus the natural log of neutron energy. From the fit the energy dependence of τ_2 is given by

$$\tau_2 = 3.90 \times E^{-0.38}\ \mu\mathrm{s} \quad \text{(A.11)}$$

with a relative error given by

$$\frac{\sigma_{\tau_2}}{\tau_2} = \sqrt{4.01 \times 10^{-3} + 2.55 \times 10^{-2}\,[\ln(E) - 6.96]}\,. \quad \text{(A.12)}$$

The bottom plot of Figure A.2 shows a comparison of fitting with and without the second tail.

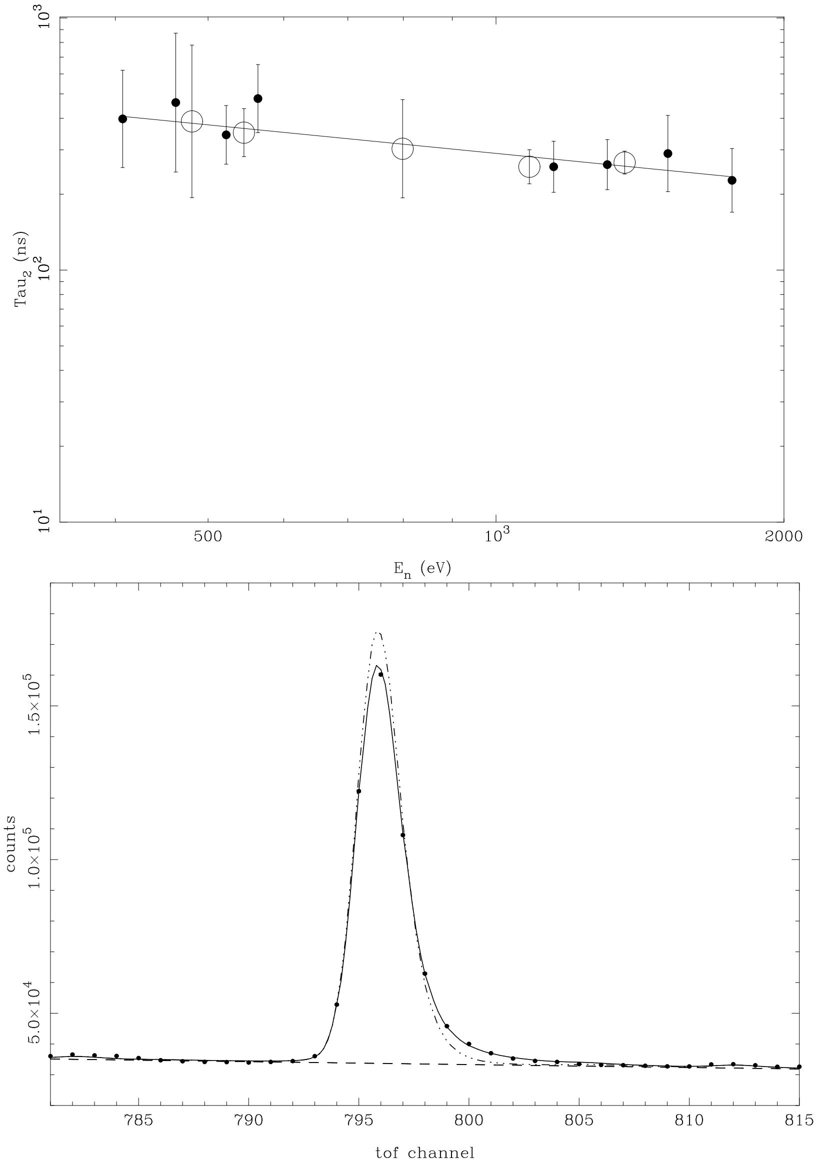

Figure A.2: Determination of τ_2. The top plot shows the energy dependence of τ_2 from fits of 13 resonances from ^{106}Pd (dots) and ^{108}Pd (circles) between the energies of 400 and 1780 eV. The bottom plot shows a fit of the 1082.3 eV p-wave in the capture spectrum of ^{108}Pd with (solid) and without (dash-dot-dot-dot) the second exponential tail.

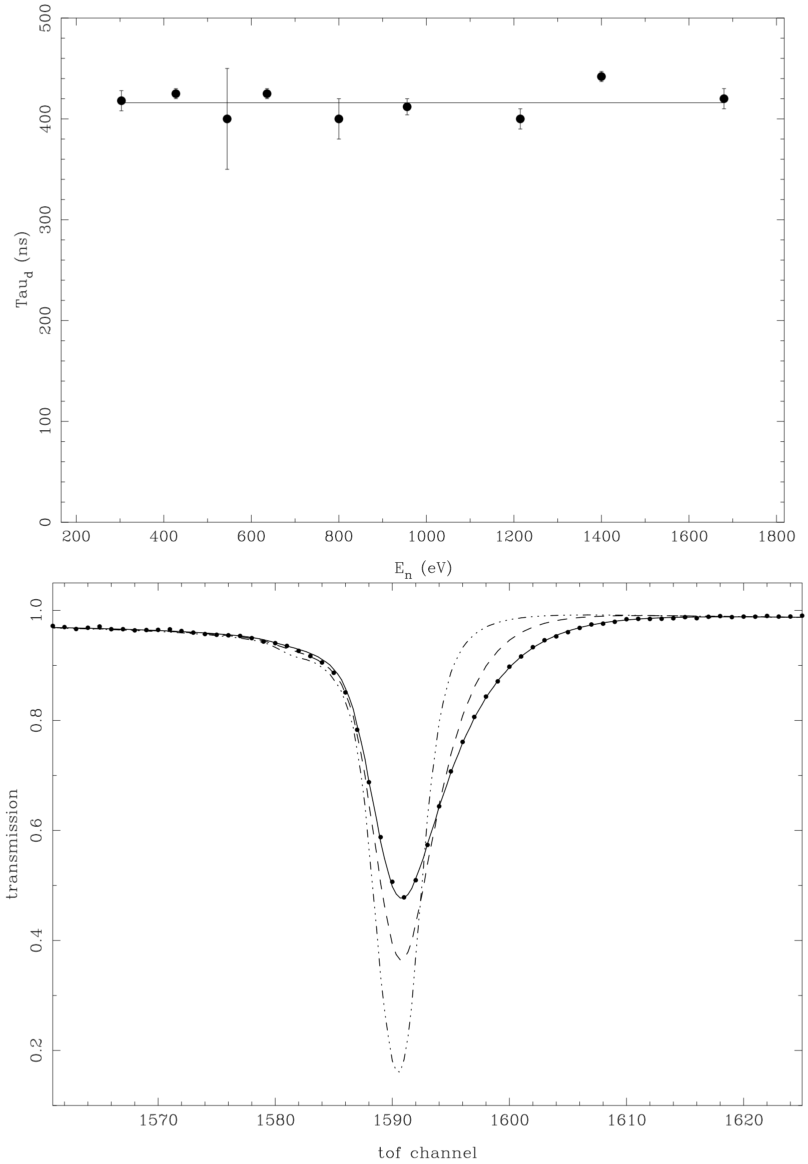

Figure A.3: Determination of τ_d. The top plot shows the τ_d values found from fitting nine ^{108}Pd resonances. The solid line shows the average value of 416 ns. The bottom plot shows a fit of the 635.3 eV s-wave in the target-in divided by target-out transmission spectrum of ^{108}Pd with $\tau_d = 10$ ns (dash-dot-dot-dot), $\tau_d = 250$ ns (dash) and $\tau_d = 416$ ns (solid).

A.3 ^{10}B-Neutron Detector Moderation Time

The spectra taken with the transmission detector show an additional broadening from the ^{10}B neutron detector. The moderation process in the ^{10}B detector is given by an exponential with characteristic decay time, τ_d. This exponential can be convoluted with $B_c(t)$ from Equation A.10 to form $B_t(t)$,

$$\begin{aligned} B_t(t) &= \frac{1}{2(\tau-\tau_d)}\left[e^{-t/\tau_d+\kappa^2/2\tau_d^2}\left(1-\operatorname{erf}(Z_d)\right)-e^{-t/\tau+\kappa^2/2\tau^2}\left(1-\operatorname{erf}(Z)\right)\right] \\ &+\frac{\epsilon}{2(\tau_2-\tau_d)}\left[e^{-t/\tau_d+\kappa^2/2\tau_d^2}\left(1-\operatorname{erf}(Z_d)\right)-e^{-t/\tau_2+\kappa^2/2\tau_2^2}\left(1-\operatorname{erf}(Z_2)\right)\right] \end{aligned} \tag{A.13}$$

where $Z=(\kappa/\tau-t/\kappa)/\sqrt{2}$, $Z_d=(\kappa/\tau_d-t/\kappa)/\sqrt{2}$ and $Z_2=(\kappa/\tau_2-t/\kappa)/\sqrt{2}$.

Averaging the best-fit values of τ_d from nine resonances in ^{108}Pd from energies 300–1220 eV gives $\tau_d=(416\pm5)$ ns, as seen in the plot at the top of Figure A.3. The bottom plot in Figure A.3 shows a comparison of fits of ^{108}Pd transmission data using several values of τ_d.

A.4 FITXS Fitting Functions and Parameters

Inserting an energy dependent flux and a polynomial in time for the background into Equations A.1 and A.2, the fitting functions can be written as

$$\mathcal{F}_c(t)=\frac{\alpha}{E^\beta}\left[B_c(t)\otimes\left[\frac{\sigma_{\gamma\mathrm{D}}(t)}{\sigma_\mathrm{D}(t)}\left(1-e^{-n\sigma_\mathrm{D}(t)}\right)\right]\right]+\sum_{n=0}^{N_{bg}-1}a_n t^n \tag{A.14}$$

and

$$\mathcal{F}_t(t)=\frac{\alpha}{E^\beta}\left[B_t(t)\otimes\left[N_\circ e^{-n\sigma_\mathrm{D}(t)}\right]\right]+\sum_{n=0}^{N_{bg}-1}\frac{a_n}{t^n}, \tag{A.15}$$

where $B_c(t)$ is from Equation A.10; $B_t(t)$ is from Equation A.13; $\sigma_{\gamma\mathrm{D}}(t)$ is from Equations A.3, 2.3 and 2.6; and $\sigma_\mathrm{D}(t)$ is from Equations A.3, 2.8 and 2.9. The s-wave and p-wave cross sections calculated using the Reich-Moore formalism as discussed in Chapter 2, due to all resonances of all allowed total angular momentum of all isotopes present in the beam, are summed to form the total and capture cross sections. The PNC asymmetry is included only with the p-waves of the target isotope as discussed in Chapter 2.

The parameters input to FITXS are of five basic types: target and apparatus parameters; beam and detection response parameters; background parameters; abundance and radius parameters; and resonance parameters. The parameters are listed in Table A.1. Table A.1 refers to different resonance "kinds". Since only resonances of the same isotope and same total angular momentum can mix in the equations of Section 2.1, each needs to be distinguished in FITXS. The resonance kind parameter makes this distinction.

Table A.1: Input parameters for FITXS.

Type	Number	Description
Target and Apparatus	1	T_{eff} (K), Effective temperature
	2	n (atoms/cm^2), Areal density
	3	Beamline length (m)
	4	Dwell time (ns)
	5	$t_\circ$-offset ($C_\circ \times$Dwell time) (ns)
	6	α $\left(\text{neutrons/monitor sum} \times 10^8\right)$, Beam intensity
	7	β, Energy exponent for the beam intensity energy dependence
Response	1	$\eta = 0.65 \times E^{-0.51}$ (μs), MLNSC moderator Gaussian width
	2	$\tau = 0.99 \times E^{-0.37}$ (μs), MLNSC moderator tail
	3	$\epsilon = 20.0\%$, Amount of second MLNSC Gaussian
	4	$\tau_2 = 3.90 \times E^{-0.38}$ (μs), Second MLNSC tail
	5	$\sigma_{elec} = 42.5,\ 85.0$ and 425 (ns), Electronic width for $100,\ 200$ and 1000 (ns) dwell
	6	$\sigma_{\text{PSR}} = 51.0$ (ns), Proton Storage Ring width
	7	$\tau_d = 416$ (ns), ^{10}B-detector tail
Background	1	N_{bg}, Number of terms in background polynomial
	2	a_0, 0$^{\text{th}}$ Order coefficient

continued on the next page

continued from the previous page

Type	Number	Description
	3	a_1, 1$^{\text{st}}$ Order coefficient
	4	a_2, 2$^{\text{nd}}$ Order coefficient
	5	a_3, 3$^{\text{rd}}$ Order coefficient
Abundances	1	N, Number of different resonance kinds including target and contaminants
	2→N+1	Abundance for each kind
	N+2→2N+2	R (fm), Effective potential scattering radius for each kind
Resonance	1	Energy (eV)
	2	L, Orbital angular momentum
	3	$g\Gamma_n$ (eV), Neutron width
	4	Γ_γ (eV), Capture γ-ray width
	5	J, Total angular momentum
	6	I, Target spin
	7	Resonance kind (see text)

Appendix B

Spin-Transport Calculations

As discussed in Section 3.4, the spin transport system consists of 50 m of wire-wrapped beam pipe. This forms a solenoidal field that preserves the neutron spin direction as the neutrons travel the length of the beam line. However, at gaps in the coils and at places where the coils change diameter, transverse components are introduced to the field which can depolarize the neutron beam. Picturing the spins classically, one can imagine a longitudinal spin reaching a coil gap, where the torque from the fringing magnetic field rotates the spin to some angle relative to the beam axis. With the spin now off axis, the neutron will precess about the longitudinal field until the next coil gap at which time it will be rotated again by an amount that depends in part on how much it has precessed since the last gap. This happens all the way down the beam line, and with 25 different coils in the TRIPLE spin-transport system, the depolarization depends on the neutron energy in a very complicated way. The depolarization has been calculated numerically for the TRIPLE beam line for the energies of interest and is described below.

B.1 Field Calculation

The radial and axial magnetic fields are found from the azimuthal vector potential derived by Jackson [Jac75] for a single current loop (in MKS units),

$$A_\phi(r,z) = \frac{\mu_\circ I a}{\pi\sqrt{(a+r)^2+z^2}}\left[\frac{\left(2-k^2\right)K\left(k^2\right)-2E\left(k^2\right)}{k^2}\right], \tag{B.1}$$

where $\mu_\circ$ is the permeability of free space, I is the loop current, a is the loop radius, r is the radial distance off axis, z is the distance along the loop axis, $K(k^2)$ and $E(k^2)$ are the complete elliptic integrals of the first and second kind, respectively and $k^2 = 4ar/\left[(a+r)^2+z^2\right]$. The elliptic integrals in Equation B.1 can be expanded to find [Wil95]

$$B_r(r,z) = \frac{\mu_\circ I}{2}\frac{az}{\left[(a+r)^2+z^2\right]^{3/2}}\sum_{n=0}^{\infty}\frac{n(2n+1)}{n+1}\left[\frac{(2n-1)!!}{2^n n!}\right]^2 k^{2n} \tag{B.2}$$

and

$$B_z(r,z) = \frac{\mu_\circ I}{2}\frac{az}{\left[(a+r)^2+z^2\right]^{3/2}}\sum_{n=0}^{\infty}(2n+1)\left(1-\frac{n}{n+1}\frac{r}{a}\right)\left[\frac{(2n-1)!!}{2^n n!}\right]^2 k^{2n}. \tag{B.3}$$

The solenoidal fields are formed by integrating the single-loop fields over the length of the solenoid. Integrating the $n=0$ and $n=1$ terms of Equations B.2 and B.3 from $z_\circ$ to $z_\circ + L$ for a solenoid of length L, radius a and N turns per meter, the fields reduce to

$$B_r(r,z) \cong \frac{\mu_\circ N I a^2 r}{4}\left[\frac{1}{\left[(a+r)^2+(z_\circ+L-z)^2\right]^{3/2}} - \frac{1}{\left[(a+r)^2+(z_\circ-z)^2\right]^{3/2}}\right] \tag{B.4}$$

and

$$B_z(r,z) \cong$$

$$\frac{\mu_\circ NI}{2}\frac{a^2}{(a+r)^2}\begin{pmatrix} \left[1+\frac{ar}{(a+r)^2}\left(1-\frac{r}{2a}\right)\right]\frac{z_\circ+L-z}{\sqrt{(a+r)^2+(z_\circ+L-z)^2}} \\ +ar\left(1-\frac{r}{2a}\right)\frac{z_\circ+L-z}{\left[(a+r)^2+(z_\circ+L-z)^2\right]^{3/2}} \\ +\left[1+\frac{ar}{(a+r)^2}\left(1-\frac{r}{2a}\right)\right]\frac{z-z_\circ}{\sqrt{(a+r)^2+(z-z_\circ)^2}} \\ +ar\left(1-\frac{r}{2a}\right)\frac{z-z_\circ}{\left[(a+r)^2+(z-z_\circ)^2\right]^{3/2}} \end{pmatrix}. \tag{B.5}$$

At the interior of the solenoid, however, the axial field given above is not a good approximation when the distance off axis is a sizable fraction of the solenoid diameter. Only with many more terms than are included in Equation B.5, is the uniform field reproduced in the interior of the solenoid. The above approximation is, therefore, inadequate.

A different approximation [Bow96b] starts with the axial field at $r=0$ and writes

$$B_z(r,z) \cong B_z(0,z) = \frac{\mu_\circ NI}{2}\left[\frac{z_\circ+L-z}{\sqrt{a^2+(z_\circ+L-z)^2}}+\frac{z-z_\circ}{\sqrt{a^2+(z_\circ-z)^2}}\right], \tag{B.6}$$

which gives a very good approximation of the field for all radii in the uniform-field region of the solenoid (solenoid interior). Near the ends of the solenoid, however, the above expression is correct only for $r=0$ but is a reasonable approximation for small distances off axis and will be used in the following calculations.

Since the magnetic field has no divergence, the radial field is related to the axial field by

$$\frac{1}{r}\frac{\partial rB_r}{\partial r} = -\frac{\partial B_z}{\partial z}. \tag{B.7}$$

Solving for B_r gives

$$B_r(r,z) \cong \frac{\mu_\circ N I a^2 r}{4}\left[\frac{1}{\left[a^2+(z_\circ+L-z)^2\right]^{3/2}} - \frac{1}{\left[a^2+(z_\circ-z)^2\right]^{3/2}}\right], \tag{B.8}$$

which agrees with the approximation made earlier in Equation B.4. For the coils shown

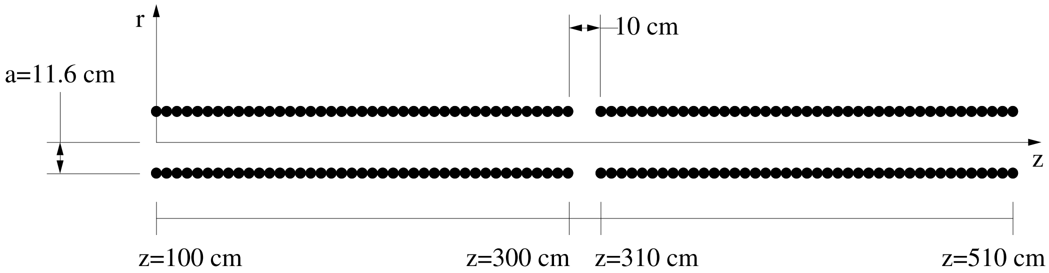

Figure B.1: Diagram of two 2 m long solenoids with a 10 cm gap between them. The radius is 11.6 cm for each solenoid.

in Figure B.1, a comparison of the exact and approximate fields from Equations B.2, B.3, B.6 and B.8 is shown in Figure B.2. The exact fields are calculated numerically by taking successively higher order terms until the next term in the sum is less than 10^{-8}.

As is shown in Figure B.2 the field approximations of Equations B.6 and B.8 are quite good inside the solenoid. In the gap, however, they differ from the exact field more strongly the farther off axis, but provide a good approximation for distances off axis less than one half the beam radius.

B.2 Depolarization Calculation

The following procedure for calculating the spin depolarization was developed by Bowman [Bow96b] and further developed by Wilburn [Wil93]. Schrödinger's equation for a neutron in a magnetic field is

$$i\hbar\frac{\partial}{\partial t}\psi = -\vec{\mu}\cdot\vec{B}\psi = -\frac{g_s\mu_{\mathrm{N}}}{2}\vec{\sigma}\cdot\vec{B}\psi, \tag{B.9}$$

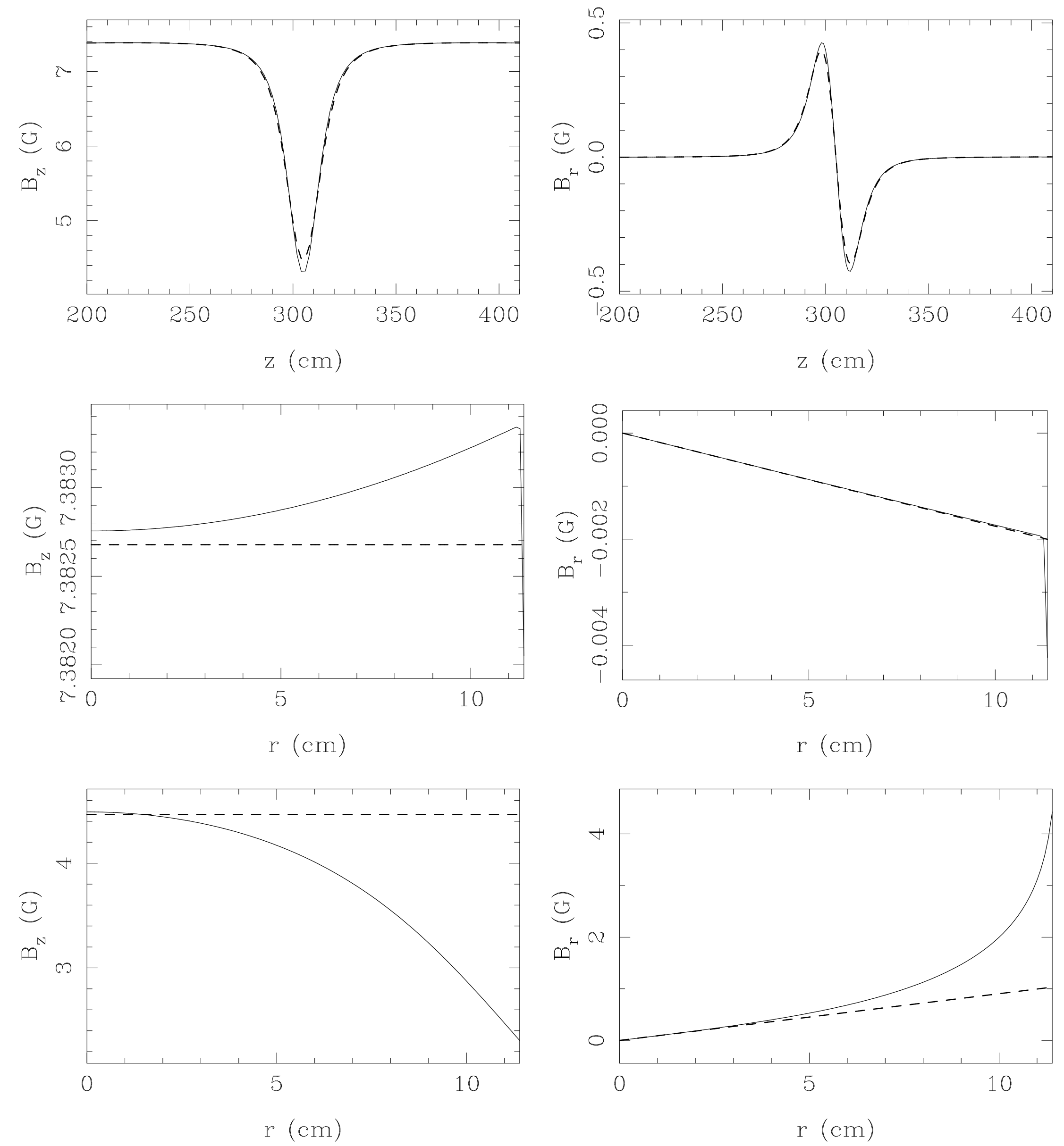

Figure B.2: Comparison of exact (solid) and approximate (dotted) calculations for the axial (left) and radial (right) fields for two coils with $a = 11.6$ cm and a gap between them of 10 cm (see Figure B.1). The top two plots are plotted versus axial distance with $r = 4$ cm. The middle two plots are plotted versus radial distance with $z = 200$ cm. The bottom two plots are plotted versus radial distance with $z = 305$ cm for the axial field and 300 cm for the radial field.

where $g_s = -3.826$, $\mu_{\rm N}$ is the nuclear magneton, ψ is the two component spinor wave function and $\vec{\sigma}$ is composed of the Pauli spin matrices,

$$\sigma_x = \begin{pmatrix} 0 & 1 \\ 1 & 0 \end{pmatrix}, \quad \sigma_y = \begin{pmatrix} 0 & -i \\ i & 0 \end{pmatrix}, \quad \text{and} \quad \sigma_z = \begin{pmatrix} 1 & 0 \\ 0 & -1 \end{pmatrix}. \tag{B.10}$$

If the distance the neutron travels in time δt is small enough, the resulting rotation can be considered infinitesimal, and the Schrödinger equation can be integrated to yield,

$$\psi(t+\delta t) = e^{i(g_s\mu_{\rm N}\delta t/2\hbar)\vec{\sigma}\cdot\vec{B}}\psi(t). \tag{B.11}$$

Since $\left(\vec{\sigma}\cdot\vec{B}\right)^2 = B^2$, the above equation can be expanded and simplified,

$$\psi(t+\delta t) = \left[\cos\left(\frac{g_s\mu_{\rm N}}{2\hbar}B\delta t\right) + i\vec{\sigma}\cdot\hat{n}\sin\left(\frac{g_s\mu_{\rm N}}{2\hbar}B\delta t\right)\right]\psi(t), \tag{B.12}$$

where $\vec{B} = B\hat{n}$. For non-relativistic neutrons with constant velocity,

$$\delta t = \delta z\sqrt{\frac{m_n}{2E}}, \tag{B.13}$$

where m_n is the mass of the neutron, E is the neutron energy and δz is the infinitesimal distance along the beam direction. From Equation B.12, the infinitesimal rotation operator can be written as

$$R(\Omega) = \cos(\Omega) + i\vec{\sigma}\cdot\hat{n}\sin(\Omega), \tag{B.14}$$

where

$$\Omega = \frac{g_s\mu_{\rm N}}{2\hbar}B\delta z\sqrt{\frac{m_n}{2E}} = \frac{\omega_{\rm L}}{2}\delta t, \tag{B.15}$$

and $\omega_{\rm L}$ is the Larmor precession frequency. The finite rotation of the neutron spin as it travels the length of the beam line is found by successive applications of the infinitesimal rotation operator. The final spinor, ψ', is related to the initial spinor, ψ, for n infinitesimal rotations by

$$\psi' = R\left(\Omega_n\right)R\left(\Omega_{n-1}\right)\cdots R\left(\Omega_1\right)\psi. \tag{B.16}$$

The depolarization, $\mathcal{D}$, is defined by

$$\mathcal{D} \equiv 1 - \frac{\langle\psi'|\sigma_z|\psi'\rangle}{\langle\psi|\sigma_z|\psi\rangle}. \tag{B.17}$$

A Monte-Carlo code calculates the rotation due to the spin transport field and the Earth's field for random trajectories down the beam line. In small steps along each trajectory the program calculates the infinitesimal spin rotation due to the ambient field. If the rotation is not equivalent to the rotation due to two half steps, then the program takes a smaller step and recalculates. This method of successive infinitesimal rotations determines the spin rotation matrix for the entire beam line for each trajectory. The depolarization values from all trajectories are then averaged.

Figure B.3 shows the depolarization for a single neutron as a function of axial distance for four different energies for the approximate fields of Figure B.2. Low energy neutrons adiabatically follow the rotating field and emerge from the gap with no depolarization. High energy neutrons pass through the gap so quickly that there is little time for the field in the gap to rotate the neutrons. Figure B.4 shows the energy dependence of the depolarization, where each point is the average of 100 neutrons with random trajectories from $z = 200$ cm to $z = 410$ cm within a beam radius of $R = 4$ cm for the approximate fields of Figure B.2. The left graph in Figure B.4 shows that the peak in the depolarization occurs at around 0.1 eV. The right graph shows what happens when a small constant field (0.3 G) perpendicular to the solenoid axis is added to the field to mimic the Earth's magnetic field. The periodicity of the peaks is a constant with respect to the time it takes the neutron to travel the 210 cm distance of this calculation. The separation between the peaks corresponds to the Larmor precession frequency.

The effect of having two 10 cm gaps is shown in Figure B.5. The graphs show that the spacing between the gaps affects the resulting depolarization. The peaks in the depolarization-versus-energy graphs are evenly spaced with respect to the time it takes the neutron to travel between the gaps, and the spacing again corresponds to the Larmor precession frequency. So, not only does each gap have a characteristic energy dependence,

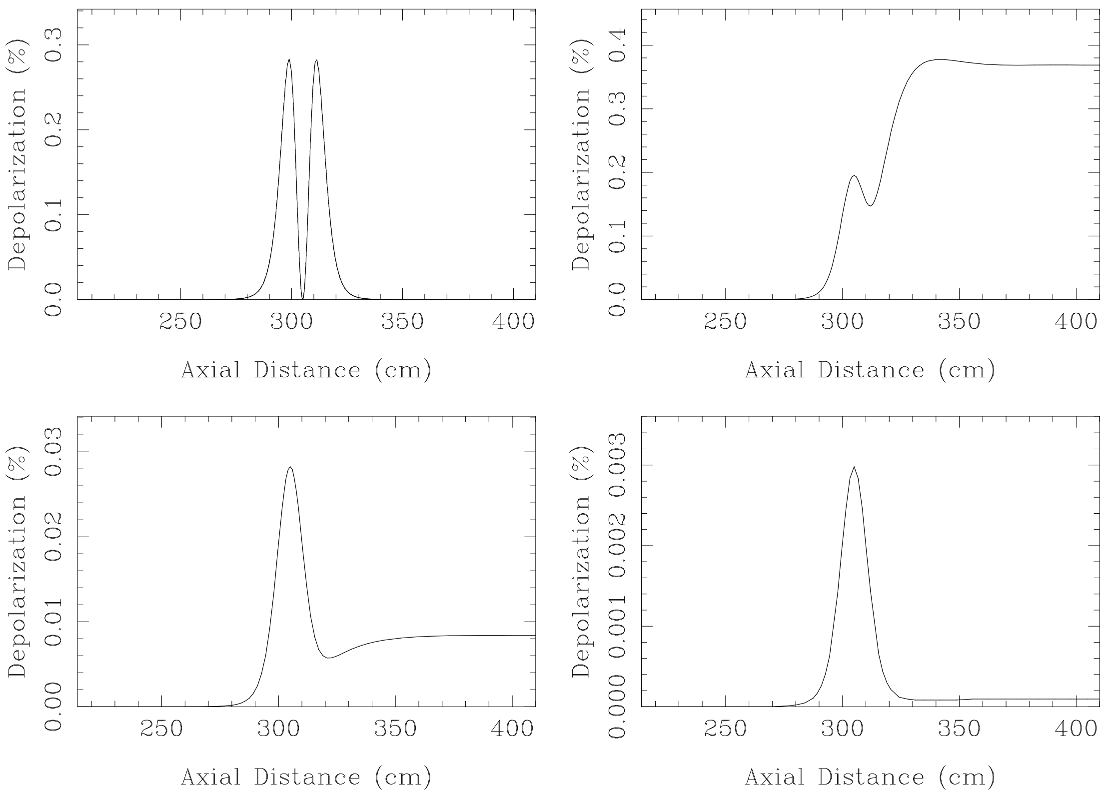

Figure B.3: Depolarization versus axial distance for four energies, 0.1 meV (top left), 1 eV (top right), 10 eV (bottom left) and 100 eV (bottom right). The calculation is for a single neutron at $r = 4$ cm for the approximate fields of Figure B.2.

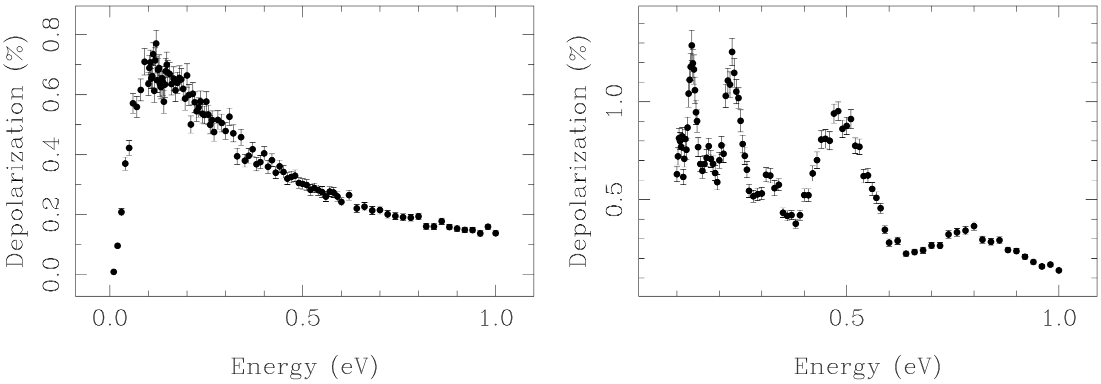

Figure B.4: Depolarization at $z = 410$ cm versus neutron energy without the Earth's field (left) and with the Earth's field (right). The Earth's field is treated as a constant field of 0.3 G directed perpendicularly to the solenoidal field. Each point is the average of 100 neutrons with random trajectories from $z = 200$ cm to $z = 410$ cm within a beam radius of $R = 4$ cm for the approximate fields of Figure B.2.

but the arrangement of a series of gaps effects the energy dependence as well. With a sufficient number of gaps, the energy dependence can be quite complicated as is the case with the TRIPLE beam line (see Figure 3.8).

Since the beam is well collimated to $R = 4.0$ cm at the spin flipper expanding slightly to $R = 4.3$ cm at the target position, for all but the 5.08 cm radius coils at the position of the target, the beam radius is less than half the coil radius (See Table 3.1). Therefore, the approximate field calculation provides an accurate field to be used in calculating the spin depolarization. For the case of the 5.08 cm radius coils, the spin depolarization for several energies was calculated using both the exact and approximate field calculations. The neutrons were transmitted from the midpoint of the first coil to the midpoint of the second. The resulting average depolarization values agree very well. For instance, at 1 eV the depolarization for the exact field is $(6.4 \pm 0.4) \times 10^{-4}$ and for the approximate field the depolarization is $(6.5 \pm 0.4) \times 10^{-4}$. The agreement is due primarily to the fact that the gap is small, so the depolarization is dominated by the effect of the Earth's field.

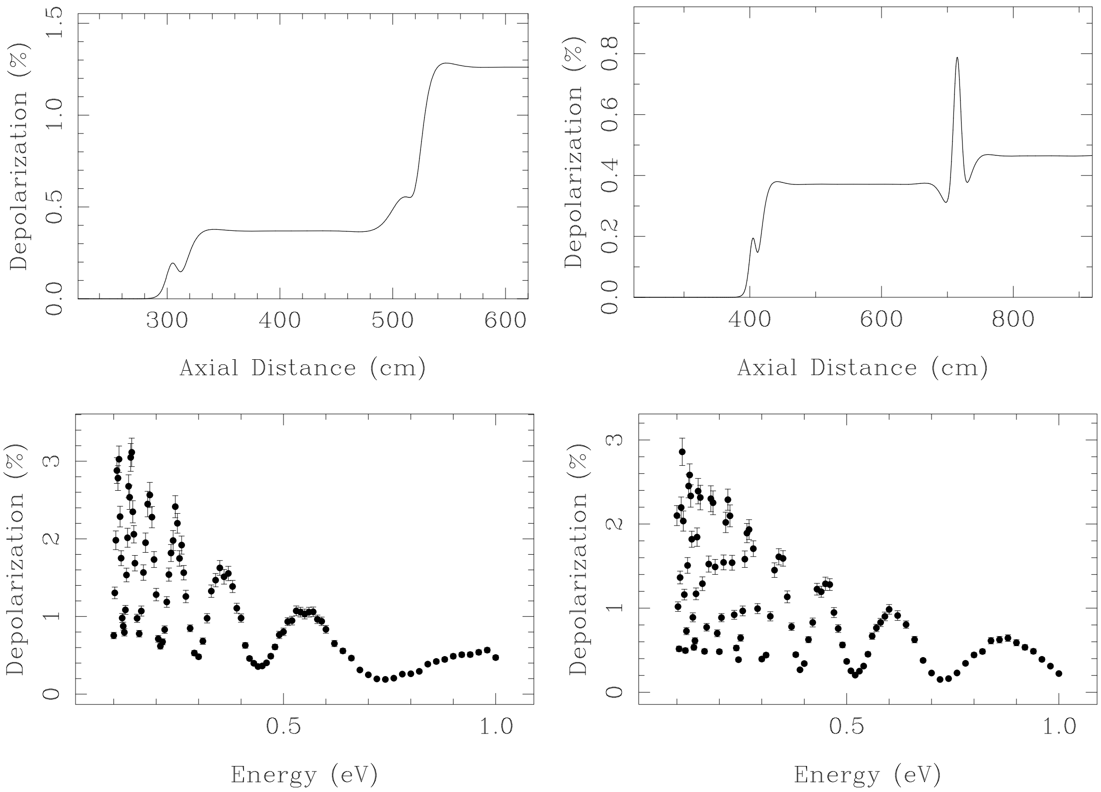

Figure B.5: Depolarization for two gaps with 2 m coils (left) and 3 m coils (right). Both groups of coils start at $z = 100$ cm. The upper curves show the depolarization versus axial distance for a single 1 eV neutron with $r = 4$ cm. The lower curves show the energy dependence of the average depolarization of 100 neutrons with random trajectories between $z = 200$ cm and $z = 620$ cm (left) and $z = 920$ cm (right) within a beam radius of $R = 4$ cm.

This example also illustrates a practical reason for using the approximate field calculations. The amount of computer time required by a Vax Alpha to calculate the depolarization for the approximate-field case was 4 s, and the amount for the exact-field case was 49 s. For the entire beam line the exact calculation would take about 40 times longer than the approximate calculation. Since the energy-dependence calculations done for the TRIPLE beam line (Figure 3.8) took 8 days with the approximate field, the use of the exact field was impractical.

Appendix C

Sample Fits and $\mathcal{P}$ Histograms

This appendix contains sample fits of all of the resonances analyzed for the ^{106}Pd, ^{108}Pd and ^{238}U data. Also included are the histograms of the $\mathcal{P}$ values for the resonances analyzed in the run-by-run analysis. The data from different run sets, e.g., positive and negative neutron polarization, have been combined to produce histograms for the entire set of data. This implicitly assumes that the polarization errors are the same for the two sets, which is true for the ^{106}Pd and ^{108}Pd isotopes. Although this is not true for the ^{238}U data, the histograms presented here demonstrate the statistical fluctuations for the run-by-run analysis. The resonances present in the spectra that are not listed in the caption are due to isotopic contamination (mostly ^{105}Pd for the Pd targets and ^{235}U for the ^{238}U target).

C.1 Sample Transmission Fits for ^{106}Pd and ^{108}Pd

The resonance energies listed in the captions are from the transmission calibration discussed in Section 4.1.3. The fits are of the sum of eleven ^{106}Pd (twelve ^{108}Pd) half-hour runs where the target was at 60° relative to the beam line, and the target-in data have been divided by the target-out data.

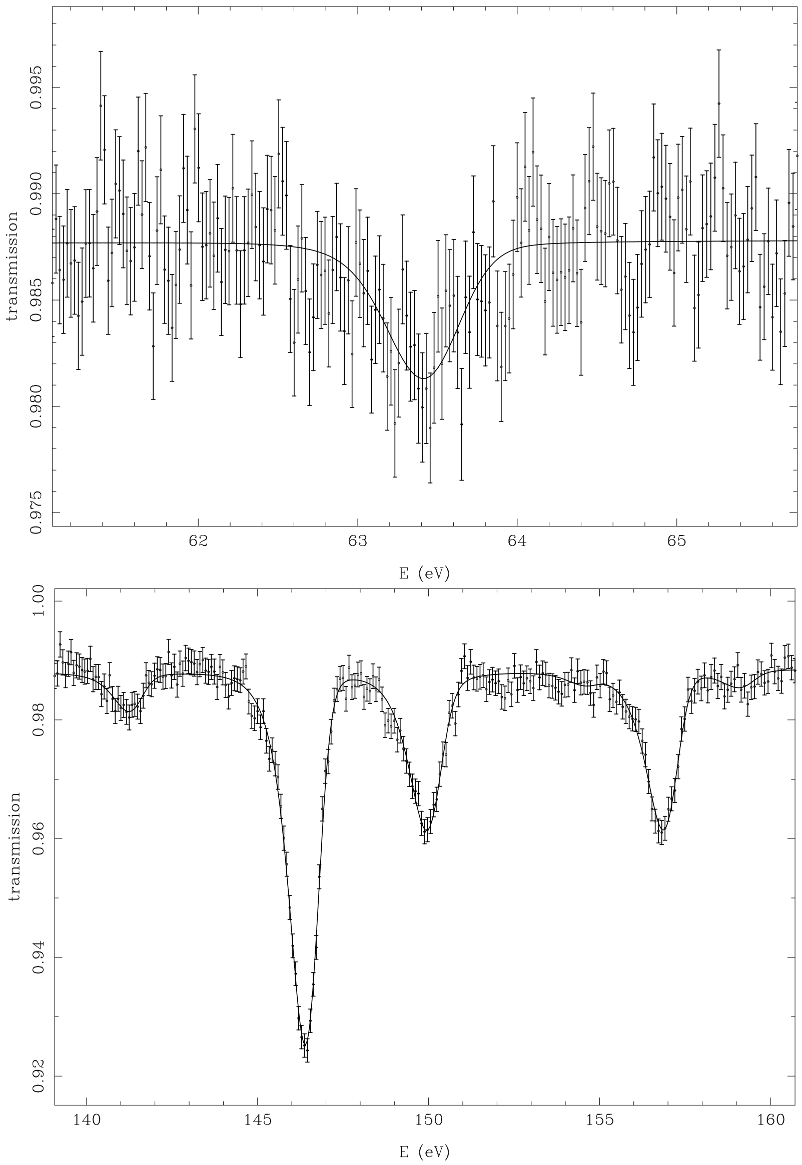

Figure C.1: Sample transmission fits of the 63.4 eV (top), 146.4 eV and 156.7 eV (bottom) resonances in ^{106}Pd.

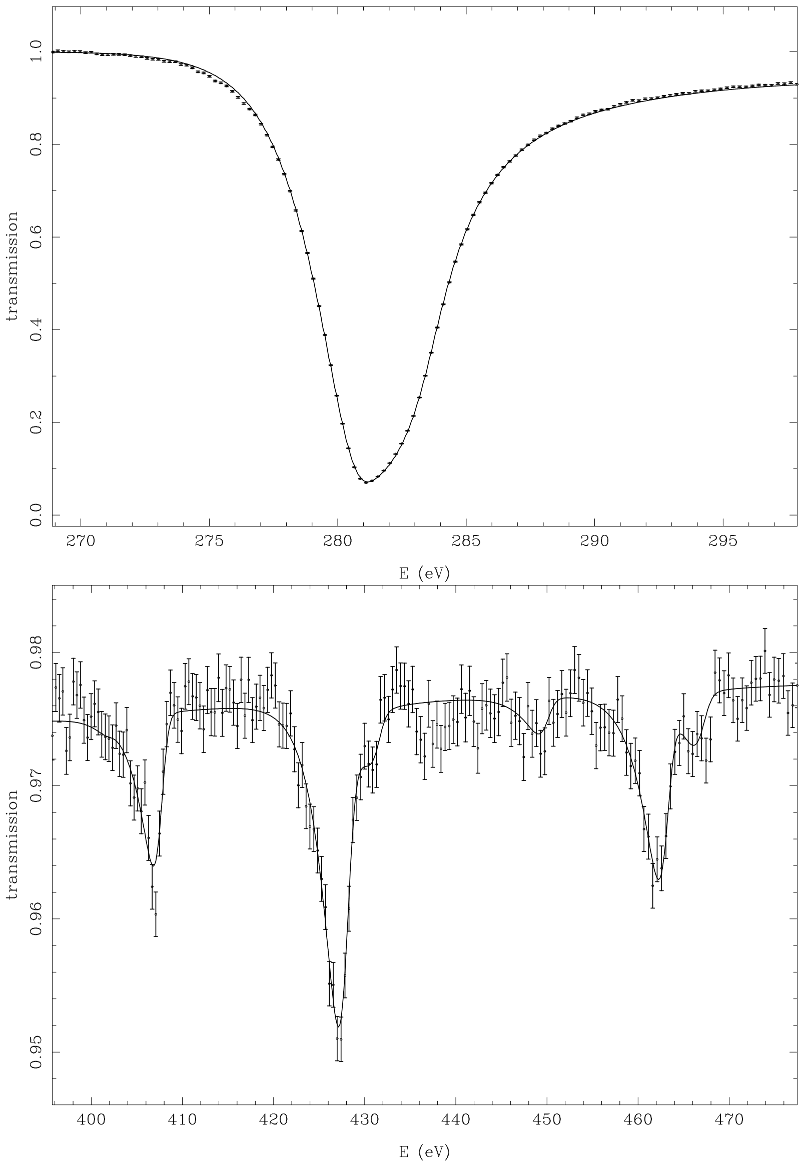

Figure C.2: Sample transmission fits of the 281.1 eV (top), 406.7 eV and 462.3 eV (bottom) resonances in ^{106}Pd.

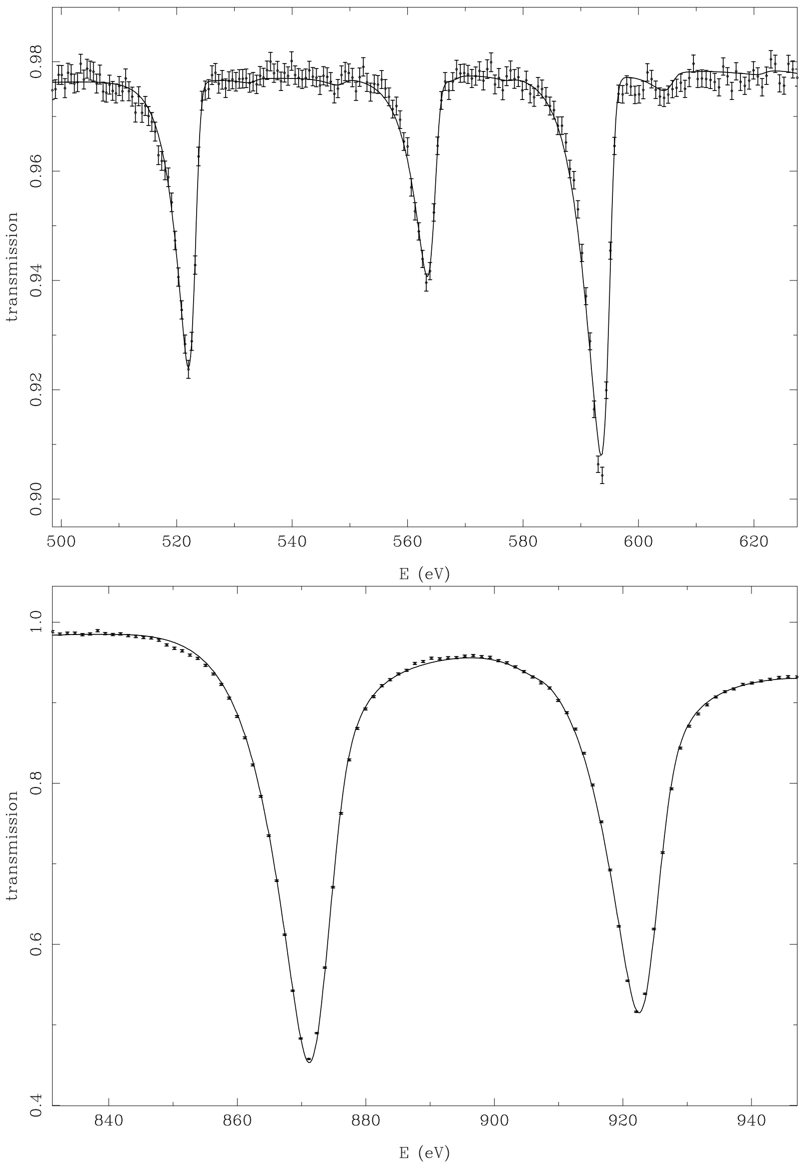

Figure C.3: Sample transmission fits of the 522.1 eV, 563.3 eV, 593.4 eV (top), 871.2 eV and 922 eV (bottom) resonances in ^{106}Pd.

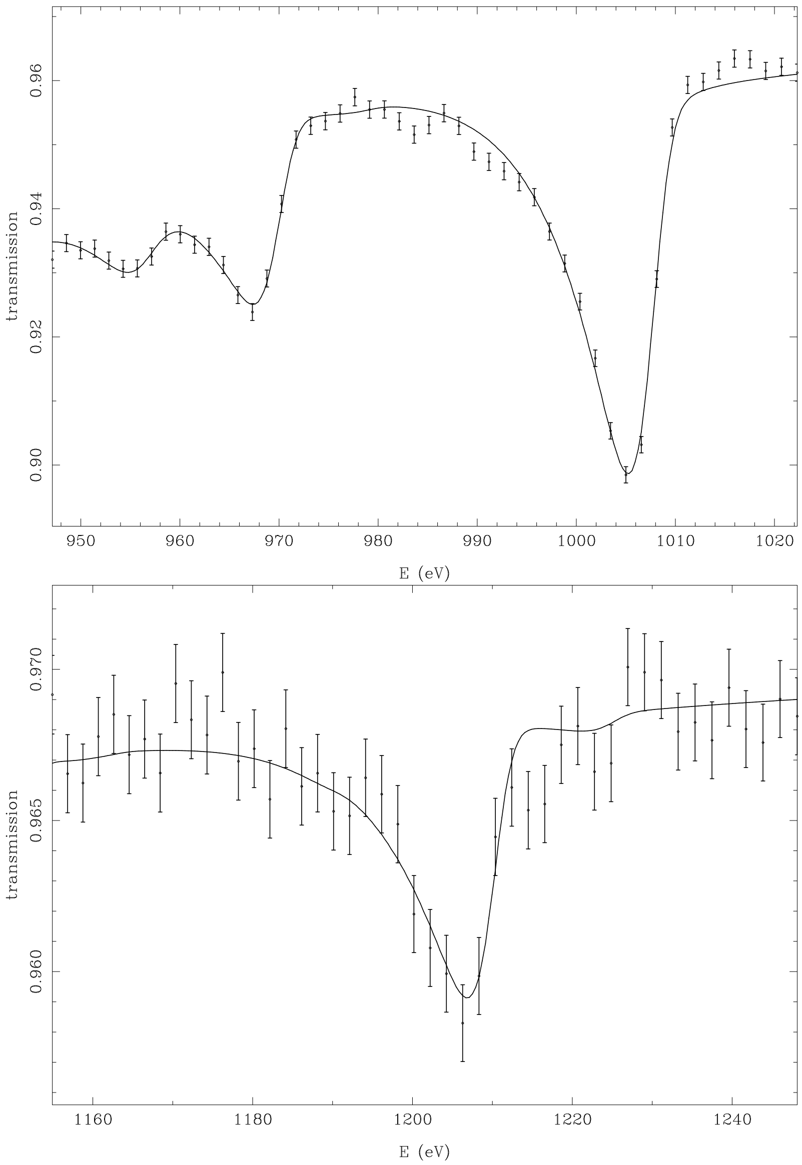

Figure C.4: Sample transmission fits of the 967 eV, 1005 eV (top) and 1207 eV (bottom) resonances in ^{106}Pd.

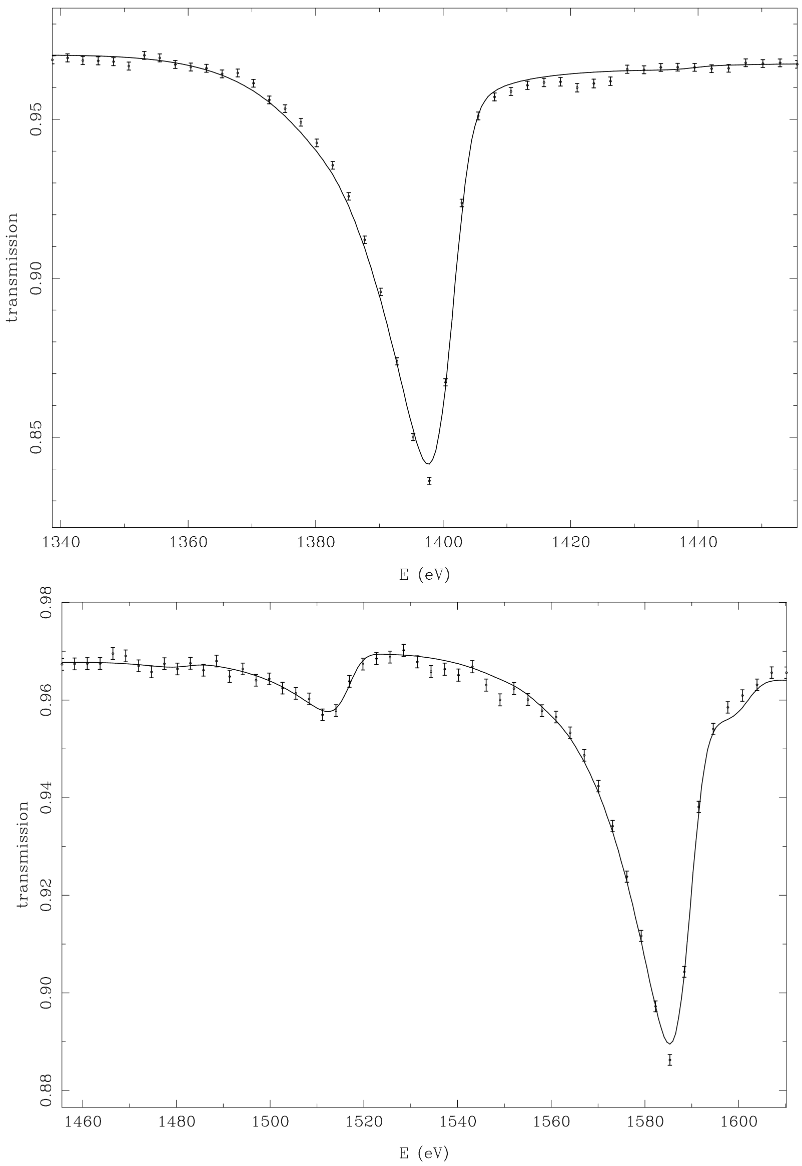

Figure C.5: Sample transmission fits of the 1398 eV (top), 1513 eV and 1586 eV (bottom) resonances in ^{106}Pd.

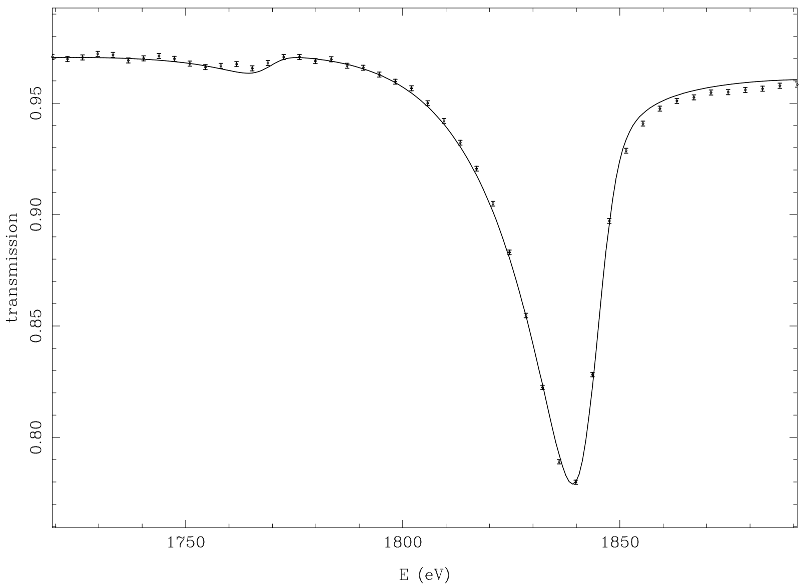

Figure C.6: Sample transmission fit of the 1839 eV resonance in ^{106}Pd.

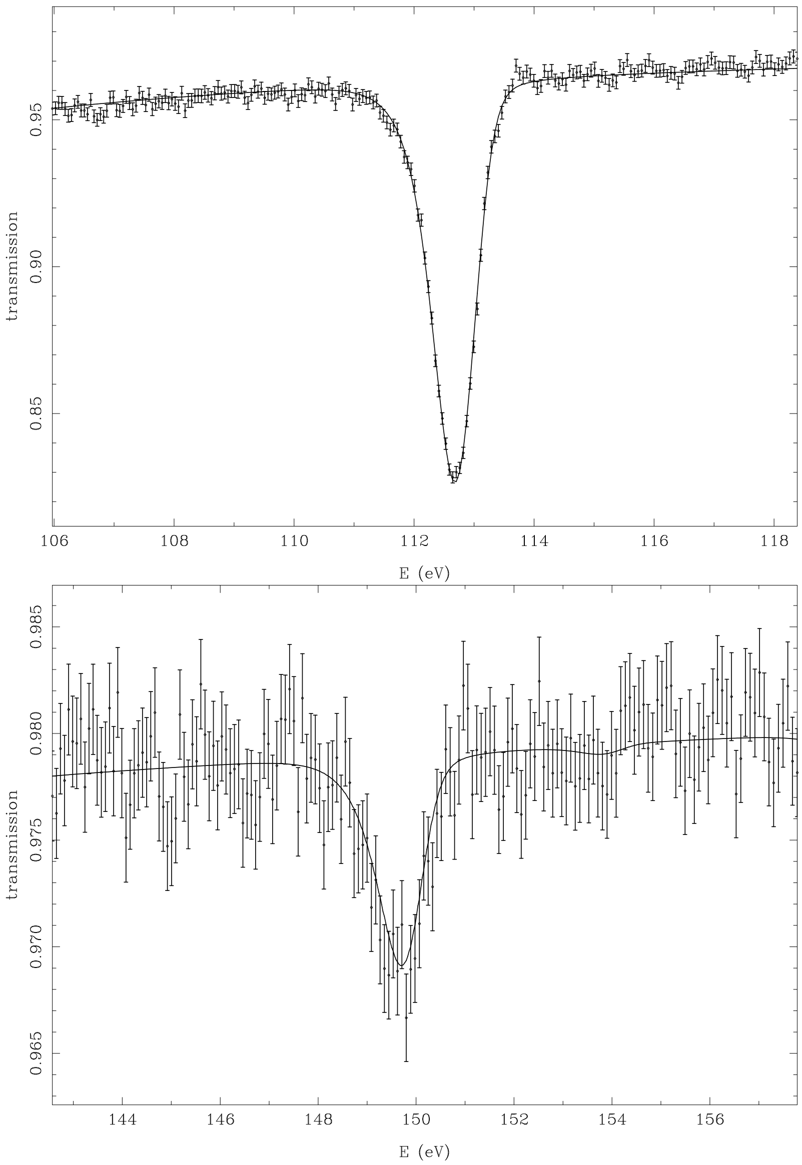

Figure C.7: Sample transmission fits of the 112.7 eV (top) and 149.7 eV (bottom) resonances in ^{108}Pd.

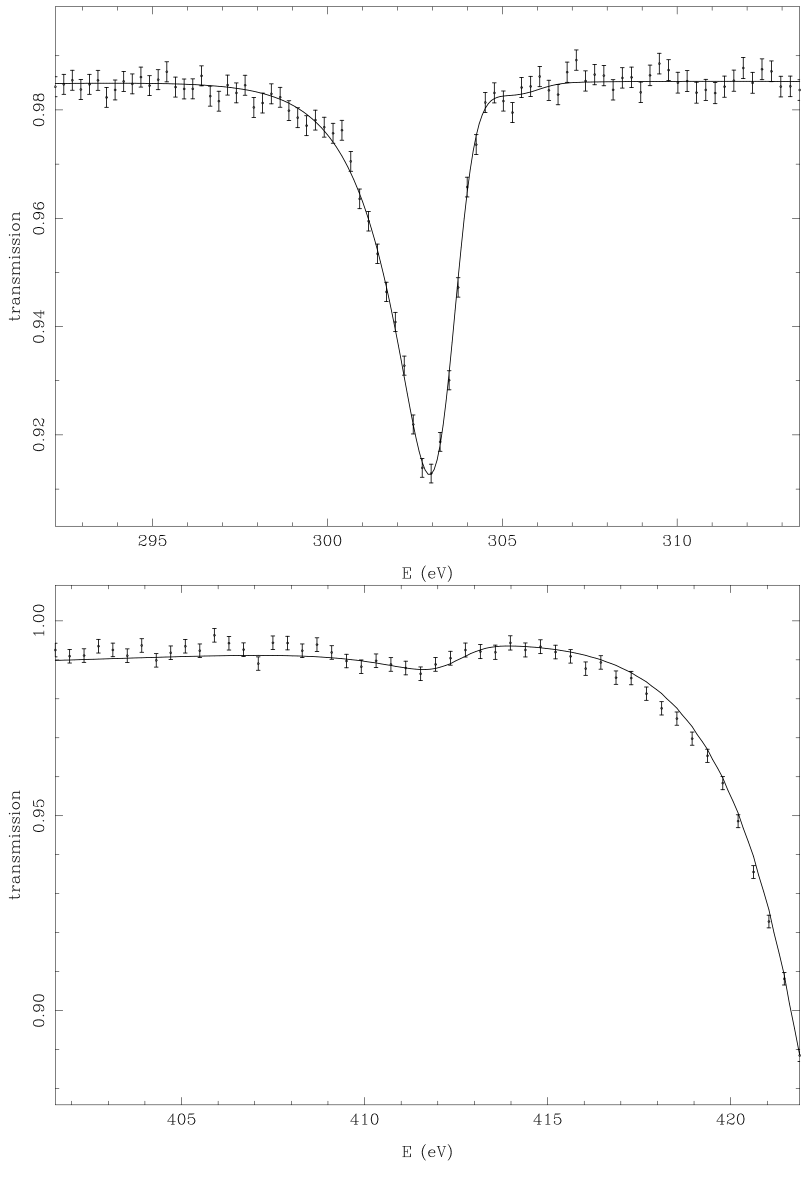

Figure C.8: Sample transmission fits of the 302.9 eV (top) and 411.6 eV (bottom) resonances in ^{108}Pd.

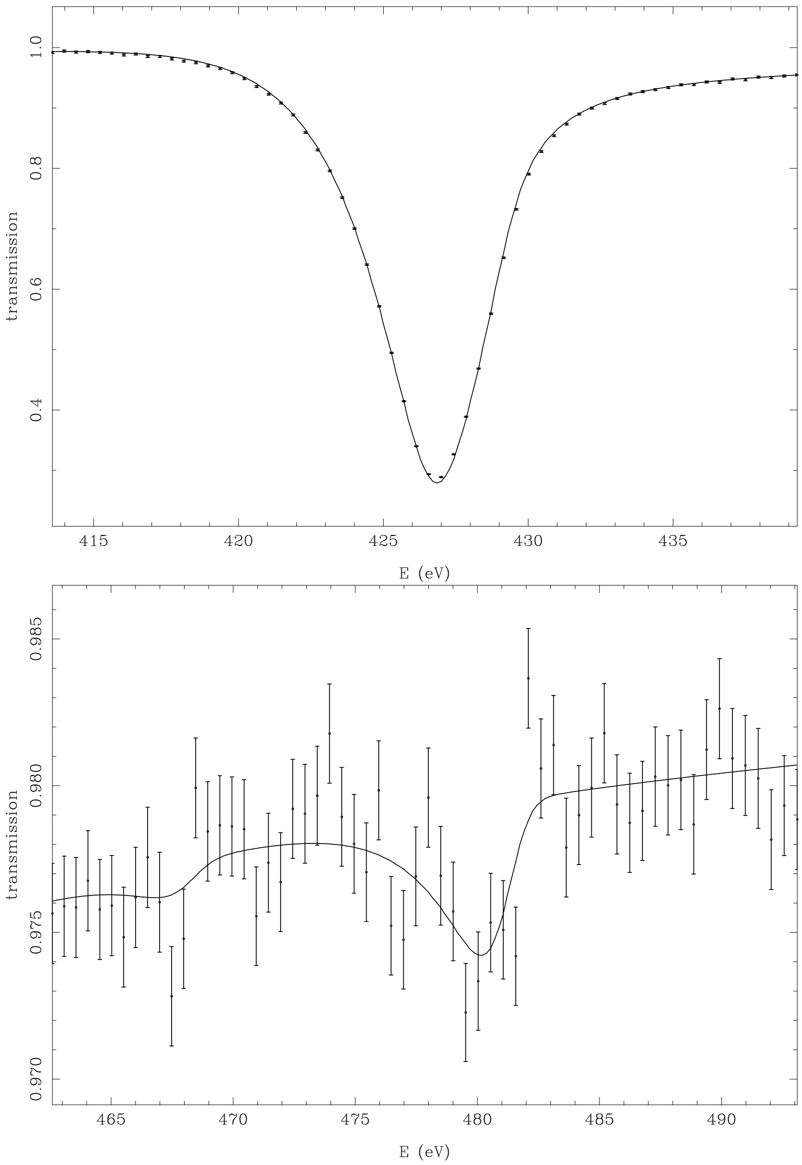

Figure C.9: Sample transmission fits of the 426.9 eV (top) and 480.1 eV (bottom) resonances in ^{108}Pd.

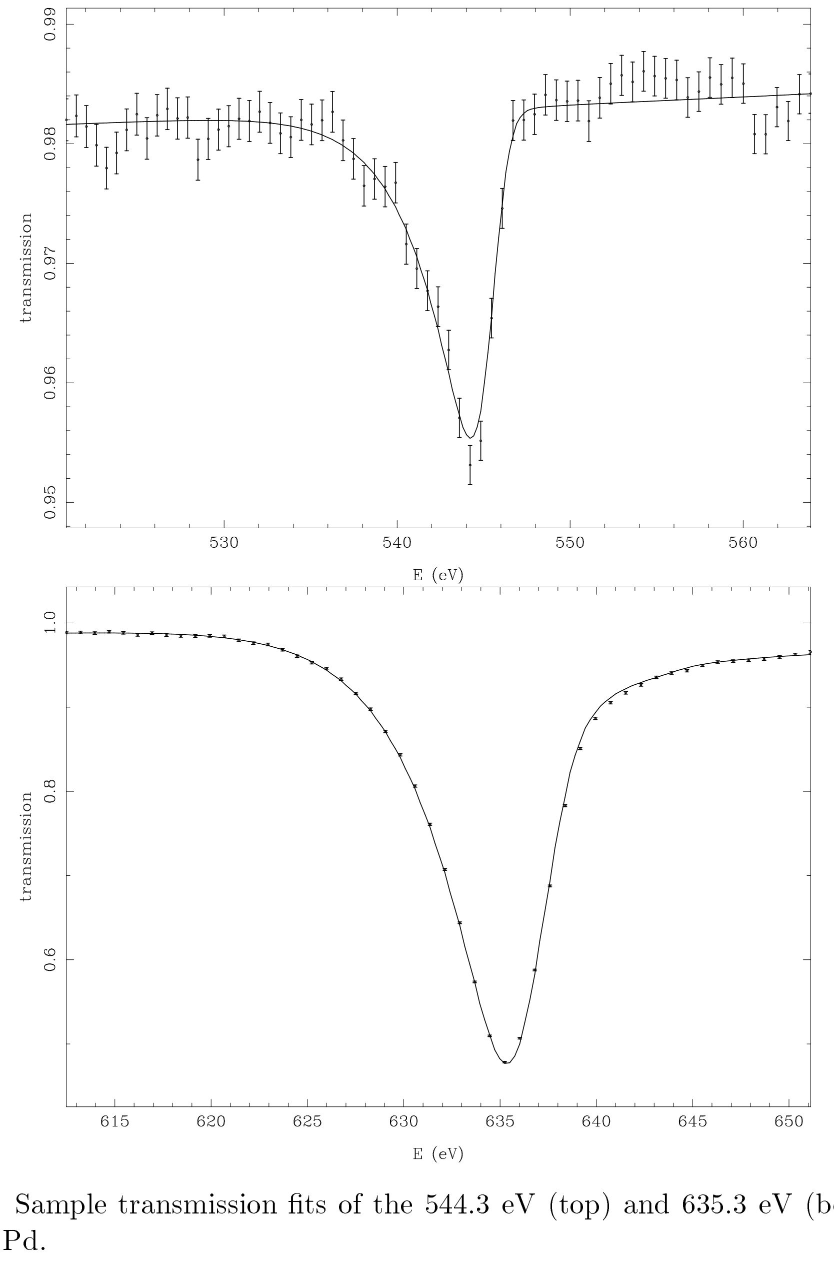

Figure C.10: Sample transmission fits of the 544.3 eV (top) and 635.3 eV (bottom) resonances in ^{108}Pd.

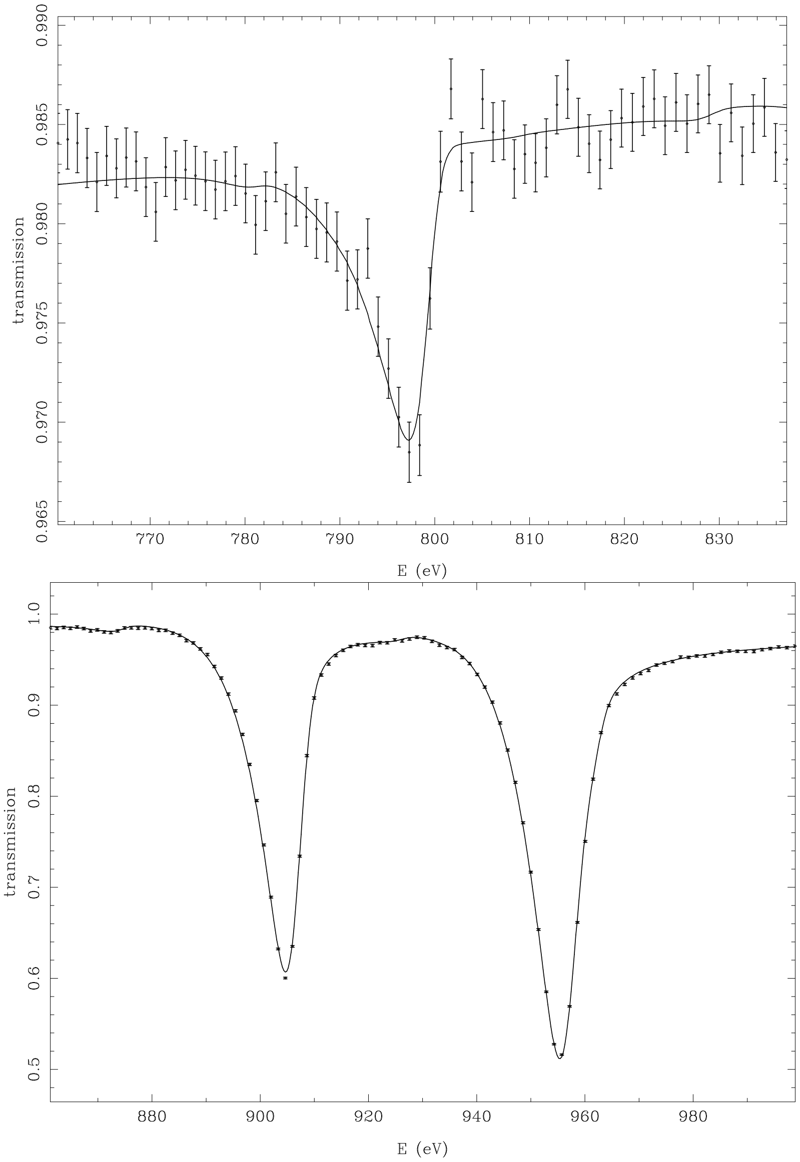

Figure C.11: Sample transmission fits of the 797.4 eV (top), 905 eV and 956 eV (bottom) resonances in ^{108}Pd.

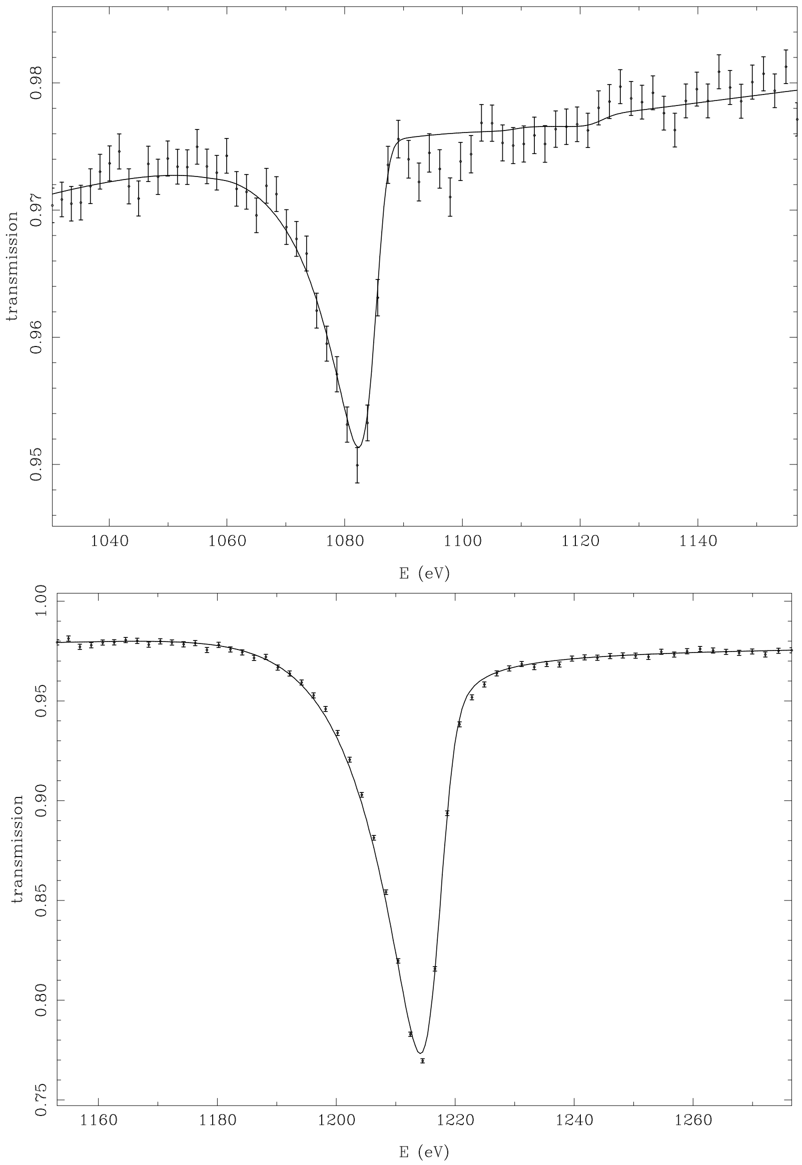

Figure C.12: Sample transmission fits of the 1082 eV (top) and 1215 eV (bottom) resonances in ^{108}Pd.

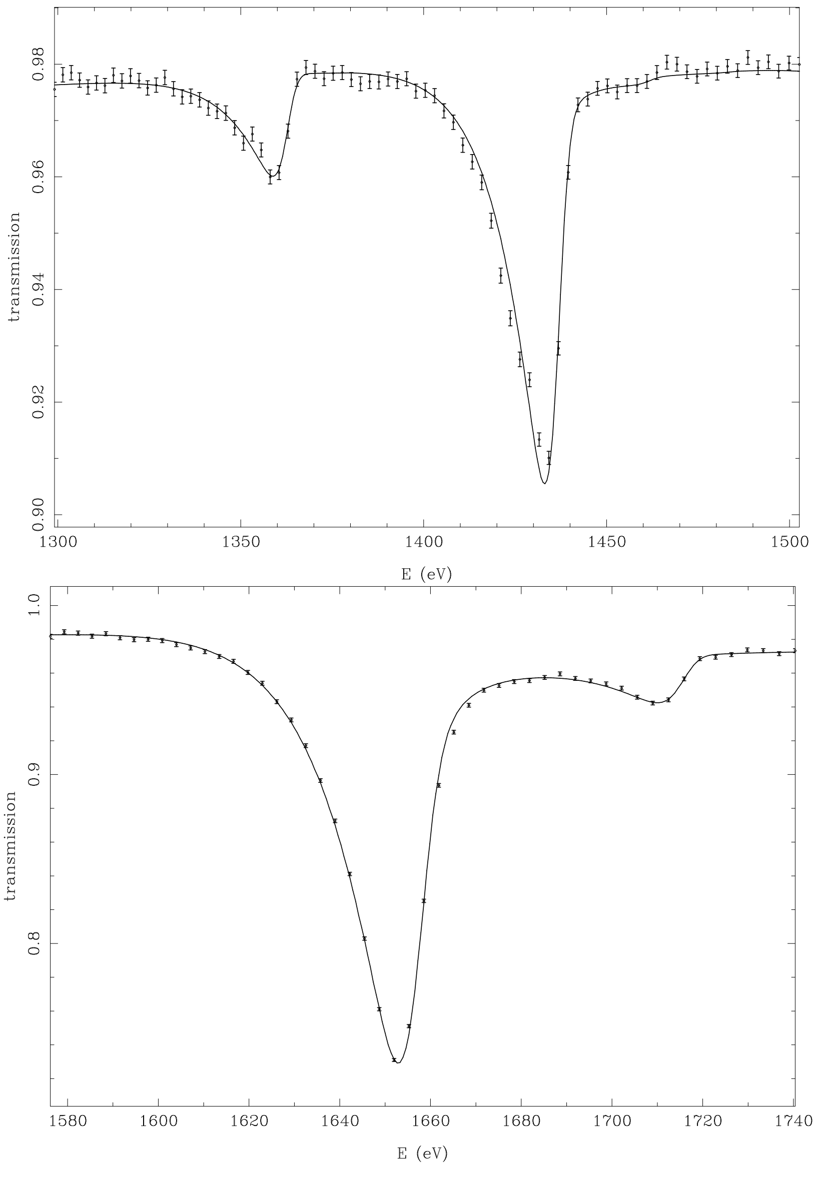

Figure C.13: Sample transmission fits of the 1358 eV, 1433 eV (top), 1652 eV and 1710 eV (bottom) resonances in ^{108}Pd.

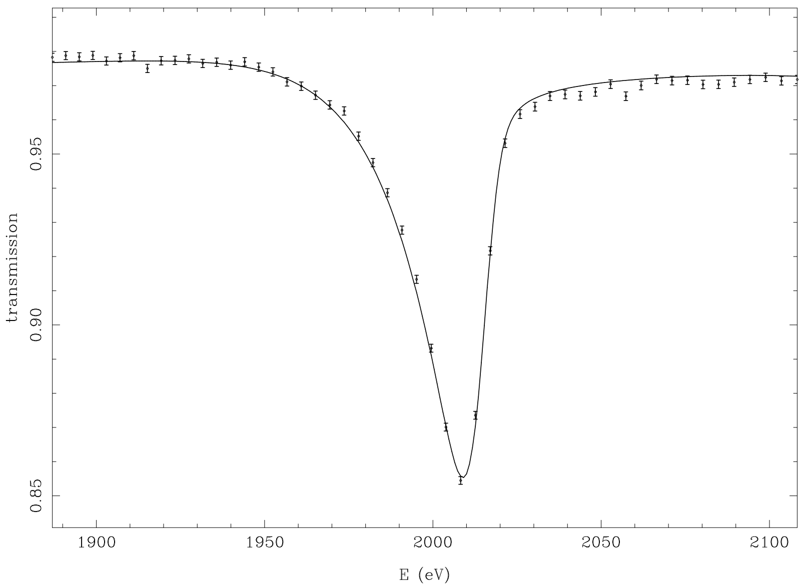

Figure C.14: Sample transmission fit of the 2008 eV resonance in ^{108}Pd.

C.2 Sample Capture Fits and $\mathcal{P}$ Histograms for ^{106}Pd and ^{108}Pd

The energies listed in the captions were found from the capture calibration described in Section 4.1.3. The fits were performed on a sum of 70 half-hour runs taken with the capture detector.

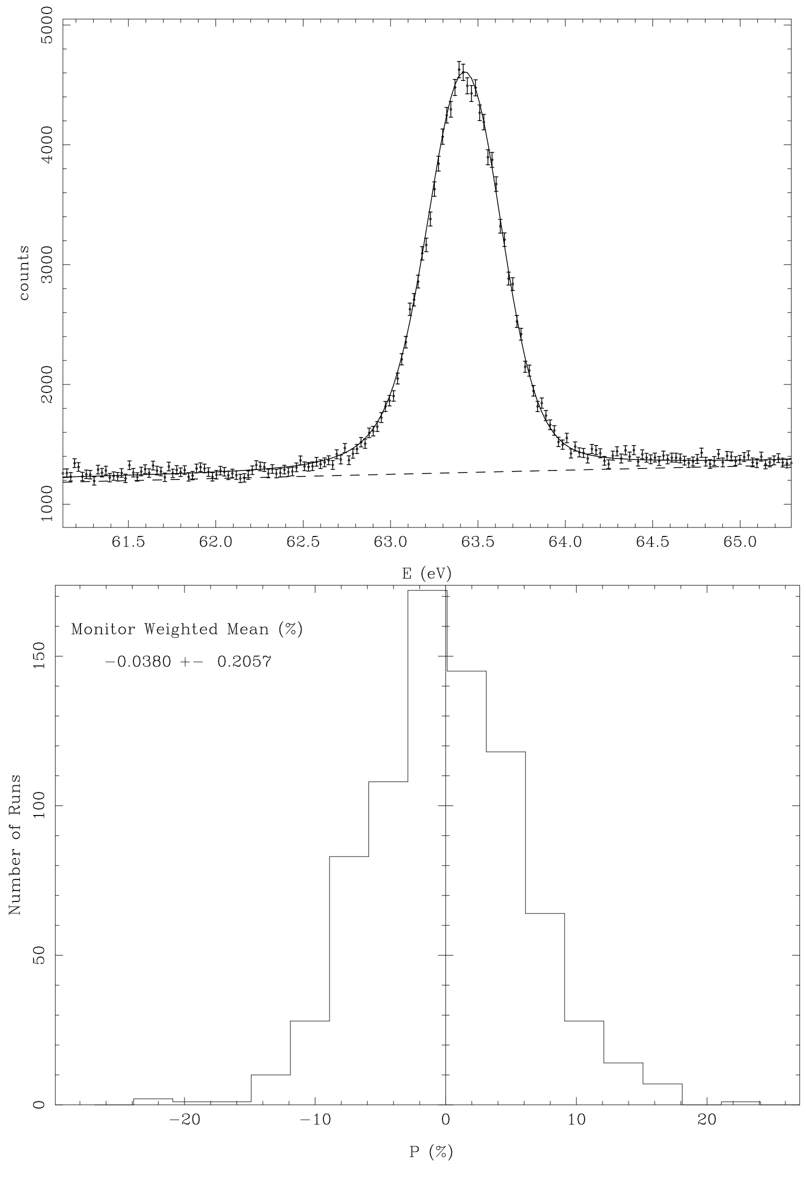

Figure C.15: Sample capture fit (top) and $\mathcal{P}$ histogram (bottom) of the 63.43 eV resonance in ^{106}Pd.

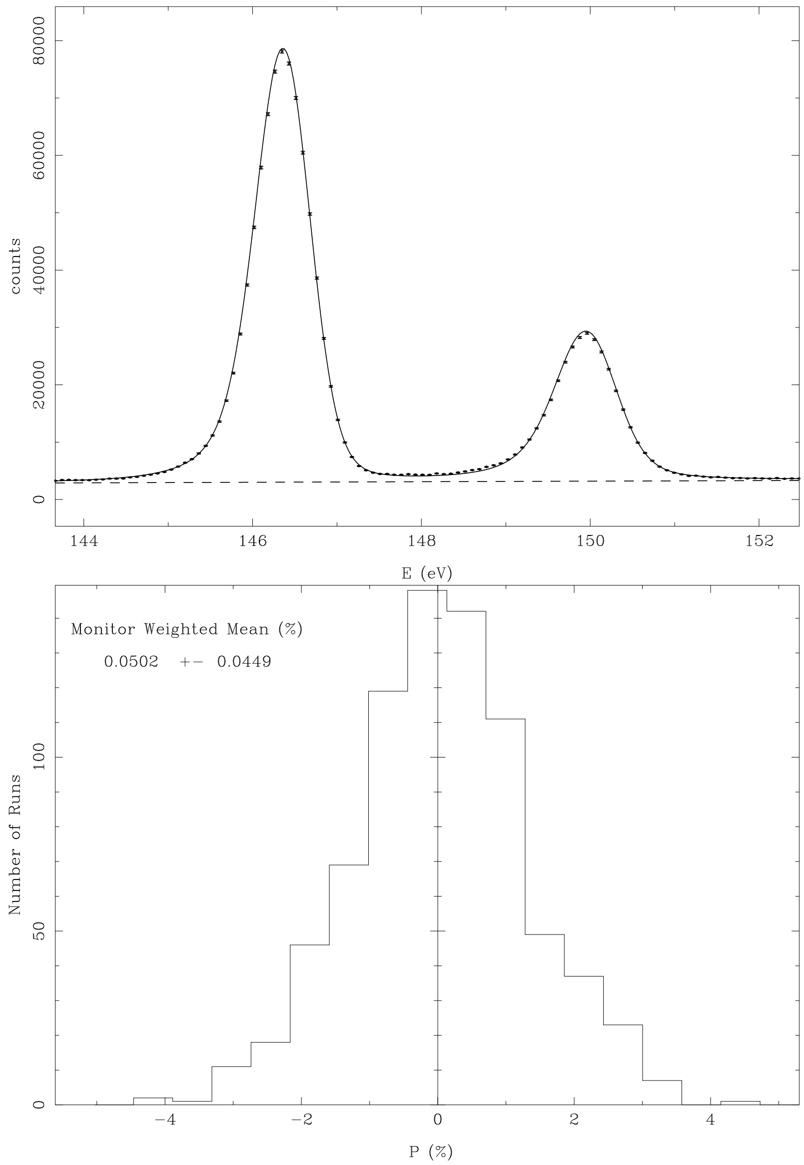

Figure C.16: Sample capture fit (top) and $\mathcal{P}$ histogram (bottom) of the 146.36 eV resonance in ^{106}Pd.

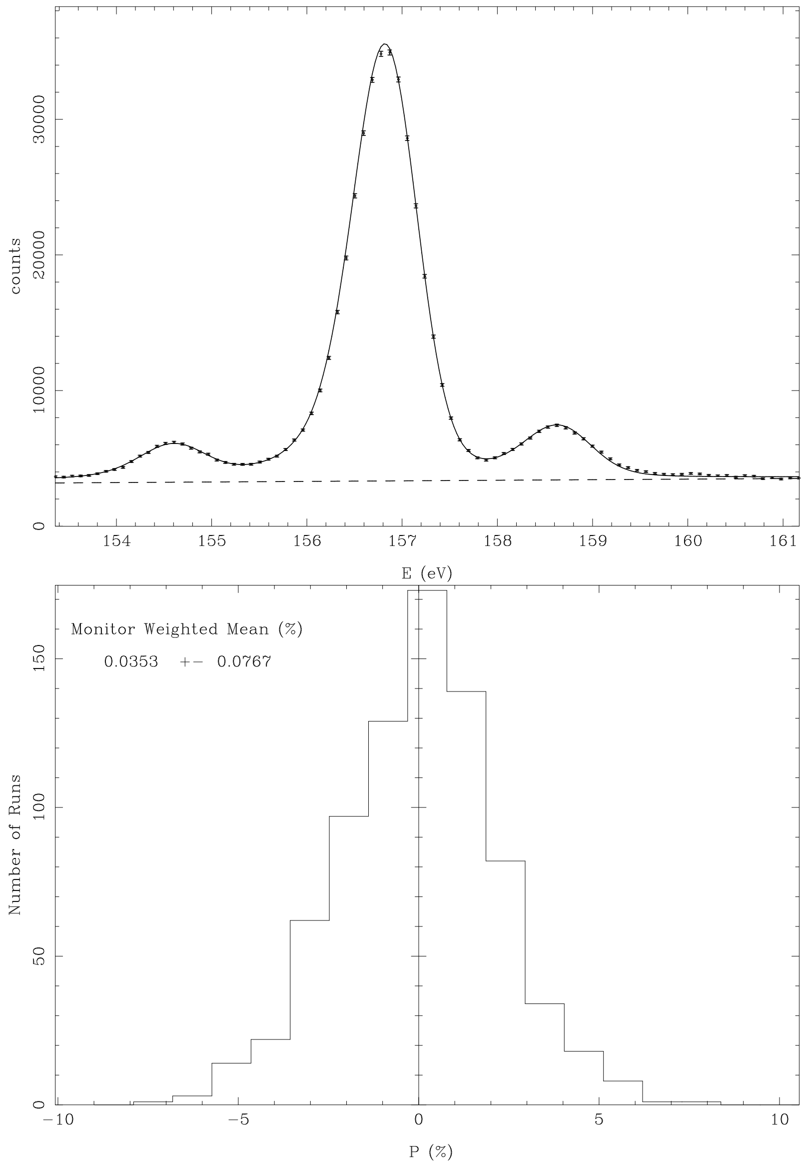

Figure C.17: Sample capture fit (top) and $\mathcal{P}$ histogram (bottom) of the 156.88 eV resonance in ^{106}Pd.

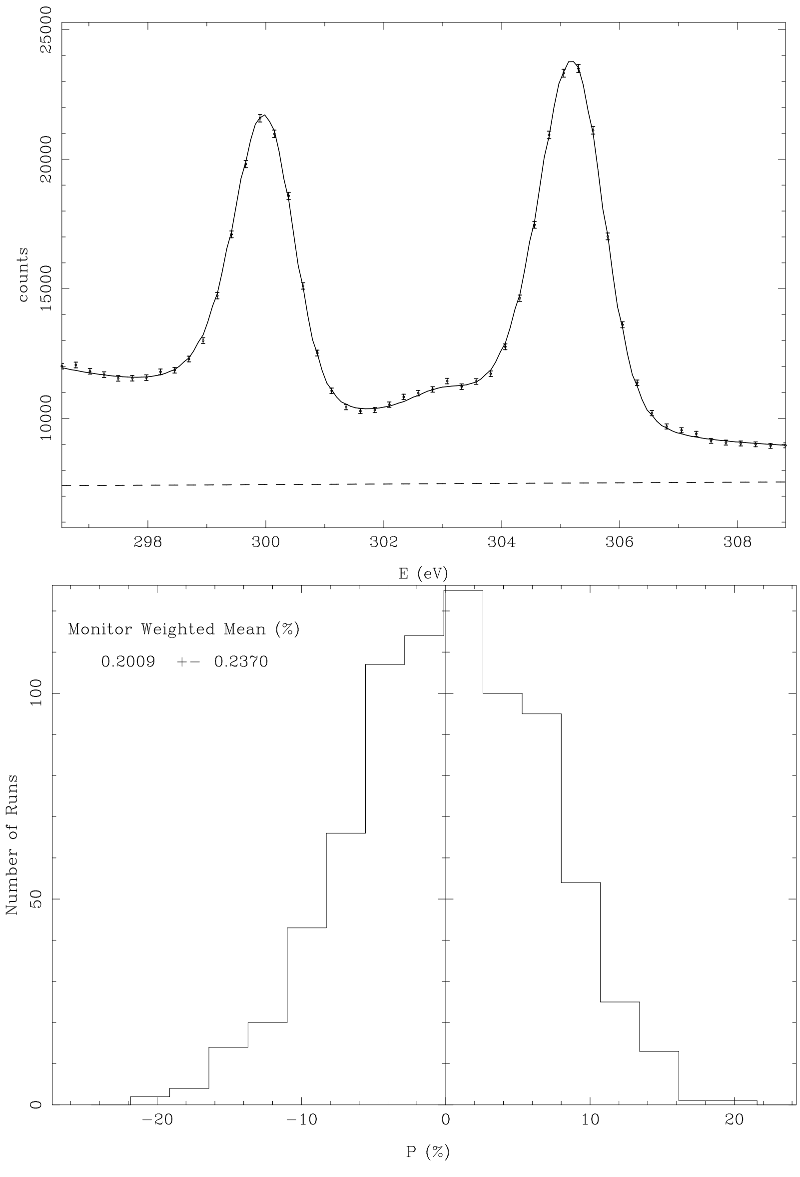

Figure C.18: Sample capture fit (top) and $\mathcal{P}$ histogram (bottom) of the 300.0 eV resonance in ^{106}Pd.

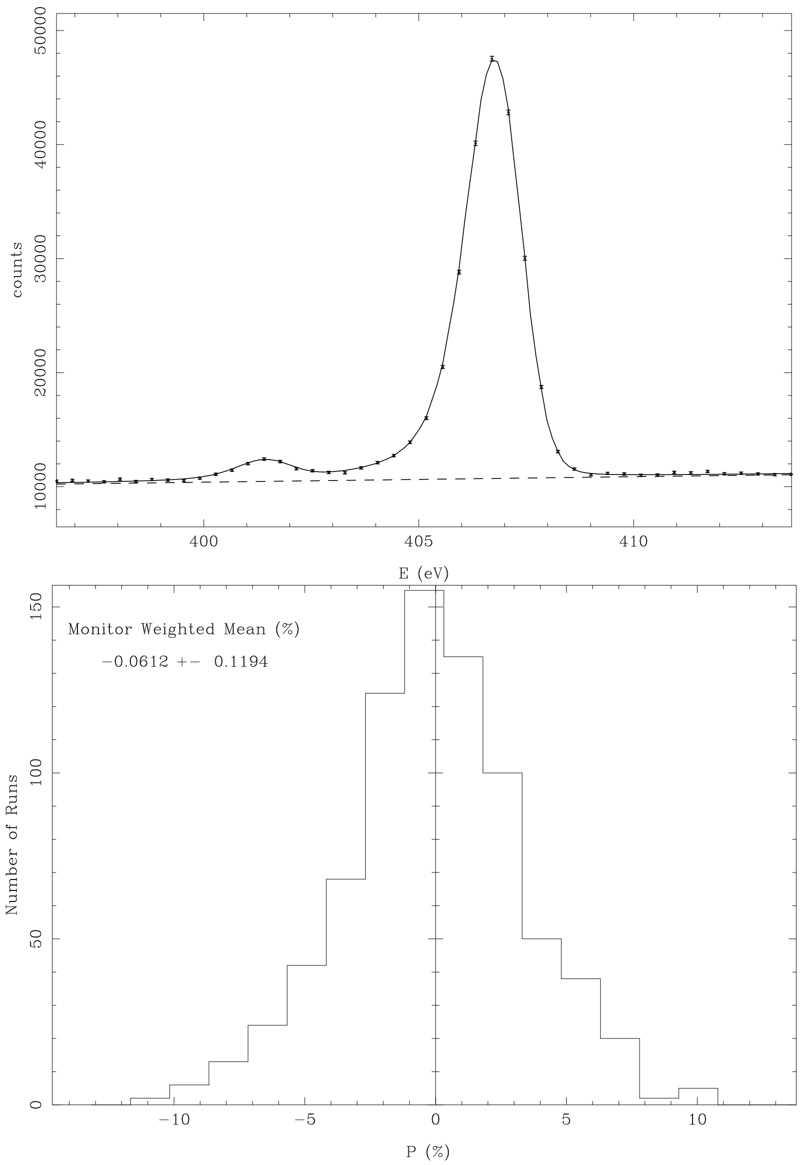

Figure C.19: Sample capture fit (top) and $\mathcal{P}$ histogram (bottom) of the 406.7 eV resonance in ^{106}Pd.

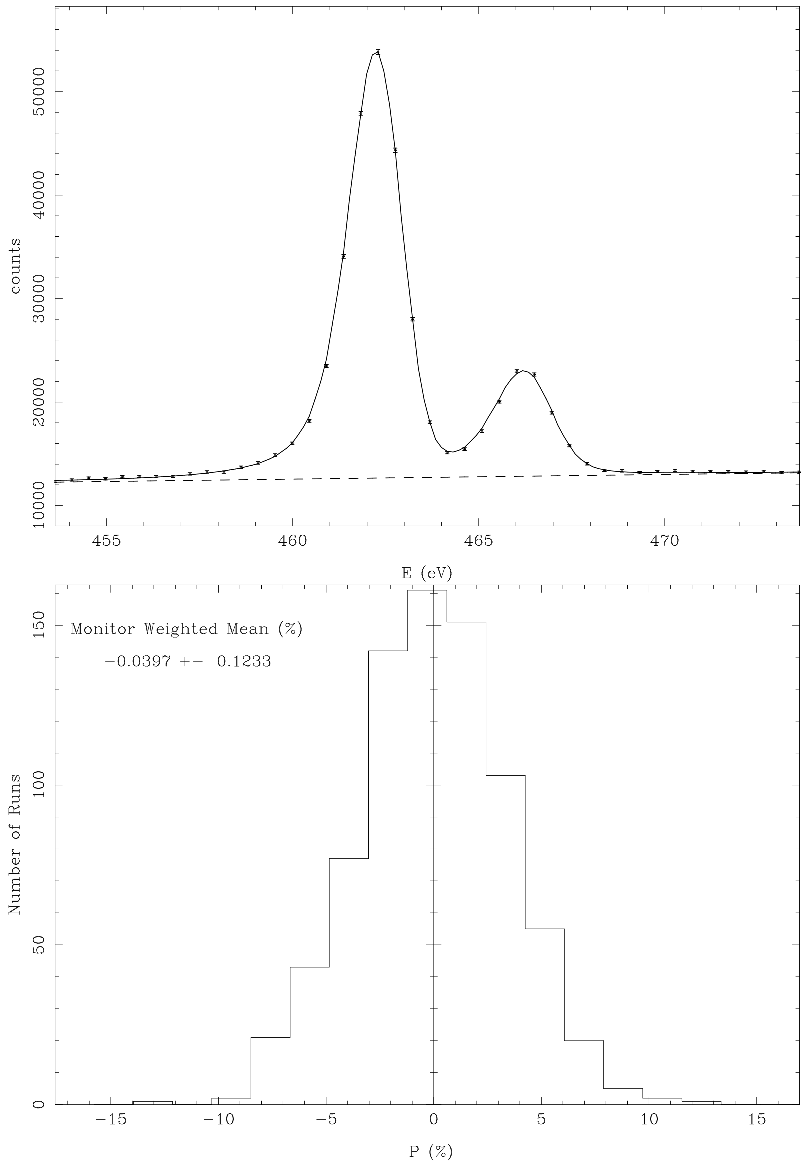

Figure C.20: Sample capture fit (top) and $\mathcal{P}$ histogram (bottom) of the 462.3 eV resonance in ^{106}Pd.

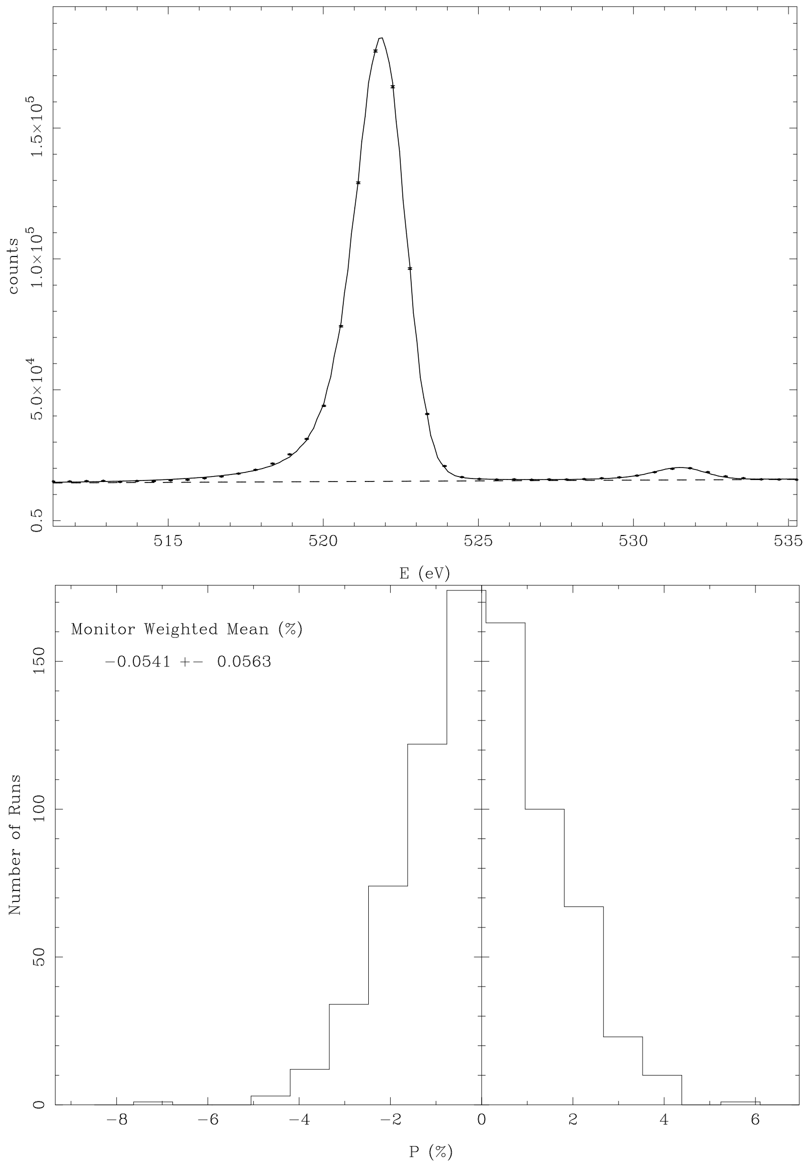

Figure C.21: Sample capture fit (top) and $\mathcal{P}$ histogram (bottom) of the 521.9 eV resonance in ^{106}Pd.

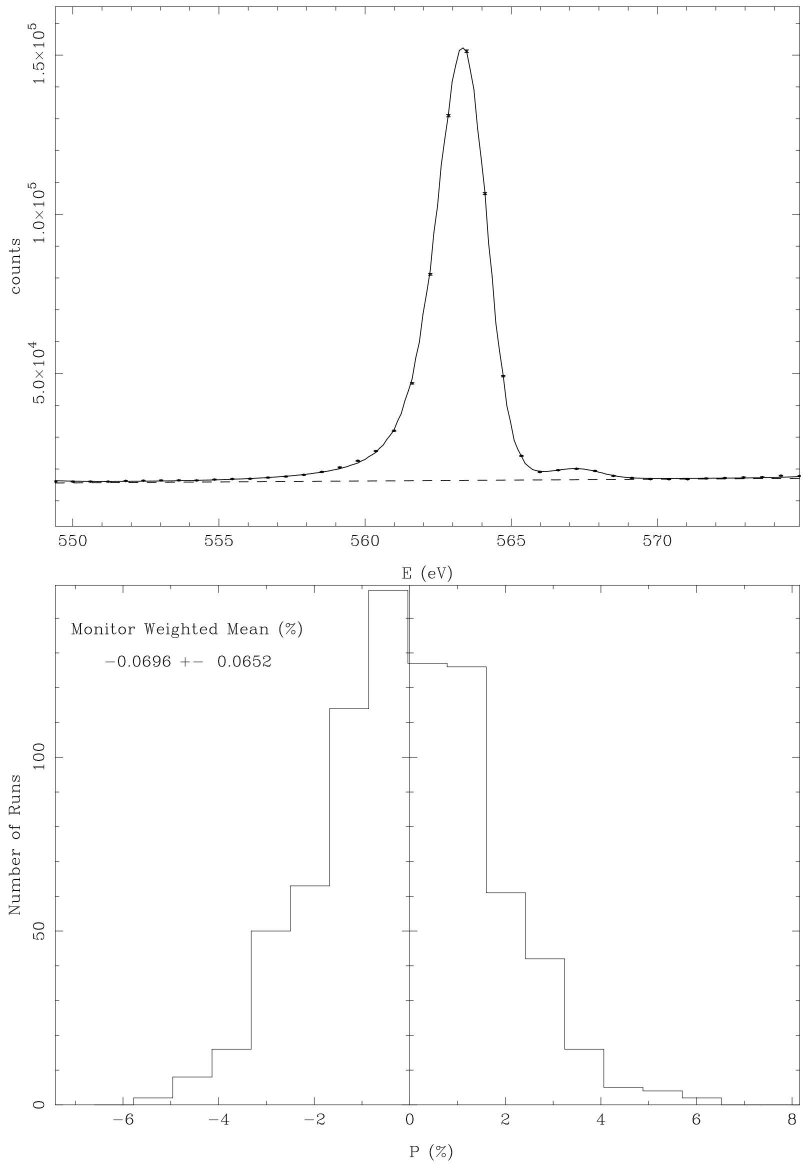

Figure C.22: Sample capture fit (top) and $\mathcal{P}$ histogram (bottom) of the 563.4 eV resonance in ^{106}Pd.

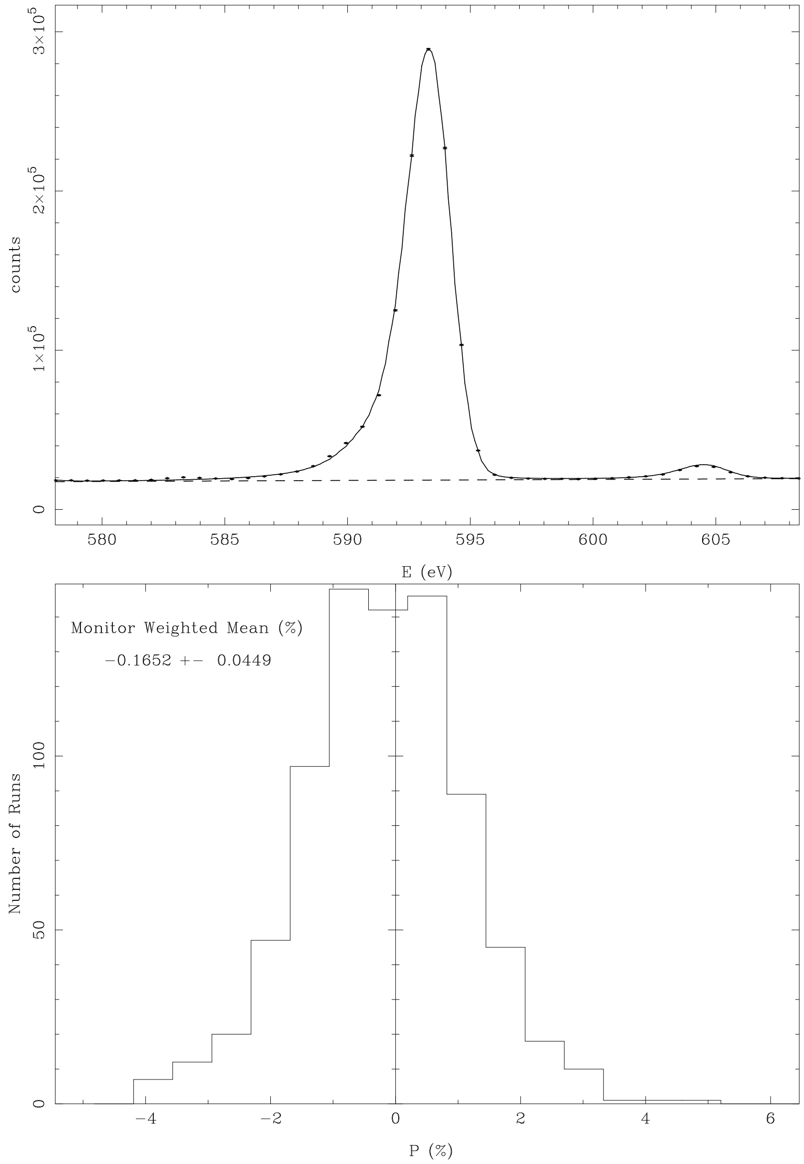

Figure C.23: Sample capture fit (top) and $\mathcal{P}$ histogram (bottom) of the 593.4 eV resonance in ^{106}Pd.

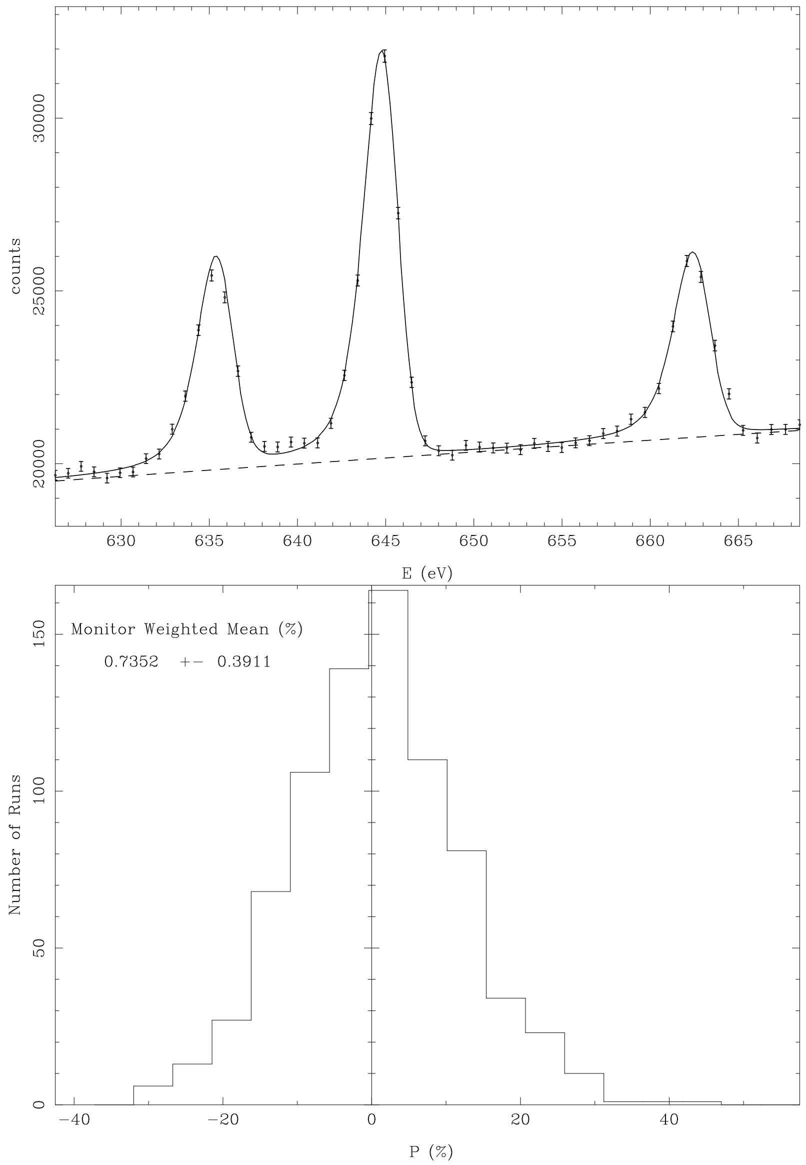

Figure C.24: Sample capture fit (top) and $\mathcal{P}$ histogram (bottom) of the 644.9 eV resonance in ^{106}Pd.

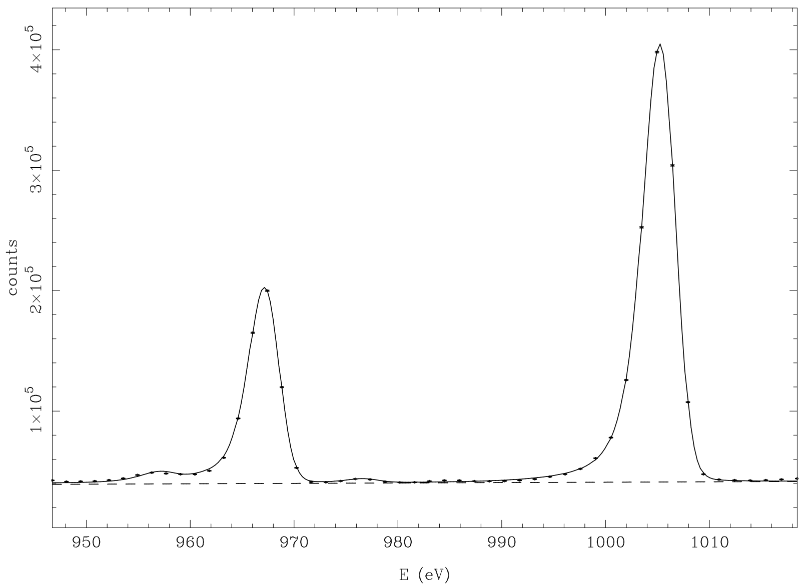

Figure C.25: Sample capture fit of the 967.5 eV and 1005.3 eV resonances in ^{106}Pd.

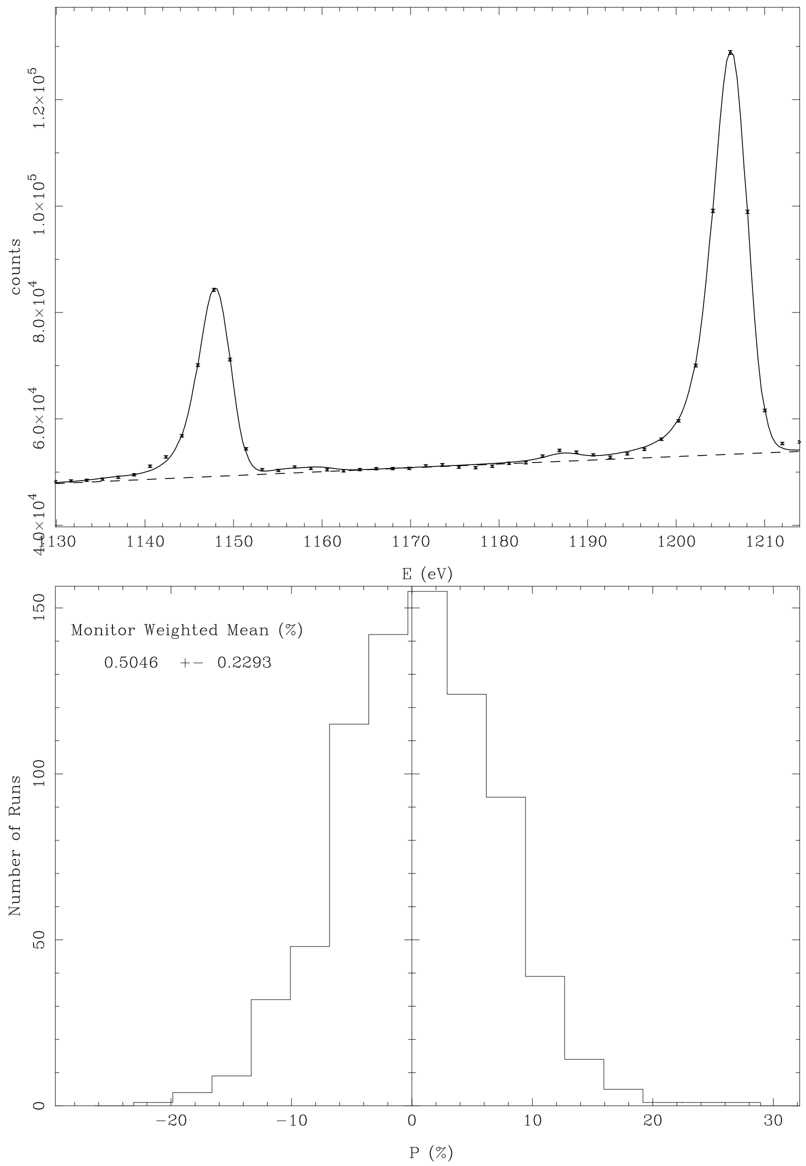

Figure C.26: Sample capture fit (top) of the 1147.9 eV and 1206.2 eV resonances and $\mathcal{P}$ histogram (bottom) of the 1147.9 eV resonance in ^{106}Pd.

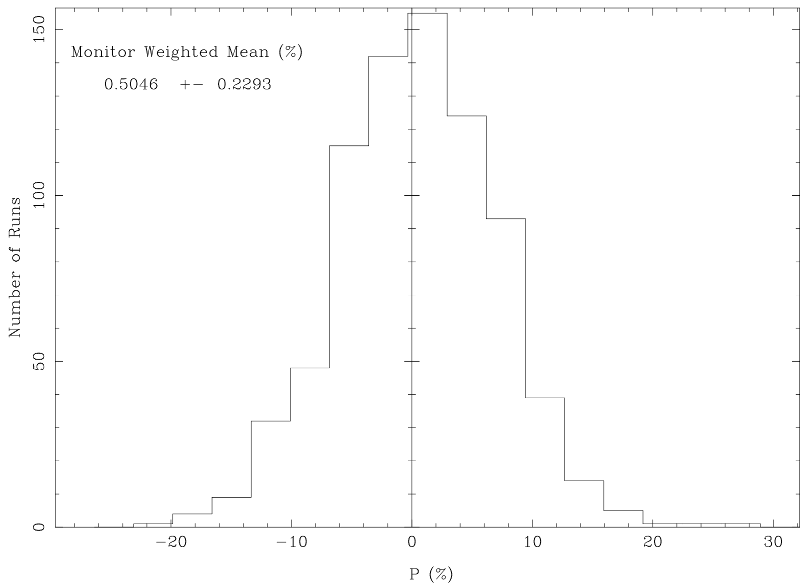

Figure C.27: $\mathcal{P}$ histogram of the 1206.2 eV resonance in ^{106}Pd.

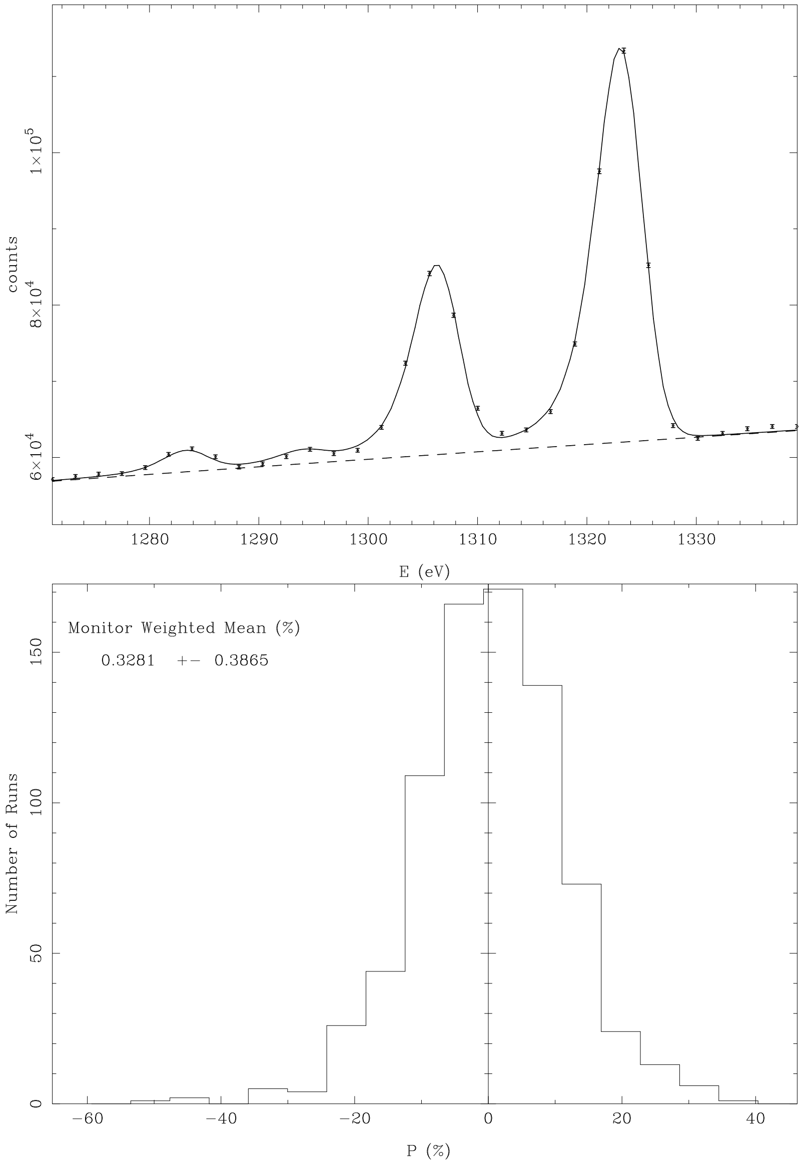

Figure C.28: Sample capture fit (top) of the the 1306 eV and 1323 eV resonances and $\mathcal{P}$ histogram (bottom) of the 1306 eV resonance in ^{106}Pd.

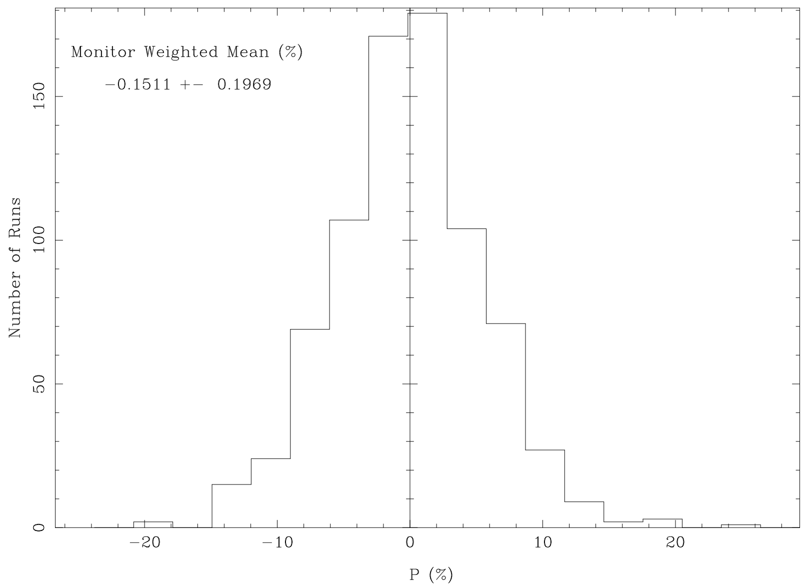

Figure C.29: $\mathcal{P}$ histogram of the 1323 eV resonance in ^{106}Pd.

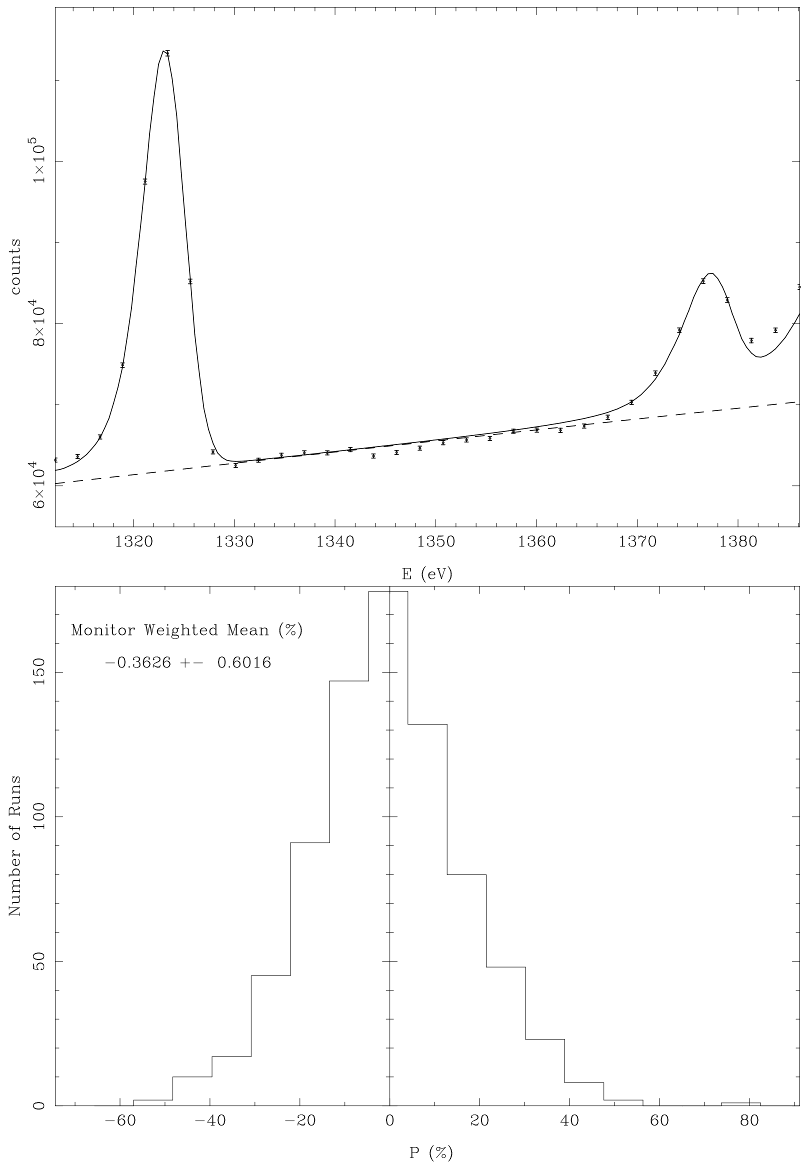

Figure C.30: Sample capture fit (top) of the 1323 eV and 1377 eV resonances and $\mathcal{P}$ histogram (bottom) of the 1377 eV resonance in ^{106}Pd.

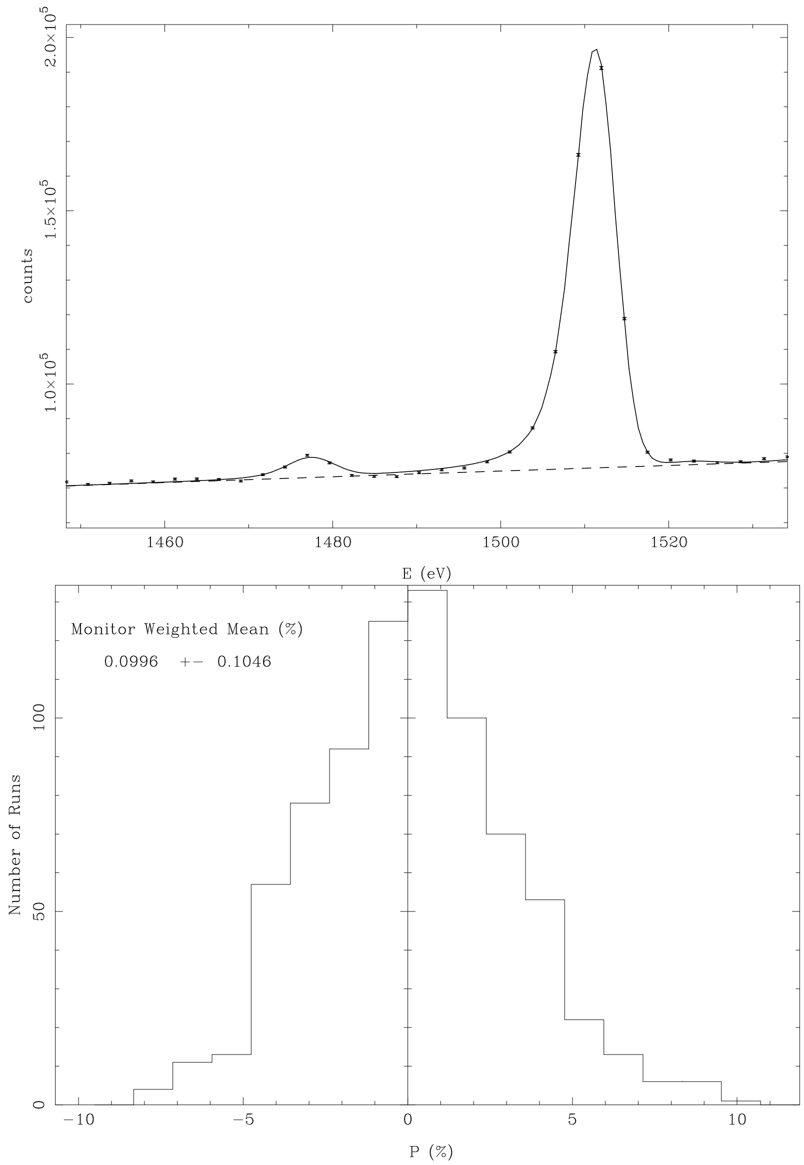

Figure C.31: Sample capture fit (top) and $\mathcal{P}$ histogram (bottom) of the 1511 eV resonance in ^{106}Pd.

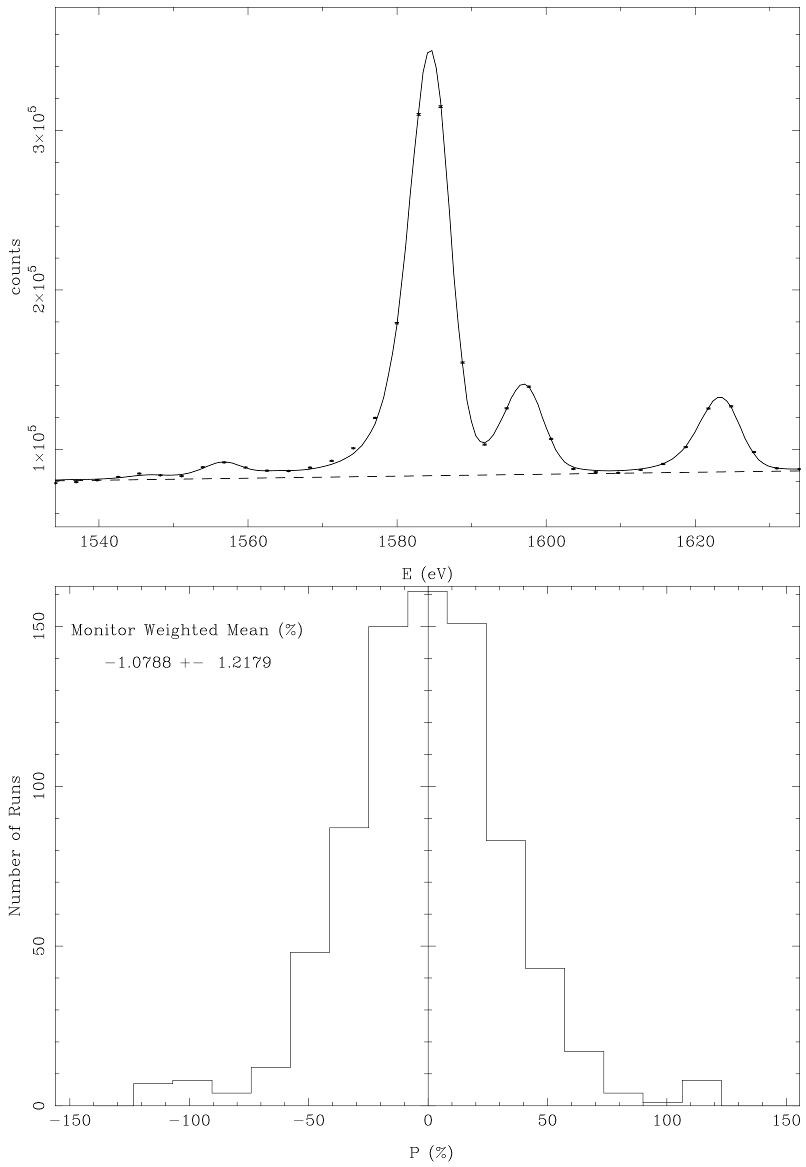

Figure C.32: Sample capture fit (top) of the 1557 eV, 1585 eV, 1597 eV and 1624 eV resonances and $\mathcal{P}$ histogram (bottom) of the 1557 eV resonance in ^{106}Pd.

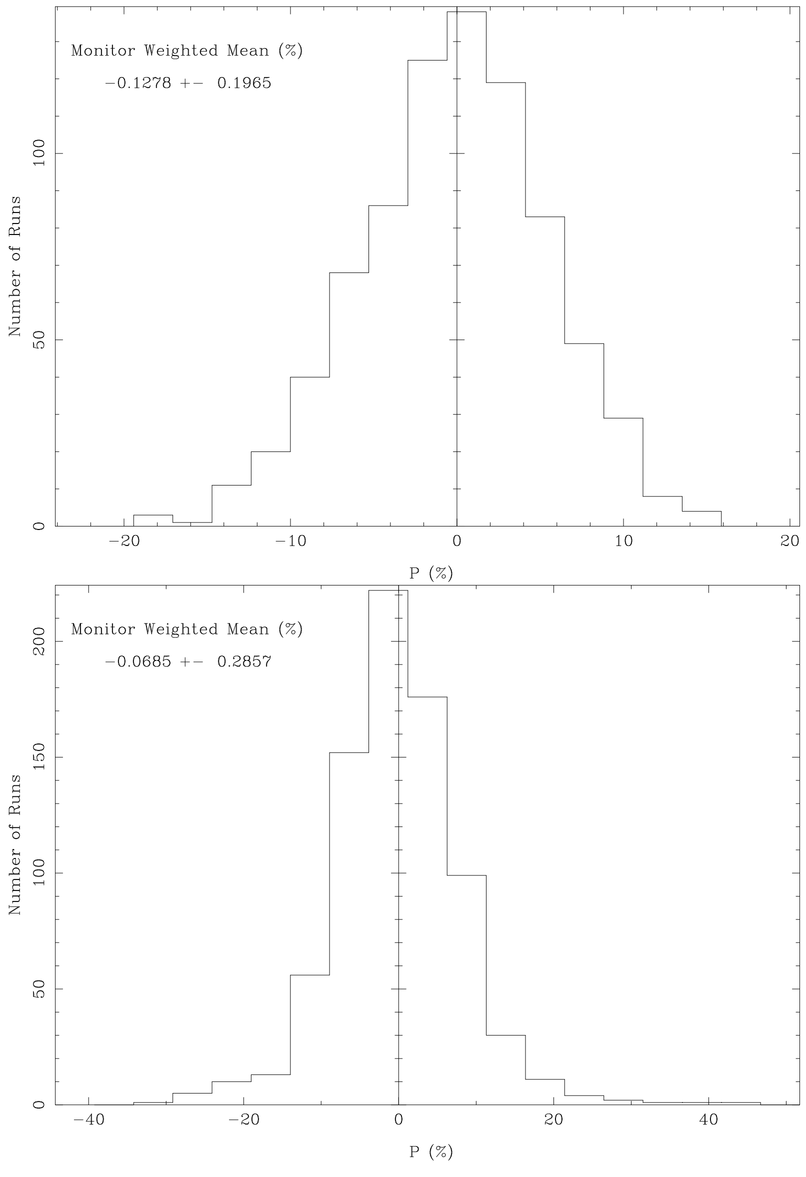

Figure C.33: $\mathcal{P}$ histograms of the 1597 eV (top) and the 1624 eV (bottom) resonances in ^{106}Pd.

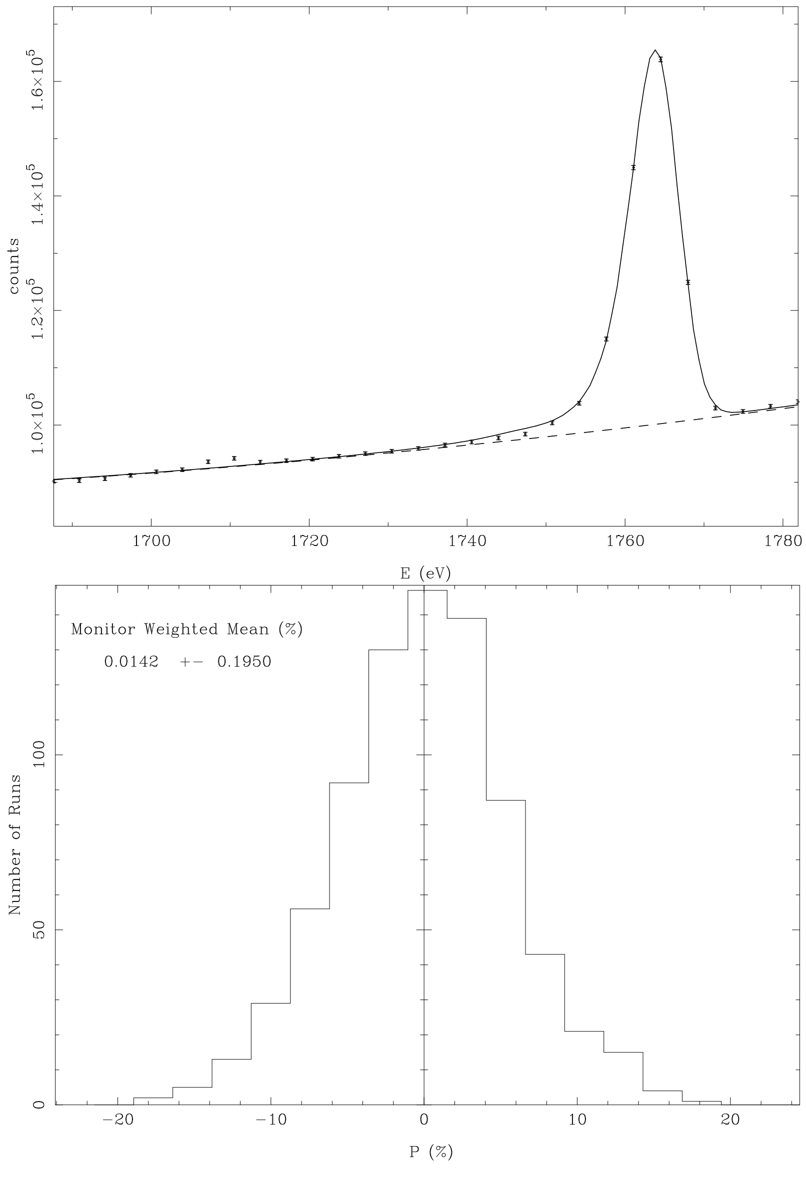

Figure C.34: Sample capture fit (top) and $\mathcal{P}$ histogram (bottom) of the 1764 eV resonance in ^{106}Pd.

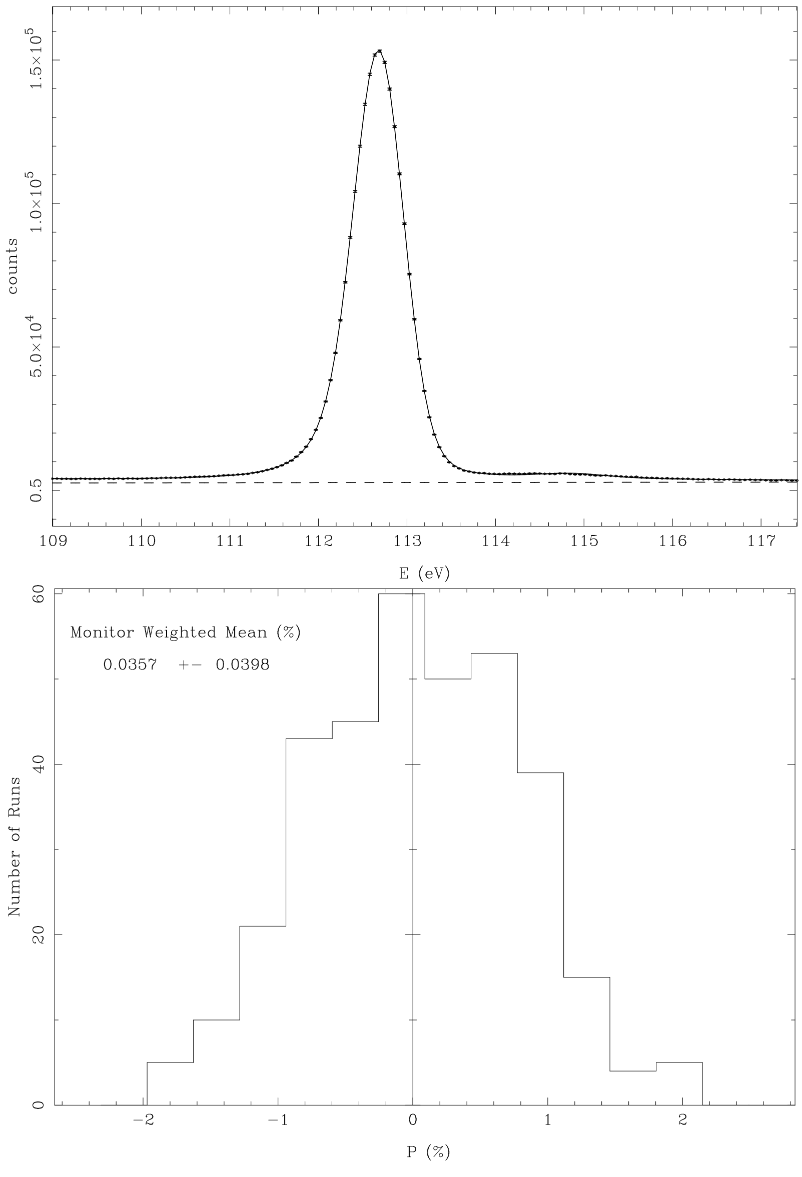

Figure C.35: Sample capture fit (top) and $\mathcal{P}$ histogram (bottom) of the 112.70 eV resonance in ^{108}Pd.

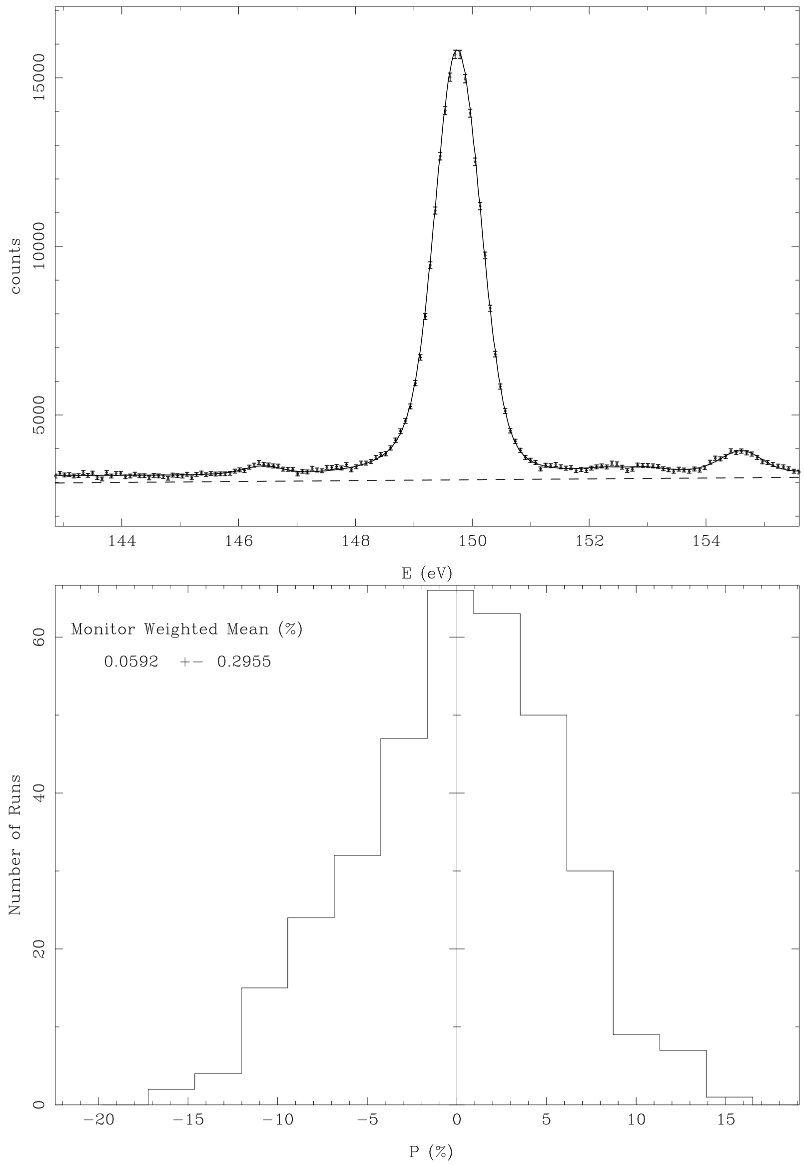

Figure C.36: Sample capture fit (top) and $\mathcal{P}$ histogram (bottom) of the 149.76 eV resonance in ^{108}Pd.

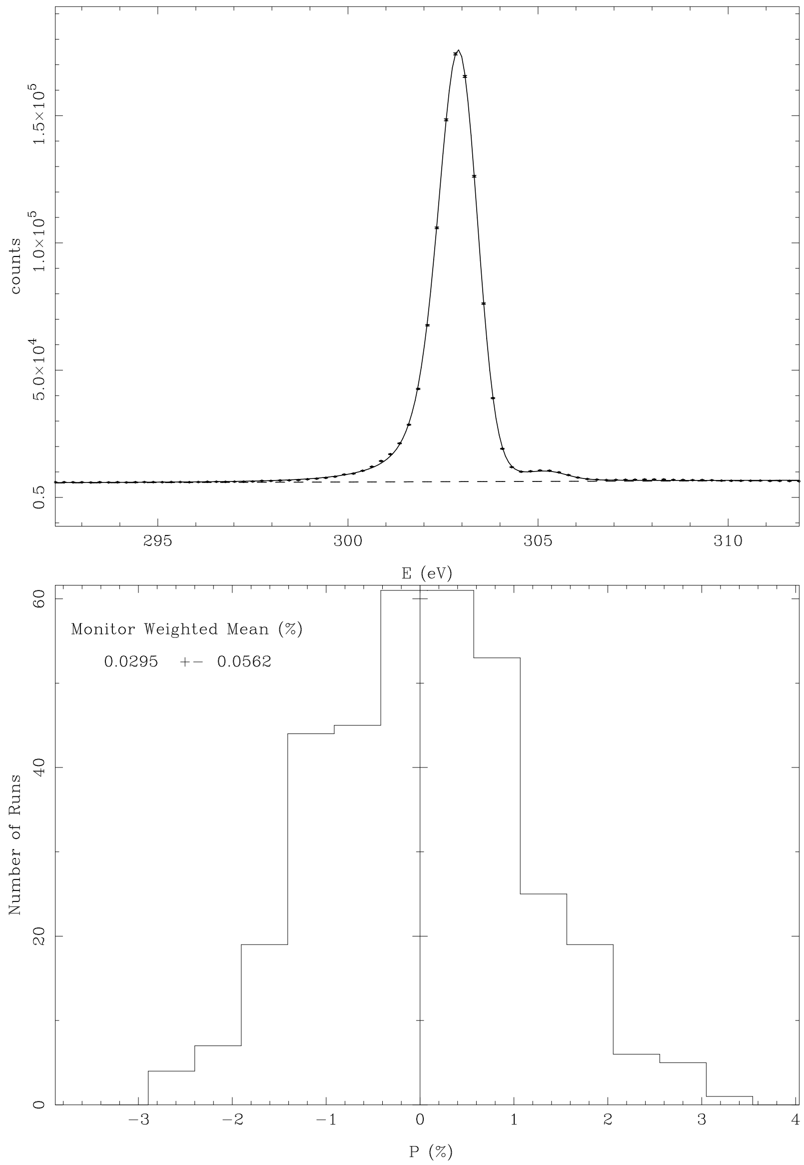

Figure C.37: Sample capture fit (top) and $\mathcal{P}$ histogram (bottom) of the 302.9 eV resonance in ^{108}Pd.

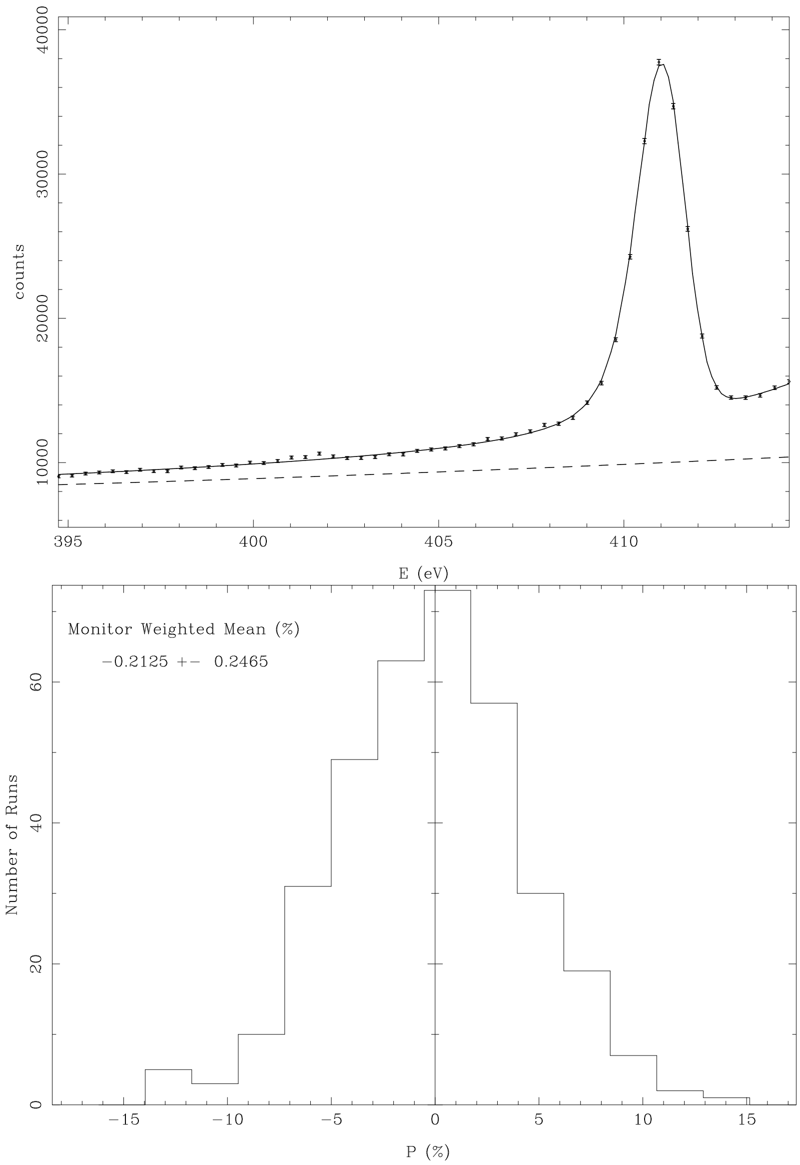

Figure C.38: Sample capture fit (top) and $\mathcal{P}$ histogram (bottom) of the 411.0 eV resonance in ^{108}Pd.

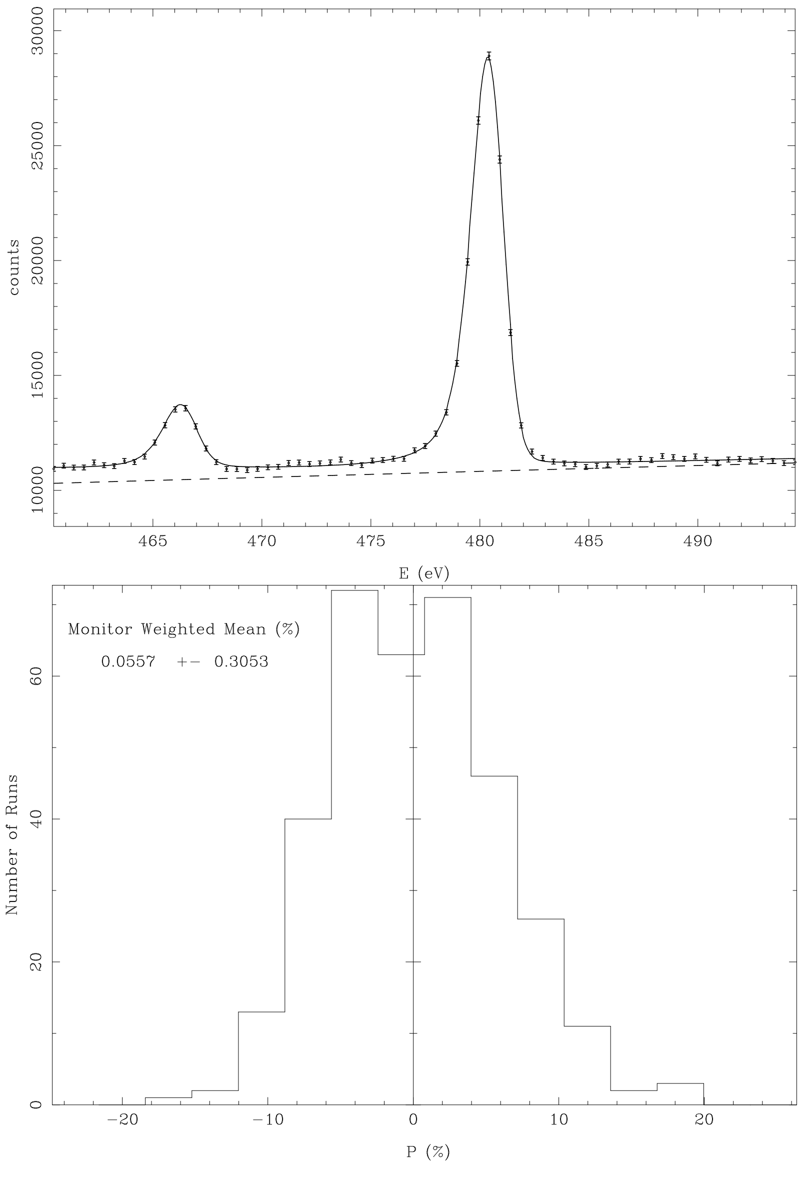

Figure C.39: Sample capture fit (top) and $\mathcal{P}$ histogram (bottom) of the 480.5 eV resonance in ^{108}Pd.

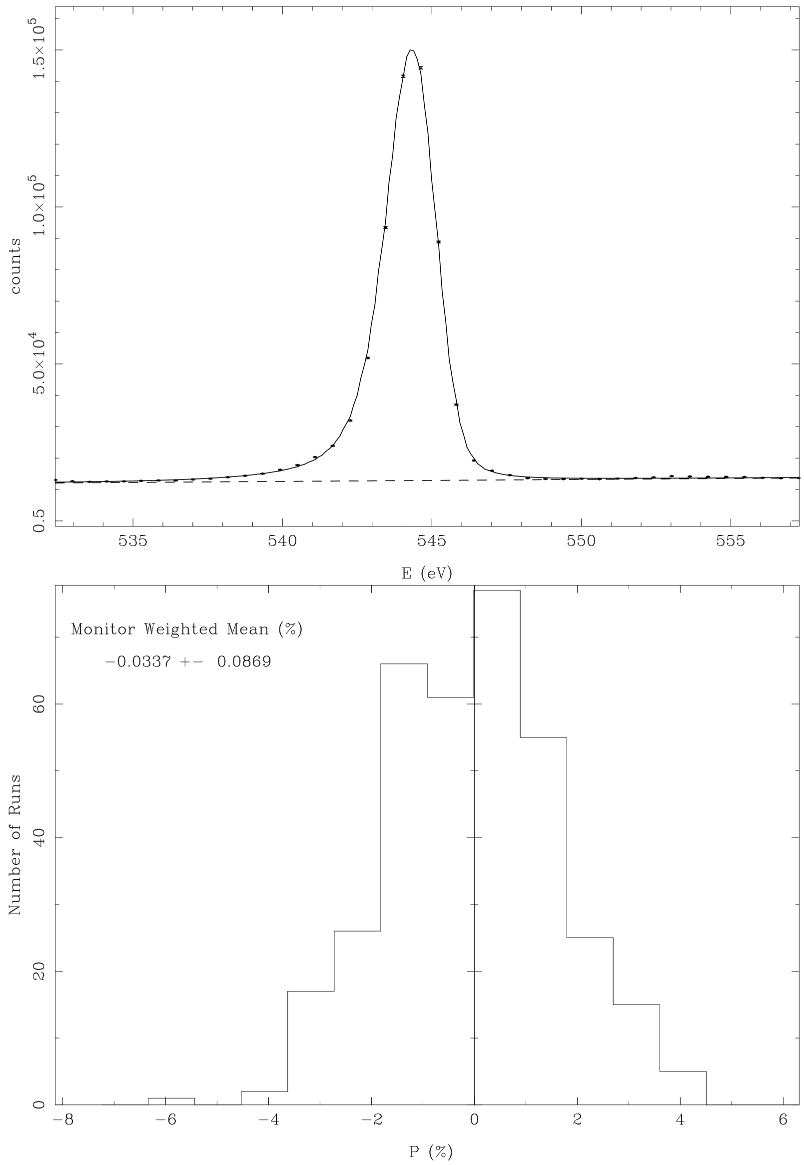

Figure C.40: Sample capture fit (top) and $\mathcal{P}$ histogram (bottom) of the 544.4 eV resonance in ^{108}Pd.

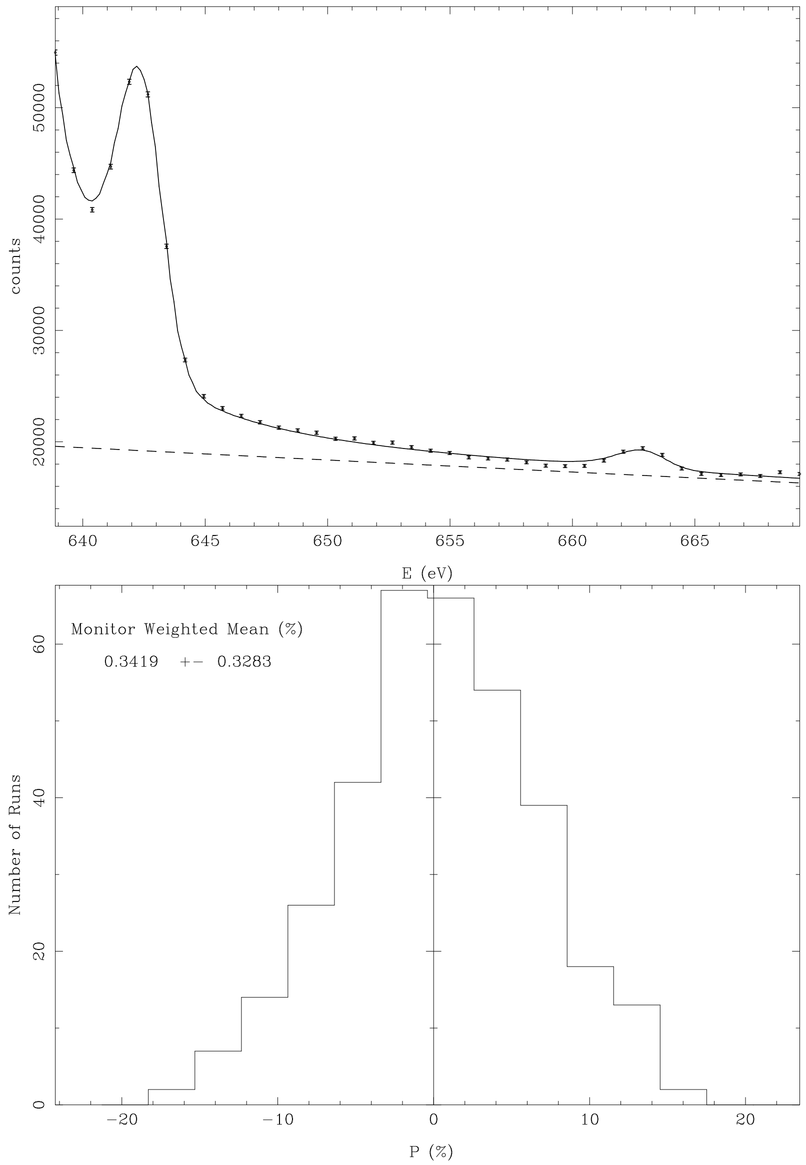

Figure C.41: Sample capture fit (top) and $\mathcal{P}$ histogram (bottom) of the 642.2 eV resonance in ^{108}Pd.

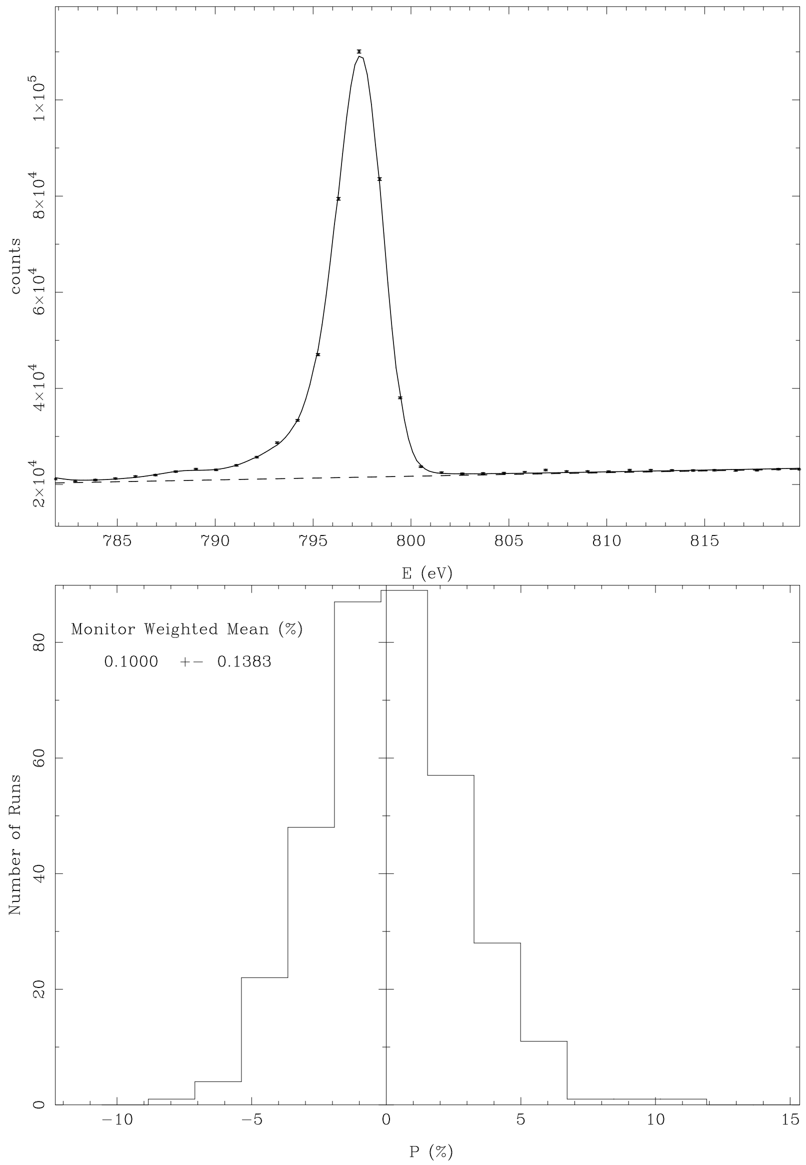

Figure C.42: Sample capture fit (top) and $\mathcal{P}$ histogram (bottom) of the 797.4 eV resonance in ^{108}Pd.

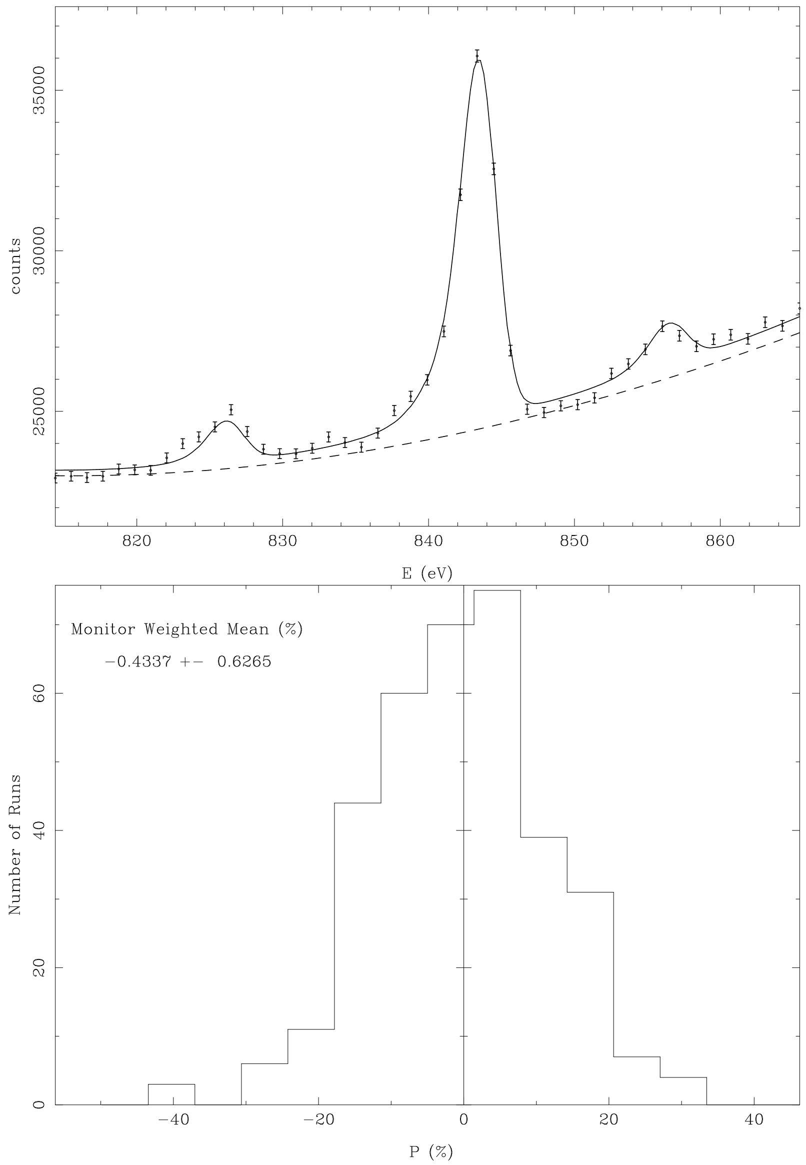

Figure C.43: Sample capture fit (top) and $\mathcal{P}$ histogram (bottom) of the 843.4 eV resonance in ^{108}Pd.

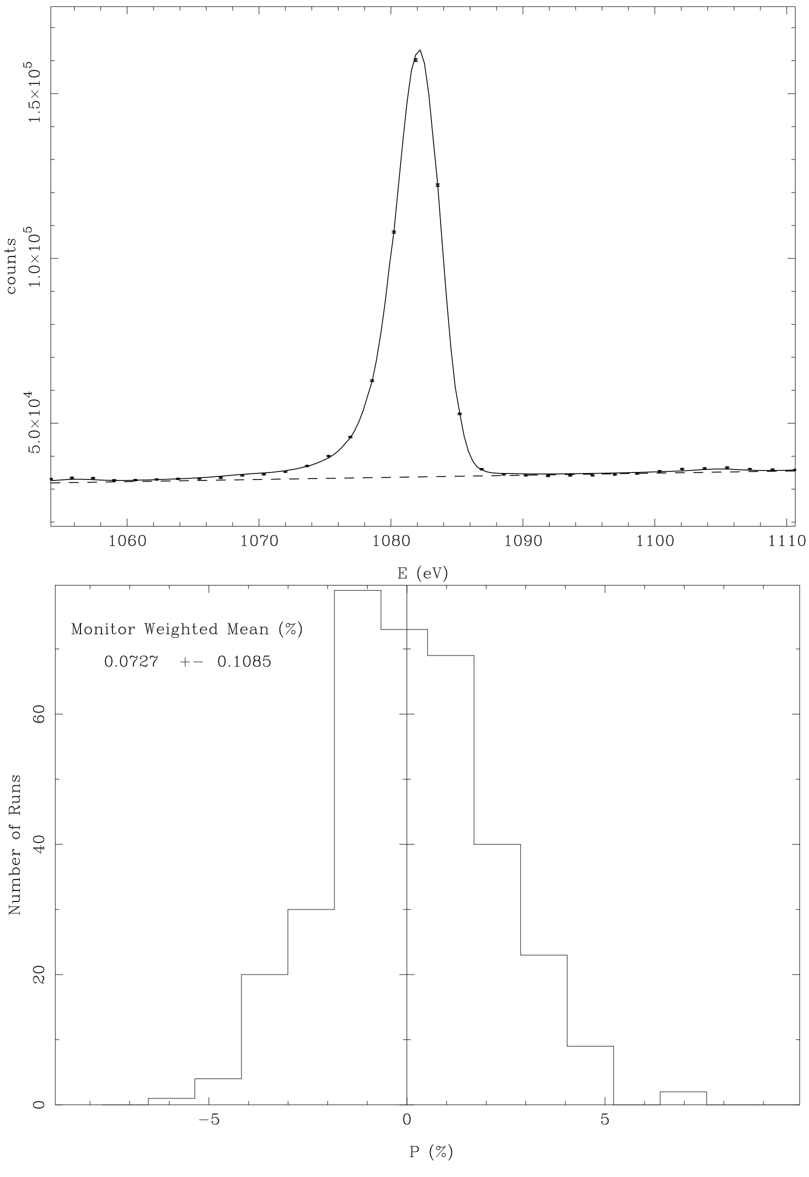

Figure C.44: Sample capture fit (top) and $\mathcal{P}$ histogram (bottom) of the 1082.3 eV resonance in ^{108}Pd.

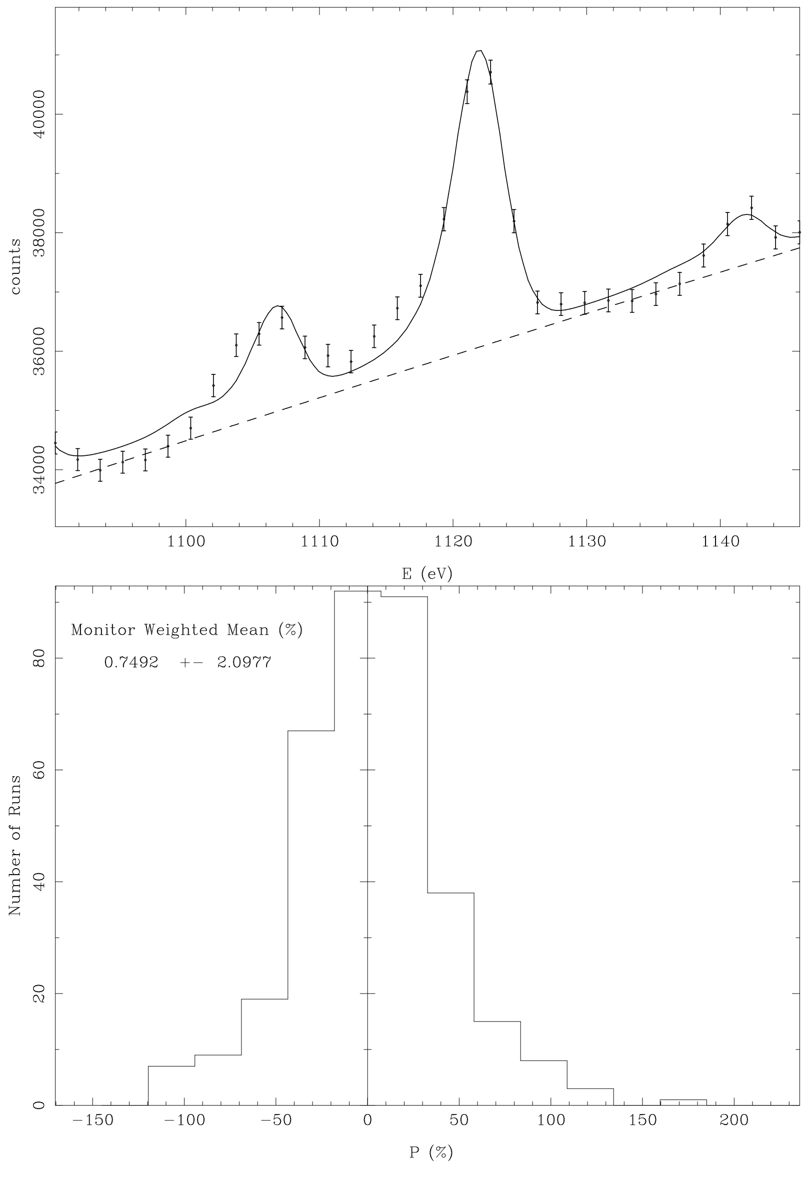

Figure C.45: Sample capture fit (top) of the 1121 eV and 1140 eV resonances and $\mathcal{P}$ histogram (bottom) of the 1121 eV resonance in ^{108}Pd.

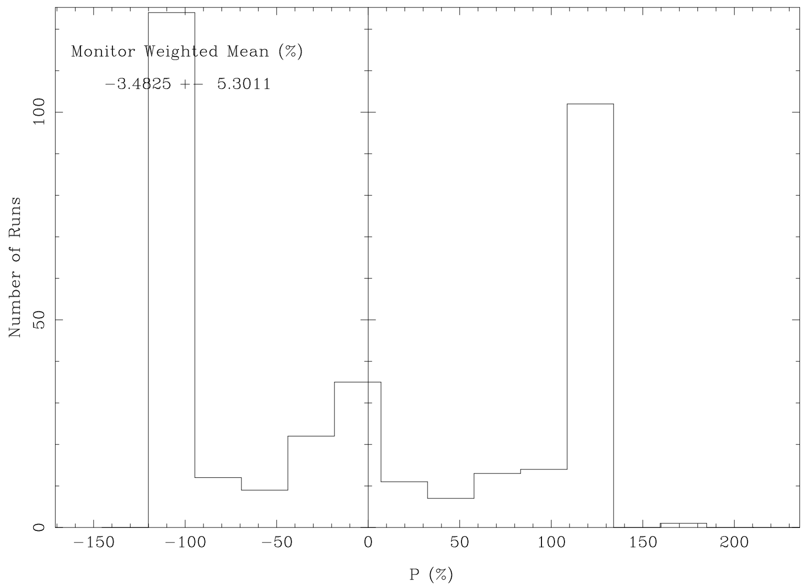

Figure C.46: $\mathcal{P}$ histogram of the 1140 eV resonance in ^{108}Pd.

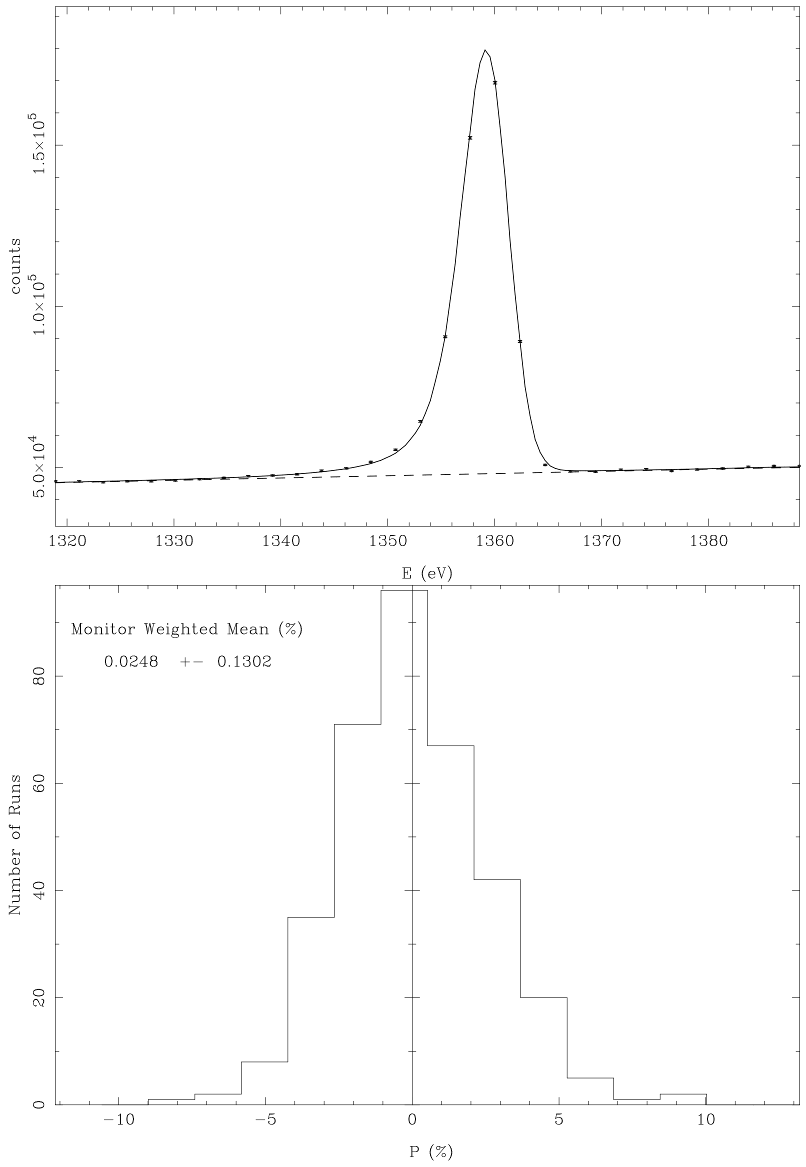

Figure C.47: Sample capture fit (top) and $\mathcal{P}$ histogram (bottom) of the 1359 eV resonance in ^{108}Pd.

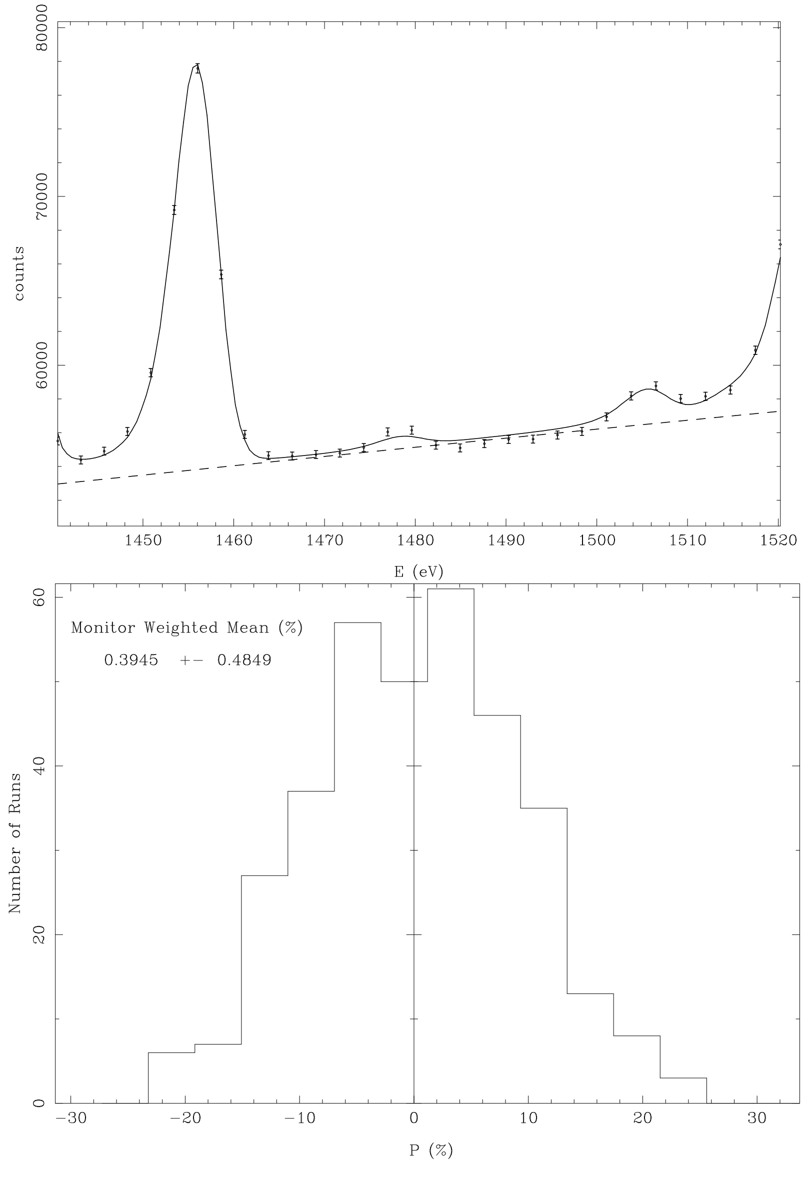

Figure C.48: Sample capture fit (top) of the 1456 eV and 1505 eV resonances and $\mathcal{P}$ histogram (bottom) of the 1456 eV resonance in ^{108}Pd.

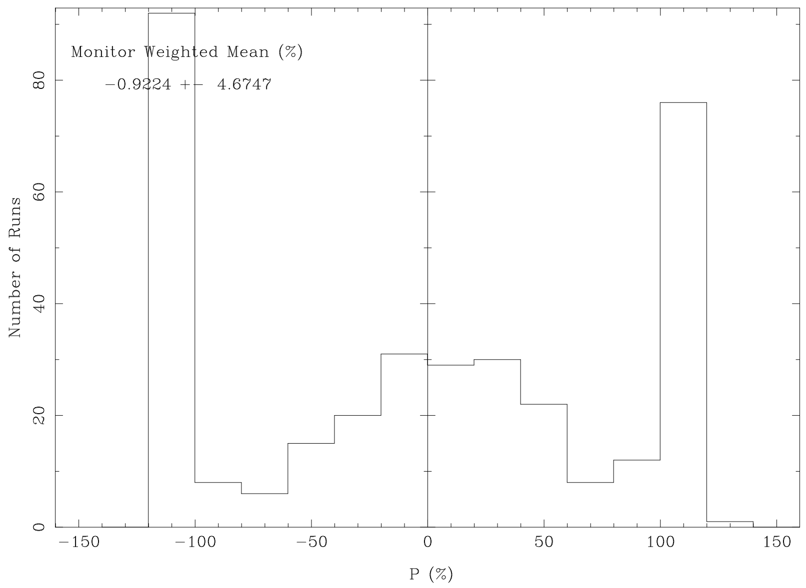

Figure C.49: $\mathcal{P}$ histogram of the 1505 eV resonance in ^{108}Pd.

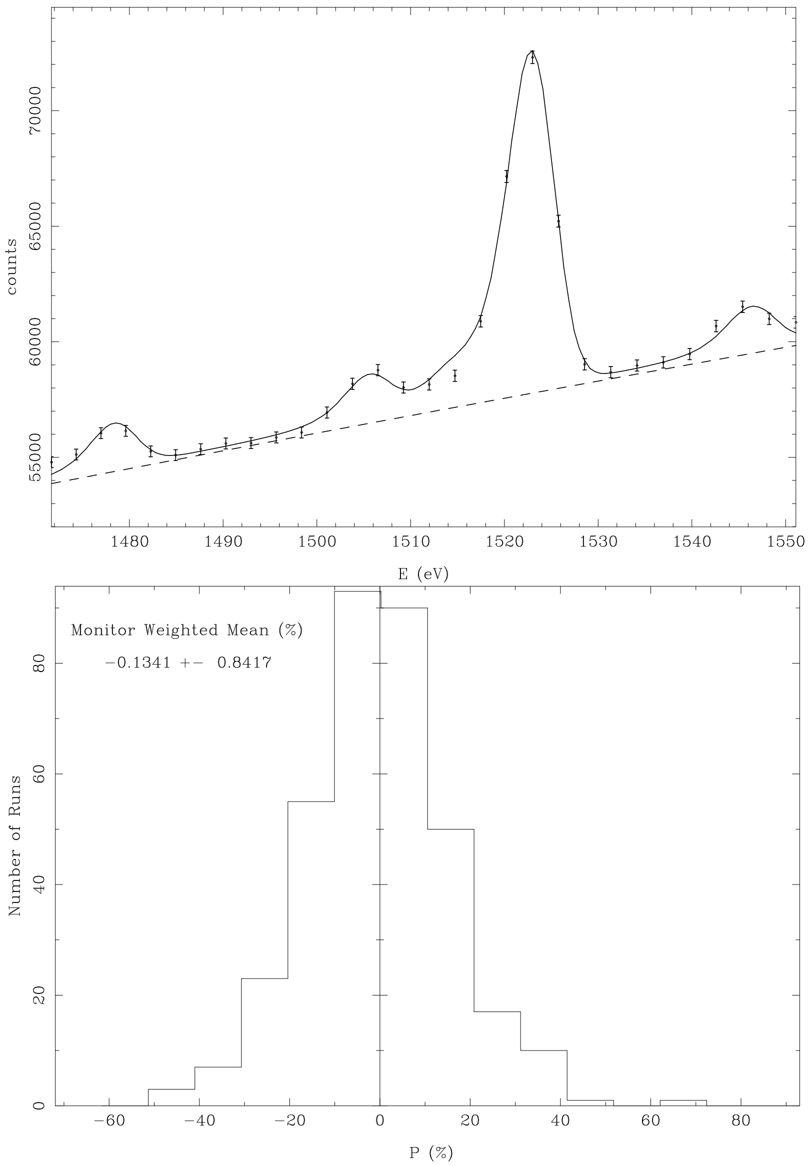

Figure C.50: Sample capture fit (top) of the 1505 eV and 1523 eV resonances and $\mathcal{P}$ histogram (bottom) of the 1523 eV resonance in ^{108}Pd.

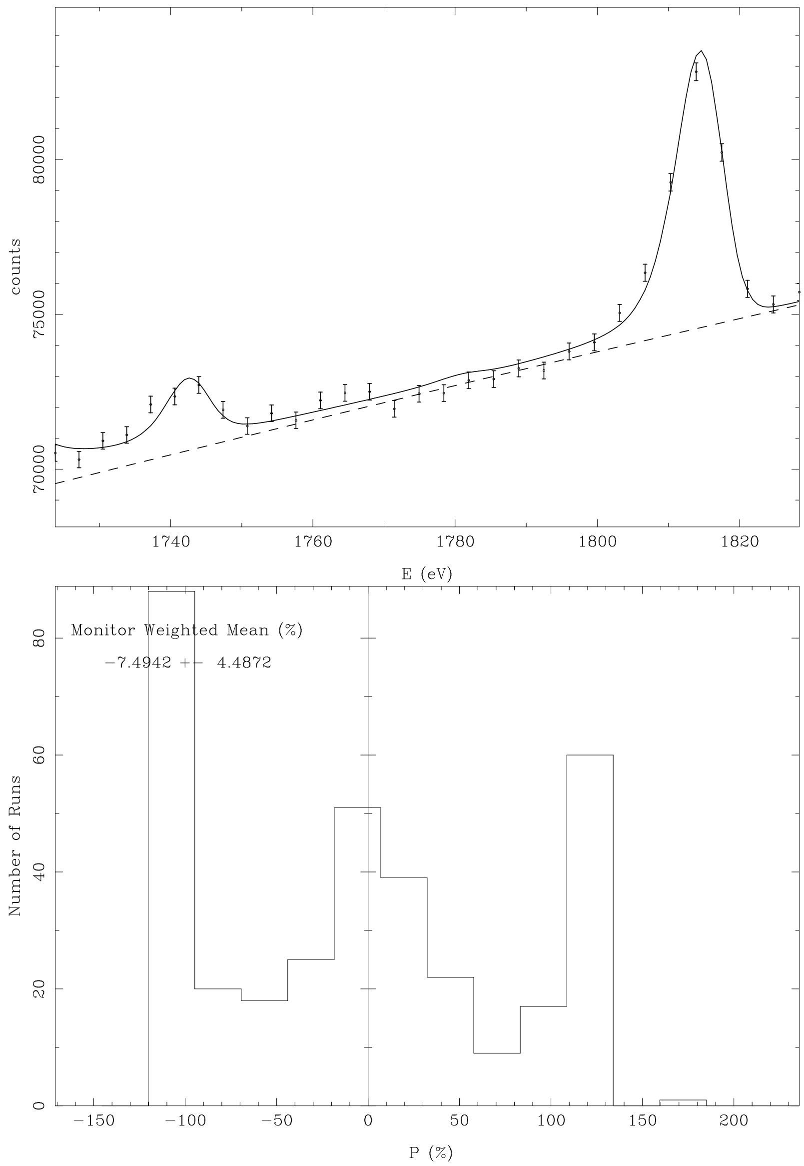

Figure C.51: Sample capture fit (top) of the 1743 eV and 1815 eV resonances and $\mathcal{P}$ histogram (bottom) of the 1743 eV resonance in ^{108}Pd.

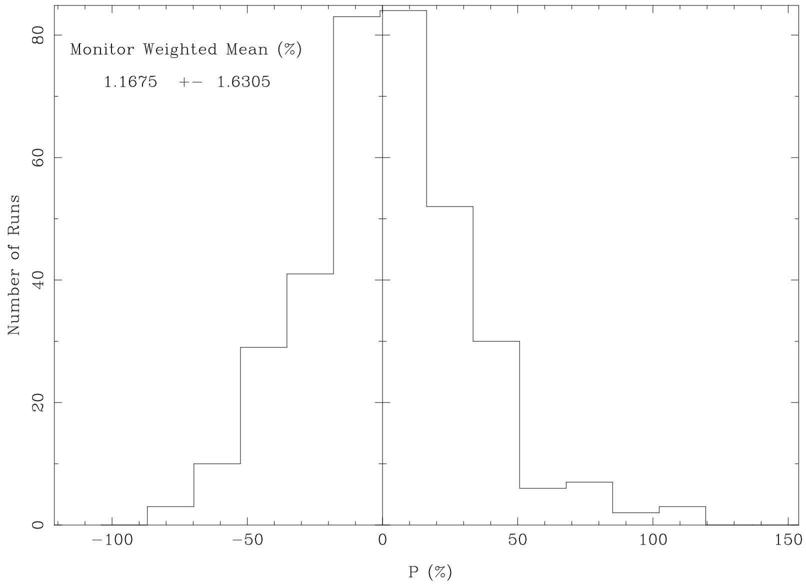

Figure C.52: $\mathcal{P}$ histogram (bottom) of the 1815 eV resonance in ^{108}Pd.

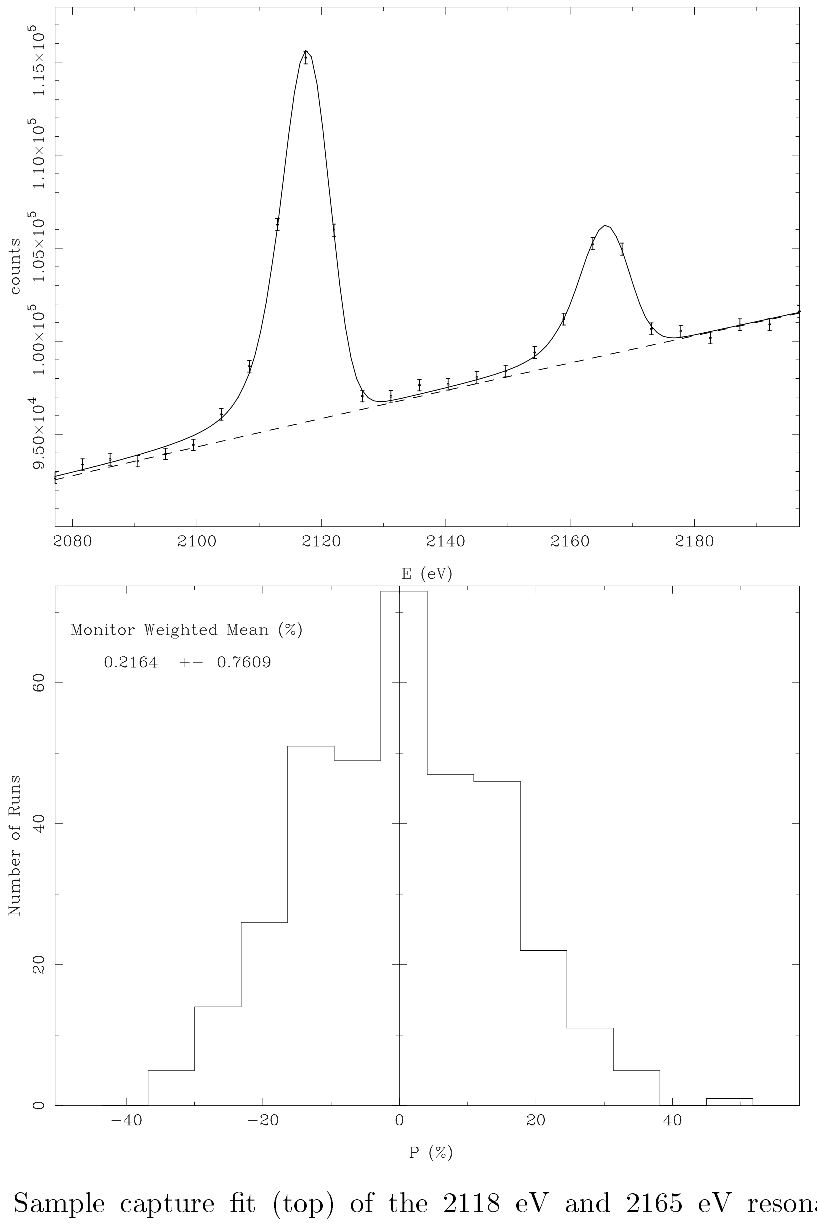

Figure C.53: Sample capture fit (top) of the 2118 eV and 2165 eV resonances and $\mathcal{P}$ histogram (bottom) of the 2118 eV resonance in ^{108}Pd.

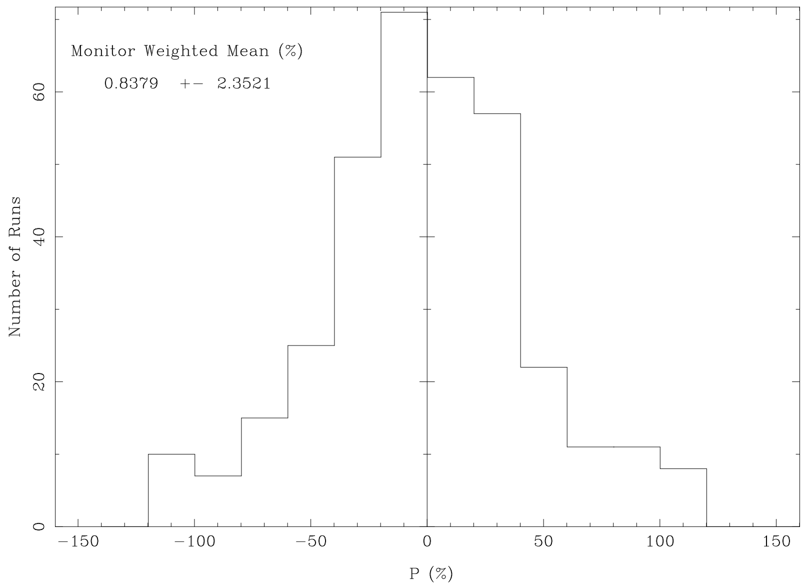

Figure C.54: $\mathcal{P}$ histogram (bottom) of the 2165 eV resonance in ^{108}Pd.

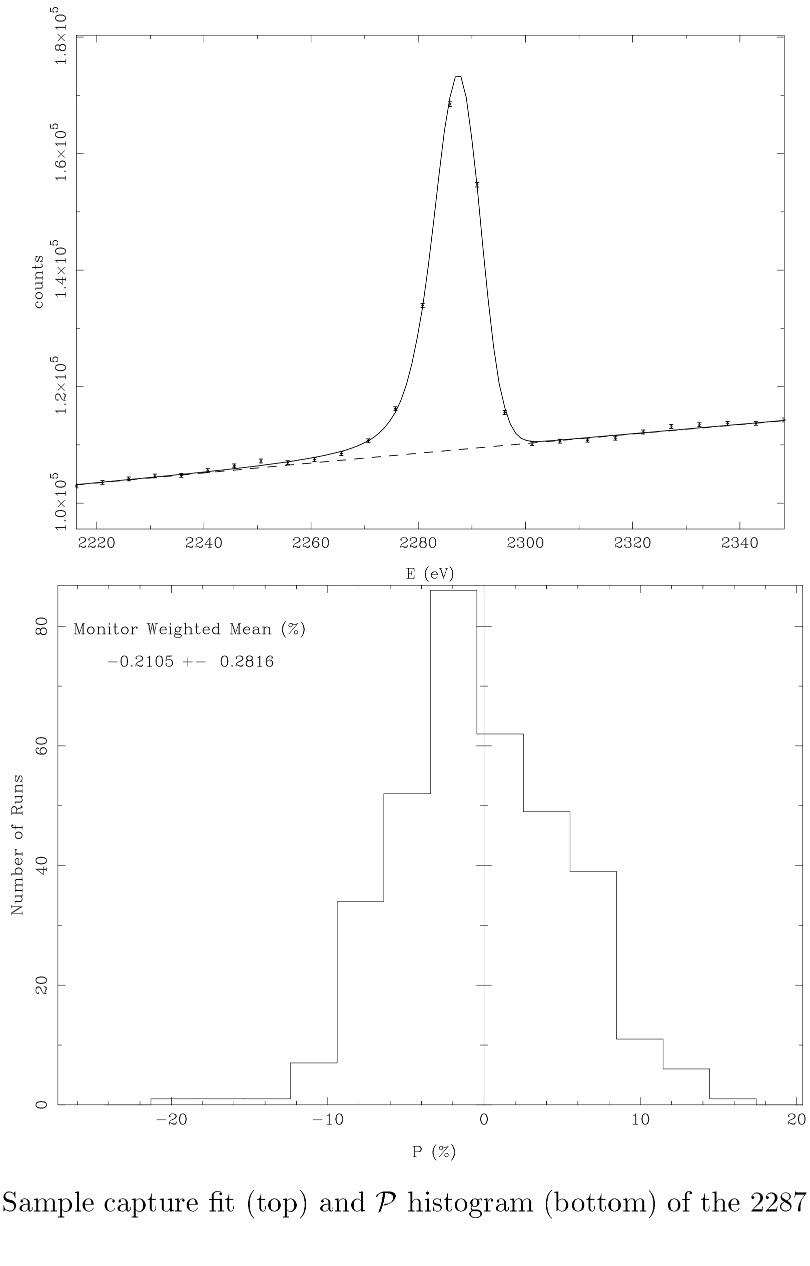

Figure C.55: Sample capture fit (top) and $\mathcal{P}$ histogram (bottom) of the 2287 eV resonance in ^{108}Pd.

C.3 Sample Fits and $\mathcal{P}$ Histograms for ^{238}U

The first five plots show large energy regions containing two to three large s-waves. The remaining plots show isolated p-waves and the $\mathcal{P}$ histograms for the run-by-run analysis. All of the sample fits are from a sum of 10 runs with the boron filter.

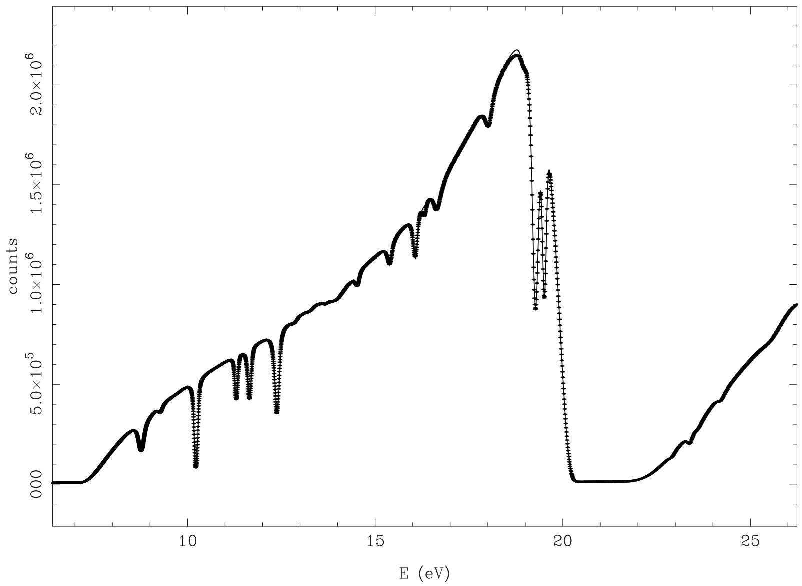

Figure C.56: Sample fit for the 6.672 eV and 20.855 eV s-wave resonances in ^{238}U.

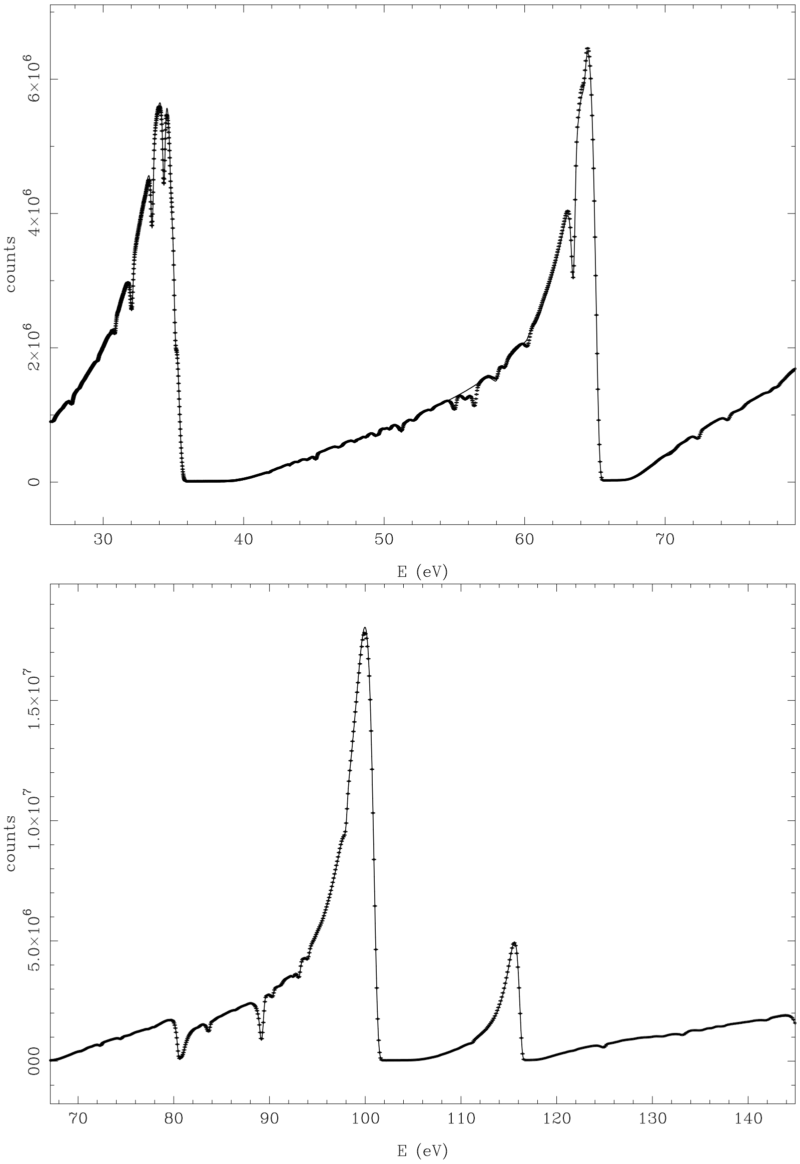

Figure C.57: Sample fit for the 36.670 eV, 65.992 eV (top), 80.732 eV, 102.53 eV and 116.85 eV (bottom) s-wave resonances in ^{238}U.

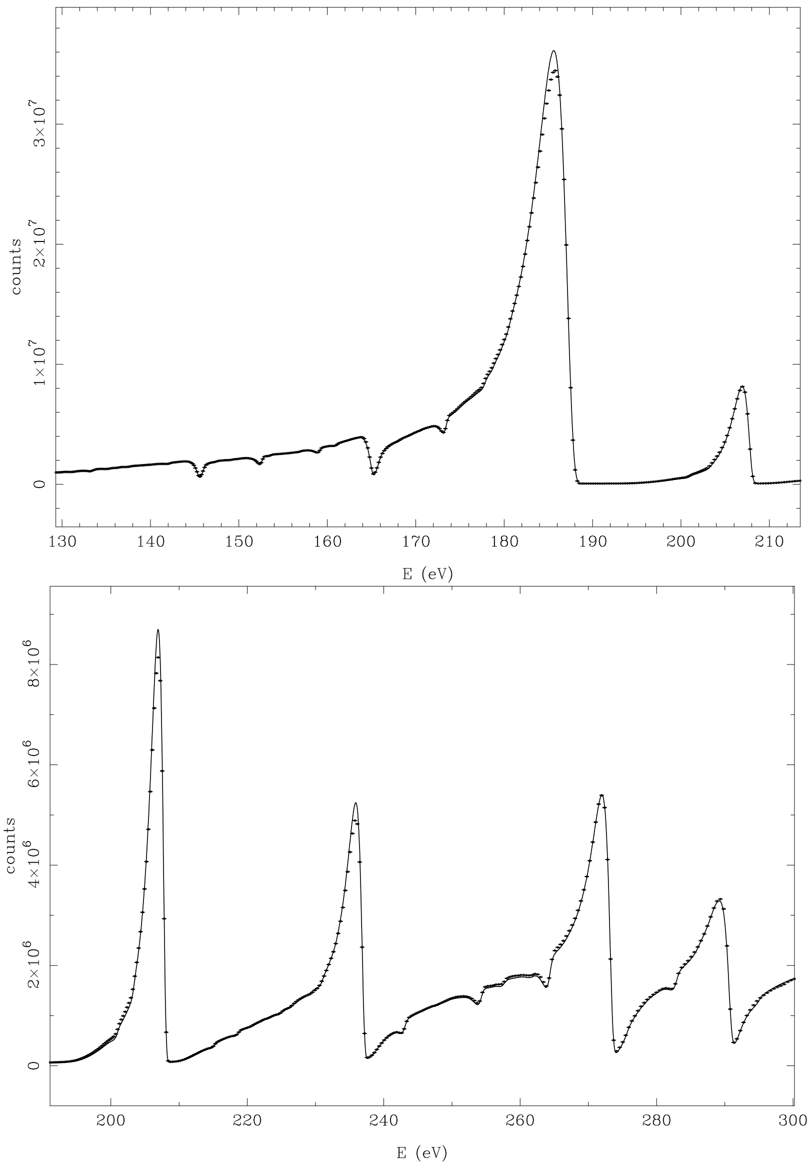

Figure C.58: Sample fit for the 145.64 eV, 165.29 eV, 189.73 eV (top), 208.46 eV, 237.31 eV, 273.63 eV and 290.97 eV (bottom) s-wave resonances in ^{238}U.

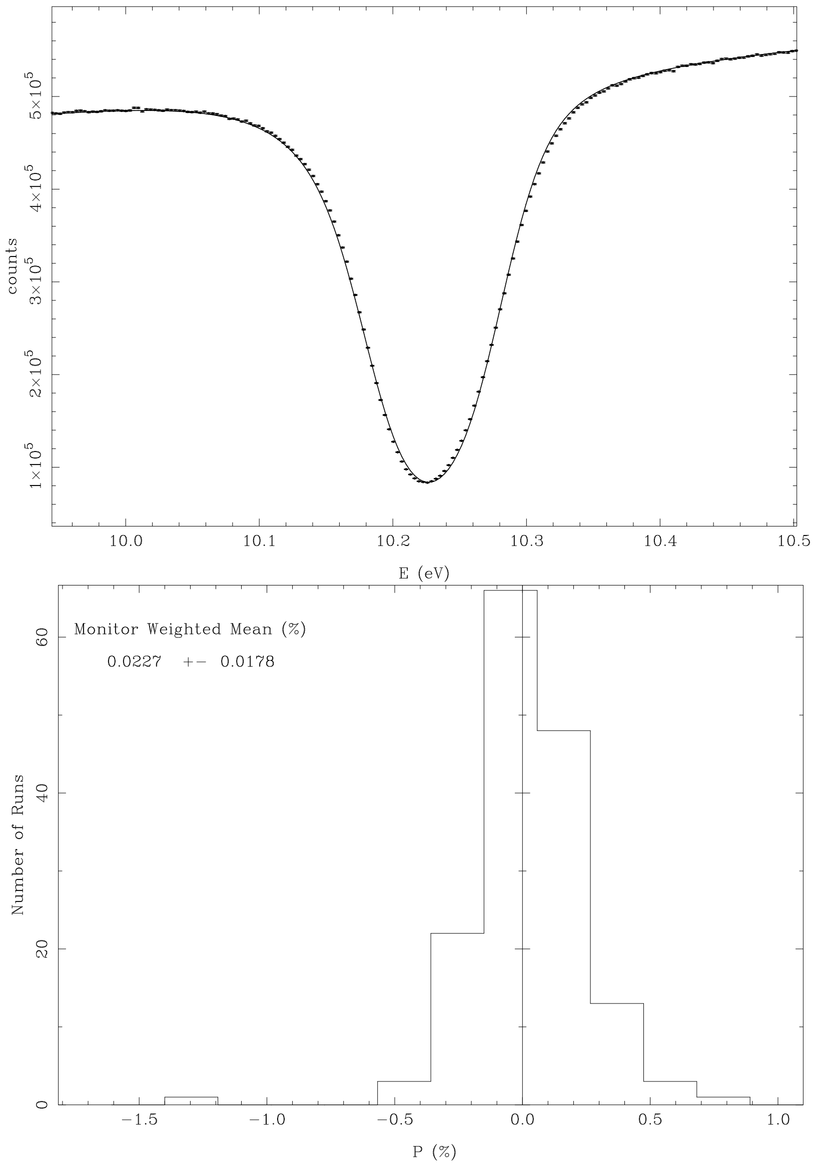

Figure C.59: Sample fit (top) and $\mathcal{P}$ histogram (bottom) for the 10.234 eV resonance in ^{238}U.

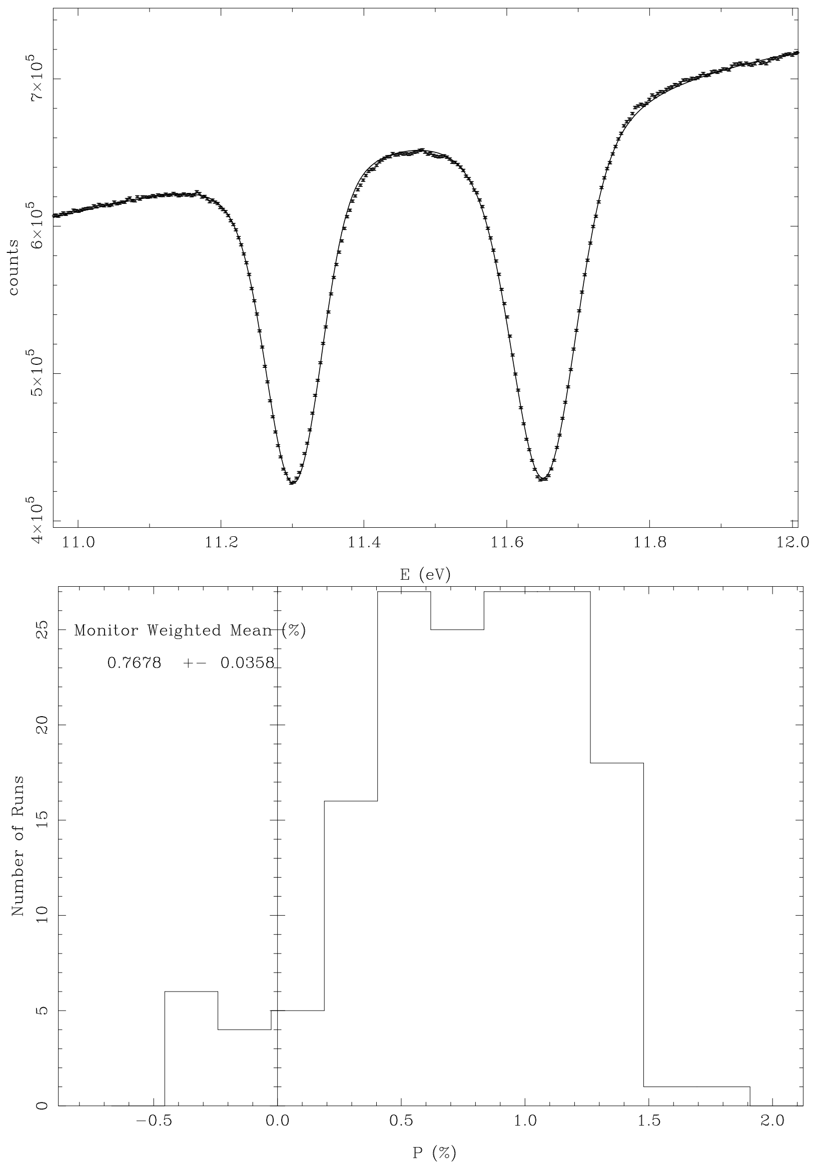

Figure C.60: Sample fit (top) and $\mathcal{P}$ histogram (bottom) for the 11.308 eV resonance in ^{238}U.

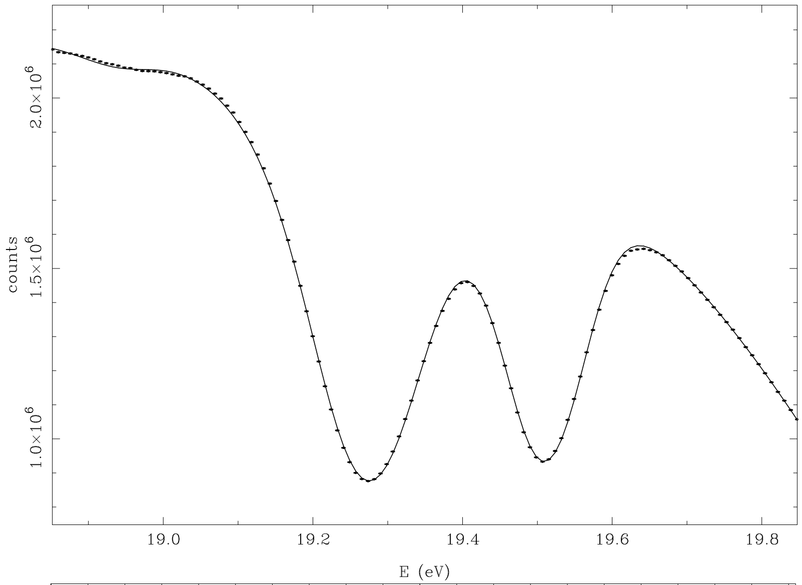

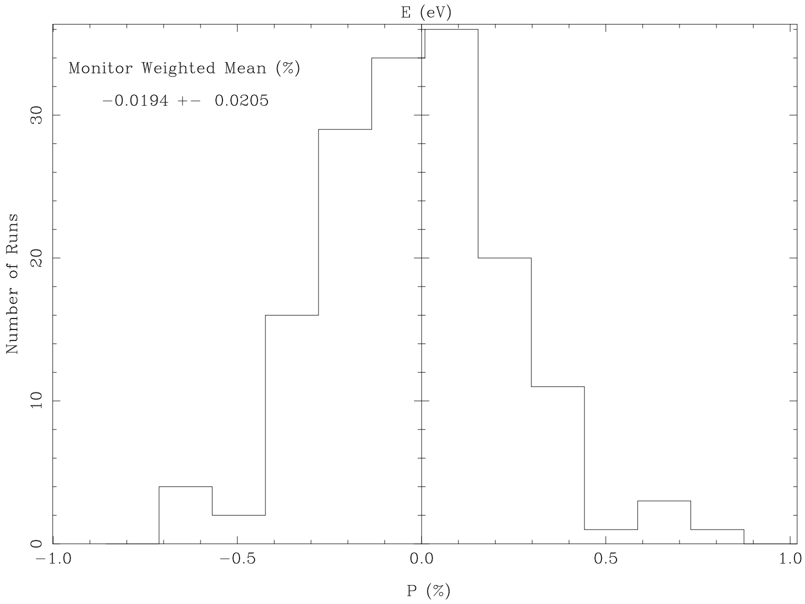

Figure C.61: Sample fit (top) and $\mathcal{P}$ histogram (bottom) for the 19.520 eV resonance in ^{238}U.

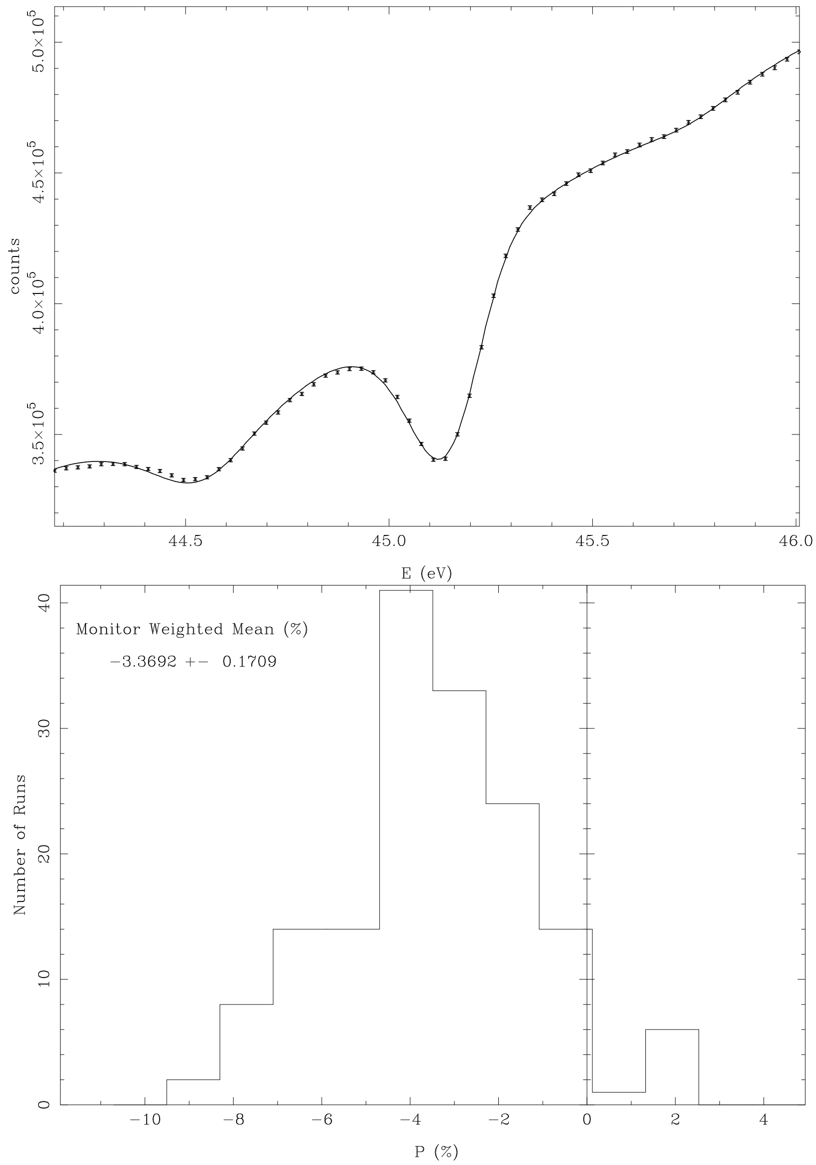

Figure C.62: Sample fit (top) and $\mathcal{P}$ histogram (bottom) for the 45.157 eV resonance in ^{238}U.

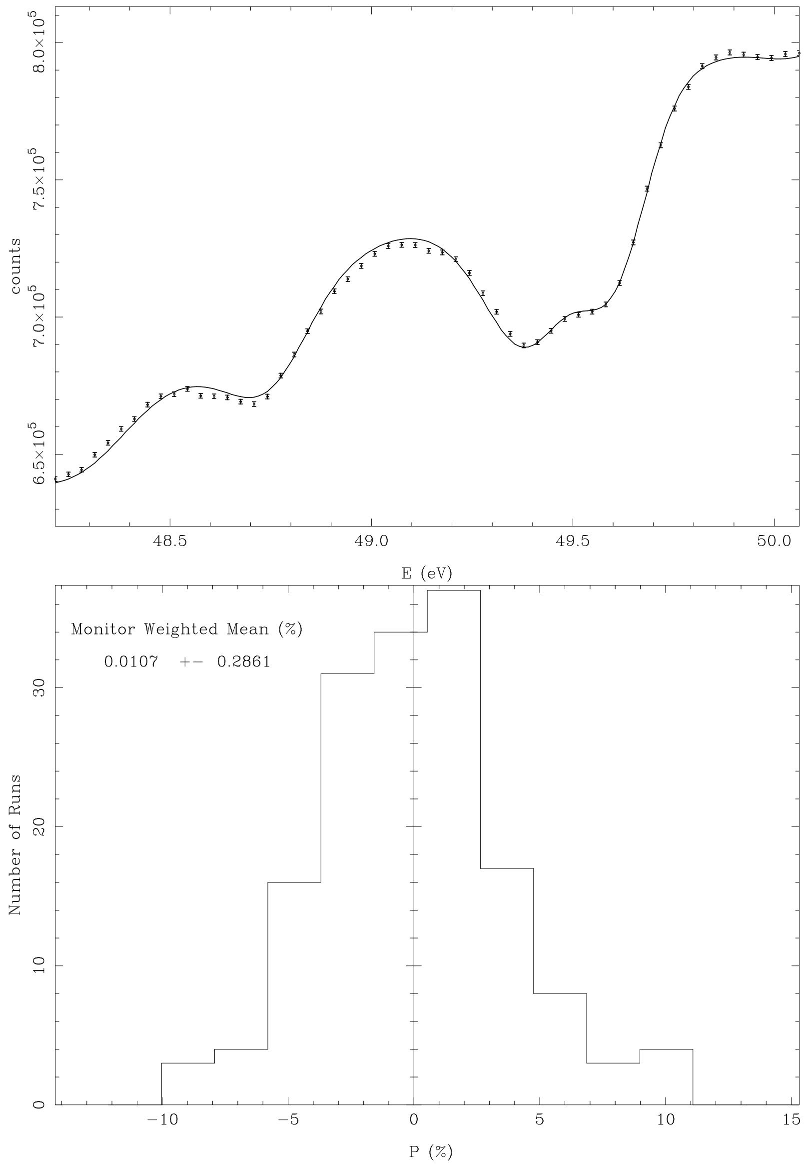

Figure C.63: Sample fit (top) and $\mathcal{P}$ histogram (bottom) for the 49.611 eV resonance in ^{238}U.

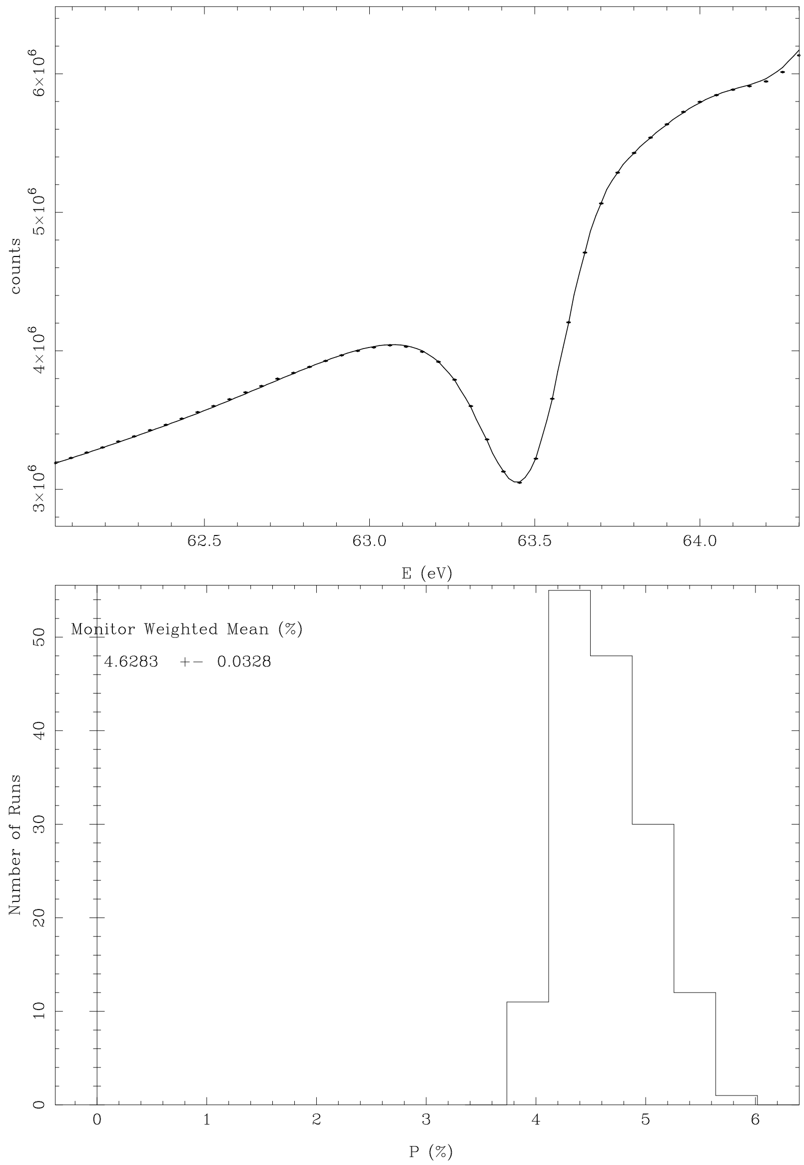

Figure C.64: Sample fit (top) and $\mathcal{P}$ histogram (bottom) for the 63.494 eV resonance in ^{238}U.

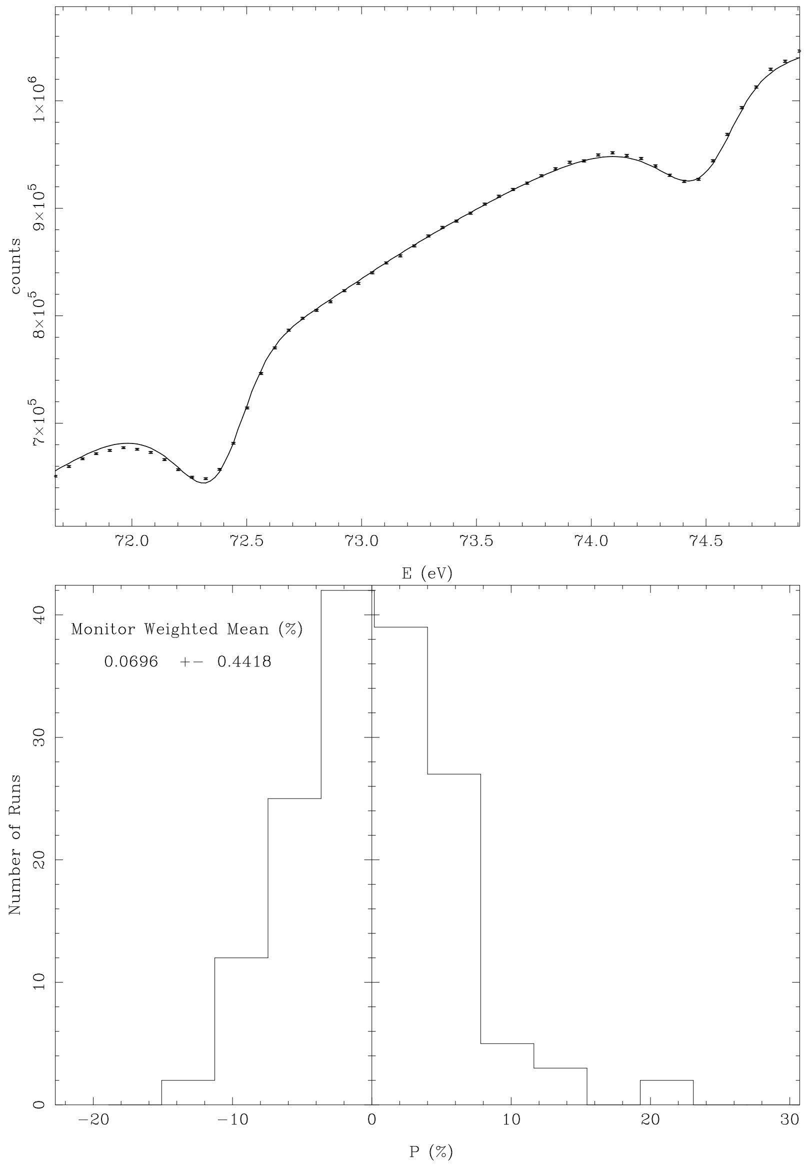

Figure C.65: Sample fit (top) and $\mathcal{P}$ histogram (bottom) for the 72.372 eV resonance in ^{238}U.

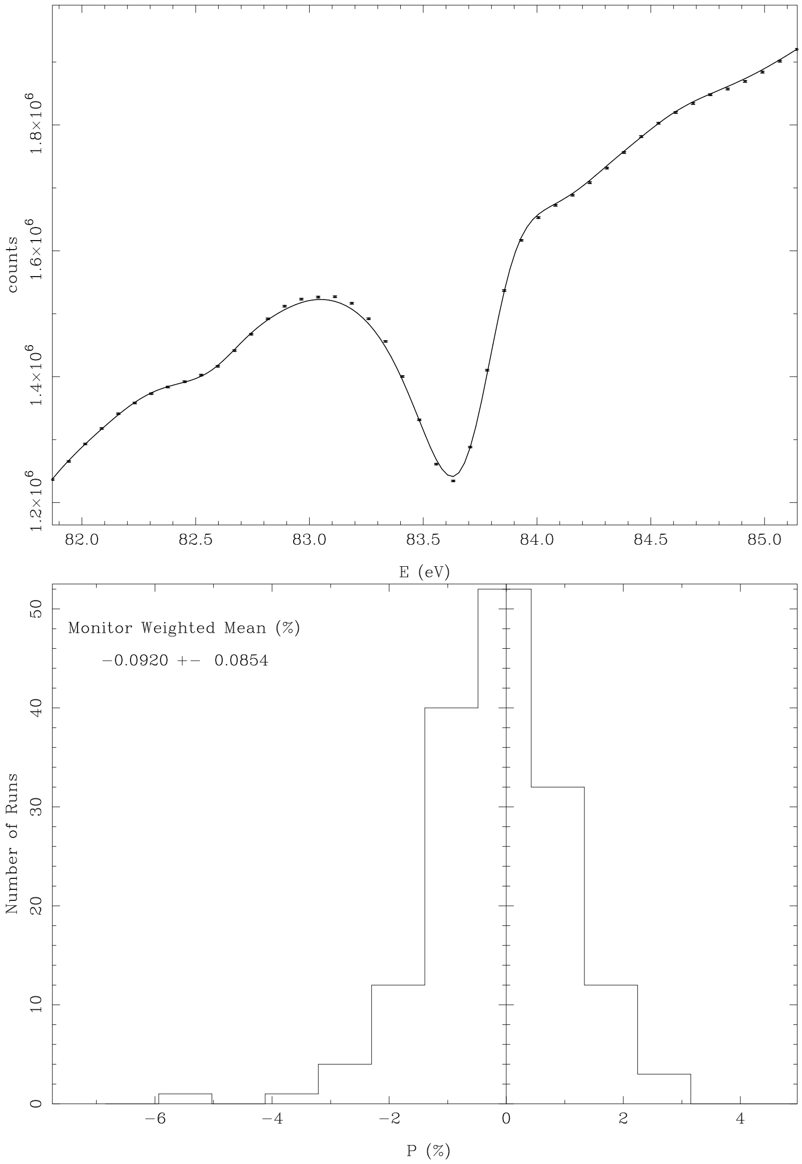

Figure C.66: Sample fit (top) and $\mathcal{P}$ histogram (bottom) for the 83.677 eV resonance in ^{238}U.

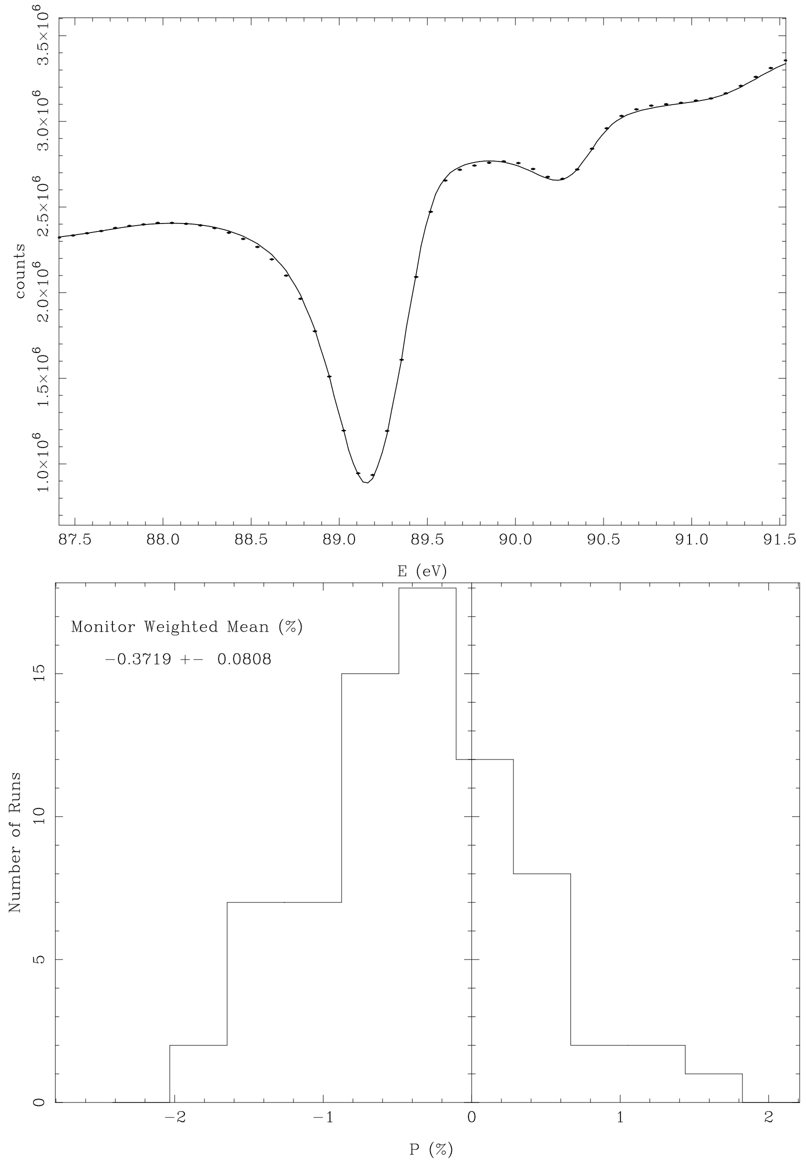

Figure C.67: Sample fit (top) and $\mathcal{P}$ histogram (bottom) for the 89.216 eV resonance in ^{238}U with the Boron filter only.

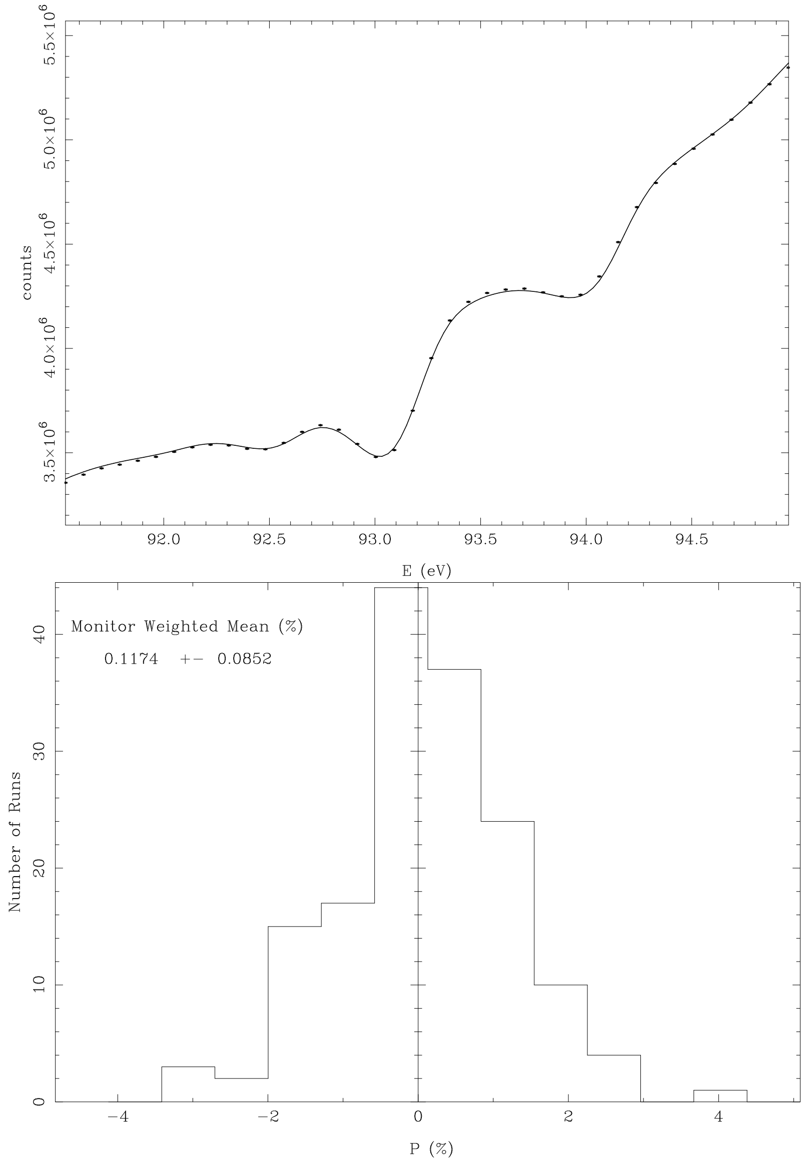

Figure C.68: Sample fit (top) and $\mathcal{P}$ histogram (bottom) for the 93.081 eV resonance in ^{238}U.

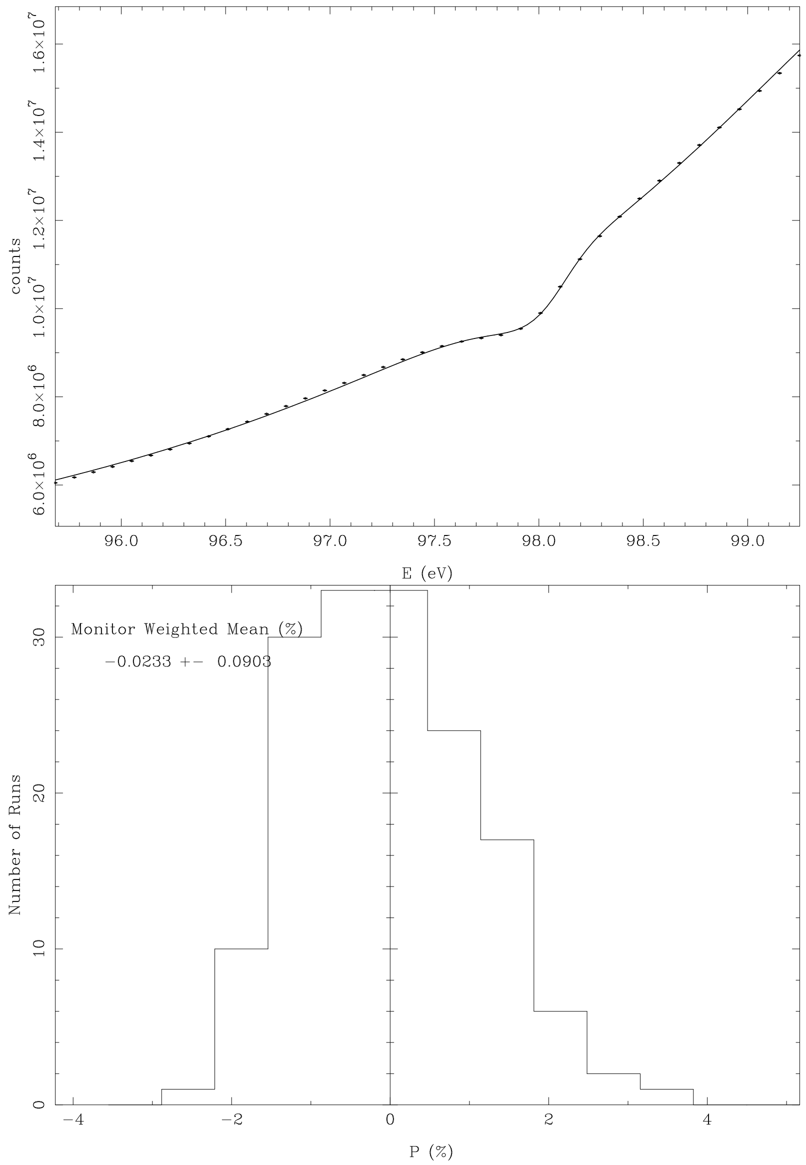

Figure C.69: Sample fit (top) and $\mathcal{P}$ histogram (bottom) for the 97.978 eV resonance in ^{238}U.

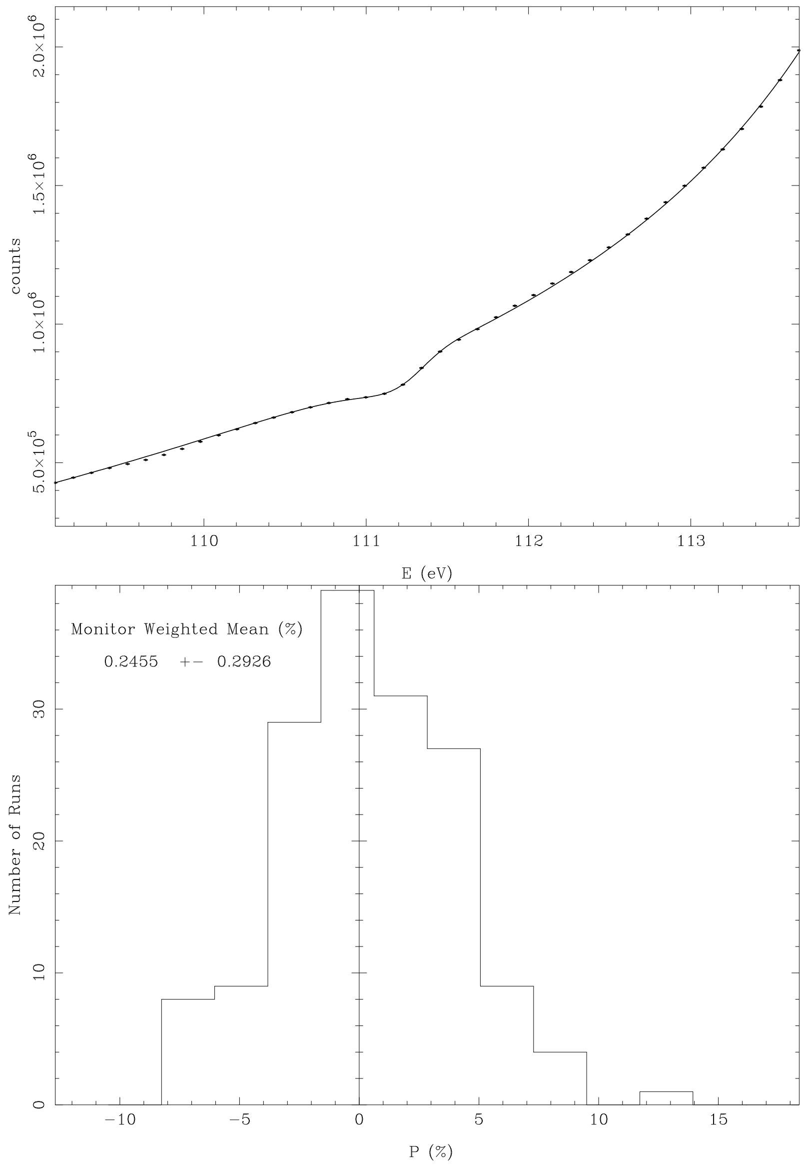

Figure C.70: Sample fit (top) and $\mathcal{P}$ histogram (bottom) for the 111.18 eV resonance in ^{238}U.

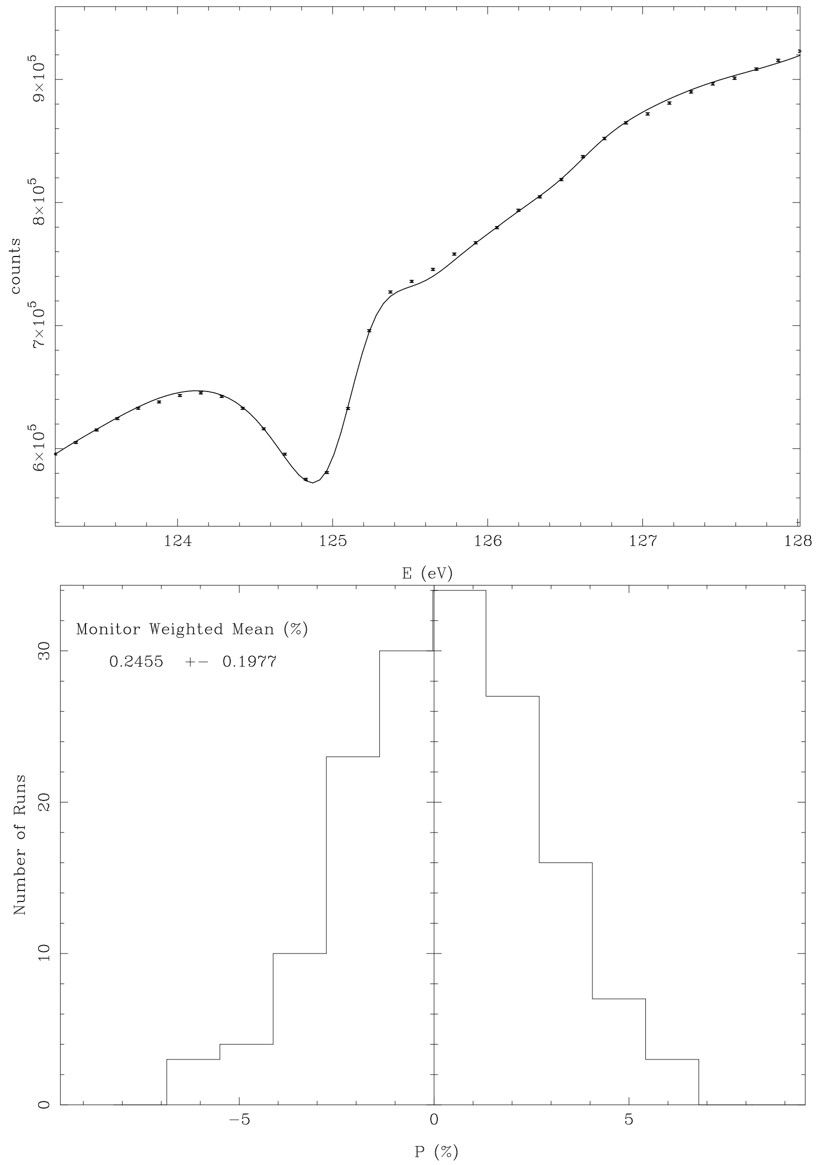

Figure C.71: Sample fit (top) and $\mathcal{P}$ histogram (bottom) for the 124.94 eV resonance in ^{238}U.

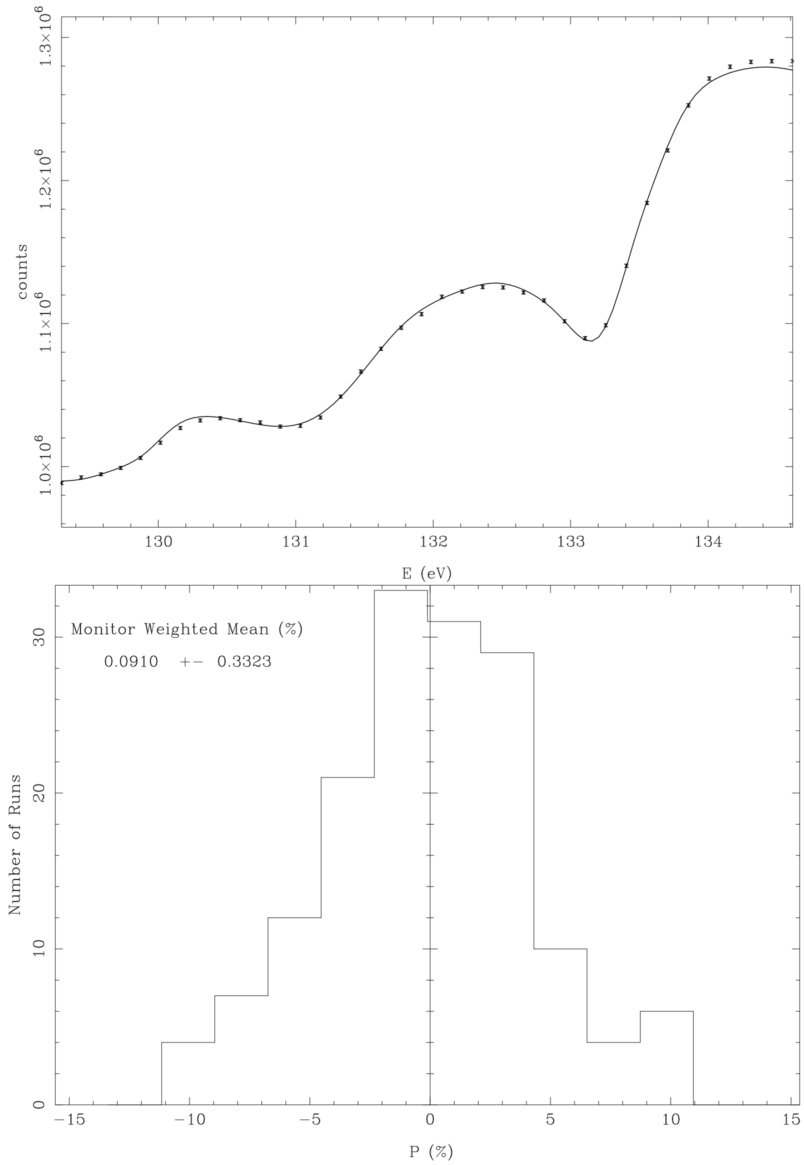

Figure C.72: Sample fit (top) and $\mathcal{P}$ histogram (bottom) for the 133.18 eV resonance in ^{238}U.

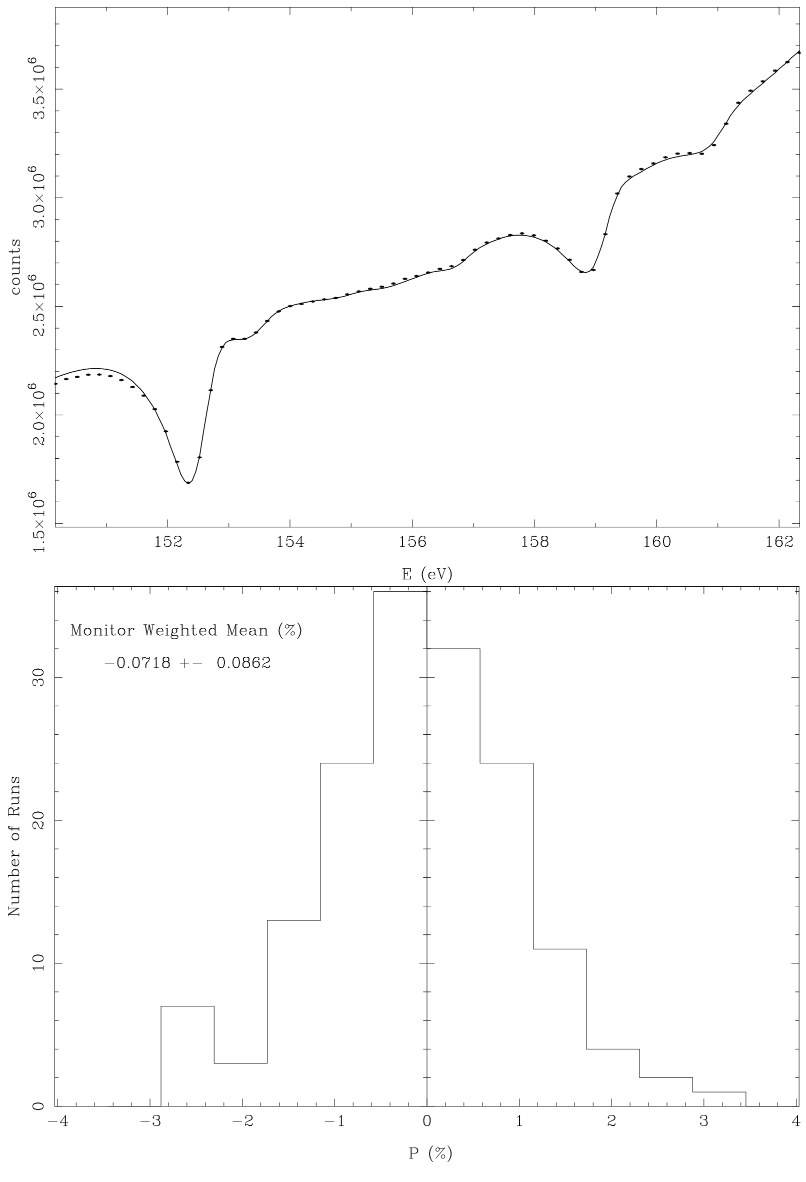

Figure C.73: Sample fit (top) for the 152.40 eV and 158.94 eV resonances and $\mathcal{P}$ histogram (bottom) for the 152.40 eV resonance in ^{238}U.

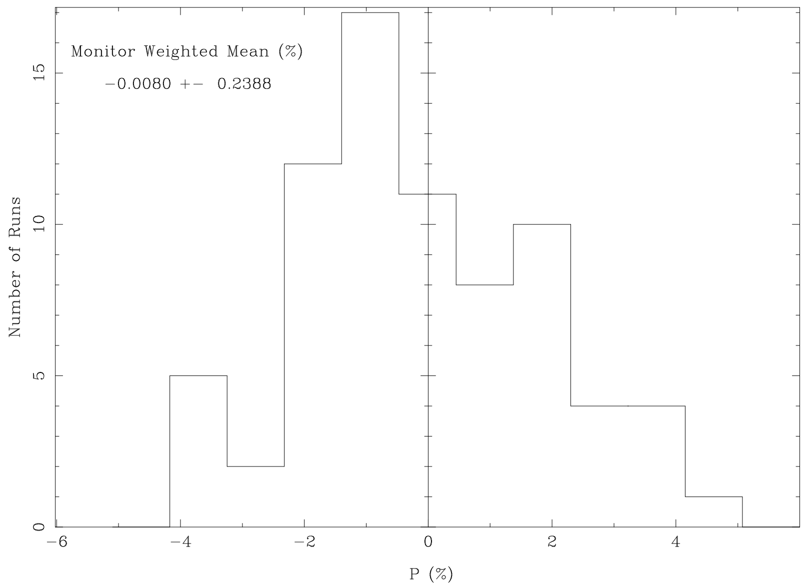

Figure C.74: $\mathcal{P}$ histogram for the 158.94 eV resonance in ^{238}U with the Boron filter only.

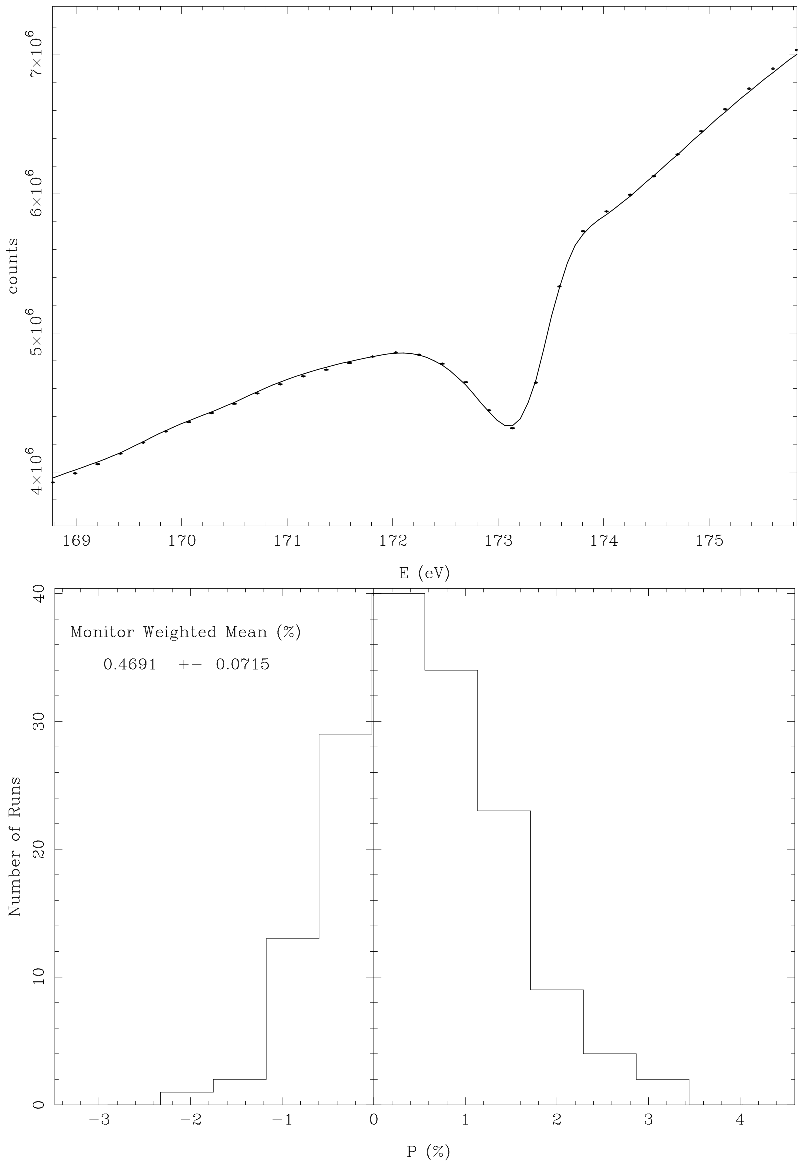

Figure C.75: Sample fit (top) and $\mathcal{P}$ histogram (bottom) for the 173.19 eV resonance in ^{238}U.

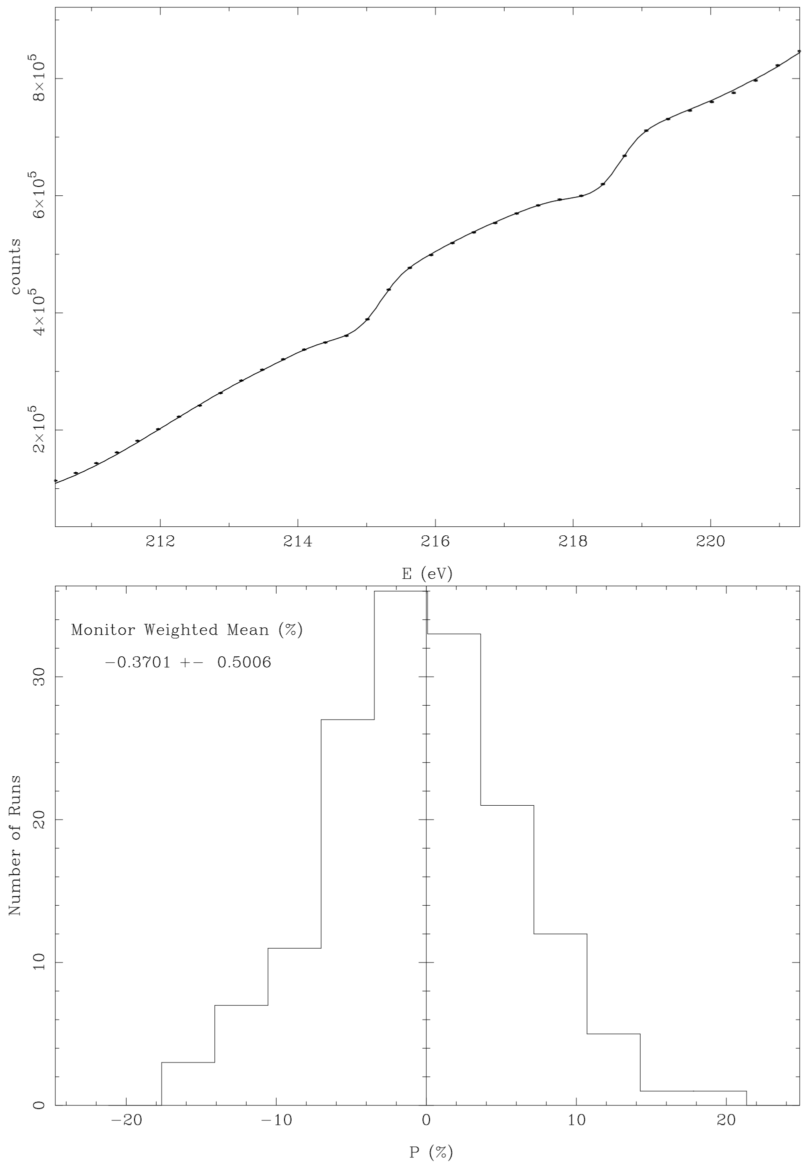

Figure C.76: Sample fit (top) of the 214.85 eV and 218.33 eV resonances and $\mathcal{P}$ histogram (bottom) for the 214.85 eV resonance in ^{238}U.

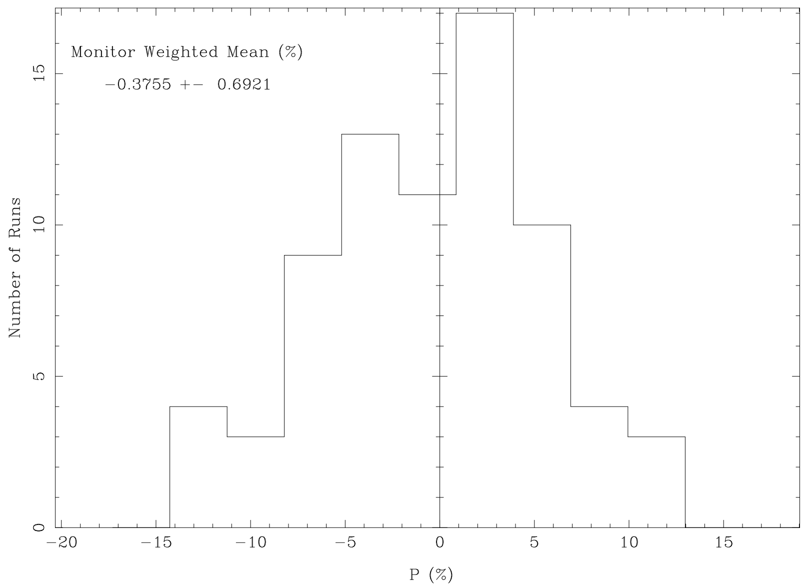

Figure C.77: $\mathcal{P}$ histogram for the 218.33 eV resonance in ^{238}U with the Boron filter only.

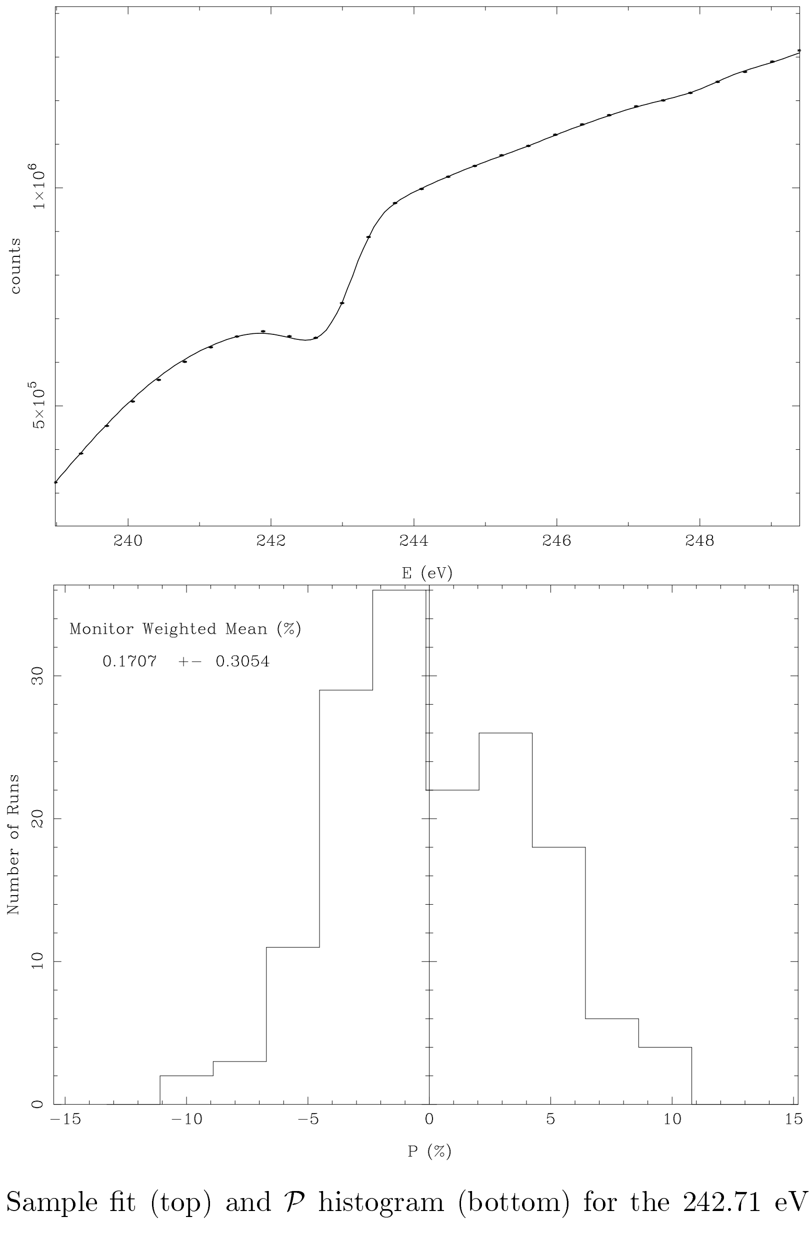

Figure C.78: Sample fit (top) and $\mathcal{P}$ histogram (bottom) for the 242.71 eV resonance in ^{238}U.

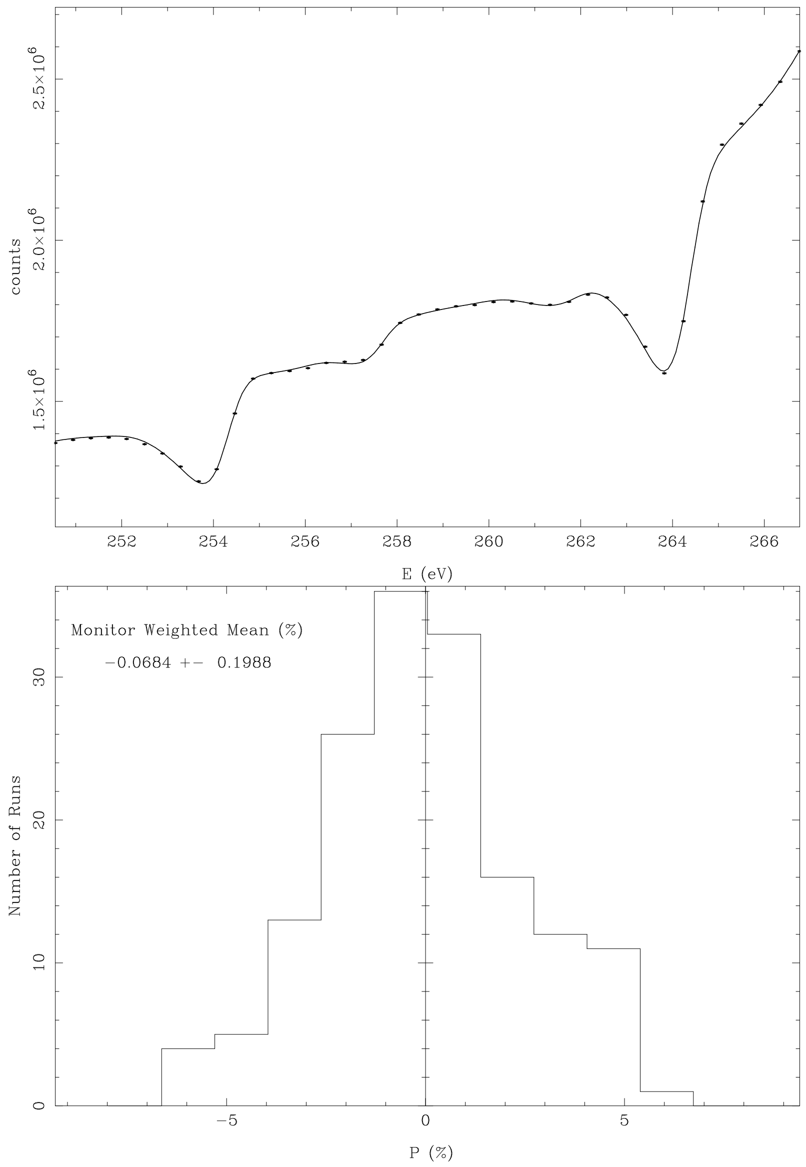

Figure C.79: Sample fit (top) of the 253.87 eV, 257.22 eV and 263.92 eV resonances and $\mathcal{P}$ histogram (bottom) for the 253.87 eV resonance in ^{238}U.

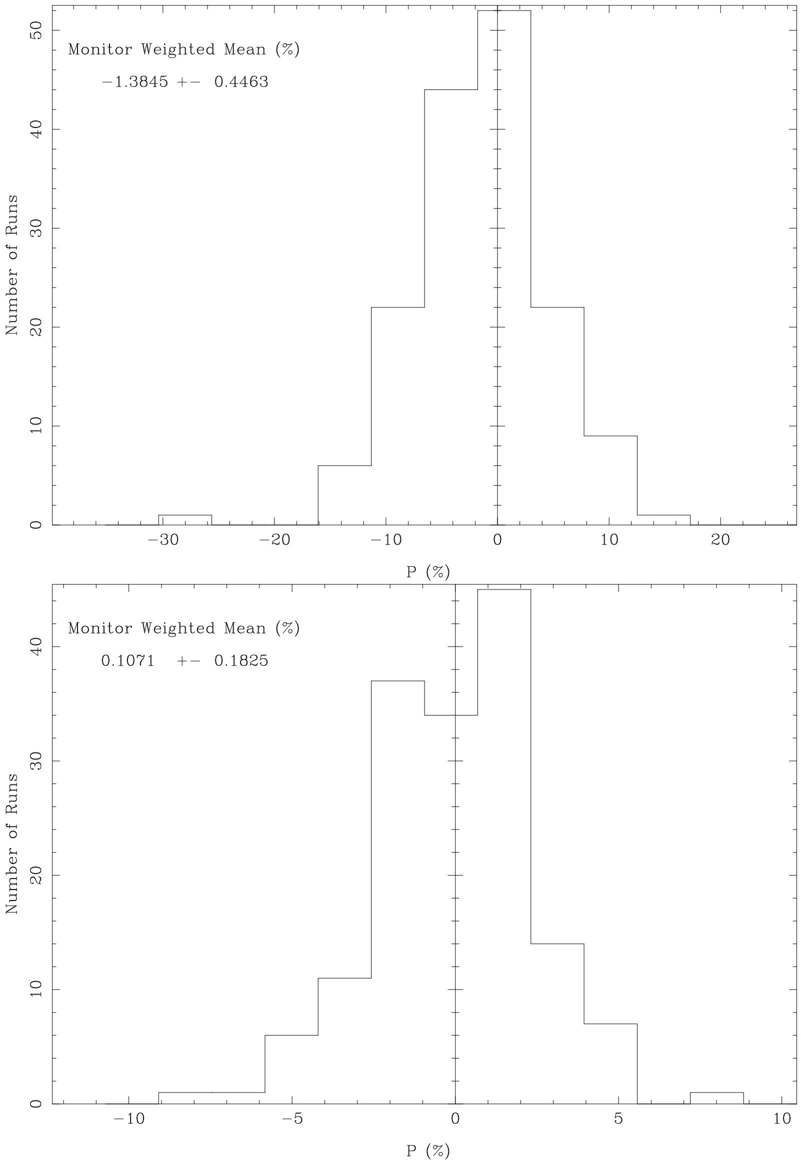

Figure C.80: $\mathcal{P}$ histograms for the 257.22 eV and 263.92 eV resonances in ^{238}U.

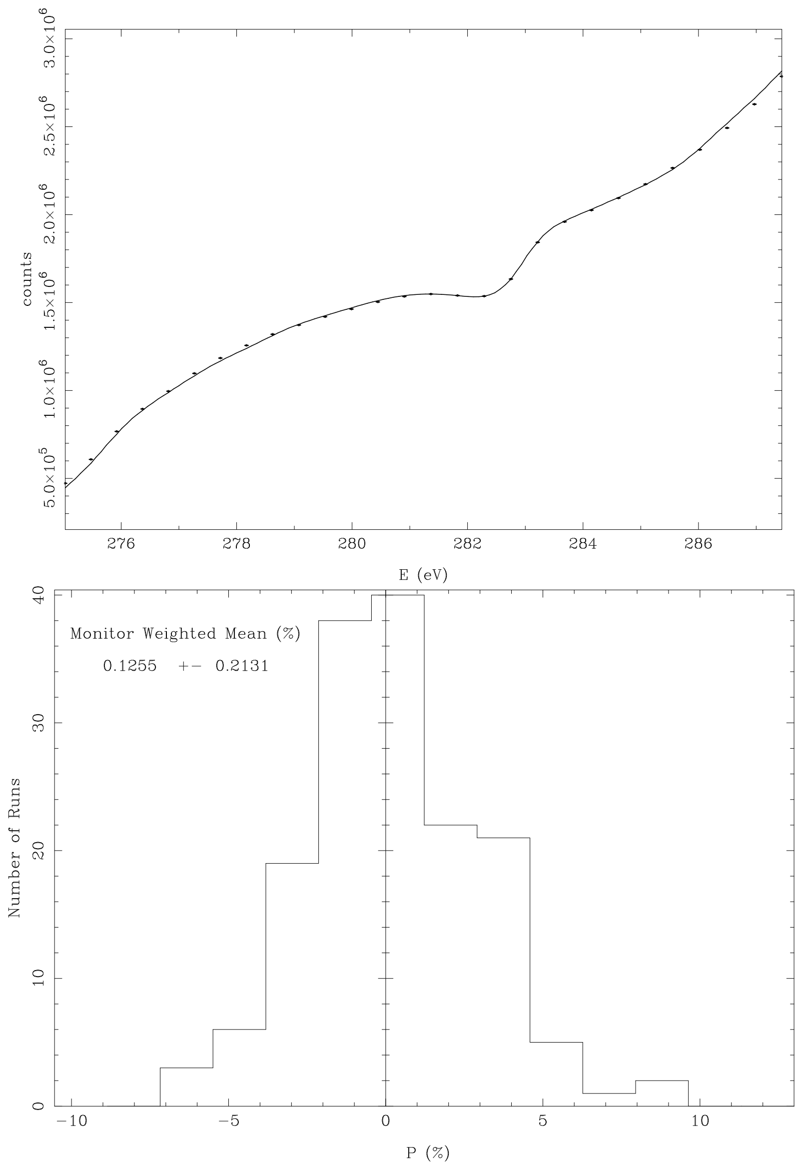

Figure C.81: Sample fit (top) and $\mathcal{P}$ histogram (bottom) for the 282.44 eV resonance in ^{238}U.

Bibliography

[Abo64] Yu. G. Abov, P. A. Krupchitskii, and Yu. A. Oratovskii. Physics Letters, **12**(1964) 25.

[Abo74] Yu. G. Abov, O. N. Ermakov, and P. A. Krupchitskii. *Violation of P Parity in the Reaction* $^{113}Cd(n,\gamma)^{114}Cd$. Soviet Physics JETP, **38**(1974) 870.

[Ade85] E. G. Adelberger and W. C. Haxton. *Parity Violation in the Nucleon-Nucleon Interaction.* Annual Review of Nuclear Particle Science, **35**(1985) 501–558.

[Alf83] V. P. Alfimenkov, S. B. Borzakov, Vo Van Thuan, Yu. D. Mareev, L. B. Pikelner, A. S. Khrykin, and E. I. Sharapov. *Parity Nonconservation in Neutron Resonances.* Nuclear Physics, **A398**(1983) 93–106.

[Ash76] Neil W. Ashcroft and N. David Mermin. *Solid State Physics.* Holt, Rinehart and Winston, New York, 1976.

[Boh88] Oriol Bohigas and Hans A. Weidenmüller. *Aspects of Chaos in Nuclear Physics.* Annual Review of Nuclear and Particle Science, **38**(1988) 421–453.

[Bol68] L. M. Bollinger and G. E. Thomas. *p-Wave Resonances of* ^{238}U. Physical Review, **171**(1968) 1293–1297.

[Bow93] J. D. Bowman, G. T. Garvey, Mikkel B. Johnson, and G. E. Mitchell. *Recent Advances in the Study of Parity Violation in the Compound Nucleus.* Annual Review of Nuclear Science, **43**(1993) 829–881.

[Bow96a] J. D. Bowman, L. Y. Lowie, G. E. Mitchell, E. I. Sharapov, and Y.-F. Yen. *Analysis of Parity Violation in Neutron Resonances.* Physical Review C, **53**(1996) 285.

[Bow96b] J. D. Bowman, S. I. Penttilä, and W. B. Tippens. *A Spin Reversal System for Polarized Epithermal Neutrons.* Nuclear Instruments and Methods in Physics Research, **A369**(1996) 195–204.

[Bun83] V. E. Bunakov and V. P. Gudkov. *Parity Violation and Related Effects in Neutron-Induced Reactions.* Nuclear Physics, **A401**(1983) 93–115.

[Cor94] F. Corvi, F. Gunsing, K. Athanassopulos, H. Postma, and A. Mauri. *The Spins of ^{238}U p-Wave Resonances.* In C. R. Gould, J. D. Bowman, and Yu. P. Popov, editors, *Time Reversal Invariance and Parity Violation in Neutron Resonances*, pages 79–83, Singapore, 1994. World Scientific.

[Des80] B. Desplanques, J. F. Donoghue, and B. R. Holstein. *Unified Treatment of the Parity Violating Nuclear Force.* Annals of Physics, **124**(1980) 449.

[Ead71] W. T. Eadie, D. Dryard, F. E. James, M. Roos, and B. Sadoulet. *Statistical Methods in Experimental Physics.* North Holland Publishing Company/ American Elsevier, 1971.

[Fes54] H. Feshbach, C. E. Porter, and V. F. Weisskopf. *Model for Nuclear Reactions with Neutrons.* Physical Review, **96**(1954) 448 – 464.

[Fod71] Anthony Foderaro. *The Elements of Neutron Interaction Theory.* The MIT Press, 1971.

[Fra91] Christen Mark Frankle. *Parity Nonconservation for Neutron Resonances in ^{81}Br and ^{232}Th.* Ph.D. thesis, North Carolina State University, 1991.

[Fra92] C. M. Frankle, J. D. Bowman, J. E. Bush, P. P. J. Delheij, C. R. Gould, D. G. Haase, J. N. Knudson, G. E. Mitchell, S. Penttilä, H. Postma, N. R. Roberson, S. J. Seestrom, J. J. Szymanski, S. H. Yoo, V. W. Yuan, and X. Zhu. *Parity Nonconservation for Neutron Resonances in ^{232}Th.* Physical Review C, **46**(1992) 779.

[Fra93a] C. M. Frankle, J. D. Bowman, S. J. Seestrom, N. R. Roberson, and E. I. Sharapov. *Measuring Parity Violation using the Neutron Capture Reaction.* In C. R. Gould, J. D. Bowman, and Yu P. Popov, editors, *Time Reversal Invariance and Parity Violation in Neutron Reactions*, page 204, Singapore, 1993. World Scientific.

[Fra93b] C. M. Frankle, S. J. Seestrom, Yu. P. Popov, E. I. Sharapov, and N. R. Roberson. *Recent Developments in the Study of Parity Violation in Neutron p Resonances.* Physics of Particles and Nuclei, **24**(1993) 401.

[Fra94] C. M. Frankle, E. I. Sharapov, Yu. P. Popov, J. A. Harvey, N. W. Hill, and L. W. Weston. *Neutron Resonance Spectroscopy on ^{113}Cd to $E_n = 15$ keV.* Physical Review C, **50**(1994) 2774–2785.

[Gil65] A. Gilbert and A. G. W. Cameron. *A Composite Nuclear-Level Density Formula with Shell Corrections.* Canadian Journal of Physics, **43**(1965) 1446.

[Gro84] Particle Data Group. *Review of Particle Properties.* Reviews of Modern Physics, **56, No. 2, Part II**(1984).

[Gro97] Cross Section Evaluation Working Group. *ENDF-102 Data Formats and Procedures for the Evaluated Nuclear Data File ENDF-6: BNL-NCS-44945.* Technical report, Brookhaven National Laboratory, 1997.

[Guh90] T. Guhr and H. A. Weidenmüller. *Isospin Mixing and Spectral Fluctuation Properties.* Annals of Physics, **199**(1990) 412–446.

[Haq82] R. U. Haq, A. Pandey, and O. Bohigas. *Fluctuation Properties of Nuclear Energy Levels: Do Theory and Experiment Agree?* Physical Review Letters, **48**(1982) 1086–1089.

[Har86] H. L. Harney, A. Richter, and H. A. Weidenmüller. *Breaking of Isospin Symmetry in Compound-Nucleus Reactions.* Reviews of Modern Physics, **58**(1986) 607–645.

[Jac75] John David Jackson. *Classical Electrodynamics.* John Wiley and Sons, New York, second edition, 1975.

[Joh91] Mikkel B. Johnson, J. D. Bowman, and S. H. Yoo. *Theory of Parity Nonconservation in Compound-Nuclear States.* Physical Review Letters, **67**(1991) 310–313.

[Kru87] P. A. Krupchitsky. *Fundamental Research with Polarized Slow Neutrons.* Springer-Verlag, Heidelberg, 1987. transl. by V. I. Kisin.

[Lan58] A. M. Lane and R. G. Thomas. *R-Matrix Theory of Nuclear Reactions.* Reviews of Modern Physics, **30**(1958) 257–353.

[Lee56] T. D. Lee and C. N. Yang. *Question of Parity Conservation in Weak Interactions.* Physical Review, **104**(1956) 254–258.

[Lis90] P. W. Lisowski et al. *The Los Alamos National Laboratory Spallation Neutron Sources.* Nuclear Science and Engineering, **106**(1990) 208–218.

[Low96] Lisa Yates Lowie. *Parity Nonconservation in Neutron Resonance in Mass $\approx$ 100 Nuclei.* Ph.D. thesis, North Carolina State University, 1996.

[Lyn68] John E. Lynn. *The Theory of Neutron Resonance Reactions.* Clarendon Press, Oxford, 1968.

[Mal70] H. Malecki, L. B. Pikel'ner, I. M. Salamatin, and E. I. Sharapov. *Statistical Analysis of the Spin Dependence of Neutron Strength Functions of Nuclei.* Soviet Journal of Nuclear Physics, **11**(1970) 61.

[Mas89] Y. Masuda, T. Adachi, A. Masaike, and K. Morimoto. *Longitudinal Asymmetry in a Neutron Radiative Capture Reaction of* ^{139}La. Nuclear Physics, **A504**(1989) 269–276.

[Mat97] Yasuyuki Matsuda. Ph.D. thesis, Kyoto University, 1997. unpublished.

[Mel53] E. Melkonian, W. W. Havens, Jr., and L. J. Rainwater. *Slow Neutron Velocity Spectrometer Studies. V, Re, Ta, Ru, Cr, Ga.* Physical Review, **92**(1953) 702.

[Mit85] G. E. Mitchell, E. G. Bilpuch, J. F. Shriner, Jr., and A. M. Lane. *Angular Correlations in Nuclear Resonance Spectroscopy.* Physics Reports, **117**(1985) 1.

[Mit88] G. E. Mitchell, E. G. Bilpuch, P. M. Endt, and J. F. Shriner, Jr. *Broken Symmetries and Chaotic Behavior in* ^{26}Al. Physical Review Letters, **61**(1988) 1473.

[Mox88] M. C. Moxon and M. G. Sowerby. ^{238}U *Resolved Resonance Parameters.* Proceedings of the 1988 International Reactor Physics Conference, Jackson Hole, Wyoming, **1**(1988) 281–291.

[Mug88a] S. F. Mughabghab. *Neutron Cross Sections*, volume 1 Part B. Academic Press, Inc., 1988.

[Mug88b] S. F. Mughabghab, M. Divadeenam, and N. E. Holden. *Neutron Cross Sections*, volume 1 Part A. Academic Press, Inc., 1988.

[Ols79] D. K. Olsen, G. de Saussure, R. B. Perez, F. C. Difilippo, R. W. Ingle, and H. Weaver. *Measurement and Resonance Analysis of Neutron Transmission Through Uranium-238.* Nuclear Science and Engineering, **69**(1979) 202–222.

[Pen94] Seppo Penttilä, J. D. Bowman, P. P. J. Delheij, C. M. Frankle, D. G. Haase, R. Mortensen, H. Postma, S. J. Seestrom, and Yi-Fen Yen. *Cryogenic Spin Filter for Polarizing an Epithermal Neutron Beam.* In C. R. Gould, J. D. Bowman, and Yu P. Popov, editors, *Time Reversal Invariance and Parity Violation in Neutron Reactions*, pages 198–203. World Scientific, 1994.

[Per87] Donald H. Perkins. *Introduction to High Energy Physics.* Addison-Wesley Publishing Company, Inc., Reading, third edition, 1987.

[Pos96] H. Postma, F. Gunsing, and F. Corvi. *Improved Analysis of Parity Violation at Neutron p-wave Resonances of* ^{238}U *Based on Resonance Spin Assignments.* Physical Review C, **53**(1996) R558.

[Pre92] William H. Press, Saul A. Teukolskii, William T. Vetterling, and Brian P. Flannery. *Numerical Recipes in Fortran: The Art of Scientific Computing.* Cambridge University Press, 1992.

[Rei58] C. W. Reich and M. S. Moore. *Multilevel Formula for the Fission Process.* Physical Review, **111**(1958) 929–933.

[Rob93] N. R. Roberson, C. D. Bowman, J. D. Bowman, P. P. J. Delheij, C. M. Frankle, C. R. Gould, D. G. Haase, J. N. Knudson, G. E. Mitchell, R. N. Mortensen, S. I. Penttilä, H. Postma, S. J. Seestrom, J. J. Szymanski, S. A. Wender, S. H. Yoo, V. W. Yuan, and X. Zhu. *An Apparatus and Techniques of Tests for Fundamental Symmetries in Compound-Nucleus Scattering with Epithermal Polarized Neutron Beams.* Nuclear Instruments and Methods in Physics Research, **A326**(1993) 549–565.

[Rus91] Gary Russell. *Spallation Physics.* From the tip of LANSCE, (1991) 1.

[See97] S. J. Seestrom, J. D. Bowman, B. E. Crawford, P. P. J. Delheij, C. M. Frankle, C. R. Gould, D. G. Haase, M. Iinuma, J. N. Knudson, P. E. Koehler, L. Y. Lowie, A. Masaike, Y. Masuda, Y. Matsuda, G. E. Mitchell, S. I. Penttilä, Yu. P. Popov, H. Postma, N. R. Roberson, E. I. Sharapov, H. M. Shimizu, D. A. Smith, S. L. Stephenson, Y. F. Yen, and V. W. Yuan. *Parity Nonconservation in Neutron Capture on* ^{113}Cd*.* To be submitted to Physical Review C, 1997.

[Sha91] E. I. Sharapov, S. A. Wender, H. Postma, S. J. Seestrom, C. R. Gould, O. A. Wasson, Yu. P. Popov, and C. D. Bowman. *The Measurements of Parity Violation in Resonant Neutron-Capture Reactions.* In Richard W. Hoff, editor, *Capture-Gamma Ray Spectroscopy*, page 756, New York, 1991. American Institute of Physics.

[Sha95] Eduard I. Sharapov, Yasuyuki Masuda, Yasuyuki Matsuda, N. Niimura, and H. Shimizu. *Doppler Broadening of Parity–Violating Lanthanum Resonance at* $E_p = 0.75\ eV$*.* unpublished, 1995.

[Shi93] H. M. Shimizu, Y. Adachi, L. Ishimoto, A. Masaike, Y. Masuda, and K. Morimoto. *Longitudinal Asymmetry and* γ*-ray Angular Distribution in Neutron Radiative Capture Reactions.* Nuclear Physics, **A552**(1993) 293.

[Sli90] Charles P. Slichter. *Principles of Magnetic Resonance.* Springer, New York, third edition, 1990.

[Smi97a] D. A. Smith, 1997. private communication.

[Smi97b] D. A. Smith. *Parity Violating Asymmetries in* ^{117}Sn*.* Bulletin of the American Physical Society, **42**(1997) 1071.

[Ste96] Sharon Louise Stephenson. *Parity Violation in* ^{232}Th *— A Study of the 'Sign Effect'.* Ph.D. thesis, North Carolina State University, 1996.

[Sus80] O. P. Sushkov and V. V. Flambaum. *Possibility of observing parity nonconservation in neutron optics.* JETP Letters, **32**(1980) 352–354.

[Sus82] O. P. Sushkov and V. V. Flambaum. *Parity Breaking in the Interaction of Neutrons with Heavy Nuclei.* Soviet Physics Uspekhi, **25**(1982) 1–12.

[Szy94] J. J. Szymanski, J. D. Bowman, P. P. J. Delheij, J. Knudson C. M. Frankle, S. Penttilä, S. J. Seestrom, S. H. Yoo, V. W. Yuan, and X. Zhu. *Ion Chamber System for Neutron Flux Measurements.* Nuclear Instruments and Methods in Physics Research, **A340**(1994) 564–571.

[Van88] J. R. Vanhoy, E. G. Bilpuch, J. F. Shriner, Jr., and G. E. Mitchell. *Nuclear Spectroscopy of Parity-Nonconserving Neutron Resonance Experiments.* Zeitschrift für Physik A, **331**(1988) 1–10.

[vE88] T. von Egidy, H. H. Schmidt, and A. N. Behkami. *Nuclear Level Densities and Level Spacing Distributions: Part II.* Nuclear Physics, **A481**(1988) 189.

[Wei89] Hans A. Weidenmüller. *What Can We Learn From tests of Fundamental Symmetries in Compound-Nucleus Reactions?* In *Fundamental Symmetries in Nuclei and Particles*, page 30. World Scientific, Singapore, 1989.

[Wig47] E. P. Wigner and L. Eisenbud. Physical Review, **72**(1947) 29.

[Wil93] Wesley Scott Wilburn. *Measurements of the Transverse Spin-Dependent Total Cross Section Differences for the Scattering of Polarized Neutrons from Polarized Protons.* Ph.D. thesis, Duke University, 1993.

[Wil95] W. S. Wilburn. private communication, 1995.

[Wu57] C. S. Wu, E. Ambler, R. W. Hayward, D. D. Hoppes, and R. P. Hudson. *Experimental Test of Parity Conservation in Beta Decay.* Physical Review, **105**(1957) 1413–1414.

[Yen94] Yi-Fen Yen, J. D. Bowman, Y. Matsuda, Seppo Penttilä, S. J. Seestrom, H. M. Shimizu, R. W. Strickland, S. Takahashi, S. H. Yoo, and V. W. Yuan. *500-MHz Neutron Detector.* In C. R. Gould, J. D. Bowman, and Yu P. Popov, editors, *Time Reversal Invariance and Parity Violation in Neutron Reactions*, pages 210–219. World Scientific, 1994.

[Yen96a] Yi-Fen Yen. private communication, 1996.

[Yen96b] Yi-Fen Yen, E. J. Pitcher, and J. D. Bowman. *Neutron Moderation Time — A Comparison Between Model Prediction and Experimental Observation.* unpublished, 1996.

[Yen97] Yi-Fen Yen, J. D. Bowman, L. Y. Lowie, Y. Masuda, and G. E. Mitchell. *Determination of the Gamma-ray Background in a Pulsed Epithermal Neutron Beam.* accepted for publication by Nuclear Instruments and Methods in Physics Research, 1997.

[Yua91] Vincent W. Yuan, C. D. Bowman, J. D. Bowman, J. E. Bush, P. P. J. Delheij, C. M. Frankle, C. R. Gould, D. G. Haase, J. J. Szymanski, B. Tippens, and X. Zhu. *Parity Nonconservation in Polarized-Neutron Transmission through* ^{139}La. Physical Review C, **44**(1991) 2187.

[Zan97] L. Zanini, F. Corvi, H. Postma, and K. Athanassopulos. *Spin and Parity Studies of* ^{107}Ag *and* ^{109}Ag *Neutron Resonances.* To be published in *V International Seminar on Interactions of Neutrons with Nuclei*, 1997.

[Zhu91] Xianzhou Zhu. *Measurement of the RMS parity violating matrix element in* ^{239}U. Ph.D. thesis, Duke University, 1991.

[Zhu92] Xianzhou Zhu, J. D. Bowman, C. D. Bowman, J. E. Bush, P. P. J. Delheij, C. M. Frankle, C. R. Gould, D. G. Haase, J. N. Knudson, G. E. Mitchell, S. Penttilä, H. Postma, N. R. Roberson, S. J. Seestrom, J. J. Szymanski, and V. W. Yuan. *Parity Nonconservation for Neutron Resonances in* ^{239}U. Physical Review C, **46**(1992) 768.

Biography

Bret Edward Crawford

Personal: Born 22 June 1966, Livermore, CA

Education:

M.A. in Physics, Duke University, Durham, NC, May 1995

M.S. in Physics, University of Vermont, Burlington, VT, October 1991

B.S. in Electrical Engineering, University of South Carolina, Columbia, SC, May 1989

Fellowships and Honors:

Henry W. Newson Fellow, Department of Physics, Duke University, 1996-1997

Charles H. Townes Fellowship, Department of Physics, Duke University, 1992-1995

Selected Publications (three of 25):

"Apparatus for Capture γ-ray Studies of Parity Violation at Los Alamos", B. E. Crawford, J. D. Bowman, C. M. Frankle, T. Haseyama, A. Masaike, Y. Matsuda, S. I. Penttilä, N. R. Roberson, S. J. Seestrom, E. I. Sharapov, S. L. Stephenson, *IV International Seminar on Interactions of Neutrons with Nuclei*, Dubna, Russia (1996) 268

"Resonant Cavities in the History of Architectural Acoustics", Robert G. Arns and Bret Crawford, Technology and Culture **36** No. 1, (1995) 104

The Invention of the Transistor, B. E. Crawford, Masters Thesis, University of Vermont, Burlington, VT (1991)

Selected Abstracts (one of four):

"Parity Violation in Neutron Resonances in ^{106}Pd and ^{108}Pd", B. E. Crawford et al., Bulletin of the American Physical Society **42**, (1997) 1071